



**HAL**  
open science

# Study and manufacturing of biosensors based on plasmonic effects and built on silicon

Michele Calvo

► **To cite this version:**

Michele Calvo. Study and manufacturing of biosensors based on plasmonic effects and built on silicon. Electronics. Université de Lyon, 2020. English. NNT : 2020LYSEI055 . tel-03125744

**HAL Id: tel-03125744**

**<https://theses.hal.science/tel-03125744>**

Submitted on 29 Jan 2021

**HAL** is a multi-disciplinary open access archive for the deposit and dissemination of scientific research documents, whether they are published or not. The documents may come from teaching and research institutions in France or abroad, or from public or private research centers.

L'archive ouverte pluridisciplinaire **HAL**, est destinée au dépôt et à la diffusion de documents scientifiques de niveau recherche, publiés ou non, émanant des établissements d'enseignement et de recherche français ou étrangers, des laboratoires publics ou privés.



UNIVERSITÉ DE  
SHERBROOKE

N°d'ordre NNT : 2020LYSEI055

**THESE de DOCTORAT DE L'UNIVERSITE DE LYON**

opérée au sein de

**L'institut national des sciences appliquées de Lyon**

En cotutelle internationale avec

**L'Université de Sherbrooke**

**Ecole Doctorale N° 160**

**Electronique, Electrotechnique et Automatique**

**Electronique, Micro et Nano-électronique, Optique et Laser /  
Nanophotonique**

Soutenue publiquement le 21/07/2020, par :

**Michele Calvo**

---

**Étude et réalisation de capteurs  
biologiques à base d'effets  
plasmoniques et fabriqués sur silicium**  
**Study and manufacturing of biosensors based on  
plasmonic effects and built on silicon**

---

Devant le jury composé de :

MONAT Christelle	Professeure Ecole Centrale de Lyon	Examinatrice (jury français)
WEEBER Jean Claude	Professeur ICB Dijon	Rapporteur
LERONDEL Gilles	Professeur UTT Troyes	Rapporteur
MENEZO Sylvie	Docteure SCINTIL Photonics	Examinatrice (jury français)
MELLONI Andrea	Professeur Politecnico di Milano	Examinateur (jury français)
CANVA Michael	Directeur de Recherche CNRS	Examinateur
OROBTCHOUK Régis	Maître de conférences INSA Lyon	Directeur de thèse
CHARETTE Paul	Professeur Université de Sherbrooke	Directeur de thèse
MONFRAY Stéphane	Ingénieur STMICROELECTRONICS	Invité (jury français)



## Département FEDORA – INSA Lyon - Ecoles Doctorales

### Quinquennal 2016-2020

SIGLE	ECOLE DOCTORALE	NOM ET COORDONNEES DU RESPONSABLE
<b>CHIMIE</b>	<b><u>CHIMIE DE LYON</u></b> <a href="http://www.edchimie-lyon.fr">http://www.edchimie-lyon.fr</a> Sec. : Renée EL MELHEM Bât. Blaise PASCAL, 3e étage <a href="mailto:secretariat@edchimie-lyon.fr">secretariat@edchimie-lyon.fr</a> INSA : R. GOURDON	M. Stéphane DANIELE Institut de recherches sur la catalyse et l'environnement de Lyon IRCELYON-UMR 5256 Équipe CDFA 2 Avenue Albert EINSTEIN 69 626 Villeurbanne CEDEX <a href="mailto:directeur@edchimie-lyon.fr">directeur@edchimie-lyon.fr</a>
<b>E.E.A.</b>	<b><u>ÉLECTRONIQUE, ÉLECTROTECHNIQUE, AUTOMATIQUE</u></b> <a href="http://edeea.ec-lyon.fr">http://edeea.ec-lyon.fr</a> Sec. : M.C. HAVGOUDOUKIAN <a href="mailto:ecole-doctorale.eea@ec-lyon.fr">ecole-doctorale.eea@ec-lyon.fr</a>	M. Gérard SCORLETTI École Centrale de Lyon 36 Avenue Guy DE COLLONGUE 69 134 Écully Tél : 04.72.18.60.97 Fax 04.78.43.37.17 <a href="mailto:gerard.scorletti@ec-lyon.fr">gerard.scorletti@ec-lyon.fr</a>
<b>E2M2</b>	<b><u>ÉVOLUTION, ÉCOSYSTÈME, MICROBIOLOGIE, MODÉLISATION</u></b> <a href="http://e2m2.universite-lyon.fr">http://e2m2.universite-lyon.fr</a> Sec. : Sylvie ROBERJOT Bât. Atrium, UCB Lyon 1 Tél : 04.72.44.83.62 INSA : H. CHARLES <a href="mailto:secretariat.e2m2@univ-lyon1.fr">secretariat.e2m2@univ-lyon1.fr</a>	M. Philippe NORMAND UMR 5557 Lab. d'Ecologie Microbienne Université Claude Bernard Lyon 1 Bâtiment Mendel 43, boulevard du 11 Novembre 1918 69 622 Villeurbanne CEDEX <a href="mailto:philippe.normand@univ-lyon1.fr">philippe.normand@univ-lyon1.fr</a>
<b>EDISS</b>	<b><u>INTERDISCIPLINAIRE SCIENCES- SANTÉ</u></b> <a href="http://www.ediss-lyon.fr">http://www.ediss-lyon.fr</a> Sec. : Sylvie ROBERJOT Bât. Atrium, UCB Lyon 1 Tél : 04.72.44.83.62 INSA : M. LAGARDE <a href="mailto:secretariat.ediss@univ-lyon1.fr">secretariat.ediss@univ-lyon1.fr</a>	Mme Emmanuelle CANET-SOULAS INSERM U1060, CarMeN lab, Univ. Lyon 1 Bâtiment IMBL 11 Avenue Jean CAPELLE INSA de Lyon 69 621 Villeurbanne Tél : 04.72.68.49.09 Fax : 04.72.68.49.16 <a href="mailto:emmanuelle.canet@univ-lyon1.fr">emmanuelle.canet@univ-lyon1.fr</a>
<b>INFOMATHS</b>	<b><u>INFORMATIQUE ET MATHÉMATIQUES</u></b> <a href="http://edinfomaths.universite-lyon.fr">http://edinfomaths.universite-lyon.fr</a> Sec. : Renée EL MELHEM Bât. Blaise PASCAL, 3e étage Tél : 04.72.43.80.46 <a href="mailto:infomaths@univ-lyon1.fr">infomaths@univ-lyon1.fr</a>	M. Luca ZAMBONI Bât. Braconnier 43 Boulevard du 11 novembre 1918 69 622 Villeurbanne CEDEX Tél : 04.26.23.45.52 <a href="mailto:zamboni@maths.univ-lyon1.fr">zamboni@maths.univ-lyon1.fr</a>
<b>Matériaux</b>	<b><u>MATÉRIAUX DE LYON</u></b> <a href="http://ed34.universite-lyon.fr">http://ed34.universite-lyon.fr</a> Sec. : Stéphanie CAUVIN Tél : 04.72.43.71.70 Bât. Direction <a href="mailto:ed.materiaux@insa-lyon.fr">ed.materiaux@insa-lyon.fr</a>	M. Jean-Yves BUFFIÈRE INSA de Lyon MATEIS - Bât. Saint-Exupéry 7 Avenue Jean CAPELLE 69 621 Villeurbanne CEDEX Tél : 04.72.43.71.70 Fax : 04.72.43.85.28 <a href="mailto:jean-yves.buffiere@insa-lyon.fr">jean-yves.buffiere@insa-lyon.fr</a>

<p><b>MEGA</b></p>	<p><b><u>MÉCANIQUE, ÉNERGÉTIQUE, GÉNIE CIVIL, ACOUSTIQUE</u></b></p> <p><a href="http://edmega.universite-lyon.fr">http://edmega.universite-lyon.fr</a>          Sec. : Stéphanie CAUVIN          Tél : 04.72.43.71.70          Bât. Direction <a href="mailto:mega@insa-lyon.fr">mega@insa-lyon.fr</a></p>	<p><b>M. Jocelyn BONJOUR</b>          INSA de Lyon          Laboratoire CETHIL          Bâtiment Sadi-Carnot          9, rue de la Physique          69 621 Villeurbanne CEDEX <a href="mailto:jocelyn.bonjour@insa-lyon.fr">jocelyn.bonjour@insa-lyon.fr</a></p>
<p><b>ScSo</b></p>	<p><b><u>ScSo*</u></b></p> <p><a href="http://ed483.univ-lyon2.fr">http://ed483.univ-lyon2.fr</a>          Sec. : Véronique GUICHARD          INSA : J.Y. TOUSSAINT          Tél : 04.78.69.72.76  <a href="mailto:veronique.cervantes@univ-lyon2.fr">veronique.cervantes@univ-lyon2.fr</a></p>	<p><b>M. Christian MONTES</b>          Université Lyon 2          86 Rue Pasteur          69 365 Lyon CEDEX 07 <a href="mailto:christian.montes@univ-lyon2.fr">christian.montes@univ-lyon2.fr</a></p>

\*ScSo : Histoire, Géographie, Aménagement, Urbanisme, Archéologie, Science politique, Sociologie, Anthropologie

# RESUME

Les dispositifs laboratoire sur puce (ou Lab-on-a-chip ou LOC) visent à miniaturiser les procédés de laboratoires pour la détection des maladies et la surveillance des patients malades, sans avoir besoin de laboratoires médicaux. Deux exemples bien connus de LOC sont les kits de test de grossesse ou les capteurs portables du VIH.

Pour être efficaces, les appareils LOC doivent être sensibles, spécifiques à l'analyte concerné, compacts et abordables. Ces critères sont possibles grâce à un transducteur, qui peut convertir la présence biologique de la molécule cible en informations électriques. Depuis le début des années 2000, la photonique intégrée a offert une solution pour un système de transduction compatible avec les besoins du LOC. En particulier, les micro-résonateurs à anneaux en silicium représentent un transducteur compact et sensible adapté aux appareils LOC.

En accord avec les exigences des dispositifs LOC, l'objectif de ce projet est de concevoir et d'évaluer les performances d'un biocapteur photonique compact. Le système sera basé sur une transduction photonique intégrée. Les exigences sont : une simple fonctionnalisation, la compatibilité avec une plateforme de fabrication industrielle et des systèmes fluidiques, avec une sensibilité égale ou supérieure à l'état de l'art. Ce projet détaille la conception, la fabrication et la caractérisation d'un tel biocapteur.

Nous avons constaté que les résonateurs en anneau avec une section transversale de guide d'ondes hybrides plasmoniques (HPWG) remplissent les exigences LOC et sont compétitifs en comparaison avec l'état de l'art des biocapteurs photoniques. Par ailleurs, basée sur un principe appelé *mode lift*, une nouvelle géométrie de HPWG a été brevetée et fera l'objet d'un article. Nous avons simulé la structure HPWG pour comprendre les mécanismes de couplage des modes photoniques à l'intérieur de la structure (plus précisément les modes plasmoniques et les modes diélectriques du guide d'onde à ruban). La fabrication a été possible grâce à la collaboration de la salle blanche industrielle de STMicroelectronics et des salles blanches universitaires de l'université de Sherbrooke et de l'Institut de Nanotechnologies de Lyon. Un avantage de la production industrielle est que nous pouvons créer de manière reproductible la géométrie des composants nécessaires pour le LOC à haut débit, réduisant ainsi le coût par unité. Une fois que les wafers de 300 mm ont été structurés, le processus de fabrication en salle blanche universitaire permet d'ajouter le métal des guides d'ondes plasmoniques. La méthode du *lift-off* a été utilisée pour la nanostructuration Au sur les dispositifs caractérisés dans ce projet.

Des mesures préliminaires ont permis de définir le liquide d'essai optimal (glucose monohydrate) ainsi que l'incertitude des mesures. Les échantillons HPWG ont montré une sensibilité expérimentale inférieure aux simulations. Après avoir ajusté les paramètres de fabrication (principalement les taux et les épaisseurs de dépôt d'au et de Cr), les dispositifs HPWG de deuxième génération suggèrent que le *mode lift* améliore la sensibilité des guides d'ondes en dessous de la coupure (la sensibilité augmente de 210 nm/RIU à 320 nm/RIU lorsque seulement 10 % du résonateur en anneau a une section HPWG). Même par rapport aux guides d'ondes au-dessus de la coupure, la sensibilité augmente de 40 nm/RIU lors de l'utilisation du *mode lift*. Nous avons également montré la compatibilité de la surface des appareils fabriqués avec la fonctionnalisation différentielle en utilisant des nanoparticules

fluorescentes. Pour des contraintes de temps, la présence des nanoparticules ne sera mesurée que dans des futures expériences.

**Mots-clés** : Lab-on-a-chip, photonique, plasmonique, photonique intégrée, résonateur en anneau, biocapteurs.

# ABSTRACT

Lab-on-a-chip (or LOC) devices scale down the laboratory processes for detecting illnesses and monitoring sick patients without the need of medical laboratories. Well-known examples of LOC are pregnancy test kits or portable HIV sensors. To be useful, LOC devices must be sensitive, specific, compact, and affordable. These criteria are made possible with a transducer that can convert the biological presence of the target molecule into electrical information. Since the early 2000s, integrated photonics have offered a possible solution for a transducer compatible with LOC needs. In particular, silicon micro-ring resonators represent a compact and sensitive choice to use as a transducer in LOC devices.

In agreement with the requirements of LOC devices, the objective of this project is to design and assess the performance of a compact photonic biosensor. The system will be based on integrated photonic transduction. The requirements are that it is compatible with an industrial fabrication platform and fluidic systems, with a sensitivity equal to or higher than the state-of-the-art and simple to functionalize in order to localize the target molecules in the sensitive regions of the sensor. This project details the design, fabrication, and characterization of such a biosensor.

We found that ring resonators with a Hybrid Plasmonic Waveguide (HPWG) cross-section fulfill the LOC requirements and outperform the state-of-the-art biosensor. Furthermore, based on a principle called mode lift, we patented new geometry of HPWG, which will be the object of an article. We simulated the HPWG structure to understand the coupling mechanisms of the modes inside the structure (more specifically, the plasmonic and the ridge dielectric modes). The fabrication was possible thanks to the collaboration of the industrial and university cleanrooms. An advantage of industrial production is that we can reproducibly create the geometric components necessary for the LOC in a high-throughput manner, thus lowering the cost per unit cell. Once the 300 mm Si wafers were patterned, the university cleanroom fabrication process adds the metallic waveguides. The Au nanopatterning on the devices characterized in this project was created using the lift-off method.

The preliminary measures define the optimal testing liquid (glucose monohydrate) and the uncertainty of the measures. The HPWG samples showed an experimental sensitivity lower than the simulations. After adjusting the fabrication parameters (mainly Au and Cr deposition rates and thicknesses), the second-generation HPWG devices suggest that the mode lift improves the sensitivity for waveguides below cutoff (the sensitivity increases from 210 nm/RIU<sup>1</sup> to 320 nm/RIU when only 10% of the ring resonator has an HPWG section and the rest is a ridge waveguide). Even in the case where ridge waveguides are above the cutoff, the sensitivity increases by 40 nm/RIU when using mode lift. We also showed the compatibility of the fabricated devices' surface with differential functionalization, by means of fluorescent nanoparticles. Due to time limitations, the presence of the nanoparticles will be measured with the fabricated devices in future experiments.

**Keywords:** Lab-on-chip, photonics, plasmonics, integrated photonics, ring resonator, biosensors.

---

<sup>1</sup> RIU = Refractive Index Unit, the unit of the refractive index, otherwise dimensionless





# Table of contents

<b>AKNOWLEDGEMENTS</b>	<b>1</b>
<b>CHAPTER 1 - INTRODUCTION AND CONTEXT</b>	<b>4</b>
<b>1.2 OBJECTIVES</b>	<b>5</b>
1.2.1 RESEARCH QUESTION	5
<b>1.3 CONTRIBUTIONS</b>	<b>7</b>
<b>1.4 PLAN OF THE DOCUMENT</b>	<b>8</b>
<b>1.5 BIBLIOGRAPHY</b>	<b>9</b>
<b>CHAPTER 2 - CONTEXT AND STATE OF THE ART</b>	<b>11</b>
<b>2.2 Waveguides: basic detection mechanisms</b>	<b>12</b>
2.2.1 Strip waveguide	12
2.2.2 Slot waveguides	14
2.2.3 Plasmonic waveguides	15
2.2.4 Hybrid plasmonic waveguides	17
2.2.5 Conclusion	18
<b>2.3 Complete devices</b>	<b>19</b>
2.3.1 Prism-based Surface Plasmon Resonance sensors	19
2.3.2 Mach-Zehnder interferometers	20
2.3.3 Ring resonators	20
2.3.4 Advanced ring resonators	22
2.3.4.1 Slot waveguide ring resonators	22
2.3.4.2 Ring resonators and Hybrid Plasmonic WaveGuides	22
2.3.5 Conclusion	23
<b>2.1 Commercial applications using photonics: from the laboratory-based machines to point-of-care systems</b>	<b>26</b>
<b>2.4 Conclusion</b>	<b>28</b>
<b>2.5 Bibliography</b>	<b>30</b>
<b>CHAPTER 3 - SIMULATION METHODS AND PHOTONIC CIRCUIT'S BASIC BUILDING BLOCKS</b>	<b>33</b>
<b>3.1 Techniques for the analysis of the photonics structures and working principles</b>	<b>33</b>
3.1.1 Dispersion of the materials	33
3.1.2 Analysis of a planar waveguide – 1D analysis	35
3.1.2.1 Coupling between two dielectric waveguides – 1D analysis	41
3.1.2.2 Plasmonic waveguides	44
3.1.3 Simulations mode-solver—2D analysis	46
3.1.3.1 Setting up the simulation	47
3.1.3.2 Bent waveguides	49
3.1.3.3 Coupling between two waveguides—2D analysis	50
3.1.4 Simulations—3D analysis	51
3.1.4.1 Mode matching method	52
3.1.4.2 FDTD simulation	52
3.1.5 Table of comparison	54

<b>3.2 Modelling and optimization of the basic building blocks</b>	<b>55</b>
3.2.1 Multimode and monomode waveguides	55
3.2.2. The multimode interferometer coupler modelling	56
3.2.3 Directional coupler	57
3.2.4 Mach-Zehnder interferometer	58
3.2.5 Ring resonator model	59
3.2.5.1 Models for racetrack and ring resonators	59
3.2.5.2 Optical response of a ring resonator	60
3.2.5.3 Models for racetrack and ring resonators—relevant parameters	62
3.2.5.4 Models for racetrack and ring resonators—parasitic resonances	65
<b>3.3 Conclusion</b>	<b>69</b>
<b>3.4 References</b>	<b>70</b>
<b>CHAPTER 4 - DESIGN OF ROUTING COMPONENTS, HYBRID PLASMONIC WAVEGUIDES AND MACH-ZEHNDER INTERFEROMETER</b>	<b>72</b>
<b>4.1 Dimensioning of the basic building blocks for light manipulation</b>	<b>72</b>
4.1.1 Dielectric ridge waveguides and bend dimensioning	73
4.1.2 Tapers	74
4.1.3 Multi mode interferometer (MMI)	74
<b>4.2 Dimensioning of the devices</b>	<b>75</b>
4.2.1 Hybrid plasmonic waveguides (HPWG) as biosensors	75
4.2.1.1 The choice of the metal	76
4.2.1.2 1D Results —Plasmonic waveguides and HPWG simulations	77
4.2.1.3 2D Results —Plasmonic waveguides and HPWG simulations—Bulk sensitivity modeling results	80
4.2.1.4 Integration of the HPWG in a ring resonator	85
4.2.1.5 Sensitivity	89
4.2.1.6 The Limit of detection	91
4.2.1.4 Results 2D—Plasmonic waveguides and HPWG simulations—Adlayer measures	92
4.2.2 Asymmetric Mach-Zehnder Interferometer	94
<b>4.3 Conclusion</b>	<b>96</b>
<b>4.4 Bibliography</b>	<b>97</b>
<b>CHAPITRE 5 - FABRICATION</b>	<b>100</b>
<b>5.1 The device: from design to characterization</b>	<b>100</b>
5.1.1 The Datacom Advanced PHotonic Nanoscale Environment platform and design rules	100
5.1.2 Designing a method to add the metal on the sides of the waveguides	104
5.1.3 The lift-off method	105
5.3.5 The CMP method	109
<b>5.2 PDMS fabrication and bonding</b>	<b>110</b>
<b>5.3 Conclusion</b>	<b>114</b>
<b>5.4 Bibliography</b>	<b>115</b>
<b>CHAPTER 6 - CHARACTERIZATION</b>	<b>116</b>
<b>6.1 Setup</b>	<b>116</b>
6.1.1 Optical setup hardware	116
6.1.1.1 Consideration on the type of measurement	118

6.1.2 Fluidic setup	119
6.1.2.1 Fluidics	119
6.1.2.2 Bulk sensing liquid decision	121
<b>6.2 Considerations on the uncertainty of the measurements</b>	<b>122</b>
6.2.1 Geometry and refractive indices	122
6.2.1.1 Geometry	122
6.2.1.2 Refractive indices	123
6.2.2 Temperature	124
6.2.3 Uncertainty calculation	125
6.2.3.1 Uncertainty along the horizontal axis	126
6.2.3.2 Uncertainty along the vertical axis	126
6.2.3.2.1 Methods to define the peak shift – peak search	127
6.2.3.2.2 Methods to define the peak shift – Fast Fourier Transform method	128
6.2.3.3 The limit of detection (LoD)	131
<b>6.3 Experimental results</b>	<b>132</b>
6.3.1 Waveguide losses	132
6.3.2 HPWG results	133
6.3.2.1 Bulk measurements – preliminary measurements	134
6.3.2.1.1 Repeatability measurements	134
6.3.2.1.2 Evaporation measurements	134
6.3.2.1.3 Linearity of the response	135
6.3.2.2 Bulk measurements – sensitivity measures	136
6.3.2.2.1 Bulk measurements – first generation devices	136
6.3.2.2.2 Bulk measurements – further characterization measurements	137
Atomic Force Microscopy measurements	137
Ellipsometry	138
6.3.2.2.3 Bulk measurements – comparison between the first and second generation devices	138
6.3.2.3 Adlayer measurements	142
6.3.2.4 Differential functionalization	142
6.3.2.5 Functionalization procedure	143
6.3.3 Mach-Zehnder results	145
<b>6.4 Conclusion</b>	<b>146</b>
<b>6.5 Bibliography</b>	<b>148</b>
<b>CHAPTER 7 - CONCLUSIONS AND PERSPECTIVES</b>	<b>150</b>
<b>7.1 Conclusion</b>	<b>150</b>
<b>7.2 Perspectives</b>	<b>151</b>
7.2.1 Bulk measurements	151
7.2.2 Adlayer measurements	151
7.2.3 Integration—towards a Lab on Chip device	151
7.2.3.1 Photonic integration	152
7.2.3.1 Fluidic integration	153
<b>7.3 Bibliography</b>	<b>154</b>
<b>ANNEX A - CMP METHOD</b>	<b>155</b>
<b>ANNEX B – Higher order mode sensors</b>	<b>159</b>
<b>RÉSUMÉ LONG EN FRANCAIS</b>	<b>163</b>

<b>Introduction</b>	<b>163</b>
<b>Etat de l'art</b>	<b>165</b>
Guides d'onde	166
Guide d'onde ruban (ridge waveguide)	166
Guides d'onde fente (slot waveguide)	167
Guides purement plasmoniques	168
Guides hybrides plasmoniques-diélectriques (Hybrid plasmonic waveguides, HPWG)	169
Conclusion	170
Dispositifs complets	172
Surface Plasmon Resonance	172
Interféromètre Mach-Zehnder asymétrique	172
Résonateurs en anneau à guides diélectriques simples	172
Résonateur en anneaux avancés	174
Conclusion	175
<b>Problématique et objectifs</b>	<b>177</b>
Hypothèses et approche proposée	178
<b>Méthodologie et conception</b>	<b>180</b>
<b>Fabrication</b>	<b>184</b>
<b>Caractérisation</b>	<b>186</b>
Mesures bulk – mesures de sensibilité	190
Mesures bulk – premiers dispositifs	190
Mesures bulk – comparaison entre la première et la deuxième série de dispositifs	191
Mesures du adlayer	196
Fonctionnalisation différentielle	196
<b>Conclusion</b>	<b>197</b>
References	199

# List of figures

Figure 1.1 The schematic principle of a biosensor for detection of analytes. The analyte interacts with the bioreceptor to change the measured signal. The transducer converts the analyte presence in a change of the measurable signal. After results' post-processing, the biosensor main properties are extracted (e.g. sensitivity, limit of detection). \_\_\_\_\_ 4

Figure 2.1 a) Schematics of a waveguide with  $\text{Si}_3\text{N}_4$  core and a cladding partly composed of  $\text{SiO}_2$  (below) and  $\text{H}_2\text{O}$  (above). b) Effective indices of the modes and their field distribution: modes  $\text{TE}_0$ ,  $\text{TE}_1$ ,  $\text{TM}_0$  and  $\text{TM}_1$  are guided modes, as opposed to  $\text{TM}_2$ , which is a radiative mode because its effective index is lower than that of  $\text{SiO}_2$ , represented by a horizontal dashed green line. \_\_\_\_\_ 13

Figure 2.2 Schematics of the working principle for adlayer detection. When the device is exposed to the target molecules, they bond to the molecules locally changing the refractive index. The binding of molecules is comparable to a uniform layer on the waveguide. The presence of the adlayer is converted from speed to intensity using a resonator or an interferometer. \_\_\_\_\_ 14

Figure 2.3: a) Cross-section of a slot waveguide with a material of index. The magnification shows the direction of normal electrical induction at the surface. b) Distribution of the light power in a slotted guide. The maximum intensity of the field is confined to the low index slot which could be, for example, the liquid detection medium. \_\_\_\_\_ 15

Figure 2.4 a) Diagram of the mechanism for guiding a surface plasmon-polariton between a dielectric and a metal (in this example gold) b) distribution of the light intensity of an electromagnetic pulse in a surface plasmon waveguide simulated by FDTD method at  $1.31 \mu\text{m}$ . The field is very intense in the dielectric material, for example the liquid medium of interest, while negligible in Au. \_\_\_\_\_ 16

Figure 2.5 a) Different geometries of hybrid plasmon guides (image modified to improve readability). b) Geometry, cross section and profile of the double-slit hybrid plasmon mode [17]. \_\_\_\_\_ 18

Figure 2.6 Schematic diagram of the Mach-Zehnder interferometer [7] \_\_\_\_\_ 20

Figure 2.7 a) Diagram of a resonant ring, b) distribution of power in the coupling zone between the bus guide and the ring, c) top view of the light power in the coupling zone and d) coupling diagram between the ring and bus guide \_\_\_\_\_ 21

Figure 2.8 SEM images of the different resonant ring structures combined with slot guides: a) ring with partial slot [24], b) fully slot ring [7], c) ring and slot bus guide [3]. \_\_\_\_\_ 22

Figure 2.9 a) Diagram of the inverted T-slot configuration and b) field distribution in the inverted configuration [25]. \_\_\_\_\_ 22

Figure 2.10 a) Plasmonic hybrid waveguide ring: the hybrid mode is formed thanks to the interaction between the waveguides in  $\text{MoO}_3$  (refractive index 2.06 at  $1.55 \mu\text{m}$ ) and  $\text{MgF}_2$  (refractive index 1.35 at  $1.55 \mu\text{m}$ ) and a metallic substrate. Field distribution shows the exponential decay at the sensor edges [4]. b) A double slot resonant ring: the hybrid mode is created between the metal Ag and the Si. The field distribution in the cross-section of the ring shows the strong confinement in the liquid [26]. \_\_\_\_\_ 23

Figure 2.11 a) Horiba Instruments Surface Plasmon Resonance Imaging, b) SPR Bio Navis, c) Biosensing Instruments Surface Plasmon Resonance Microscopy \_\_\_\_\_ 26

Figure 2.12 Genalyte detection by ring resonators: a) complete system with the source, detection, microfluidic channels and packaging, b) detail of the ring resonator \_\_\_\_\_ 26

Figure 3.1 Dispersion from 1 to  $1.7 \mu\text{m}$  of the real and imaginary part of the refractive index of Au, Cr, SiN,  $\text{SiO}_2$  and  $\text{H}_2\text{O}$ . The solid lines represent the fit and the dots and dashed lines represent the data points respectively. \_\_\_\_\_ 34

Figure 3.2 Multilayer structure analyzed by the transfer matrix method: on the left the structure composed of a stack of layers with different dielectric constants along x. Each interface is described by an interface matrix while the homogeneous parts are described by a propagation matrix. \_\_\_\_\_ 38

Figure 3.3.a, 3.3.c and 3.3.e show the real part of the refractive index along x, perpendicular to the direction of propagation. Figure 3.3.b, 3.3.d and 3.3.f show the absolute value of the normalized Poynting vector, which describes the power distribution of the mode in the different layers for a TE mode. The  $n_{eff}$  and the losses for the modes are:  $n_{eff} = 1.83$  and losses = 0 dB/cm for the fundamental mode (figure 3.b),  $n_{eff} = 1.59$  and

losses = 0 dB/cm for the first order mode (figure 3.d) and $n_{eff} = 1.36$ and losses = 25000 dB/cm for the radiated mode (figure 3.f).	40
Figure 3.4.a and 3.4.c show the real part of the refractive index along $x$ , perpendicular to the direction of propagation. Figure 3.4.b and 3.4.d absolute value of the normalized Poynting vector for the even and odd modes respectively. Figure 3.4.e plot of the $n_{eff}$ of the isolated, odd and even modes as well as the coupling length of the modes.	43
Figure 3.5 Schematic of the interface between two materials and the forward and backward waves in each layer.	45
Figure 3.6 a real part of the refractive index along $x$ . 3.6.b power distribution of the plasmonic mode across the interface, as two decaying exponentials. The effective refractive index is $n_{eff} = 1.33$ and losses = 554 dB/cm at $1.31\mu\text{m}$ wavelength.	46
Figure 3.7 the error in the convergence test when changing the maximum number of points of the simulation window $n_x \text{ max}$ . The convergence is reached above $n_x \text{ max} = 500$ which represents the optimal tradeoff between speed and precision.	48
Figure 3.8.a and 3.8.b show the diagram of the conformal transformation from a conventional waveguide profile to a profile with a conformal transformation. 3.8.c and 3.8.d show the final transformation field distribution of the mode when the conformal transformation is applied.	49
Figure 3.9 Example of coupling geometry between two waveguides. 3.9.a) top view of two dielectric waveguides A and B in proximity to the coupling region $L_{int}$ . 3.9.b) cross section of the coupling region of the device	50
Figure 3.10.a Plot of the field $E_y$ of the even mode ( $n_{eff} = 1.558$ ). 3.10.b Plot of the field $E_y$ of the odd mode ( $n_{eff} = 1.513$ ).	50
Figure 3.11.a schematic of the coupling waveguides before and after the discretization. 3.11.b example of interface with the forward and backward waves used for the calculation.	52
Figure 3.12 Yee unit cell for 2D and 3D meshing. It can be noticed that the points for the calculation of the E and H are shifted.	53
Figure 3.13.a Image of the waveguide, the cross section and 3D view. 3.13.b the $n_{eff}$ as a function of the width of the waveguide. The power distribution for modes at $W_{wg} = 1.4 \mu\text{m}$ are shown.	56
Figure 3.14.a example of the geometry of a MMI. b. Image of the power in the $1 \times 2$ MMI coupler with the mode matching solver.	57
Figure 3.15.a directional coupler schematics, 17.b field distribution calculated with mode matching method.	58
Figure 3.16 Schematics of a Mach-Zehnder interferometer. The input intensity $A^+$ is split in the two arms of the interferometer. The arms are asymmetric so when the signals recombine in the output MMI they interfere. The interference is quantified by analyzing the output intensity $B^+$ .	58
Figure 3.17 Different kinds of resonator existing in literature: (a) all-pass circular ring resonator b) all-pass racetrack ring resonator and c) add-drop ring resonator. The parameters are bent radius $R_r$ , width of the loop waveguide $W_{loop}$ , $t_{dist1}$ the coupling gap with the waveguide, $W_{bus}$ the width of the bus waveguide, $t_{dist2}$ the coupling gap between the loop and the drop waveguide, $W_{add}$ the width of the add waveguide, $W_{drop}$ the width of the drop waveguide, $L_1$ the horizontal length of the straight part of the racetrack and $L_2$ the vertical length of the straight part of the racetrack.	60
Figure 3.18 racetrack resonator with detail on the coupling section and coupling coefficient $k$ and transmission coefficient $t$ .	61
Figure 3.19 Examples of transmission of a ring resonator with significant parameters. The orange curve is the curve at rest and the blue curve represents a shift due to a refractive index change.	63
Figure 3.20.a simplified diagram of the device with the PDMS reservoir walls. The PDMS walls are represented in green, the inside of the pool is the light blue region in the center (the sensing liquid in $\text{H}_2\text{O}$ in this case) and the outermost regions are air outside the reservoir. 3.20.b example of transmission for a highly perturbed signal with the parasitic interference. The orange circles indicate the parasitic resonances and the blue one the ring resonance peak.	65
Figure 3.21.a diagram of the ring resonator with a Fabry-Perrot interferometer in the bus waveguides, represented by the vertical bars. 3.21.b modified model to include the thickness of the interfaces. 3.21.c result of the model compared to characterization results (the orange curve represents the simulation and the blue one the characterization).	66

Figure 3.22 the principle of the back and forward reflections in the PDMS reservoir. Each reflection and transmission is accounted for up to infinity, as a series.	67
Figure 4.2 a) cross-section of the 2 $\mu\text{m}$ waveguide for input butt coupling, b) cross-section of the waveguide for propagation in the photonic chip and c) cross-section of the waveguide for ring resonators' coupling.	73
Figure 4.2 Schematics of a taper in SiN that ideally goes from $W_{in}$ 2 $\mu\text{m}$ to $W_{out}$ 0.6 $\mu\text{m}$ .	74
Figure 4.3 a) MMI geometry and b) simulation by means of the mode matching technique.	75
Figure 4.4 a) geometry and effective refractive index of 1D dielectric waveguides and the plasmonic waveguides, b) coupling between two plasmonic waveguides divided in even and odd modes as a function of the distance between the two plasmonic interfaces, c) coupling between the even and odd plasmonic modes and the dielectric mode, also divided between the hybrid even and odd modes.	78
Figure 4.5.a) Simulation of the filling factor, i.e. the percentage of the field in the target liquid (water) for different gaps and core widths. b) Losses in dB/cm of the structures for different gaps and core widths. Insets: geometry of the structures.	79
Figure 4.6 From the 1D simulation to the 2D cross section simulation	80
Figure 4.7 Study of the SiN hybrid waveguide with Au (a) and Al (b). The multiple lines represent different gaps between the metal surface of the plasmonic waveguide and the SiN dielectric waveguide core. The black dotted line shows the $n_{eff}$ as a function of the width of the dielectric waveguide. The red dotted line is the index of the SiO <sub>2</sub> , in other words, the limit above which the waveguides support guided modes.	81
Figure 4.8: Fill factor (a, b), difference of effective refractive index when changing the liquid by one refractive index unit (c, d) and losses in dB/ $\mu\text{m}$ (e, f). The red continuous line represents the limit beyond which the hybrid mode is below the cutoff. The purple dashed line represents the limit beyond which the dielectric mode is below the cutoff. (RIU stands for Refractive Index Unit.)	82
Figure 4.9 Field distribution of the mode for different geometries: a-b) gap = 100 nm, c-d) gap = 300 nm, e-f) gap = 500 nm, g-h) gap = 1000 nm. When the metal is close to the SiN waveguide, the mode is confined in the gap while, for large gaps, the mode is deconfined towards the substrate.	83
Figure 4.10 Two examples of the desired distribution of power to maximize sensitivity in the case of: a) large molecules and b) small molecules.	84
Figure 4.11 the study of the sensitivity of the device as a function of the location of a square of biological material with a side of 5 nm. The detection is not done at the surface of the SiO <sub>2</sub> but around 5nm above. This can be an advantage because in most cases the target molecules are not located on the surface but on a layer of bio-receptors which is about ten nanometers.	85
Figure 4.12 a) Bulk sensitivity of the HPWG ring resonator and b) Q factor as a function of the width of the core waveguide and the gap between the core and the metallic walls	86
Figure 4.13 Schematics of the hybrid plasmonic ring resonator	87
Figure 4.14.a) Directional coupler schematic b) field distribution calculated with mode propagation.	87
Figure 4.15 Plan of the complete circuit of the racetrack ring resonator. The parameters chosen for the ring resonator and the MMI are explained in the dedicated sections. All the bend radii are 20 $\mu\text{m}$ .	89
Figure 4.16: a) Schematics of the device, a racetrack resonator hybridized with Au. The sensitive area is between the SiN waveguide (in orange) and the metallic sides (in yellow). b) Shift of the resonance peak as a function of the gap size and the width of the core waveguide for a racetrack with 20 $\mu\text{m}$ radius bends, coupling length $L_{coup} = 10 \mu\text{m}$ and vertical length $L_v = 20 \mu\text{m}$ . The lines represent the limits beyond which the hybrid mode and the dielectric mode are below the cutoff. The green dashed box is the area corresponding to the geometry of the fabricated devices in this project. c) Quality factor as a function of the gap and the width of the central waveguide. d) Graph of the minimum detectable shift and the bulk sensitivity as a function of the HPWG percentage occupation of the ring circumference.	90
Figure 4.17.a concept of orthogonal differential functionalization to improve high signal in a low concentration regime. 18.b differential functionalization in the article by Palazon, 2015 (scale bar is 100 $\mu\text{m}$ ).	92
Figure 4.18 Model of Bovine Serum Albumin or BSA by Bloomfield. Structure A is the model of the protein divided in a compact core (central dashed part) and a less dense envelope (approximate values of $a = 30 \text{ nm}$ and $b = 3 \text{ nm}$ ). B, C and D show the spherical model of the protein.	93
Figure 4.19 adlayer simulations a) when functionalizing Au or b) the dielectrics (SiO <sub>2</sub> and SiN).	94
Figure 4.20 Mach-Zehnder interferometer dimensions of the final design	95



Figure 5.1 Graphic Data System (GDS) of the industrial photolithography mask. a) devices to calculate the losses in the waveguides. b) dielectric part of the HPWG ring with the alignment marks to align the Au plasmonic waveguides. c) Mach-Zehnder interferometer use to experimentally measure the effective refractive index. _	101
Figure 5.2 Schematics representing the geometry and the materials of the DAPHNE platform _____	102
Figure 5.3 possible geometries of the devices at the end of the industrial fabrication process _____	103
Figure 5.4 a) Transmission Electron Microscopy (TEM) image of a SiN waveguide. b) test of reproducibility on the waveguide core layer thickness. _____	103
Figure 5.5 a) the full wafer and b) the wafer after cleaving with the diamond pen c) after the dicing of the Université de Sherbrooke d) sample from STMicroelectronics. _____	104
Figure 5.6 the main steps of the lift-off process from the substrate coming from the STMicroelectronics cleanroom to the final device with the lift-off. _____	105
Figure 5.7 a) the electron beam microscopy image of the ring resonator before lithography, b) the center of the alignment marks (add the picture of the dielectric waveguide). _____	107
Figure 5.8 Ellipsometry measurements of a) the real part of the relative permittivity and b) the extinction coefficient $k$ as a function of the wavelength. The curves represent different deposition speeds and the comparison with the Johnson and Christy data. _____	107
Figure 5.9 fabrication steps associated with the cleanroom images of the process. a) spin-coater, b) the sample inside the scanning electron microscope c) image of the sample after the development. The trapezoidal marks are the hole is the resist. d) The machine for electron beam evaporation Leybold, e) mixer RotoMix type 48200 on which the sample is immersed in acetone, f) final devices with Au patches successfully left of the substrate in correspondence of the holes in the resist. _____	109
Figure 5.10 Process flow of the CMP method. _____	110
Figure 5.11 Image of the mold for the PDMS and for the sample holder _____	111
Figure 5.12 a) PDMS mold b) PDMS shaped c) PDMS pool on the sample glued with plasma bonding. _____	112
Figure 5.13.a image of the microfluidic mold .b Image of the mold glued to the sample _____	112
Figure 6.1 a) schematic of the optical set up from the source to the spectrometer b) sketch of the cross section of the stage with the PDMS reservoir and the input and output fibers, c) picture of the setup and the sample. _____	116
Figure 6.2 Example of two coupling methods on a photonic chip from a fiber: grating coupling in the red square and butt coupling in the blue square _____	117
Figure 6.3 top view of the chip while injecting and collecting light by the butt coupling method for the input waveguide (left side) and output waveguide (right side). _____	118
Figure 6.4 a) Sample holder design with the software Blender b) printed sample holder and sample glued with the PDMS reservoir c) loading the sample with the PDMS reservoir on the sample holder. The two fit together to keep the sample in place _____	119
Figure 6.5 a) Microfluidic channel on the sample during the waterproof test in the cleanroom, b) sample on the set up with the input and output channels _____	120
Figure 6.6 HPWG ring resonator after exposure to glycerol. The residues of organic material stick to the surface, changing the response of the device _____	121
Figure 6.7 Comparison of Sellmeier and Cauchy equations fitted to the experimental data from Kedengurg 2012. Kedengurg's data are shown in red and green dots. The fits with Cauchy and Sellmeier are performed only with the data shown in red ( $0.4\mu\text{m} - 1\mu\text{m}$ ). Sellmeier equation gives a better estimate at wavelengths outside the fitting range. _____	124
Figure 6.8 a) example of calibration curve with the error bars along X and Y representing the uncertainty. The dotted red lines represents the uncertainty interval on the fit of the straight line. The slope is the sensitivity. b) Example of transmission curve for different concentrations of analyte, c) zoom on the transmission curve where the blue points are an example of the measurement points, the green curve represents an error on the intensity and the red curve an error on the resonance wavelength. _____	126
Figure 6.9 Picture of the cross correlation. The insets show the two functions of which on calculate the cross-correlation. The gray hatched area is the overlap of the two curves. Cross-correlation is proportional to the area of the overlap: when the two curves are perfectly overlapped, cross correlation is maximal. _____	128
Figure 6.10 illustrates the FFT method: a) the reference and the measurement spectra and b) transmission spectra after normalization and inversion. c-d) Example of result of the cross-correlation. e-f) Example of the amplitude of the Fourier transform and linear fit of the phase to estimate the delay. _____	130

Figure 6.11.a) schematic of the layout of the device to test linear losses. b) losses in waveguides of different lengths as a function of the wavelength. c) losses (blue) with error bounds (red) as a function of wavelength.	132
Figure 6.12.a) Transmitted power for the spirals of 700nm width. b) losses (blue) with error bounds (red) as a function of the wavelength	133
Figure 6.13 transmission of 5 measurements after changing the DI H <sub>2</sub> O to validate the cleaning procedure and the procedure to change fluids. The maximum resonance peak change is around 10pm.	134
Figure 6.14 a. Transmission spectra of the HPWG device for different glucose monohydrate dilutions in H <sub>2</sub> O. 6.14.b Calibration curve to calculate the sensitivity as the slope of the linear fit of the peak shift as a function of the difference of refractive index of the fluids: "A" represents the reference measurement in pure water, "B": 2g/100 mL, "C": 3g/100 mL, "D": 5g/100 mL and "E": 6g/100mL. The slope of the fitted line, the sensitivity, is 275 nm/RIU.	135
Figure 6.16 Comparison between simulation with the Jonhson and Cristy Au (Au JC - dark blue bars) and experimental results with peak-search (green) and FFT (light blue)	137
Figure 6.15 cross section of the three considered samples with the gap measured at the Electron Scanning Microscope.	137
Figure 6.17.a) image of the AFM tip, inclination of 20°. b) Cross section of the simulated waveguides. c) Average profile over a SiN waveguide.	138
Figure 6.18 comparison of the sensitivity for simulated devices and the experimental results for three samples, PR22_4G, PR23_4G and PR12_10P.	139
Figure 6.19 simulation of the losses of three samples, PR22_4G, PR23_4G and PR12_10P, with different types of Au and Cr. The Cr and the Au INL both contribute to increase losses.	140
Figure 6.20 Experimental sensitivity of the resonators for two SiN waveguide widths and two configurations (Au INL slow deposition compared with the ring resonators without Au).	141
Figure 6.21 schematic of differential functionalization for thiols, streptavidin, biotin and nanoparticles with rhodamine and the different estimated thicknesses	143
Figure 6.22 result of the differential functionalization. a) image of the fluorescent light, b) image of the visible light where the lighter part is the Au, superposition of the two where the red points are the fluorescent light of the nanoparticles.	144
Figure 6.23 Mach-Zehnder interferometer - comparison between the experimental results (red curve) and the nonlinear fit (blue curve). The inset shows the cross section of the waveguide.	145
Figure 7.1 schematic of an improved plasmonic waveguide configuration for a more efficient functionalization	151
Figure 7.2 a) setup where neither the source nor the detection are integrated, b) setup where the detection is integrated, c) setup where both the source and the detection are integrated.	152
Figure A.1 Process flow of the CMP method.	155
Figure A.2 schematic of the ICP etching	155
Figure A.3.a side view of the etched patch. We can notice that there is no more resist present that the roughness is rather high. A.3.b Side view of the etched patch	156
Figure A.4.a schematics of the deposition process. A.4.b-d SEM cross-sections of depositions at different angles ( $\vartheta = 20^\circ$ , $\vartheta = 30^\circ$ and $\vartheta = 45^\circ$ ).	157
Figure A.5 Result of the CMP of one ring resonator and one Au patch. The pictures were colored to underline the different materials. The yellow is the Au and the orange is the SiN while the rest is SiO <sub>2</sub> .	158
Figure A.6 etching rate. Each point is an average of three SEM measures. The calculated etching time is 110 nm/min	158
Figure B.1.a single mode bus waveguide and mode profile. 1.b two-mode waveguide where the first order mode profile is shown (effective index is 1.45, close to the cutoff). 1.c shows the two waveguides close to each other and the coupling between the two modes.	160
Figure B.2 Scanning electron microscope image of the higher order mode ring resonator. A zoom on the coupling section is shown as well as the schematic showing the cross section.	160
Figure B.3.a transmissions spectra for the higher order mode device for different glucose monohydrate dilutions in H <sub>2</sub> O. 3.b Calibration curve to calculate the sensitivity as the slope of the linear fit: "A" represent the reference measurement in water, "B": 2g/100mL, "C": 3g/100mL and "D": 6g/100mL. Sensitivity is of 212 nm/RIU.	161

Figure R1.1 Schéma du fonctionnement d'un biocapteur : deux composantes principales (le test biochimique et le transducteur) qui donnent comme résultat un signal mesurable.	163
Figure R1.2 Schéma du fonctionnement de la détection de surface.	164
Figure R1.3 a) Schéma d'un guide d'onde avec un cœur de $\text{Si}_3\text{N}_4$ et une gaine composée en partie par du $\text{SiO}_2$ et de $\text{H}_2\text{O}$ . b) Distribution des modes et leur cartographie de champ : les modes A, B, D et E sont des modes guidés, par opposition à C qui est un mode radiatif car son indice effectif est inférieur celui du $\text{SiO}_2$ , représenté par une ligne horizontale verte sur la figure.	167
Figure R1.4 : a) Schéma d'un guide fente avec un matériau d'indices de réfraction $n_1 > n_2$ . L'agrandissement montre la direction de l'induction électrique normale la surface. b) Distribution de la puissance lumineuse dans un guide fente. L'intensité maximale du champ est localisée dans la fente de faible indice de réfraction qui pourrait être, par exemple, le milieu liquide de détection.	168
Figure R1.5 a) Schéma du mécanisme de guidage d'un plasmon-polariton de surface entre un diélectrique et un métal (dans cet exemple de l'or) b) Distribution de l'intensité lumineuse d'une impulsion électromagnétique dans un guide plasmon de surface. Le champ est très intense dans le matériau diélectrique, par exemple le milieu liquide d'intérêt, près de l'interface métal/diélectrique et négligeable dans l'or. La simulation a été faite avec un moteur FDTD à $\lambda = 1.31\mu\text{m}$ .	169
Figure R1.6 a) Différentes géométries de guides d'onde plasmonique hybrides (image modifiée pour améliorer la lisibilité) [1], b) Géométrie, coupe transversale et profil du mode guidé double fente hybride plasmonique [23].	170
Figure R1.7 Schéma d'un interféromètre Mach-Zehnder utilisé comme capteur [7].	172
Figure R1.8 a) Schéma d'un anneau résonant, b) distribution de la puissance dans la zone de couplage entre le guide bus et l'anneau, c) vue de dessus de la puissance lumineuse dans la zone de couplage et d) schéma de couplage entre l'anneau et le guide bus	173
Figure R1.9 Images MEB des différentes structures en anneau résonant combinées avec des guides d'onde à fente : a) anneau avec une portion de guide d'onde à fente [21], b) anneau totalement à fente [24], c) anneau et guide d'onde bus à fente [11].	174
Figure R1.10 a) Schéma de la configuration fente en T inversé et b) distribution de champ dans la configuration inversée [12].	174
Figure R.11 a) Anneau guide hybride plasmonique : le mode hybride est formé grâce à l'interaction entre les guides en $\text{MoO}_3$ (indice de réfraction de 2.06 à $\lambda = 1.55\mu\text{m}$ ) et $\text{MgF}_2$ (indice de réfraction de 1.35 à $\lambda = 1.55\mu\text{m}$ ) et un substrat métallique. La cartographie de champ montre le profil exponentiel en surface du capteur [16], b) un anneau résonant double slot : le mode hybride est créé entre le métal Ag et le Si. La distribution de champ dans la section de l'anneau montre le fort confinement dans le liquide [22].	175
Figure R1.12 Exemple de la géométrie d'un résonateur en anneau et de sa transmission	180
Figure R1.13 a) Schéma de la coupe transversale du guide d'onde et de la distribution de la puissance lumineuse calculée par l'outil de calcul de modes ( $W = 300\text{nm}$ , $h = 600\text{nm}$ , $\text{gap} = 300\text{nm}$ ). b) Schéma du dispositif en 3D avec les interactions biologiques. Le rayon de courbure des virages est de $20\mu\text{m}$ , assez grands pour considérer les pertes nulles dans ces zones.	182
Figure R1.14 Processus d'optimisation des paramètres géométriques selon les besoins de performances.	183
Figure R1.15 Etapes de fabrication du procédé Lift off illustrées par des images prises en salle blanche durant la réalisation. a) dépôt de la résine à la tournette, b) Lithographie électronique c) image d'un échantillon après le développement. Les papillons trapézoïdaux représentent les trous dans la résine. d) Evaporation du metal par canon à electron Leybold, e) Lift off dans le mixer RotoMix type 48200 où l'échantillon est immergé dans l'acétone, f) Echantillon en fin de procédé.	185
Figure R1.16 a) Vue en coupe du guide de Nitrure de Silicium. b) Différence entre couplage par réseau de diffraction et couplage par la tranche c) Schéma du montage optique.	187
Figure R1.17 Banc de caractérisation a) Synoptique du banc de caractérisation b) Schéma du banc de caractérisation avec la partie microfluidique c) photographie du banc de caractérisation et du réservoir en PDMS	189
Figure R1.19 Etude comparative de la sensibilité du dispositif entre les simulations en considérant l'indice de réfraction de l'Au Jonhson et Cristy (bleu foncé barres d'erreurs en noir) et les résultats expérimentaux obtenus avec les méthodes peak-search (vert) and FFT (bleu clair)	191

<i>Figure R1.18 cross section of the three considered samples with the gap measured at the Electron Scanning Microscope.</i>	191
<i>Figure R1.21 Simulation des pertes de propagation des 3 échantillons PR22_4G, PR23_4G et PR12_10P, pour différentes configurations Au. Au INL dépôt rapide, Au+Cr et Au+Cr INL dépôt rapide. L'ajout de la couche d'accroche de Cr et la porosité induit par le dépôt rapide induisent un surcroît de pertes de propagation.</i>	193
<i>Figure R1.20 comparison of the sensitivity for simulated devices and the experimental results for three samples, PR22_4G, PR23_4G and PR12_10P.</i>	193
<i>Figure R1.22 Sensibilité mesurée pour différents résonateurs avec 2 largeurs de guides d'onde SiN et avec ou sans Au.</i>	195

# List of tables

<i>Table 2.1 Waveguides for Integrated Photonic Detection: Benefits and disadvantages</i>	18
<i>Table 3.1 Dispersion formulae for the real part of the refractive index of SiO<sub>2</sub>, SiN and H<sub>2</sub>O</i>	34
<i>Table 3.2 The simulation methods included in this thesis</i>	54
<i>Table 4.1 Metals available at STMicroelectronics and their characteristics that helped to choose the most appropriate metal: the plasmonic behaviour in the infrared, the compatibility with the biology test existing and the compatibility with nano-patterning fabrication constraints.</i>	76
<i>Table 4.2 Dimensions of the BSA protein in different studies [24]</i>	93
<i>Table 6.1 Advantages and drawbacks of each method</i>	120
<i>Table 6.2 Coefficients of thermal expansion for SiN, Au and SiO<sub>2</sub></i>	125
<i>Table 6.3 Advantages and drawbacks of the two main methodologies</i>	130
<i>Table 6.4 Table of uncertainty along the horizontal and vertical axis</i>	131
<i>Table 6.5 comparison of the coefficients of the fitting <math>n_{eff}</math> model found by theoretical simulation and the experimental values found with the nonlinear fit.</i>	146
<i>Table A.1 Parameters of the ICP etching recipe Si<sub>3</sub>N<sub>4</sub>_T</i>	156
<i>Tableau R1.1 Guides d'onde pour la détection photonique intégrée : avantages et inconvénients</i>	170

# ACKNOWLEDGEMENTS

A Ph.D. is a complicated and demanding journey and this one was not an exception. This project could not be completed without the constant help of the people surrounding me. I would like to be able to thank all of you on this short page but unfortunately, the space is limited so I will limit myself to the people with whom I spent more time but all of you are in my memory.

I would start thanking my supervisors Regis Orobtcchouk, Paul Charette and Stephane Monfray for believing in me from the beginning. Thank you for your patience and for being there when I needed you. I would also like to thank Michael Canva and Pedro Rojo Romeo for the many fruitful discussions as well as and Frederic Boeuf for believing in me.

My first year was in Lyon so I will start with the people who helped me the most there. Thank you, Tulio, Thais, PV, Prabir, Remi, Nicolas, Florian, Ali, Malik, Jeremy, Florian, Tom, Jordan, Anais, Alberto, Eirini, Samir, Jimmy, Solene, Annie, Virginie, Maurin, Greta, Jeremie, Sarah, Seif, Eva, Paul, Marco, Getenet, Remi, Pierre, Raphael, Panthea, Kokou, Remi, Maxime, Amalric, Sylvain and Sebastian. Thank you for the time you took to talk and listen to me and thank you for your technical and moral support. I would also like to thank the staff of the cleanroom and the beautiful people who started with me the Student Chapter.

I then went to Sherbrooke. At first, I would like to thank Guillaume Beaudin for all the time, patience and for your bright and always spot-on suggestions. Thank you to all the colleagues that, despite the cold Canadian winter, managed to warm this experience even in the coldest moments. Thank you Marine, Stephanie, Marion, Jean-Francois, Ulrike, Yann, Valerie, Olivier, Fanny, Quentin, Tigran, Arthur, Zhor, Maxime, Clement, Pedro, Gwénaëlle, Alexandre, Frederic, Gwénaëlle, Julien, Romain, Guillaume, Abdelatif, Laurence, Marie-Josée, Laurence, Pauline, Etienne, Felix, Adham, Daniel, Caroline, Serge, Marina, Emmanuel, Regis, Mikel. Thank you as well to all the members of the CASS for this great experience.

I cannot forget the help of the team of friends with whom I shared the passion of Lindy Hop, Rockabilly Jive and "Fakecoast". Thanks to you I was able to turn on the light even in the darkest of times. Thank you, Jessica, Celine, Carlos, Maria, Myrtho, Anika, Elodie, Scott, Andrée-Anne, Alexandre, Jessica, Josée, Jean-Francois, Marianne, Marie-Eve, Marc, Mercedes, Kenza, Cora, Yoanna, Aurelien. Thank you for your unconditioned affection. Thank you to the friends of the "maison jaune" that kept me young during my stay in Canada. A special thank you to Christiane because living with you was an incredible experience. Thank you for making me discover how amazing people can be. Thank you for the meals together, for the many discoveries and unforgettable discussions.

Thanks to Michael and Natacha for always taking care of me, in particular during the hardest moments. I will never forget all the delicious hot meals to cheer me up after a particularly difficult day.

Volevo ringraziare inoltre gli amici di lunga data che mi hanno sostenuto nonostante la distanza. Grazie al gruppo dei Tacchini per il sostegno sempre e comunque. Grazie a Stefano e Lara, per le risate a crepapelle. Grazie a Stefano e alle sue amiche per il sostegno soprattutto all'inizio di quest'avventura.

Un enorme grazie alla mia famiglia che mi ha seguito passo a passo, che ha condiviso le mie vittorie e le sconfitte. Grazie per avermi sostenuto durante questa esperienza. Grazie mamma, papa, Paola e Saverio per avermi ancora una volta fatto vedere che siete la più bella famiglia che potessi avere. Vorrei ringraziare di cuore anche Elia e Gino per il magico aiuto sempre presente, anche da molto lontano. Grazie a zia Silvia, zio Mario, Chiara, Giulio e Edo per il vostro affetto incondizionato.

To conclude, I would like to thank Jaime for always supporting me with a smile, for cheering me up and listening when things were complicated. Thank you for your bright and inspiring personality that taught me so much.





# CHAPTER 1 - INTRODUCTION AND CONTEXT

The detection of biological molecules is of major interest in different fields: from public health to food quality control, from animal nutrition to military defence [1]–[6]. Biosensors were invented roughly 60 years ago (the first publication in 1962 [7]) to answer these needs. The success of biosensors is well known in literature and it is marked by great success such as the glucose pen and the electronic nose [8], [9].

More precisely, a biosensor consists of a transducer converting the phenomenon of interest into a measurable signal, as shown in Figure 1.1. Based on the application of the sensor, the phenomenon can range from the presence of a molecule in a complex medium to the dynamic of a reaction. The transducer converts the result of the biochemical test into an (often electrically) measurable signal. The signal is compared to the calibration curve of the sensor, representing the standard values of the sensor response. In this way, the information about the analyte (or target molecule) is determined.

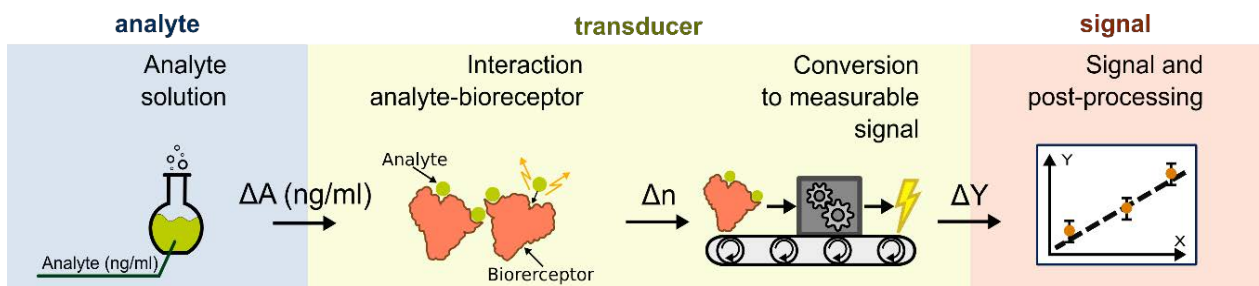


Figure 1.1 The schematic principle of a biosensor for detection of analytes. The analyte interacts with the bioreceptor to change the measured signal. The transducer converts the analyte presence in a change of the measurable signal. After results' post-processing, the biosensor main properties are extracted (e.g. sensitivity, limit of detection).

One of the main objectives of a biosensor is to optimize its sensitivity. However, there is more to this: based on the application, a biosensor needs to be small and affordable to successfully help users, reducing the volume of the material under analysis and making analysis on site possible [10]. These systems are equivalent to an analysis laboratory integrated in a hand-held device. This is why they are referred to as *lab-on-a-chip* or *lab-on-chip* or *LOC* [11]. Such a system is by definition heterogeneous, because it integrates several domains, such as electronics, photonics, microfluidics and biology. This is why they appeared around the 1980s and '90s when thin-film technology allowed the production of miniaturized micro pumps, flow sensors and integrated fluidic systems [12], [13].

## 1.2 OBJECTIVES

The long-term goal of this work is to build a LOC system, focusing on four main goals: sensitive biological transduction, compatible with industrial manufacturing (which provides large volumes at low cost), compact and versatile for different biological targets.

This PhD project is the result of a collaboration between three entities: the *Institut National des Sciences Appliquées de Lyon* (INSA de Lyon), the *Université de Sherbrooke* and STMicroelectronics. The participation of an industrial partner to the project constitutes a realistic example of a mass production environment.

### 1.2.1 RESEARCH QUESTION

The research question at the heart of this research is the following:

How to design, manufacture and test a compact biosensor based on integrated photonic transduction, simple to functionalize, compatible with an industrial platform and lab-on-chip, having a sensitivity comparable or higher than the state of the art?

In other words, the objective of this doctorate is to identify and assess the potential of an integrated photonic transducer compatible with LOC characteristics. Therefore, throughout this work the choices of the device parameters (e.g. materials and geometry) are done taking into account their compatibility with industrial and LOC constraints. In such a multidisciplinary context, it is fundamental to consider all the perspectives to have a realistic candidate, easy to convert into a potentially commercializable product.

After deciding the most adequate device based on literature, its potential is assessed by simulation, manufacture and characterization. As explained in the next chapter, the transducer considered in this study is a ring resonator based on a dielectric-metal hybrid waveguide, also known as Hybrid Plasmonic Waveguide or HPWG. The literature shows that HPWG devices are sensitive, compatible with chemical functionalization, versatile and compatible with industry manufacturing, thus a good candidate for the LOC application.

As stated before, 4 factors are taken into consideration when choosing and designing the device:

The **photonic transduction** must be chosen to allow specific detection of the target molecules and a measurable signal at the output.

From a **biological** standpoint the molecules of interest must be able to reach the detection zone. Furthermore, analytes should be encouraged to occupy preferentially the detection zone other than the other “dead” zones of the device. Therefore, the detection zone must be accessible for target molecules and adapted for differential chemistry.

For the **microfluidic** part, the substrate used must be compatible with a bonding of microchannels produced for example with polydimethylsiloxane or PDMS, a polymer often used in microfluidics. LOC rely on these type of channels to manipulate complex solutions.

Finally, the materials and dimensions of the device must be adapted to **industrial manufacturing** processes. Considering the infrastructure of the industrial partner STMicroelectronics, the device must be designed with the materials already available in their industrial environment, respecting their design rules, such as the width and thicknesses of layers fixed by their standards of production.

From these characteristics, the goals developed during these 3 years and fundamental for the development of the work are:

- Understand and model the physical mechanisms at the base of the transducer during the interaction with the biological molecules. The hypothesis made in this preliminary part allow the evaluation of possible applications and optimizing the design based on the needs.
- Choose a manufacturing process that takes into account the compatibility with an industrial environment, allowing low production costs and high reliability required from the market.
- Design a system for characterization: optical setup to test the photonic chips (source, detection and optical filters) considering the multi-physical nature of the device (microfluidic channels, functionalization, adapted sample holders). Although the characterization setup is not all integrated in one chip, the system is conceived to be compatible with future integration.

The medium-term objective, after the end of the thesis, will be to build a functional prototype using techniques as close as possible to those commercially available. At this stage the device is a proof of concept, which means that constraints are less strict compared with industrial products. For example, all the manufacturing stages are not necessarily compatible with industrial cleanrooms and the device does not yet include an integrated source and detector. For these advanced steps, the perspective and annexes at the end of this document show our solution proposals.

## 1.3 CONTRIBUTIONS

This study allowed 4 international conferences, one peer reviewed paper and two papers that are about to be submitted.

Conferences:

- **CMOS Compatible Photonic SiN Platform**, Invited oral presentation ICTON 2020, E. Kempf, M. Calvo, F. Domengie, P. G. Charette, S. Monfray, R. Orobtcchouk
- **Improving Silicon Nitride Ring Resonator Performances On 300 mm Industrial Environment For Point of Care Applications**, Oral Presentation, Photonics Europe 2020, Strasbourg, France, 29 March 2020, M. Calvo, G. Beaudin, L. Mercier-Coderre, P. Girault, P. Rojo Romeo, R. Stricher, S. Ecoffey, D. Drouin, F. Bœuf, M. Canva, S. Monfray, R. Orobtcchouk, P. G. Charette.
- **Photonic integrated nanojet**, Oral Presentation, META 2019 International Conference on Metamaterials, Photonic Crystals and Plasmonics, Lisbon, Portugal, July 2019, A. Belaruci, M. Calvo, O. Hudz, P. Rojo Romeo, R. Orobtcchouk.
- **Ring Resonator Designed for Biosensing Applications Manufactured on 300 mm SOI in an Industrial Environment**, International Conference on Solid State Devices and Materials (SSDM), Oral Presentation, Tokyo, Japan, September 2018. M. Calvo, S. Guerber, G. Beaudin, M. Canva, C. Baudot, P. Rojo Romeo, F. Boeuf, S. Monfray, R. Orobtcchouk, P. G. Charette.
- **Demonstration of silicon nitride based photonic bio-sensing in 300 mm industrial environment**. In Photonics North, Poster Section, Montreal, Canada, June 2018. M. Calvo, S. Guerber, G. Beaudin, M. Canva, C. Baudot, F. Boeuf, S. Monfray, R. Orobtcchouk, P. G. Charette.

Patent:

- **Mode Lift** N° B18040PTC, April 2019. M. Calvo, R. Orobtcchouk, P. G. Charette, S. Monfray.

Published articles:

- **Ring resonator designed for biosensing applications manufactured in 300 mm SOI in an industrial environment**, Peer Reviewed Article, Japanese Journal of Applied Science, 2019. M. Calvo, S. Guerber, G. Beaudin, M. Canva, P. Rojo Romeo, C. Baudot, F. Boeuf, P. G. Charette, R. Orobtcchouk, S. Monfray.

Articles soon in submission:

- **Mode lift in hybrid plasmonic waveguides: modelling and characterization for integrated photonic sensing**, journal: Optica, M. Calvo, G. Beaudin, Pedro Rojo-Romeo, L. Mercier-Coderre, M. Canva, F. Boeuf, S. Monfray, P. G. Charette, R. Orobtcchouk.

- **Higher order modes ring resonators for sensing**, journal: Optica M. Calvo, G. Beaudin, Pedro Rojo-Romeo, L. Mercier-Coderre, M. Canva, F. Boeuf, S. Monfray, P. G. Charette, R. Orobtschouk.

## 1.4 PLAN OF THE DOCUMENT

The following chapters are organized to guide the reader in what we hope it is a linear and natural development of the study. Since this document resumes three years of highly nonlinear work, only the relevant and final information is given to the reader in order to simplify the reading. Interesting information not essential for the basic understanding is found in the annexes.

Chapter 2 starts with the goals defined in this chapter, from which follows the analysis of the existing literature in relation to the research topic, integrated photonic sensors. The comparison of the existing literature with our goals leads to the decision of the final device under examination and it concludes chapter 2.

Once the structure under analysis is defined, as mentioned before the HPWG, chapter 3 details the theory and simulations used to study the detection mechanism and the performance of the device. The goal of this section is to inform the reader of the different simulation techniques and their use during the study, while simulation results are detailed in chapter 4.

The simulation results and the working mechanism of the HPWG device are explained in chapter 4. The simulation results determined the design choices (material and dimensions) used for devices' fabrication.

Chapter 5 summarizes the fabrication procedure, from the industrial design to the process in the university cleanroom. There were mainly two methods that were considered: the first one, able to provide the first devices, is explained in detail. The second one, 100% compatible with the industrial platform, is detailed in annex because it did not yet provide any working device.

After the fabrication, chapter 6 shows the characterization setup, the experimental results and their discussion. Chapter 7 contains the conclusions of the study and the perspectives.

## 1.5 BIBLIOGRAPHY

- [1] U. Ghoshdastider *et al.*, “Molecular effects of encapsulation of glucose oxidase dimer by graphene,” *RSC Adv.*, vol. 5, no. 18, pp. 13570–13578, Jan. 2015, doi: 10.1039/C4RA16852F.
- [2] M. R. Monroe, G. G. Daaboul, A. Tuysuzoglu, C. A. Lopez, F. F. Little, and M. S. Ünlü, “Single Nanoparticle Detection for Multiplexed Protein Diagnostics with Attomolar Sensitivity in Serum and Unprocessed Whole Blood,” *Anal Chem*, vol. 85, no. 7, pp. 3698–3706, Apr. 2013, doi: 10.1021/ac4000514.
- [3] G. G. Daaboul, A. Yurt, X. Zhang, G. M. Hwang, B. B. Goldberg, and M. S. Ünlü, “High-Throughput Detection and Sizing of Individual Low-Index Nanoparticles and Viruses for Pathogen Identification,” *NanoL*, vol. 10, no. 11, pp. 4727–4731, Nov. 2010, doi: 10.1021/nl103210p.
- [4] L. Asensio, I. González, T. García, and R. Martín, “Determination of food authenticity by enzyme-linked immunosorbent assay (ELISA),” *Food Control*, vol. 19, no. 1, pp. 1–8, Jan. 2008, doi: 10.1016/j.foodcont.2007.02.010.
- [5] T. Petänen, M. Virta, M. Karp, and M. Romantschuk, “Construction and use of broad host range mercury and arsenite sensor plasmids in the soil bacterium *Pseudomonas fluorescens* OS8,” *Microb Ecol*, vol. 41, no. 4, pp. 360–368, May 2001, doi: 10.1007/s002480000095.
- [6] S. Atay, K. Pişkin, F. Yılmaz, C. Çakır, H. Yavuz, and A. Denizli, “Quartz crystal microbalance based biosensors for detecting highly metastatic breast cancer cells via their transferrin receptors,” *Anal. Methods*, vol. 8, no. 1, pp. 153–161, Dec. 2015, doi: 10.1039/C5AY02898A.
- [7] L. C. Clark and C. Lyons, “Electrode Systems for Continuous Monitoring in Cardiovascular Surgery,” *Annals of the New York Academy of Sciences*, vol. 102, no. 1, pp. 29–45, 1962, doi: 10.1111/j.1749-6632.1962.tb13623.x.
- [8] “Electronic Nose: Current Status and Future Trends | Chemical Reviews.” [Online]. Available: <https://pubs.acs.org/doi/full/10.1021/cr068121q>. [Accessed: 17-Feb-2020].
- [9] M. Mascini, “A Brief Story of Biosensor Technology,” in *Biotechnological Applications of Photosynthetic Proteins: Biochips, Biosensors and Biodevices*, Boston, MA: Springer US, 2006, pp. 4–10.
- [10] C. D. Chin, V. Linder, and S. K. Sia, “Lab-on-a-chip devices for global health: Past studies and future opportunities,” *Lab Chip*, vol. 7, no. 1, pp. 41–57, Dec. 2006, doi: 10.1039/B611455E.
- [11] B. W. Soutter, “What is a Lab-on-a-Chip ? Role of Nanotechnology,” pp. 1–4, 2012.
- [12] J. B. Angell, P. W. Barth, and S. C. Terry, “Silicon micromechanical devices,” *Scientific American*, vol. 248, pp. 44–55, Apr. 1983, doi: 10.1038/scientificamerican0483-44.

[13] A. Manz, N. Graber, and H. M. Widmer, "Miniaturized total chemical analysis systems: A novel concept for chemical sensing," *Sensors and Actuators B: Chemical*, vol. 1, no. 1, pp. 244–248, Jan. 1990, doi: 10.1016/0925–4005 (90)80209-I.

## CHAPTER 2 - CONTEXT AND STATE OF THE ART

The goal of this chapter is to show the reasoning that leads from the objectives of this study, defined in the previous chapter, to the decision of the device structure to analyze and optimize. The analysis of the literature is crucial to be aware of the other available methods and compare them to the chosen one.

As explained in the previous chapter, the objective of this PhD is to identify and assess the potential of an integrated photonic transducer, suitable for lab-on-chip (or LOC) applications, compatible with industrial production, sensitive and compatible with easy functionalization for biosensing. As shown in literature, integrated photonic biosensors are able to measure the phenomenon of interest (for example the surface concentration of specific biomolecules) by observing its effect on the refractive index of the environment surrounding the sensor. Furthermore, integrated photonic devices such as Mach-Zehnder interferometer or waveguide-based resonators measure the variation of the surrounding index from its effect on the devices' parameters (e.g. shift of the interference pattern or change of the resonance wavelength).

Before going into the details of the state of the art, it is necessary to define the performance parameters based on which the existing devices are compared:

- **Sensitivity:** for a resonator-based biosensor, it is generally defined as the offset of the resonance wavelength ( $\Delta\lambda_{res}$ ) as a function of the change in the refractive index of the medium ( $\Delta n_{bulk}$ ) and it is called bulk sensibility, i.e.  $S_{bulk} = \Delta\lambda_{res} / \Delta n_{bulk}$  measured in nm/RIU (Refractive Index Unit). In the case of detection of a bio-functionalized surface, it is more relevant to speak of surface sensitivity, generally defined as the shift of the resonance wavelength ( $\Delta\lambda_{res}$ ) as a function of the change in layer thickness ( $\Delta a$ ) ( $S_{ad} = \Delta\lambda_{res} / \Delta a$  in nm/nm) or the change in surface density of the detected species,  $\Delta p$  ( $S_{ad} = \Delta\lambda_{res} / \Delta p$  in nm).
- **Limit of detection, LOD:** it represents the smallest detectable change of the experiment variable of interest. It strongly depends on the experimental conditions (for example the characteristics of the source and the detection). Its unit of measurement changes according to the analyte and the detection method (it can be in RIU for measurements of index liquids or in g/L for measurements of molecule concentration).
- **Industrial environment compatibility:** materials and manufacturing techniques must be compatible with the STMicroelectronics DAPHNE platform (Datacom Advanced PHotonic Nanoscale Environment) is the reference for the industrial platform.
- **Surface functionalization:** the surface functionalization localizes the molecules on the sensitive surface of the device. More specifically, the functionalization has to be robust and specific (or differential) to attract molecules only at the sensing surface areas.
- **Device dimensions:** the long-term goal is to have an integrated chip where multiple sensors perform the measurement of different analytes in parallel.



Once the main performance parameters are clear, it is possible to analyze the state of the art of similar integrated photonic sensors. The review is organized in three main parts: the first part explains the principle of multiple types of waveguides used in biosensors. The second one details the emerging devices using the waveguides discussed in the first part. At last, the third part presents the existing commercialized systems working on biosensing with photonics. Throughout this chapter, only the principles fundamental for the understanding of the literature are given while further details about theory and simulation techniques are detailed in chapter 3.

## 2.2 Waveguides: basic detection mechanisms

This section is dedicated to the description of the waveguides' geometries used in biosensors. It is important to know their details and differences because they determine the fundamental behaviour of light in the sensor. However, by themselves they do not represent a complete sensor because they need a system that can convert the phase change caused by the presence of the analyte to a measurable quantity. Common examples are interferometry systems and resonant systems that convert a phase difference in intensity difference measurable with a photodetector. These complex systems are detailed in the following section 2.2 "Complete devices."

### 2.2.1 Strip waveguide

The simplest example of a waveguide in integrated optics is the *strip waveguide*. A strip waveguide is composed of a high refractive index material, called *core*, surrounded by materials with a lower refractive index, called *cladding*. Figure 2.1.a represents the schematics of a strip waveguide with the core of silicon nitride or  $Si_xN_y$ , (refractive index around 1.9 in the near infrared) and cladding of dioxide of silicon  $SiO_2$  (refractive index of around 1.44 in the near infrared) and  $H_2O$  (index of around 1.32 in the near infrared).

The electromagnetic wave propagates in the waveguide with different possible field distributions called *guided modes* or simply modes, as it is detailed in chapter 3. Each guided mode has an effective index given by the ratio between the phase velocity of the mode and the one in vacuum. Furthermore, modes can have a transverse magnetic (TM) or transverse electric (TE) polarization, depending on which component of the magnetic and electric field normal to the direction of propagation is dominant. The number of existing guided modes in a waveguide depends on its geometry and the refractive indices of the materials. In some specific cases, for example in the case of an asymmetric waveguide, below some critical dimensions there will be no guided mode. In this case the waveguide is said to be *below the cutoff*, as it will be shown in chapter 3.

Figure 2.1.b shows a graph of the effective indices of the guided modes for the 2 polarizations when varying the width of a strip waveguide, calculated by a mode solver developed in the INL laboratory. In the case of a waveguide where all the materials are dielectrics, e.g. a dielectric strip waveguide, the greatest proportion of light energy is normally confined in the core, unless the mode is very close to the cutoff. The field in the cladding is called evanescent field and decreases exponentially depending on the index difference between the core and

the cladding. In the case of an integrated photonics sensor, the sensing medium (in liquid or gas form) is typically in contact with the core of the guide and therefore acts as a cladding. A change in the refractive index of the sensing medium, caused for example by a change in concentration of a target molecule, modifies the properties of the waveguide and of its guided modes. Therefore, a change in the analyte concentration influences the phase velocity of the guided modes. Interferometers or resonators convert the phase velocity change to an intensity variation.

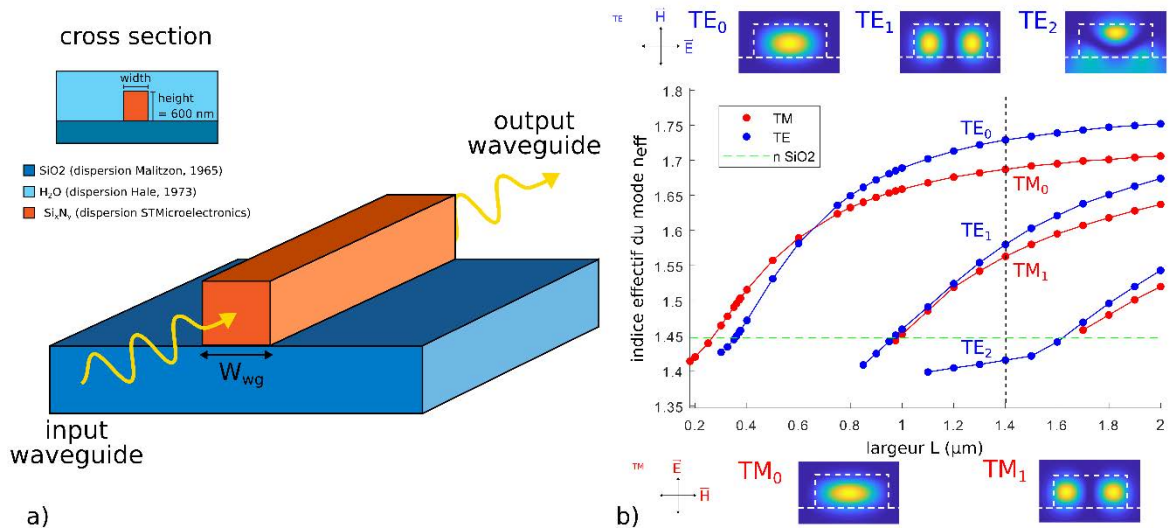


Figure 2.1 a) Schematics of a waveguide with Si<sub>3</sub>N<sub>4</sub> core and a cladding partly composed of SiO<sub>2</sub> (below) and H<sub>2</sub>O (above). b) Effective indices of the modes and their field distribution: modes TE<sub>0</sub>, TE<sub>1</sub>, TM<sub>0</sub> and TM<sub>1</sub> are guided modes, as opposed to TM<sub>2</sub>, which is a radiative mode because its effective index is lower than that of SiO<sub>2</sub>, represented by a horizontal dashed green line.

As it is shown in chapter 3, the greater the portion of total light energy in the sensing medium, the more the phase velocity varies improving the sensitivity of the sensor.

In case of surface detection, the detection process begins with the exposure of the analyte solution to the receptors located on the surface of the biosensor, as shown in Figure 2.2. From the point of view of integrated photonics, the binding of analytes to the surface receptors will have the equivalent effect of a thin layer deposition of biological material with a distinct dielectric constant. Figure 2.2 shows the steps of surface detection. The difference of the signal before and after the target molecule binding is able to provide information about the biological layer (e.g. thickness and refractive index).

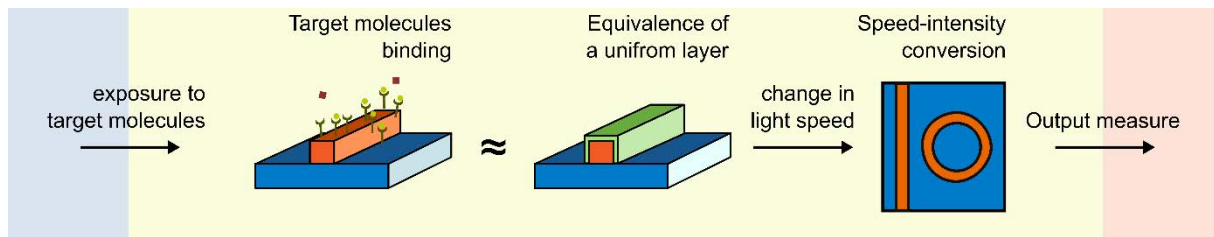


Figure 2.2 Schematics of the working principle for adlayer detection. When the device is exposed to the target molecules, they bond to the molecules locally changing the refractive index. The binding of molecules is comparable to a uniform layer on the waveguide. The presence of the adlayer is converted from speed to intensity using a resonator or an interferometer.

## 2.2.2 Slot waveguides

A way to increase the sensitivity of a ridge waveguide biosensor is to put the major part of the mode outside the core, where the analyte to be detected is present. One possibility is to use a slot waveguide. Slot waveguides are similar to strip waveguides with the exception of a thin low index material strip in the middle of the core. The cross section is shown in picture 3. When considering sensing applications, slot waveguides are particularly interesting because the power of their mode is concentrated in the low index material (i.e. the target environment). Discovered in 2004 at Cornell University[1], slot waveguides have had success in the area of biodetection [2]–[6].

In order to understand how slot waveguides work, we consider the general equations of the continuity of electric displacement field at an interface between two materials. Suppose an interface between a dielectric 1 of index  $n_1$  and a dielectric 2 of index  $n_2$ , the continuity equation established that the normal electrical induction components at the interface are continuous.

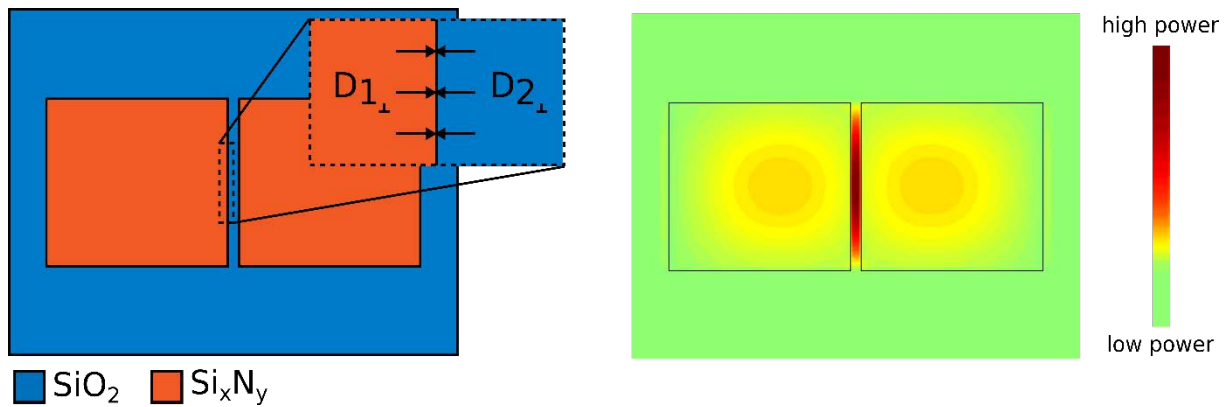


Figure 2.3: a) Cross-section of a slot waveguide with a material of index. The magnification shows the direction of normal electrical induction at the surface. b) Distribution of the light power in a slotted guide. The maximum intensity of the field is confined to the low index slot which could be, for example, the liquid detection medium.

Another relation to keep in mind is the constitutive equation linking the electric field with the electric displacement field ( $\vec{D} = \epsilon \vec{E}$ ). The following formula expresses the relationship between the intensity of the electric field at the interface and the refractive index of the materials constituting the interface:

$$D_{\perp 1} = D_{\perp 2} \rightarrow \epsilon_1 E_{\perp 1} = \epsilon_2 E_{\perp 2} \rightarrow n_1^2 E_{\perp 1} = n_2^2 E_{\perp 2}$$

where  $D_{\perp 1}$  and  $D_{\perp 2}$  are the electric displacement fields perpendicular to the interface,  $\epsilon_1$  and  $\epsilon_2$  are the dielectric constants in media 1 and 2 respectively and  $n_1$  and  $n_2$  are the refractive indices of the two materials of the interface.

If  $n_1 < n_2$ , then  $E_{\perp 1} > E_{\perp 2}$  for the equation to hold true. In other words, the electric field is more important in the material of low index rather than in that of high index. If the two interfaces are close enough, the two electric fields in low index environments interact to create a guided mode. Figure 2.3.a and Figure 2.3.b show the geometry and field distribution of the slot waveguide modes. Since the energy is mainly located in the low index material in the slot, a change in the refractive index of the slot has more impact on the effective index of the mode than in the case of a strip waveguide. The advantage of slot waveguide sensors compared to strip waveguides is their greater sensitivity. However, it is important to note here that the slot is generally very narrow. In the case of a Si<sub>x</sub>N<sub>y</sub> waveguide in water, the sensitivity is highest for widths of 40 nm at 1.31 μm [7]. This indicates both an access problem for the molecules and a manufacturing challenge.

### 2.2.3 Plasmonic waveguides

Several biosensors are designed based on surface plasmon-polariton waveguides (or SPP), or more simply surface plasmon waveguides or plasmonic waveguides. In literature the term “plasmon” sometimes can refer to SPP or to the angular interrogation of the SPP, called Surface Plasmon Resonance or SPR.

Let us consider Surface Plasmon Polaritons: surface plasmon polariton are types of guided modes that exist at the interface between two materials and this is why they are called *surface*

modes, as it will be shown in the next chapter. The interface has to have particular characteristics, for example it has to be between a material with a metallic behaviour and a material with a dielectric behaviour<sup>2</sup>. When a photon with enough energy interacts with the metallic interface, it excites the electronic cloud of the metal. Similar to waves in the ocean, electrons move locally with the electromagnetic excitation, as depicted in Figure 2.4.a. A quantum of these collective oscillations is called *plasmon*. Since the electric field cannot propagate inside the metal, the electronic wave remains on the surface. The term *polariton* is a generic term for the interaction between light and a polarization wave. The polarization wave can be a phonon, a plasmon or even an exciton (an electron-hole pair). It is clear then why the name of this phenomenon, taking place on the surface of the metal and produced thanks to the interaction between an electromagnetic wave and a plasmon, is called Surface Plasmon Polariton.

The distribution of the electromagnetic field has the form of two decreasing exponentials on both sides of the interface. Figure 2.4.b shows the distribution of the intensity of the plasmonic mode field for a pulse at the interface between *Au* and *H<sub>2</sub>O* at 1.31  $\mu\text{m}$ . It should be noted that the exponential profile decreases much faster in the metal compared to the dielectric. This is why only the decreasing profile in the latter is visible in the image.

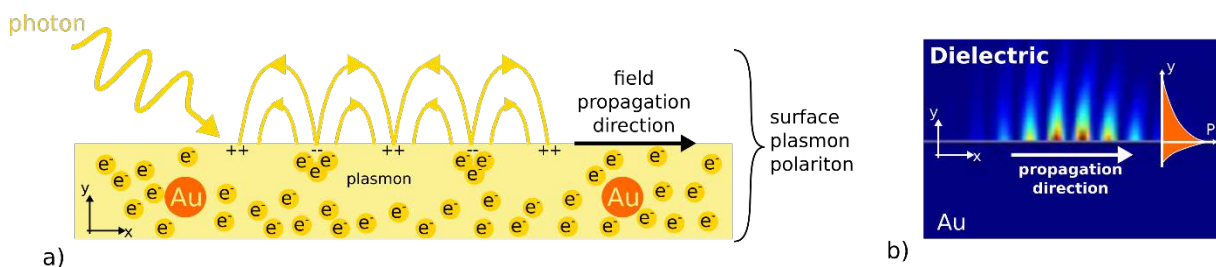


Figure 2.4 a) Diagram of the mechanism for guiding a surface plasmon-polariton between a dielectric and a metal (in this example gold) b) distribution of the light intensity of an electromagnetic pulse in a surface plasmon waveguide simulated by FDTD method at 1.31  $\mu\text{m}$ . The field is very intense in the dielectric material, for example the liquid medium of interest, while negligible in Au.

Moreover, the electron sea inside the metal has a natural resonance frequency, known as plasma frequency. If the excitation wavelength is below the plasma frequency, the system supports SPPs otherwise, it behaves like a dielectric material. For most metals, like Au, Al, Cu, Ag, the plasma frequency corresponds to wavelengths in the ultraviolet spectrum.

<sup>2</sup> It is better to speak of a material with a metallic behaviour rather than metal, because what it is commonly identified as a metal (e.g. Au, Ag, Cu, Al) can behave like a transparent medium and lose its plasmonic properties depending on the excitation wavelength. Thereafter, in order to make the text easier to read, the expression “material with a metallic behaviour” will be substituted by metal, implying that the work is carried out under the metal plasma frequency. Moreover, it is also true that there are dielectrics with metallic behaviors, but they are not considered in the context of this project because of their compatibility with the industrial process and their complicated differential functionalization.

SPP and SPR are very interesting for biosensing applications because the majority of light energy of the propagating mode is in the sensing medium. Several publications show sensors with values of experimental sensitivity up to ten times higher than dielectric structures, as shown in Table 1 of the review article [8], [9], [10]. Moreover, the propagation losses of SPPs are high because the metal absorbs the light energy (details on the losses are given in chapter 3). In addition, compared to the dielectric waveguides, they only support TM propagation modes [11]. While dielectric waveguides can provide two simultaneous pieces of information by using both TE and TM detection (for example the thickness and the refractive index of the biological adlayer), SPP based systems need more complicated measures to do the same.

## 2.2.4 Hybrid plasmonic waveguides

Hybrid plasmonic-dielectric waveguides (or hybrid plasmonic waveguides or HPWG) combine two very different waveguides: originally used to reduce the size of devices in optical telecommunications [12], HPWG modes are the result of a combination of a dielectric ridge waveguide mode and a plasmonic mode. In fact, if a ridge waveguide mode and a plasmonic mode are sufficiently close, the overall mode becomes a combination of the two isolated modes, as it will be detailed in chapter 3. These overall modes, also called *supermodes*, mix the qualities of both waveguide modes, having interesting properties for many applications: polarization control devices, directional couplers, optical tweezers, non-linear devices and, of course, biosensors[13]–[16]. The possible geometries to achieve these objectives are illustrated in figure 2.5.a [11].

In particular, an interesting geometry which combines the concepts of slot waveguides with plasmonic waveguides is called a dual-slot hybrid plasmonic waveguide (DSHP) [17]. Figure 2.5.b shows the geometry of a DSHP waveguide used as a sensor whose field is strongly confined in the low index liquid [17]. Another aspect that makes the HPWG promising for a biosensor is the advantages concerning surface functionalization: being made up of both dielectric and metallic parts, orthogonal functionalization methods can be used to preferentially attract analytes toward the sensing surface.

HPWG also share the drawback of the plasmonic waveguides of high losses. However, losses can be modulated by changing the geometry of the waveguide, as it will be studied in chapter 5, when analyzing the results of the simulations. Moreover, the analysis and understanding of the working principle of HPWG require the use of numerical simulations [18], [19].

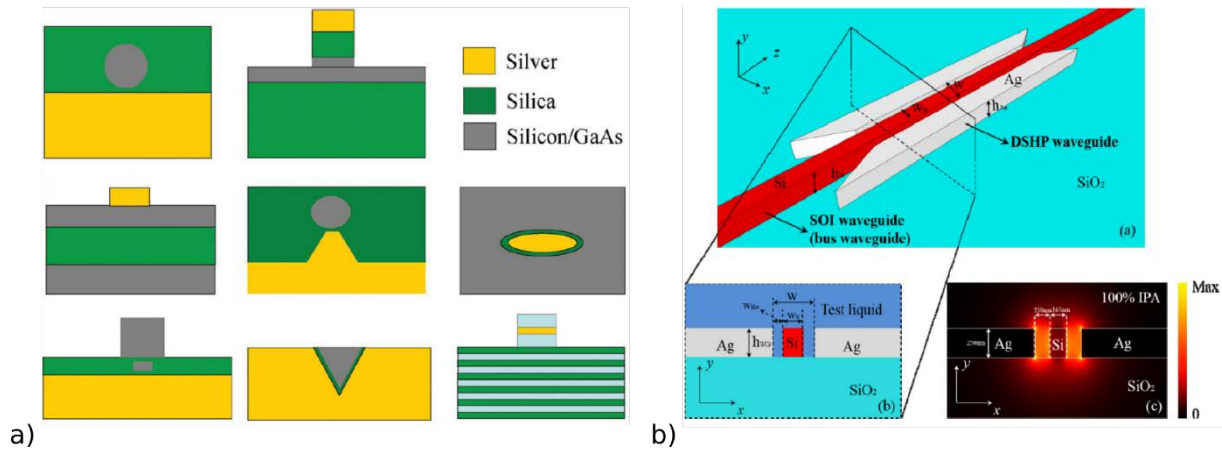


Figure 2.5 a) Different geometries of hybrid plasmon guides (image modified to improve readability). b) Geometry, cross section and profile of the double-slit hybrid plasmon mode [17].

## 2.2.5 Conclusion

Table 2.1 summarizes the advantages and drawbacks of the different types of waveguides analyzed in this section. The data indicated are not quantitative because in most cases the performance of the complete sensor also depends on the characteristics of the complete device. Quantitative performances are shown in the following section dedicated to *complete devices*.

Table 2.1 Waveguides for Integrated Photonic Detection: Benefits and disadvantages

Devices	Advantages	Drawbacks
strip waveguides	<ul style="list-style-type: none"> <li>• Low losses</li> <li>• Easy to manufacture</li> <li>• TE/TM modes</li> </ul>	<ul style="list-style-type: none"> <li>• Low sensitivity</li> <li>• Difficult differential surface functionalization</li> </ul>
Slot waveguides [1], [5]	<ul style="list-style-type: none"> <li>• Sensitive (high interaction between light and the environment)</li> <li>• TE/TM modes</li> </ul>	<ul style="list-style-type: none"> <li>• Difficult access for large molecules</li> <li>• Difficult to manufacture due to the small spacing</li> <li>• Difficult differential surface functionalization</li> </ul>

Plasmonic waveguides[9], [10], [20]	<ul style="list-style-type: none"> <li>• Very sensitive</li> <li>• Simple differential surface functionalization</li> </ul>	<ul style="list-style-type: none"> <li>• High losses (which can also be an advantage depending on the detection method)</li> <li>• TM mode only</li> </ul>
Hybrid Plasmonic WaveGuides [18], [19]	<ul style="list-style-type: none"> <li>• Sensitive (more sensitive than a dielectric waveguide, but less than a plasmonic guide)</li> <li>• TE/TM modes</li> <li>• Simple differential surface functionalization</li> </ul>	<ul style="list-style-type: none"> <li>• Compromise at the level of losses and sensitivity between plasmonic mode and dielectric</li> </ul>

## 2.3 Complete devices

The previous section provided an overview of the photonic structures used in integrated photonics for biosensing. In order to provide a measurable signal, they have to be inserted in an interference or resonant system. In this section, the complete devices (waveguide associated with the desired speed-intensity conversion system) are described.

### 2.3.1 Prism-based Surface Plasmon Resonance sensors

A well-known detection system in biology laboratories is Surface Plasmon Resonance (SPR) sensors, often used for surface detection of biological layers. SPR devices are composed of a light source (for BioNavis SPR systems emitting at 670 nm and 785 nm, system used later in this project [21]), a prism to couple light to the chip, a thin metal layer (often made of Au) and a photodetector. The measurement is performed by varying the incidence angle of the light source thanks to micro-motors. For a particular angle, the incident light excites the plasmonic mode and the reflection is almost zero. This generates an absorption peak depending on the incidence angle.

Several devices are commercialized using with this method. However, SPRs are not compatible with the industrial platform considered in this study, their working wavelength is in the visible and they are usually bulky systems. SPRs method will be used as a control test to verify the properties of the biological layers deposited when functionalizing the surface (e.g. thiols, proteins, nanoparticles).



## 2.3.2 Mach-Zehnder interferometers

The principle of the Mach-Zehnder interferometer (or MZI) is to have interferences between the light that passes through a detection path and a reference path (Figure 2.6). According to the measured optical signal, it is possible to deduce the optical properties of the target object. Further details about the working principle and theory behind this structure is explained in chapter 3. The sensitivity being a function of the length of the optical path, the size of a sensitive device is at the millimetre scale, rather bulky for our application [22]. Mach-Zehnder interferometers have been produced with slot waveguides and HPWG [4], [17]. The details of the performances are in the table at the end of this section.

## 2.3.3 Ring resonators

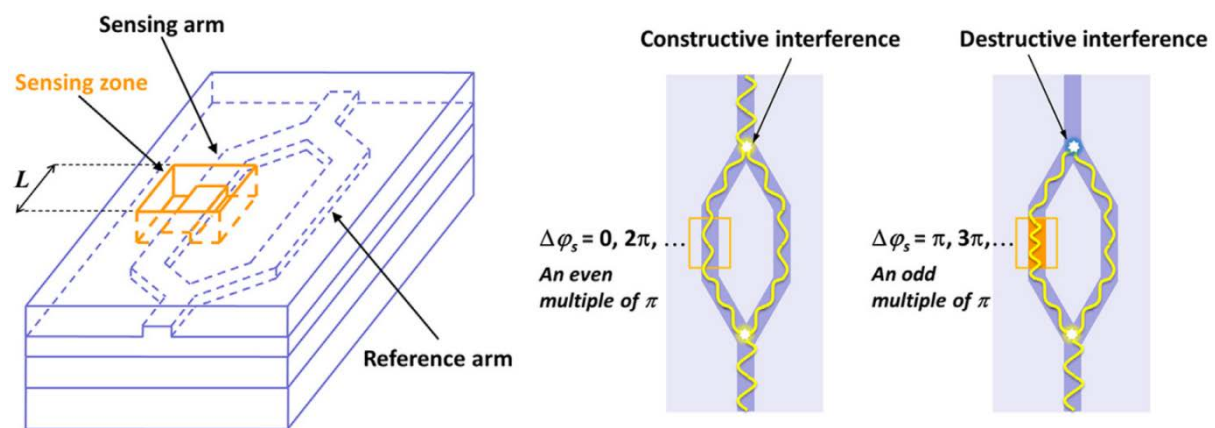


Figure 2.6 Schematic diagram of the Mach-Zehnder interferometer [7]

Ring resonators are essentially directional couplers where one output waveguide injects back to its corresponding input waveguide. In the simplest case, they are composed of an injection/collection waveguide (often called *bus waveguide*) and ring-shaped waveguide as shown in Figure 2.6.a. Once the light injected in the bus waveguide reaches the coupling region indicated in the figure 2.6.a, a portion of its energy is coupled into the ring by direct coupling between the bus and the ring waveguide. Figures 2.6.b and Figure 2.6.c show the cross section and the top view of the power distribution in the coupling zone.

The proportion of energy transferred from the bus waveguide to the ring is calculated using the coupling coefficient, which depends on the geometry and the materials of the coupling zone, as detailed in chapter 3 in the section dedicated to the model of directional couplers. The proportion of light which is not transferred to the ring remains in the bus guide and continues towards the output. Meanwhile, the light propagating in the ring circles back to the coupling zone where it splits again between the ring and the bus waveguide. The light coupling back to the bus waveguide interferes with the light that stayed in the bus waveguide. This mechanism is illustrated in figure 2.7.d, where the area of coupling is represented by a 4-port box.

With a judicious choice of coupling parameters, total extinction of the transmitted light can be achieved. The light at a specific wavelength is then blocked in the ring. This phenomenon is called resonance and it translates to a drop in the transmission of the device. More details about the models that were used to describe ring resonators are explained in chapter 3.

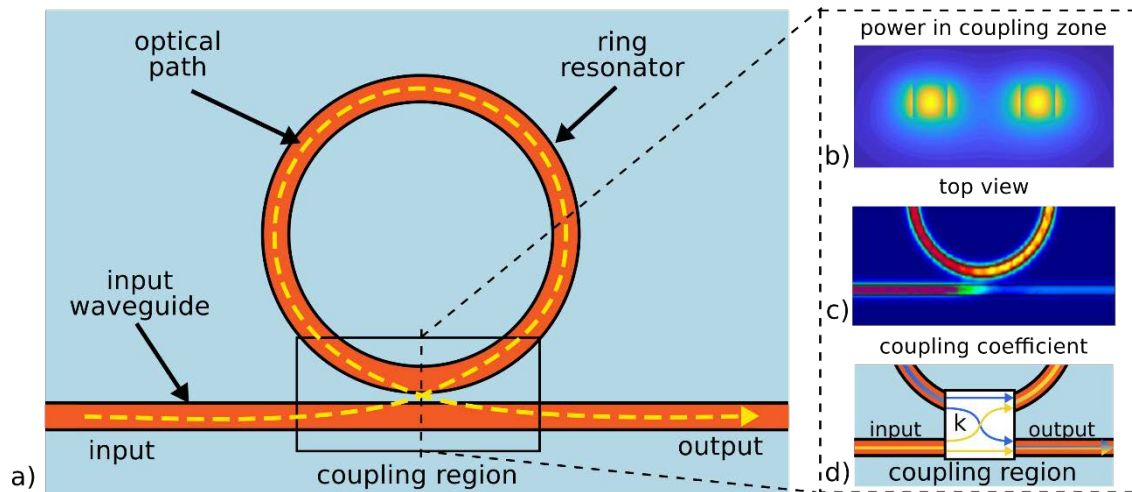


Figure 2.7 a) Diagram of a resonant ring, b) distribution of power in the coupling zone between the bus guide and the ring, c) top view of the light power in the coupling zone and d) coupling diagram between the ring and bus guide

Ring resonators are of great interest for biosensing applications because they are sensitive to their surroundings as shown in literature [6], [23]–[25]. Furthermore, ring resonators allow building devices more compact than with Mach-Zehnder interferometers. When built with rib waveguides, they have a typical bulk sensitivity value of around 100 nm/RIU [6], [20], [25]. A first ring resonator can be combined with a second ring which increases the sensitivity of the sensor thanks to the Vernier effect [24], originally used to improve the accuracy of length measurements in calipers.

The disadvantages of this structure are a relatively complicated surface differential functionalization and the need to integrate a tunable source at the input and/or a spectrometer at the output, compared to a monochromatic source and a simple photo-detector in the case of an interferometer.

## 2.3.4 Advanced ring resonators

### 2.3.4.1 Slot waveguide ring resonators

Ring resonators can be designed based on slot waveguides, which improve sensitivity by increasing the light energy in the sensing liquid. Several geometries have been studied in the literature where slot waveguides are used in part of the ring (106 nm/RIU in Si) [26], in the entire ring (141 nm/RIU in SiN) [7], or both in the ring and in the bus guide (298 nm/RIU in Si) [3]. Figure 2.8 shows electron microscope images of the three types of rings with slot waveguides.

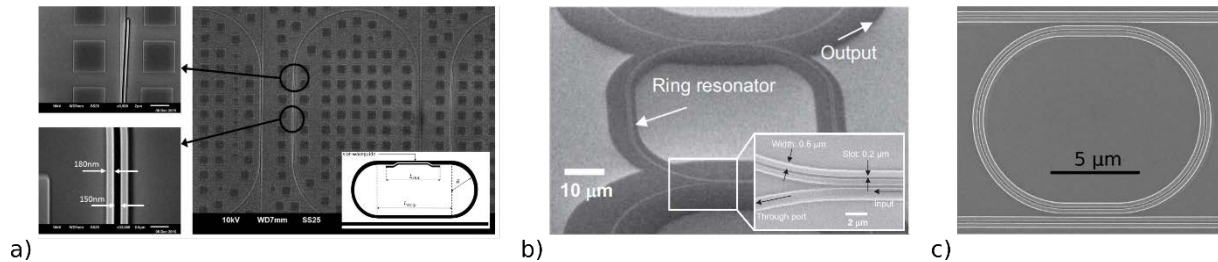


Figure 2.8 SEM images of the different resonant ring structures combined with slot guides: a) ring with partial slot [24], b) fully slot ring [7], c) ring and slot bus guide [3].

Also, the shape of the slots in the waveguides can be modified to optimize the interaction of the mode with the liquid of interest. An example is the “T inverted” cross-section waveguide: in addition to the vertical slot in the middle, there is a second horizontal one, as described in figure 2.9 [27]. In the article, the authors do not speak of a bulk sensitivity with liquids of different index, but they define the sensitivity as the variation of resonance peak in response to a thin layer of biological functionalized layer. With this structure, a theoretical sensitivity value of  $S = 0.0011 \text{ nm}^{-1}$  can be reached. The article reports only simulation results.

### 2.3.4.2 Ring resonators and Hybrid Plasmonic WaveGuides

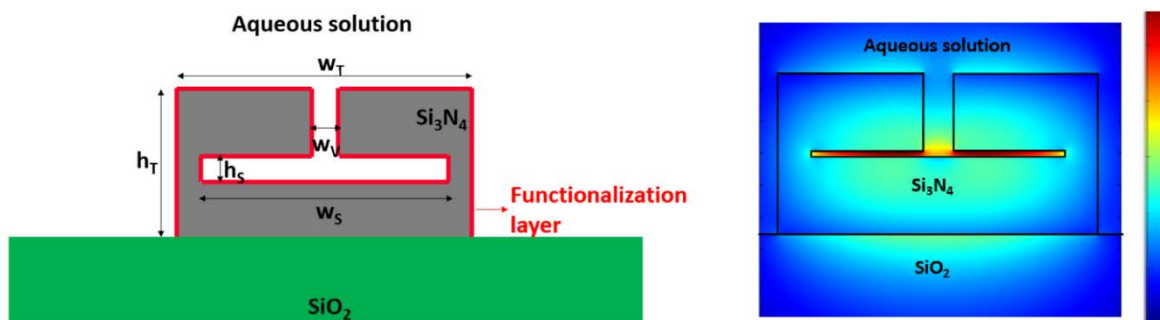


Figure 2.9 a) Diagram of the inverted T-slot configuration and b) field distribution in the inverted configuration [25].

Ring resonators can also be composed by hybrid plasmonic waveguides. Here, two examples are shown: the first one consists in a waveguide on a metallic substrate, where the hybrid mode is formed thanks to the interaction between the guides in MoO<sub>3</sub> (refractive index 2.06 at 1.55μm), MgF<sub>2</sub> (refractive index 1.35 at 1.55μm) and a metallic substrate (theoretical sensitivity of 408 nm/RIU [4]). Another example is a double-slot hybrid plasmonic waveguide (or DSHP) where the hybrid mode is created between the metal, Ag, and the Si (688 nm/RIU experimental) [28]. The field distribution in the cross section of the ring shows its strong

confinement in the liquid. Figure 2.10.a and figure 2.10.b show the geometries of these two configurations. The presence of metal on both sides of the Si waveguide allows a functionalization of the metal/dielectric differential surface.

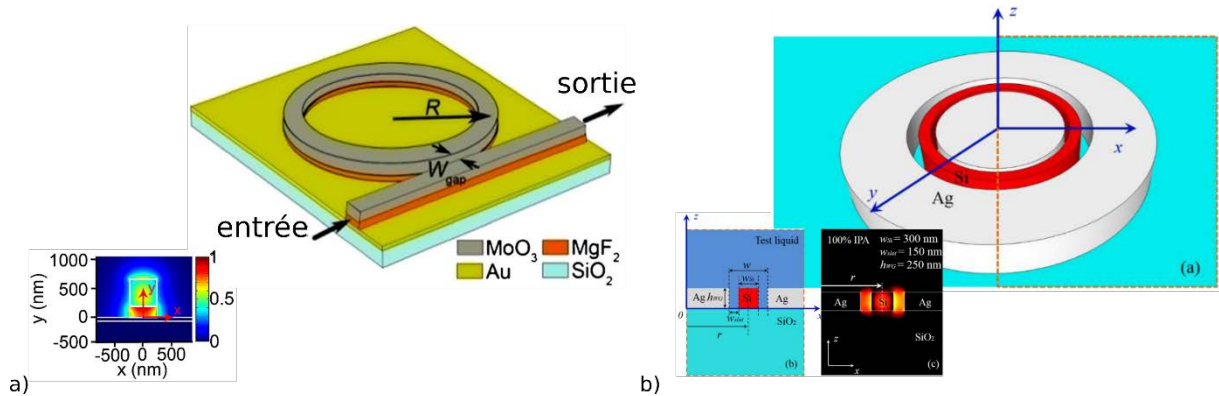


Figure 2.10 a) Plasmonic hybrid waveguide ring: the hybrid mode is formed thanks to the interaction between the waveguides in MoO<sub>3</sub> (refractive index 2.06 at 1.55  $\mu\text{m}$ ) and MgF<sub>2</sub> (refractive index 1.35 at 1.55  $\mu\text{m}$ ) and a metallic substrate. Field distribution shows the exponential decay at the sensor edges [4]. b) A double slot resonant ring: the hybrid mode is created between the metal Ag and the Si. The field distribution in the cross-section of the ring shows the strong confinement in the liquid [26].

### 2.3.5 Conclusion

In Table 2.2, the performances of the devices mentioned are summarized in order to compare the main parameters of interest.

Detection method	Waveguide type	Sensitivity	Detection limit	Industrial platform compatibility	Differential functionalization on metal/dielectric	Footprint
SPR	Prism and angular scan [21]	10–300 ng/mL	10 pg/m <sup>2</sup>	-	-	-
Mach-Zehnder	Dielectric [22]	1600 $\pi\text{rad}/\text{RIU}$		YES	NO	large (> 1 mm <sup>2</sup> )

interferometer	slot [4]	2663 $\pi rad/RIU$	$5.4 \times 10^{-6} RIU$	YES	NO	large (> 1 $mm^2$ )
	Double slot hybrid plasmonic [29]	1061 $nm/RIU$		YES	YES	large (> 4000 $\mu m^2$ )
Ring resonator	Dielectric [6], [20], [25]	163 $nm/RIU$	$7.6 \times 10^{-7} RIU$	YES	NO	compact (226 $\mu m^2$ )
	Vernier (2 rings) [24]	2169 $nm/RIU$	$8.3 \times 10^{-6} RIU$	YES	NO	large (> 30000 $\mu m^2$ )
Slot ring resonator	Partial slot [26]	106 $nm/RIU$		YES	NO	acceptable (2720 $\mu m^2$ )
	Full slot [7]	141 $nm/RIU$ 50 $ng/mL$ (PSA <sup>3</sup> )	10 $ng/mL$ (PSA)	YES	NO	compact (< 1000 $\mu m^2$ )
	Full slot and bus waveguide [3]	298 $nm/RIU$	$4.2 \times 10^{-5} RIU$	YES	NO	compact (130 $\mu m^2$ )
	T inverse slot [27]	0.0011 $nm^{-1}$	1 $ng/mL$ (lung cancer <sup>4</sup> )	YES	NO	acceptable (2200 $\mu m^2$ )

<sup>3</sup> PSA is the Prostate-Specific Antigen

<sup>4</sup> In this study 5 proteins of the human serum related to lung cancer have been tested: Alpha-1 antitrypsin (A1AT), cytokeratin fragment 21-1 (Cyfra 21ff1), insulin-like growth factor 1 (IGF1), regulated upon activation normal T cell expressed and secreted (RANTES), and alpha-fetoprotein (AFP)

HPWG ring resonator	Metal substrate [30]	408.7 nm/RIU	$2.13 \times 10^{-4}$ RIU	NO	YES	compact (< $200 \mu m^2$ )
	Double slot HPWG [28]	687.5 nm/RIU	$5.37 \times 10^{-6}$ RIU	YES	YES	compact (< $200 \mu m^2$ )

## 2.1 Commercial applications using photonics: from the laboratory-based machines to point-of-care systems

To conclude the study of the state of the art, it is important to present the existing commercial products using the techniques described above. Not only does it allow a better overview of the existing products, but it gives an idea of the complexity of a complete working system.

Today the photonic approaches such as Surface Plasmon Resonance (SPR) and photonic integrated circuits (e.g. ring resonators and interferometers) are well known in the diagnostic market. There are many examples of companies that use SPR photonic diagnostic tools, for example Horiba Instruments, Bio Navis and Biosensing Instrument (see Figure 2.11.a 2.11.b and 2.11.c respectively). The main differences compared to our study are the price and the size: often they are rather bulky and they cost several thousands of euros<sup>5</sup>.



Figure 2.11 a) Horiba Instruments Surface Plasmon Resonance Imaging, b) SPR Bio Navis, c) Biosensing Instruments Surface Plasmon Resonance Microscopy

An example of photonic products close to the technology used in this PhD project is the company Genalyte (Maverick technology) which uses conventional ring resonators for detection. Genalyte uses ridge based ring resonators with a sensitivity of 163nm/RIU [25]. The transducers are well integrated while the source and the detection are external. Figure 2.12.a and 2.12.b show the complete system and the detail of the ring resonators respectively.

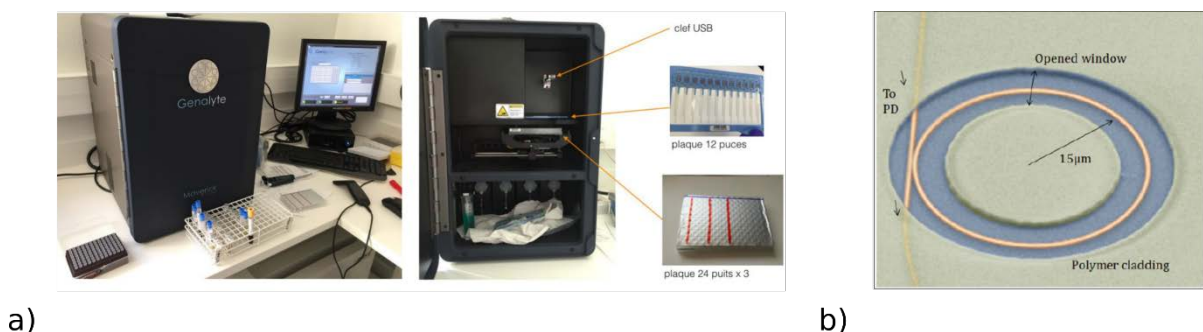


Figure 2.12 Genalyte detection by ring resonators: a) complete system with the source, detection, microfluidic channels and packaging, b) detail of the ring resonator

<sup>5</sup> The price ranges between tens of thousands and several hundreds of thousands US dollars.

In our work, we take into account the possible light source and detection integration techniques, compatible with the DAPHNE industrial environment. More details on the integrated source and detection are given in the perspectives in chapter 7.



## 2.4 Conclusion

After the analysis and comparison of main integrated photonic biosensing mechanisms, it is possible to determine which solution is most adapted to answer the research question of this PhD project. The reasoning behind the choice of the studied structure concludes this chapter.

Since it is desirable to have a versatile sensor, it must allow a generic, stable, reproducible and simple surface chemistry. In addition, an important feature of surface functionalization is to be spatially selective, i.e. to be able to position the targets selectively on the sensitive surface of the sensor and not on the so-called “dead” zones. This maximizes the sensitivity of the sensor for low concentration of the specific analyte. Within the framework of this project, the parameters of differential functionalization (for example, the choice of materials) are based on research by the chemistry and nanobiotechnology team of the Institute of Nanotechnologies of Lyon (INL) [31]. When considering differential functionalization, the solution is a system that integrates dielectrics and metals, such as plasmonic waveguides.

However, the conventional plasmonic integrated sensors are relatively large and light only travels only once in the sensitive area. As pointed out before, one of the objectives is to reduce the size of the device in order to increase the quantity of transducers per unit of area and to minimize the volume of reagents necessary for the operation of the sensor. Therefore, the ring resonator was the preferred choice because it is sensitive, it has a high interaction with the analyte and it is compact.

However, ring resonators rarely integrate metals in their structure because they absorb light causing high losses. In absence of amplification, losses in a ring resonator affect the signal to noise ratio (or SNR). Thus, if losses are too important the limit of detection (LoD) can rapidly degrade. Plasmonic waveguides have losses of the order of 1000 dB/cm while dielectric waveguides have losses of the order of 1 dB/cm. A completely plasmonic ring would therefore have a degraded LoD. In the final device amplification could be added to reach even more sensitive sensors at the cost of a more complex integration.

Hybrid plasmonic waveguides provide a solution to this dilemma. Similar to slot waveguides, they consist of two parallel waveguides, one dielectric and the other plasmonic, separated by a gap. The modes of these waveguides have lower losses than the purely plasmonic modes but higher than the dielectric ones. However, the losses can be mitigated by adjusting the distance between the metal and the dielectric, which makes it possible to adapt them for the resonant ring structure. As shown in Chapter 4, parameters such as the distance between the metal and the dielectric (or gap), the length of the ring, the choice of the metal, the width of the central dielectric guide are used to find an acceptable compromise between sensitivity and losses. This implies that the parameters must be optimized based on the chosen application. Hybrid plasmon waveguides represent a valid configuration for a compact and sensitive biosensor in integrated photonics [18], [28].

Finally, the fabrication must be compatible with a mass production platform to have low-cost devices. The DAPHNE platform, an industrial environment originally developed for telecommunications by STMicroelectronics, is well-suited to evaluate the compatibility with

mass production. As shown in chapter 5 dedicated to fabrication, it is possible to manufacture HPWGs with the DAPHNE platform.

In conclusion, the study of literature points out that the HPWG is a valuable candidate to fulfill our requirements because it is sensitive, adapted for differential surface functionalization, versatile and compact. HPWG also has a good compromise between optical losses and sensitivity being a mix of a plasmonic waveguide (lossy but sensitive) and a dielectric one (lossless but with low sensitivity).

## 2.5 Bibliography

- [1] V. R. Almeida, Q. Xu, C. A. Barrios, and M. Lipson, "Guiding and confining light in void nanostructure," *Optics Letters*, vol. 29, no. 11, p. 1209, Jun. 2004, doi: 10.1364/OL.29.001209.
- [2] A. Kargar and C.-Y. Chao, "Design and optimization of waveguide sensitivity in slot microring sensors," *J. Opt. Soc. Am. A, JOSAA*, vol. 28, no. 4, pp. 596–603, Apr. 2011, doi: 10.1364/JOSAA.28.000596.
- [3] T. Claes, J. G. Molera, K. D. Vos, E. Schacht, R. Baets, and P. Bienstman, "Label-Free Biosensing With a Slot-Waveguide-Based Ring Resonator in Silicon on Insulator," *IEEE Photonics Journal*, vol. 1, no. 3, pp. 197–204, Sep. 2009, doi: 10.1109/JPHOT.2009.2031596.
- [4] Q. Liu *et al.*, "Highly sensitive Mach–Zehnder interferometer biosensor based on silicon nitride slot waveguide," *Sensors and Actuators B: Chemical*, vol. 188, pp. 681–688, Nov. 2013, doi: 10.1016/j.snb.2013.07.053.
- [5] C. Ciminelli, F. Dell'Olio, D. Conteduca, F. Innone, T. Tatoli, and M. N. Armenise, "New microphotonic resonant devices for label-free biosensing," in *2016 18th International Conference on Transparent Optical Networks (ICTON)*, 2016, pp. 1–4, doi: 10.1109/ICTON.2016.7550326.
- [6] C. Ciminelli, F. Dell'Olio, D. Conteduca, C. M. Campanella, and M. N. Armenise, "High performance SOI microring resonator for biochemical sensing," *Optics & Laser Technology*, vol. 59, no. Supplement C, pp. 60–67, Jul. 2014, doi: 10.1016/j.optlastec.2013.12.011.
- [7] T. Taniguchi *et al.*, "Detection of antibody-antigen reaction by silicon nitride slot-ring biosensors using protein G," *Optics Communications*, vol. 365, pp. 16–23, Apr. 2016, doi: 10.1016/j.optcom.2015.11.068.
- [8] B. Spackova, P. Wrobel, M. Bockova, and J. Homola, "Optical Biosensors Based on Plasmonic Nanostructures: A Review," *Proceedings of the IEEE*, vol. 104, no. 12, pp. 2380–2408, Dec. 2016, doi: 10.1109/JPROC.2016.2624340.
- [9] P. Berini, "Bulk and surface sensitivities of surface plasmon waveguides," *New Journal of Physics*, vol. 10, no. 10, p. 105010, Oct. 2008, doi: 10.1088/1367-2630/10/10/105010.
- [10] W. L. Barnes, A. Dereux, and T. W. Ebbesen, "Surface plasmon subwavelength optics," *nature*, vol. 424, no. 6950, p. 824, 2003.
- [11] M. Z. Alam, J. S. Aitchison, and M. Mojahedi, "A marriage of convenience: Hybridization of surface plasmon and dielectric waveguide modes," *Laser & Photonics Reviews*, vol. 8, no. 3, pp. 394–408, May 2014, doi: 10.1002/lpor.201300168.
- [12] R. F. Oulton, V. J. Sorger, D. A. Genov, D. F. P. Pile, and X. Zhang, "A hybrid plasmonic waveguide for subwavelength confinement and long-range propagation," *Nature Photonics*, vol. 2, no. 8, p. 496, Aug. 2008, doi: 10.1038/nphoton.2008.131.

- [13] J. Chee, S. Zhu, and G. Q. Lo, "CMOS compatible polarization splitter using hybrid plasmonic waveguide," *Opt. Express, OE*, vol. 20, no. 23, pp. 25345–25355, Nov. 2012, doi: 10.1364/OE.20.025345.
- [14] M. Z. Alam, J. N. Caspers, J. S. Aitchison, and M. Mojahedi, "Compact low loss and broadband hybrid plasmonic directional coupler," *Opt. Express, OE*, vol. 21, no. 13, pp. 16029–16034, Jul. 2013, doi: 10.1364/OE.21.016029.
- [15] X. Yang, Y. Liu, R. F. Oulton, X. Yin, and X. Zhang, *LETTER pubs.acs.org/NanoLett Optical Forces in Hybrid Plasmonic Waveguides*. 2011.
- [16] S. Aldawsari and B. R. West, "Hybrid plasmonic waveguides for nonlinear applications," in *2012 Photonics Global Conference (PGC), 2012*, pp. 1–4, doi: 10.1109/PGC.2012.6458075.
- [17] X. Sun, L. Thylén, and L. Wosinski, "Hollow hybrid plasmonic Mach–Zehnder sensor," *Optics Letters*, vol. 42, no. 4, p. 807, Feb. 2017, doi: 10.1364/OL.42.000807.
- [18] M. Z. Alam, "Hybrid Plasmonic Waveguides theory and Applications.," Library and Archives Canada = Bibliothèque et Archives Canada, Ottawa, 2013.
- [19] M. Z. Alam, J. S. Aitchison, and M. Mojahedi, "Theoretical Analysis of Hybrid Plasmonic Waveguide," *IEEE Journal of Selected Topics in Quantum Electronics*, vol. 19, no. 3, pp. 4602008–4602008, May 2013, doi: 10.1109/JSTQE.2013.2238894.
- [20] A. Samusenko *et al.*, "A SiON Microring Resonator-Based Platform for Biosensing at 850 nm," *Journal of Lightwave Technology*, vol. 34, no. 3, pp. 969–977, Feb. 2016, doi: 10.1109/JLT.2016.2516758.
- [21] "BioNavis: résumé." <http://www.bionavis.com/fr/> (accessed Mar. 19, 2020).
- [22] S. J. Choo, J. Kim, K. W. Lee, D. H. Lee, H.-J. Shin, and J. H. Park, "An integrated Mach–Zehnder interferometric biosensor with a silicon oxynitride waveguide by plasma-enhanced chemical vapor deposition," *Current Applied Physics*, vol. 14, no. 7, pp. 954–959, Jul. 2014, doi: 10.1016/j.cap.2014.04.016.
- [23] T. Barwicz, M. A. Popovic, P. T. Rakich, H. A. Warts, E. P. Ippen, and H. I. Smith, "Microring-resonator-based add-drop filters in SiN: Fabrication and analysis," *Optics Express*, vol. 12, no. 7, pp. 1437–1442, 2004, doi: 10.1364/OPEX.12.001437.
- [24] T. Claes, W. Bogaerts, and P. Bienstman, "Experimental characterization of a silicon photonic biosensor consisting of two cascaded ring resonators based on the Vernier-effect and introduction of a curve fitting method for an improved detection limit," *Opt. Express, OE*, vol. 18, no. 22, pp. 22747–22761, Oct. 2010, doi: 10.1364/OE.18.022747.
- [25] M. Iqbal *et al.*, "Label-Free Biosensor Arrays Based on Silicon Ring Resonators and High-Speed Optical Scanning Instrumentation," *IEEE Journal of Selected Topics in Quantum Electronics*, vol. 16, no. 3, pp. 654–661, 2010, doi: 10.1109/JSTQE.2009.2032510.

- [26] P. Steglich *et al.*, "Hybrid-Waveguide Ring Resonator for Biochemical Sensing," *IEEE Sensors Journal*, vol. 17, no. 15, pp. 4781–4790, Aug. 2017, doi: 10.1109/JSEN.2017.2710318.
- [27] F. Dell'Olio, "New ultrasensitive resonant photonic platform for label-free biosensing," *OSA*, Oct. 2015.
- [28] X. Sun, D. Dai, L. Thylén, and L. Wosinski, "Double-Slot Hybrid Plasmonic Ring Resonator Used for Optical Sensors and Modulators," *Photonics*, vol. 2, no. 4, pp. 1116–1130, Nov. 2015, doi: 10.3390/photonics2041116.
- [29] X. Sun, D. Dai, L. Thylén, and L. Wosinski, "High-sensitivity liquid refractive-index sensor based on a Mach-Zehnder interferometer with a double-slot hybrid plasmonic waveguide," *Opt. Express, OE*, vol. 23, no. 20, pp. 25688–25699, Oct. 2015, doi: 10.1364/OE.23.025688.
- [30] T. Ma *et al.*, "Highly Sensitive Biochemical Sensor Based on Two-Layer Dielectric Loaded Plasmonic Microring Resonator," *Plasmonics*, vol. 12, no. 5, pp. 1417–1424, Oct. 2017, doi: 10.1007/s11468-016-0401-4.
- [31] F. Palazon *et al.*, "Orthogonal chemical functionalization of patterned gold on silica surfaces," *Beilstein Journal of Nanotechnology*, vol. 6, pp. 2272–2277, Dec. 2015, doi: 10.3762/bjnano.6.233.

# CHAPTER 3 - SIMULATION METHODS AND PHOTONIC CIRCUIT'S BASIC BUILDING BLOCKS

This chapter explains the methods and simulations used in this work as well as the design of the basic components for guiding light from the input fiber, to the chip up to the output fiber. At first, we describe and compare the principles of each simulation method, specifying when and why they were used in this work. We dedicate the second part of this chapter to illustrate how these methods were used for the optimization of the basic building blocks for the routing of light on the chip (e.g. 1x2 MMI, directional couplers, ...). This chapter intends to provide all the simulation basics and scientific approach allowing a better understanding of chapter 4, which focuses on the simulation results of the Hybrid Plasmonic WaveGuides (HPWG).

## 3.1 Techniques for the analysis of the photonics structures and working principles

Whether we need to find the eigenmodes of a photonic structure, to visualize the time evolution of an electromagnetic field or to find the resonance modes of a photonic cavity, electromagnetic simulations have one objective: solving Maxwell's equations. Maxwell's equations are a set of four equations : Gauss's Law for electric fields, Gauss's Law for magnetic fields, Faraday's Law and Ampere-Maxwell's law [1], as shown in equations 1-4.

$$\vec{\nabla} \cdot \vec{E} = \frac{\rho}{\epsilon_0} \quad (1)$$

$$\vec{\nabla} \cdot \vec{B} = 0 \quad (2)$$

$$\vec{\nabla} \times \vec{E} = -\frac{\partial \vec{B}}{\partial t} \quad (3)$$

$$\vec{\nabla} \times \vec{B} = \mu_0 \left( \vec{J} + \epsilon_0 \frac{\partial \vec{E}}{\partial t} \right) \quad (4)$$

where  $\vec{E}$  is the electric field,  $\vec{B}$  the magnetic field,  $\vec{J}$  the electric current density,  $\rho$  is the conductivity,  $\epsilon_0$  is the vacuum permittivity,  $t$  is the time variable and  $\mu_0$  is the permeability.

### 3.1.1 Dispersion of the materials

Before solving Maxwell's equations, the materials constituting the structure under analysis as well as their optical properties need to be considered. The materials mainly used in this thesis are  $Si_3N_4$ ,  $SiO_2$ ,  $H_2O$  and  $Au$ .  $Si_3N_4$  and  $SiO_2$  were chosen from the industrial environment (STMicroelectronics),  $H_2O$  was chosen because it represents the natural environment for biosensing characterization and  $Au$  was selected because it is a plasmonic metal in the infrared, as it will be detailed in chapter 4.

The dispersion of  $Si_xN_y$  was provided by ellipsometry (Horiba Scientific Spectroscopic Ellipsometry), the dispersion of  $SiO_2$  was found in literature [2] and the dispersion of  $H_2O$  was at first taken from [3] and then measured with the refractometer (Schmidt Haensch Refractometer). Dispersion formulae are shown in table 3.1 are the one used for the simulations. The  $Si_xN_y$  dispersion was fitted with a 3<sup>rd</sup> degree polynomial function, whereas  $SiO_2$  and  $H_2O$  were fitted with Sellmeier laws[3] as shown in figure 3.1.

Table 3.1 Dispersion formulae for the real part of the refractive index of  $SiO_2$ ,  $SiN$  and  $H_2O$

Material	Wavelength range ( $\mu\text{m}$ )	Dispersion formula of n (Sellmeier and polynomial fits)
$SiO_2$	0.21 – 6.7	$\sqrt{1 + \frac{0.6961663\lambda^2}{\lambda^2 - 0.0684043^2} + \frac{0.4079426\lambda^2}{\lambda^2 - 0.1162414^2} + \frac{0.8974794\lambda^2}{\lambda^2 - 9.896161^2}}$
$SiN$	0.2 – 1.7	$-0.0101\lambda^3 + 0.0459\lambda^2 - 0.0963\lambda + 1.9835$
$H_2O$	0.5 – 1.75	$\sqrt{1 + \frac{0.75831\lambda^2}{\lambda^2 - 0.01007} + \frac{0.08495\lambda^2}{\lambda^2 - 8.91377}}$

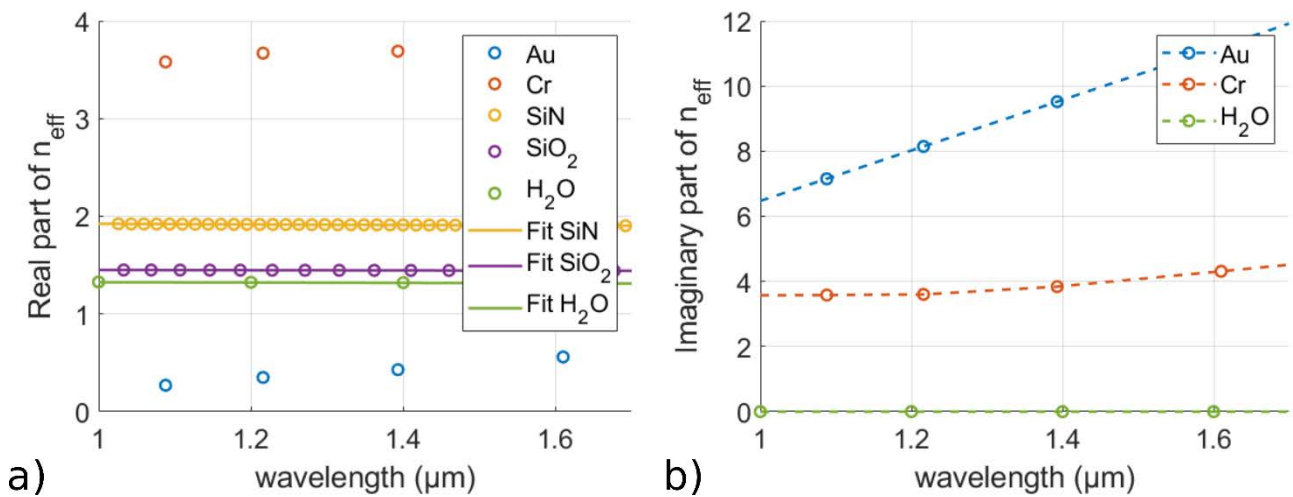


Figure 3.1 Dispersion from 1 to 1.7  $\mu\text{m}$  of the real and imaginary part of the refractive index of Au, Cr, SiN,  $SiO_2$  and  $H_2O$ . The solid lines represent the fit and the dots and dashed lines represent the data points respectively.

Once the materials are defined, Maxwell's equations can be solved by either analytical or numerical simulation methods in order to dimension the devices. In the following paragraphs, we describe the simulation methods and their properties, starting from the 1D analysis of a planar waveguide up to the 3D analysis of more complex structures.

### 3.1.2 Analysis of a planar waveguide – 1D analysis

One of the classical guided optics' problems is to solve Maxwell's equations in a multilayer 1D structure. The hypotheses are that  $\vec{J} = 0$ ,  $\rho = 0$  and that the materials, and thus the fields, are invariant along  $y$  (as shown later in Figure 3.2). We also suppose that the time variation of the field is described by equation 5 [4]:

$$\vec{E} = E \exp(j\omega t) + E^* \exp(-j\omega t) \quad (5)$$

After these hypotheses, Maxwell's equations are simplified to two sets of independent equations 5.a-c and 6.a-c called Transverse Electric (TE) and Transverse Magnetic (TM) respectively.

$$\left\{ \begin{array}{l} \frac{\partial H_x}{\partial z} - \frac{\partial H_z}{\partial x} = -j\epsilon_0 \epsilon_r \omega E_y \\ -\frac{\partial E_y}{\partial z} = j\mu_0 \omega H_x \\ \frac{\partial E_y}{\partial x} = j\mu_0 \omega H_z \end{array} \right. \quad \begin{array}{l} (5.a) \\ (5.b) \\ (5.c) \end{array} \quad TE(E_y, H_x, H_z)$$

$$\left\{ \begin{array}{l} \frac{\partial E_x}{\partial z} - \frac{\partial E_z}{\partial x} = j\mu_0 \omega H_y \\ -\frac{\partial H_y}{\partial z} = -j\epsilon_0 \epsilon_r \omega E_x \\ \frac{\partial H_y}{\partial x} = -j\epsilon_0 \epsilon_r \omega E_z \end{array} \right. \quad \begin{array}{l} (6.a) \\ (6.b) \\ (6.c) \end{array} \quad TM(H_y, E_x, E_z)$$

where  $H_x$ ,  $H_y$  and  $H_z$  are the components of the magnetic field respectively along the spatial directions  $x$ ,  $y$  and  $z$ ,  $E_x$ ,  $E_y$  and  $E_z$  are the components of the electric field respectively along the spatial directions  $x$ ,  $y$  and  $z$ ,  $\epsilon$  the relative dielectric constant,  $\omega$  the frequency and  $i$  the imaginary unit. TE refers to the system 5.a-c with zero longitudinal electric field ( $E_z = 0$ ) while TM refers to the system 6.a-c with zero longitudinal magnetic field ( $H_z = 0$ ). Furthermore, TE and TM are called orthogonal polarization states, and this means that the solutions of these systems are independent and do not influence power between them.

Each of the TE and TM system can be written as a single differential equation of the Helmholtz form by substituting equation 5.b and 5.c in equation 5.a. The resulting equation, shown in equation 7, is called wave equation.

$$\frac{\partial^2}{\partial z^2} U(x, z) + \frac{\partial^2}{\partial x^2} U(x, z) = -k_0^2 n_i^2 U(x, z) \quad (7)$$

$$\text{with } \begin{cases} k_0 = \sqrt{\omega^2 \epsilon_0 \mu_0} \\ n_i = \sqrt{\epsilon} \end{cases}$$

where  $U(x, z)$  is  $E_y$  for TE polarization and  $H_y$  for TM polarization. In the case of a planar waveguide, the system is invariant also along  $z$ . Thus, all derivatives along  $z$  are zero and  $k_z$  is constant along  $x$ . Equation 7 simplify and their solution is of the form [4] :



$$U(x, z) = (A^- e^{-jk_x x} + A^+ e^{jk_x x}) e^{-jk_z z} \quad (8)$$

where the wavevector  $k_x = \sqrt{k_0^2 n^2 - k_z^2}$ ,  $k_z$  is the propagation constant,  $A^-$  and  $A^+$  amplitude coefficients. We understand that the field component  $U(x, z)$  is composed of a forward and a backward wave

Once the field component  $U(x, z)$  is known, all the other components of the field can be calculated using equations 5.a-c and 6.a-c (i.e.  $H_x, H_z$  for TE and  $E_x, E_z$  for TM).

Once that Maxwell's equations are solved for a general 1D space, we can find the relation between propagating and counter propagating waves in both homogeneous media and at interfaces. Furthermore, the solution can be expressed in matrix form: the *transfer* and *scattering* matrices (formula 8 et 9 respectively) represent two possible representations of the wave propagation.

$$\begin{pmatrix} w^{i,+}(x) \\ w^{i+1,-}(x) \end{pmatrix} = \begin{bmatrix} S_{11} & S_{12} \\ S_{21} & S_{22} \end{bmatrix} \begin{pmatrix} w^{i,-}(x) \\ w^{i+1,+}(x) \end{pmatrix} \quad (8)$$

$$\begin{pmatrix} w^{i,+}(x) \\ w^{i,-}(x) \end{pmatrix} = \begin{bmatrix} T_{11} & T_{12} \\ T_{21} & T_{22} \end{bmatrix} \begin{pmatrix} w^{i+1,+}(x) \\ w^{i+1,-}(x) \end{pmatrix} \quad (9)$$

where  $w^{i,+}$  is the propagating wave in the  $i^{th}$  medium ( $w^{j,+} = A^- e^{-jk_x x}$ ),  $w^{i,-}$  is the counter-propagating wave in the  $i^{th}$  medium ( $w^{j,-} = A^+ e^{jk_x x}$ ).  $S_{11}, S_{12}, S_{21}$  and  $S_{22}$  are the elements of the scattering matrix  $S$  and  $T_{11}, T_{12}, T_{21}$  and  $T_{22}$  are the elements of the transfer matrix  $T$ .

In a homogeneous medium, light undergoes a phase shift while propagating. The transfer and scattering matrices simplify to formula 10, and they are called *propagation* matrices  $Q$  in the  $i^{th}$  homogeneous medium.

$$Q_T = \begin{pmatrix} e^{jk_x^i e^i} & 0 \\ 0 & e^{-jk_x^i e^i} \end{pmatrix} \text{ and } Q_S = \begin{pmatrix} 0 & e^{-jk_x^i e^i} \\ e^{-jk_x^i e^i} & 0 \end{pmatrix} \quad (10)$$

where  $k_x^i$  is the  $x$  component of the wavevector  $k$  in medium  $i$  (the wavevector  $k = k_0 n_i$ ,  $k_0$  is defined in formula 7,  $n_i$  is the refractive index of the medium  $i$ ) and  $e_i$  is the thickness of the homogeneous medium  $i$ . As shown in Figure 3.2, the propagation matrices describe the propagation between interfaces.

At an interface between two materials, we have four coefficients to solve: the forward and backward wave in both layers. By adding the hypothesis that the  $E_y$  and its derivative are continuous for the TE field, the problem is written in the matrix form. The transfer and scattering matrix can be simplified as follows, also called *interface* or  $I$  matrices :

$$I_T = \begin{bmatrix} \frac{k_x^i + k_x^{i+1}}{2k_x^i} & \frac{k_x^i - k_x^{i+1}}{2k_x^i} \\ \frac{k_x^i - k_x^{i+1}}{2k_x^i} & \frac{k_x^i + k_x^{i+1}}{2k_x^i} \end{bmatrix} \text{ and } I_S = \begin{bmatrix} \frac{k_x^i - k_x^{i+1}}{k_x^i + k_x^{i+1}} & \frac{2k_x^{i+1}}{k_x^i + k_x^{i+1}} \\ \frac{2k_x^{i+1}}{k_x^i + k_x^{i+1}} & \frac{k_x^{i+1} - k_x^i}{k_x^i + k_x^{i+1}} \end{bmatrix} \quad (11. a)$$

$$I_T = \begin{bmatrix} \frac{k_x^i}{n_i^2} + \frac{k_x^{i+1}}{n_{i+1}^2} & \frac{k_x^i}{n_i^2} - \frac{k_x^{i+1}}{n_{i+1}^2} \\ 2 \frac{k_x^i}{n_i^2} & 2 \frac{k_x^{i+1}}{n_{i+1}^2} \\ \frac{k_x^i}{n_i^2} - \frac{k_x^{i+1}}{n_{i+1}^2} & \frac{k_x^i}{n_i^2} + \frac{k_x^{i+1}}{n_{i+1}^2} \\ 2 \frac{k_x^i}{n_i^2} & 2 \frac{k_x^{i+1}}{n_{i+1}^2} \end{bmatrix} \text{ and } I_S = \begin{bmatrix} \frac{k_x^i}{n_i^2} - \frac{k_x^{i+1}}{n_{i+1}^2} & 2 \frac{k_x^{i+1}}{n_{i+1}^2} \\ \frac{k_x^i}{n_i^2} + \frac{k_x^{i+1}}{n_{i+1}^2} & \frac{k_x^i}{n_i^2} + \frac{k_x^{i+1}}{n_{i+1}^2} \\ 2 \frac{k_x^{i+1}}{n_{i+1}^2} & \frac{k_x^{i+1}}{n_{i+1}^2} - \frac{k_x^i}{n_i^2} \\ \frac{k_x^i}{n_i^2} + \frac{k_x^{i+1}}{n_{i+1}^2} & \frac{k_x^i}{n_i^2} + \frac{k_x^{i+1}}{n_{i+1}^2} \end{bmatrix} \quad (11. b)$$

where  $k_x^i$  is the  $x$  component of the wavevector  $k$  in medium  $i$  and where  $k_x^{i+1}$  is the  $x$  component of the wavevector  $k$  in medium  $i + 1$ ,  $n_i$  and  $n_{i+1}$  are the refractive indices of layer  $i$  and  $i + 1$  respectively. As shown in Figure 3.2, the interface matrices describe the behaviour of propagation between interfaces.

Once all the propagation and interface matrices of each layer are calculated, a global matrix  $M$  describes the 1D multilayer structure either by using transfer of scattering matrices. Although the two matrices can describe the same structures, the transfer matrix has an easier way to solve multilayer structures since the transfer matrix of the complete structure is simply the multiplication of the transfer matrix of each layer and interface.

$$M_T = \begin{bmatrix} M_{T11} & M_{T12} \\ M_{T21} & M_{T22} \end{bmatrix} = I_{T_1} \times Q_{T_1} \times I_{T_2} \times Q_{T_2} \times \dots \times I_{T_n} \quad (12)$$

Scattering matrices are slightly more complex to combine because they need a Redheffer product  $\otimes$  described below.

$$M_S = \begin{bmatrix} M_{S11} & M_{S12} \\ M_{S21} & M_{S22} \end{bmatrix} = I_{S_1} \otimes Q_{S_1} \otimes I_{S_2} \otimes Q_{S_2} \otimes \dots \otimes I_{S_n} \quad (13)$$

where the Redheffer product  $\otimes$  is defined as

$$S^1 \otimes S^2 = \begin{bmatrix} S_{11}^1 + \frac{S_{12}^1 S_{11}^2 S_{21}^1}{1 - S_{22}^1 S_{11}^2} & \frac{S_{12}^1 S_{12}^2}{1 - S_{22}^1 S_{11}^2} \\ \frac{S_{12}^2 S_{21}^1}{1 - S_{22}^1 S_{11}^2} & S_{22}^2 + \frac{S_{21}^2 S_{22}^1 S_{12}^2}{1 - S_{22}^1 S_{11}^2} \end{bmatrix}. \quad (14)$$

In spite of the more complex combination, scattering matrices are more stable because of their intrinsic structure: both exponentials of their propagation matrices have the same sign (see equation 10), avoiding terms of the same matrix to be several orders of magnitude apart making the system unstable. This condition becomes more evident when working with devices with a significant imaginary part, as in case of plasmonic structures. This is why in our study we prefer to use scattering matrices.

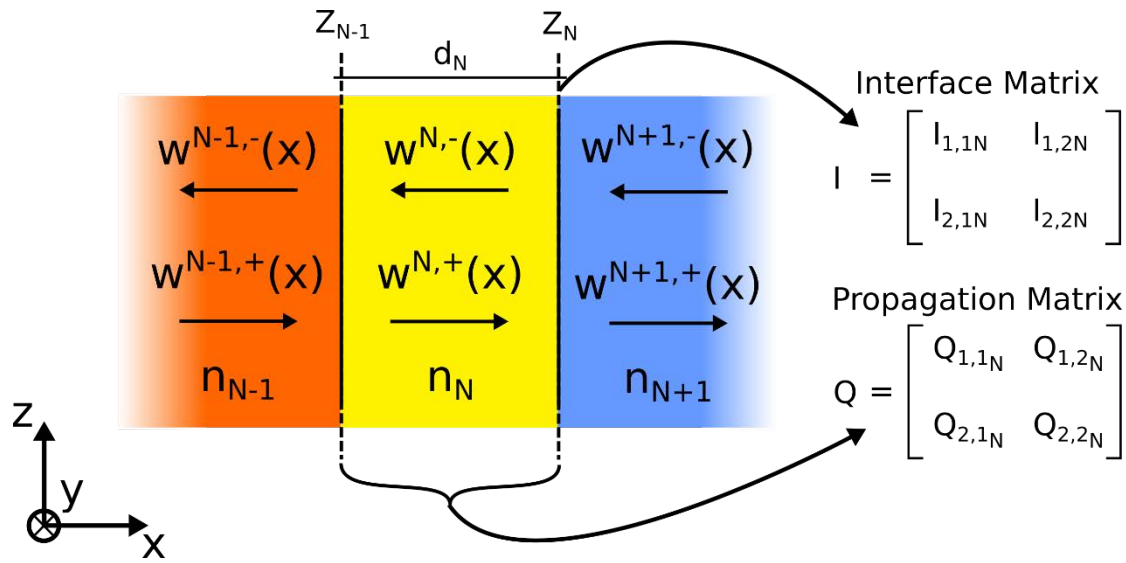


Figure 3.2 Multilayer structure analyzed by the transfer matrix method: on the left the structure composed of a stack of layers with different dielectric constants along  $x$ . Each interface is described by an interface matrix while the homogeneous parts are described by a propagation matrix.

The global matrix is useful to find the reflection  $R_{tot} = M_{11}$  and transmission  $T_{tot} = M_{21}$  of the structure.

Another interesting property of the overall scattering matrix is that it contains the characteristics of the modes of the structure. Modes are particular solution of Maxwell's equations existing without external excitation and they are described by the eigenvalues and eigenvector of the equation. They can be either TM or TE modes, depending on which independent set of equations is considered (equations 5.a-c for TE modes and system 6.a-c for TM modes). The following hypotheses hold true to find the modes and their properties:

- There is no forward travelling wave in the first layer (where  $w^{0,+} = 0$ )
- There are no backward propagating waves the last layer (Sommerfeld radiation condition [5],  $w^{n,-} = 0$ ).

The equation that we aim to solve is that the  $T_{tot}(k_z) = 0$  or, in global matrix term, that

$$M_{T_{22}}(k_z) = 0, \text{ or } \frac{1}{M_{S_{11}}(k_z)} = 0 \quad (15)$$

The  $k_z$  vectors that satisfy equation 14 are the solutions of the problem and they are expressed as

$$k_z = k_0 n_{eff} = \frac{2\pi n_{eff}}{\lambda_0} \quad (16)$$

where  $n_{eff}$  is the *effective refractive index*. The real part of  $n_{eff}$  can be interpreted as the average speed of the mode and it is useful to understand the interaction between modes. Its imaginary part  $\alpha$  is related to the extinction ratio of the mode i.e. when the mode will lose  $1/e$  of its energy while propagating. Depending on its sign, it can be interpreted as losses or gain of the mode. For each value of  $n_{eff}$ , the field distribution can be found throughout the whole structure by finding the amplitude coefficients defined in equation 8 for each layer.

Figure 3.4 shows the result of the transfer matrix method coded with MATLAB for a slab waveguide, represented by a central slab of higher index, called *core*, and two side slabs with lower index called *substrate* and *cover* [4], as shown in figure 3.4.a-c. In this example,  $n_{core} = 1.9$ ,  $n_{sub} = 1.44$  and  $n_{cov} = 1.32$ . When the real part of  $n_{eff}$  is between the value of the core and the highest value between the substrate and the cover, the mode is called *guided*. In the example, in figures 3.3.a and 3.4.c the purple line represents the  $n_{eff}$  of the mode which confirms that the mode is guided. This means that the field is decaying exponentially outside the *core* slab, as it can be noticed by looking at figures 3.3.4.b and 3.3.d. Furthermore, these modes have zero losses because the simulation included only perfect dielectric materials (i.e. with  $k = 0$ ). In conclusion, the two modes shown in the example are guided ( $n_{eff} = 1.83$  for the fundamental mode and  $n_{eff} = 1.59$  for the first order mode) and lossless (losses = 0 dB/cm for both modes). When  $n_{eff}$  is below either the substrate or cover index, the mode leaks and energy is lost. These modes are called radiation modes and their  $\alpha$  is nonzero. Image 3.3.e and 3.3.f shows the example of a distribution of a radiated mode with  $n_{eff} = 1.36$  and losses = 25000 dB/cm. The number of guided modes in a waveguide depends both on the size of the core and the refractive index difference between the core and the surrounding material and the dimension of the core. We define the cutoff as the condition for which one mode stops being guided. Modes *above the cutoff* are guided while modes *below cutoff* are radiated. A waveguide with only one guided mode is called *monomode*, while a waveguide with more than one mode is called *multimode*.

To distinguish modes in a multimode waveguide, we associate each one of them to an order. In figure 3.3a-b show the mode 0 (or fundamental mode) and Figure 3.3c-d show the mode 1 or first order mode. The shape of the field is also linked to the order of the mode: when the

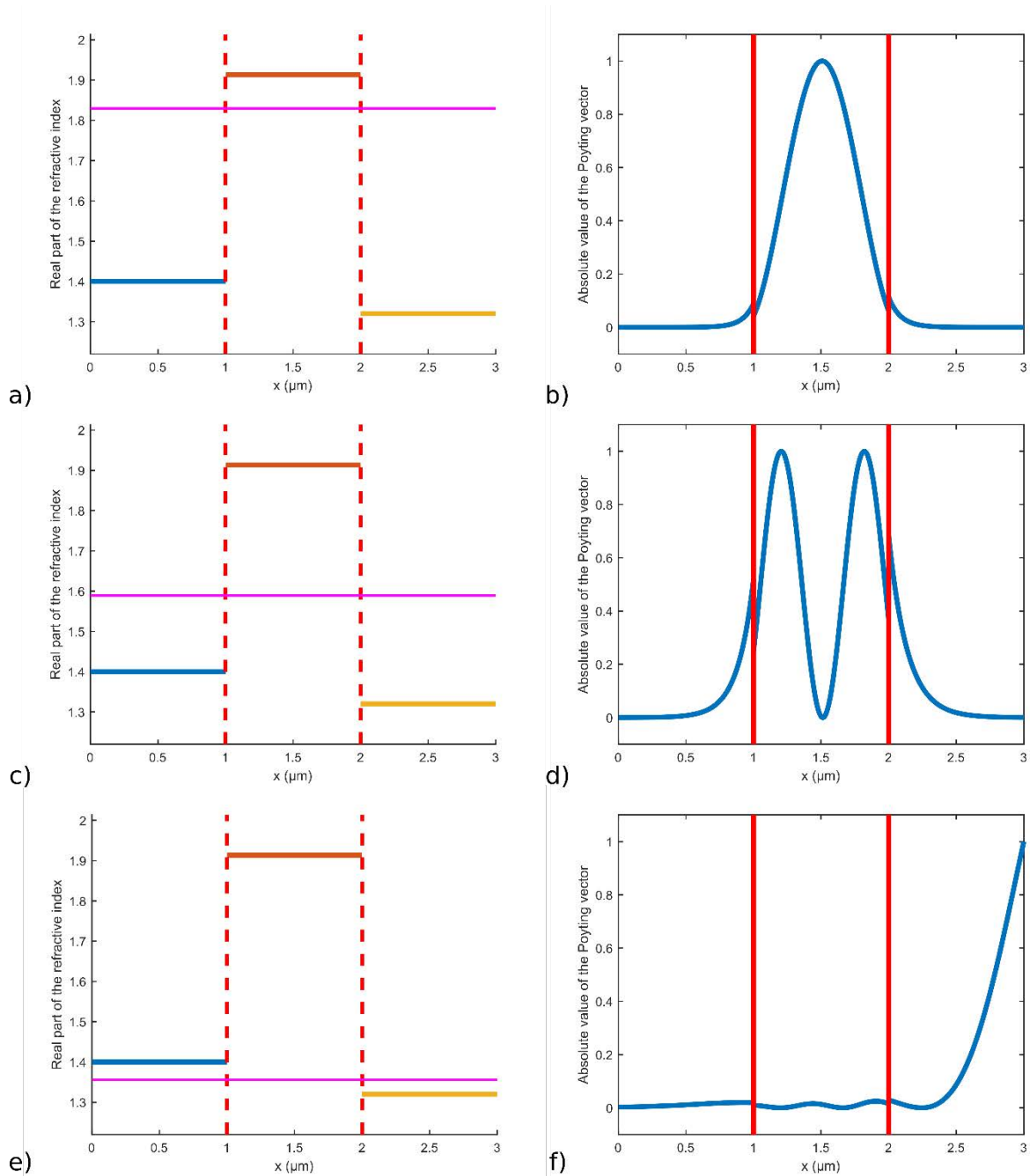


Figure 3.3.a, 3.3.c and 3.3.e show the real part of the refractive index along  $x$ , perpendicular to the direction of propagation. Figure 3.3.b, 3.3.d and 3.3.f show the absolute value of the normalized Poynting vector, which describes the power distribution of the mode in the different layers for a TM mode. The  $n_{eff}$  and the losses for the modes are:  $n_{eff} = 1.83$  and losses = 0 dB/cm for the fundamental mode (figure 3.b),  $n_{eff} = 1.59$  and losses = 0 dB/cm for the first order mode (figure 3.d) and  $n_{eff} = 1.36$  and losses = 25000 dB/cm for the radiated mode (figure 3.f).

order of the mode increases, the number of peaks in the core slab increases as well as it can be noticed for the first two modes of the slab shown in pictures 3.3.b and 3.3.d. In the case of a symmetric slab, the fundamental TE mode is above the cutoff for any positive value of core width.

Another characteristic of guided modes that is interesting to calculate, especially when making biosensors, is called the filling factor. The filling factor is the portion of energy confined to a defined region of the simulation window. It is defined as

$$filling\ factor = \frac{\int^R P_z(\vec{s}) ds}{\int^\infty P_z(\vec{s}) ds} \quad (18)$$

where  $P_z$  is the power of the mode and  $R$  is the portion of the simulation window where the power is calculated. In other words, the filling factor is the power of the mode in  $R$  over the power along the whole simulation window, theoretically infinite. For sensing applications, the filling factor is useful to estimate the percentage of power in the target liquid and have a better idea of the interaction between the analyte and the sensor response, as it will be shown in chapter 4.

In conclusion, this section showed how to derive the modes of a photonic multilayer structure from Maxwell's equations and their characteristics: the polarization (TE or TM), the order and the  $n_{eff}$ , which determines if the mode is guided or radiated and the losses.

The next sections are dedicated to two 1D examples: the coupling between two dielectric waveguides and the plasmonic modes.

### 3.1.2.1 Coupling between two dielectric waveguides – 1D analysis

In integrated photonics, modes of different structures can exchange power when placed sufficiently close. This phenomenon is called *coupling* and it is of paramount importance when designing ring couplers, direction couplers, or hybrid plasmonic structures. In this section, an example of coupling between two waveguides is detailed.

Let us consider two waveguides A and B, far apart from each other. To keep the example simple, let us suppose that the two waveguides are identical, monomode and with TE polarization only. The field profile of each one looks similar to the one in figure 3.3.b. When bringing them close together, the modes of the two waveguides interact. Figures 3.4.a and 3.4.c show the  $n_{eff}$  distribution of the simulation, where two waveguides are in close proximity to each other. The two modes found are quite different from the modes in the isolated waveguides. Figures 3.4.b and 3.4.d show the two guided modes calculated by the mode-solver. The two modes are called *even* and *odd* (Figure 3.4.b and 3.4.d respectively) because of the parity of the amplitude with respect to the X axis. In other words, the two isolated modes couple in the odd and even modes when the waveguides are in proximity. It can be noticed in figure 3.4.e that the odd and even  $n_{eff}$  are progressively further apart when the gap between the two waveguides decreases. This means that even and odd modes have different speeds and the total power is transferred from one waveguide to another periodically. When the two modes are in phase, power is concentrated in waveguide A, while when they are in phase opposition (phase shift of  $\pi$ ) all the power is in waveguide B. The periodicity of this phenomenon depends on the gap between the waveguides and the speed difference between the odd and even modes. To define the strength of the coupling between

the waveguides, it is convenient to define two quantities: the coupling length  $L_\pi$  and the coupling coefficient in amplitude  $k$ :

$$L_\pi = \frac{\pi}{\beta_{\text{even}} - \beta_{\text{odd}}} \quad (19)$$

$$k = A_0 \cdot \sin\left(\frac{\pi L}{2L_\pi}\right) \quad (20)$$

where  $\beta_{even}$  and  $\beta_{odd}$  are the propagation constants of the even and odd modes respectively.  $L_{\pi}$  and L represent respectively the coupling length and the length of the coupler. Total energy transfer occurs when  $L = L_{\pi}$ . The amplitude  $A_0$  can be calculated with the overlap of the modes between the single waveguide and the even and odd modes of the twin waveguides.

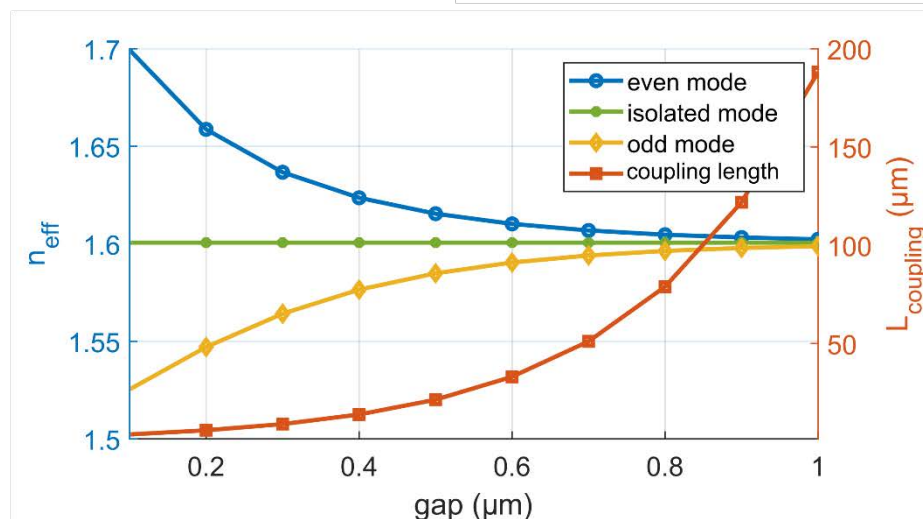
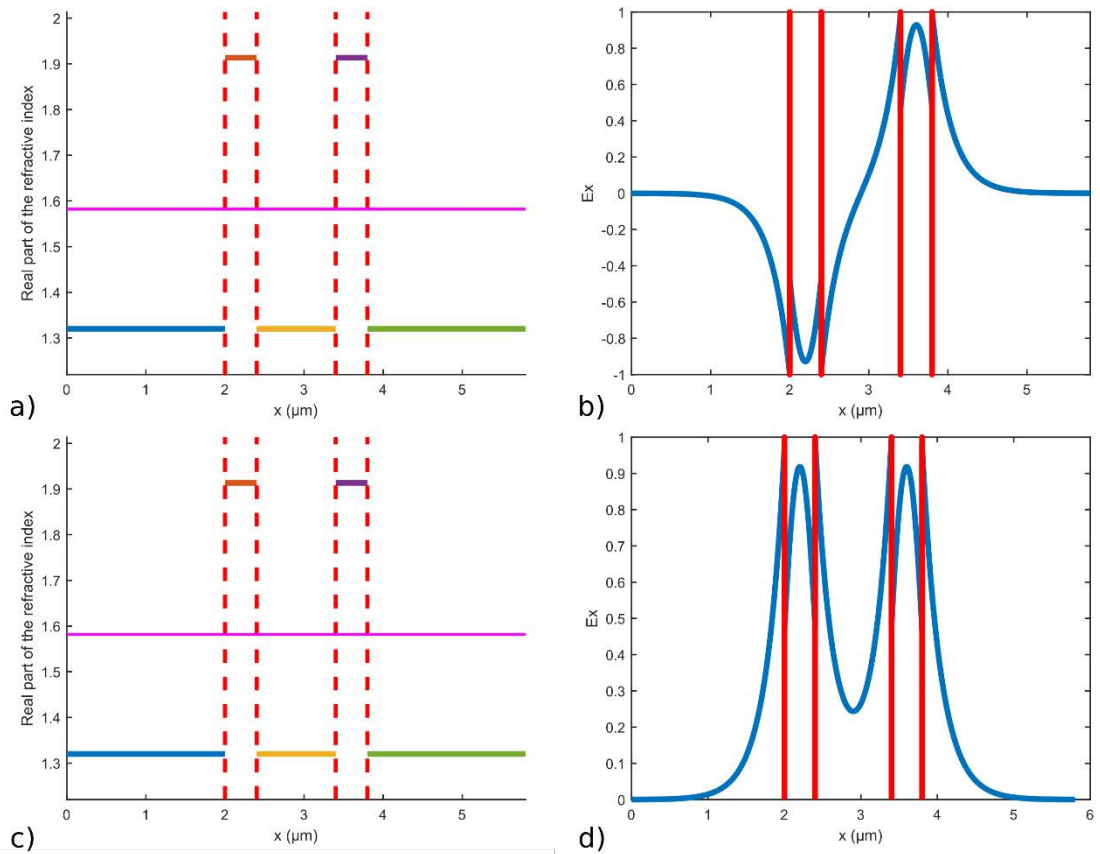


Figure 3.4.a and 3.4.c show the real part of the refractive index along  $x$ , perpendicular to the direction of propagation. Figure 3.4.b and 3.4.d absolute value of the  $E_x$  component of the electric field for the even and odd modes respectively. Figure 3.4.e plot of the  $n_{eff}$  of the isolated, odd and even modes as well as the coupling length of the modes.



The right ordinate axis of figure 3.4.e shows the evolution of  $L_\pi$  as a function of the gap of the waveguides. As expected,  $L_\pi$  grows when the two waveguides are further apart because  $\beta_{even}$  and  $\beta_{odd}$  are closer. Thus, the speed of the odd and even mode are closer, leading to a slower power transfer. Furthermore,  $L_\pi$  can be adjusted to separate power between two waveguides.

While this problem is rather simple in 1D, the 2D problem is more complex and requires more approximations, as it will be shown later in this chapter.

### 3.1.2.2 Plasmonic waveguides

This section is dedicated to plasmonic waveguides, a peculiar type of waveguide consisting of an interface between two materials of dissimilar properties, supporting *surface modes*. Like in

the analysis of dielectric waveguides, the field is divided in backward and forward propagating waves in each layer, as shown in figure 3.5.

Taking into account the condition to find guided modes of a structure (i.e.  $w^{1,+}(x) = 0$  to consider no excitation of the system and  $w^{2,-}(x) = 0$  is the Sommerfeld condition [5]), the system associating the four waves is the following:

$$\begin{pmatrix} 0 \\ w^{1,-}(x) \end{pmatrix} = \begin{bmatrix} S_{11} & S_{12} \\ S_{21} & S_{22} \end{bmatrix} \begin{pmatrix} w^{2,+}(x) \\ 0 \end{pmatrix} \quad (21)$$

Writing the first equation of the matrix system, we obtain the following equation:

$$S_{11} w^{2,+}(x) = 0 \rightarrow S_{11} = 0 .$$

Depending on the polarization, from the system (11.a-b) we can find the two conditions:

$$S_{TE11} = \frac{k_{x2} + k_{x1}}{2k_{x1}}, \quad k_{x2} = -k_{x1} \quad (22)$$

$$S_{TM11} = \frac{\frac{k_{x2}}{n_2^2} + \frac{k_{x1}}{n_1^2}}{2 \frac{k_{x1}}{n_1^2}}, \quad \frac{k_{x2}}{n_2^2} = -\frac{k_{x1}}{n_1^2} \quad (23).$$

Equation 22 is true only if both wavevectors  $k_{x1} = 0$  and  $k_{x2} = 0$ . This means that for TE polarization no guided modes exist. On the other hand, for equation 23 there is a possibility of a solution for non-zero  $k_{x1}$  and  $k_{x2}$ , that is having an imaginary refractive index  $n_1$  or  $n_2$ . Since  $n^2 = \epsilon_r$ , the guided modes exist provided that the sign of the dielectric constant changes across the interface. For example, this condition is satisfied at the interface between a metal (characterized by a complex refractive index) and a dielectric (characterized by a real

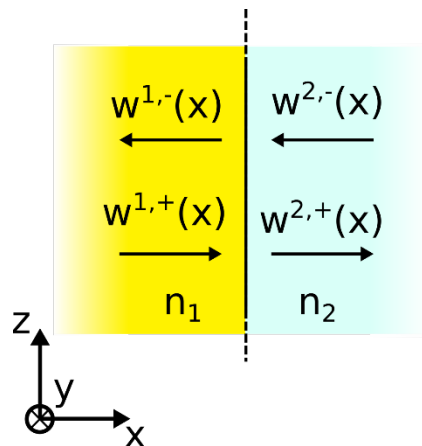


Figure 3.5 Schematic of the interface between two materials and the forward and backward waves in each layer.

refractive index). Equation 23 is called the existence condition for plasmonic modes. The plasmonic existence equation expresses a relation between the slope of the decaying

exponential fields and the absolute value of the dielectric constants: for example, when the absolute value of the dielectric constant of the metal is high, the percentage of power in the dielectric increases and vice-versa. Figure 3.6.a and 3.6.b show the distribution of the refractive index of this example and the power profile. The resulting mode exists because the existence condition is satisfied ( $\epsilon_{r_{Au}} = -79$  while  $\epsilon_{r_{H_2O}} = 1.74$  at  $1.31 \mu\text{m}$  [3], [6]). As expected, the exponential decay is more significant in the metal side.

Another interesting property of plasmonic modes are the limits of their  $n_{eff}$ : unlike dielectric modes that have an  $n_{eff}$  bounded between the core and the substrate index, plasmonic modes have an  $n_{eff}$  higher than both refractive indices of materials of the interface. In the example shown in figure 3.6,  $n_{H_2O} = 1.32$ ,  $n_{Au} = 0.392$  while the mode has  $n_{eff} = 1.33$ . The reason why the  $n_{eff}$  needs to be higher than both  $n_{H_2O}$  and  $n_{Au}$  is because one of the decaying exponential would become a complex propagating sinusoid, allowing power leakage. In fact, if  $n_{eff}$  is below one of the two refractive indices of the interface, the mode is radiated.

Moreover, plasmonic modes are lossy. Since one of the two materials is a metal, its absorption coefficient is non-negligible,  $k \neq 0$ . A plasmonic mode between at  $Au$  and  $H_2O$  interface has losses of 554 dB/cm at  $1.31\mu\text{m}$  wavelength.

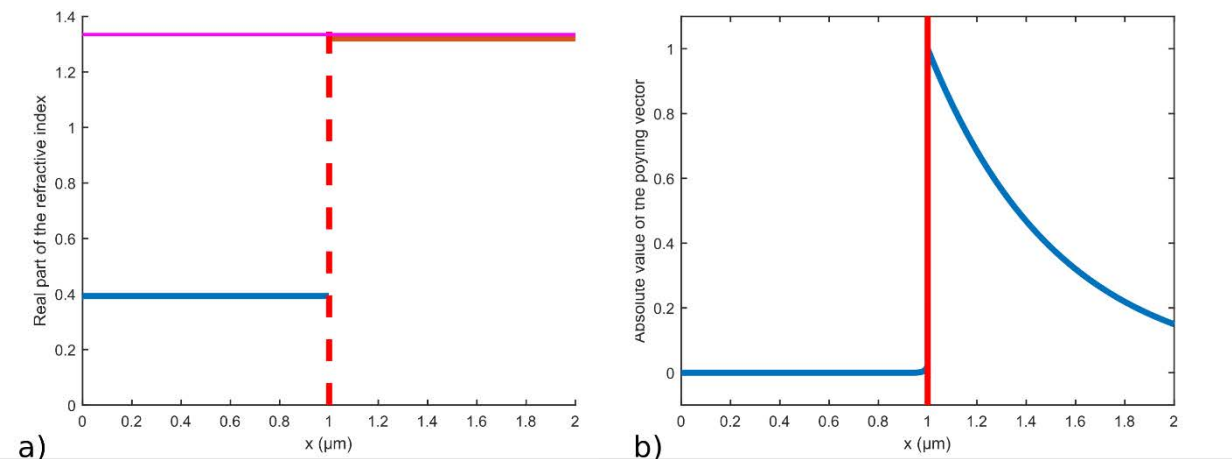


Figure 3.6 a real part of the refractive index along  $x$ . 3.6.b power distribution of the plasmonic mode across the interface, as two decaying exponentials. The effective refractive index is

$$n_{eff} = 1.33 \text{ and losses} = 554 \text{ dB/cm at } 1.31\mu\text{m wavelength.}$$

In this section, we detailed the properties of plasmonic waveguides. These properties are fundamental to understand HPWG modes, explained in chapter 4.

### 3.1.3 Simulations mode-solver—2D analysis

In the previous section, we detailed the solution for “slab” waveguides. In this section, we consider waveguides where confinement takes place also in the  $y$  direction (in the film plane). The solution of the problem is a set of coupled partial differential equations that do not have an analytic solution [4]. However, numerical methods are available to find the solutions of the system. Well-known examples of numerical methods are finite difference methods (FDM) and finite element methods (FEM).

FDMs are used to solve differential equations by converting them in an approximate problem that can be solved by matrix algebra techniques. The computational domain is subdivided into a rectangular grid and solved by approximating the derivative with the difference of two adjacent points divided by their distance. The solution at each point of the grid is found by calculating the solution, taking into account the neighboring points [7]. FEMs convert the simulation domain in smaller parts called *elements*. Coupled solutions for each element are expressed in matrix form so a global solution can be found. Unlike FDMs, the elements of the mesh do not have to be rectangles. The method approximates the result over the domain while minimizing an error function [8].

When these methods are applied to find the mode characteristics of a given structure (e.g. field distribution, filling factor,  $n_{eff}$ ) they are called *mode-solvers*. In this work, we used two types of mode-solver software: one developed in the INL laboratory using FDM and a commercial software by Photon Design (FIMMWAVE) with the possibility of using both FEM and FDM. Both solvers differ in calculation speed and complexity of the code. In particular, the mode-solver developed at INL uses transparent boundary conditions and a 9 point scheme to avoid using index averaging at the interfaces[9]. This property is interesting when the index difference between the core and the cladding is large ( $>1$ ). In our case, simulations from both tools converged to the same results.

### 3.1.3.1 Setting up the simulation

Once the structure geometry and the materials are defined, the simulation window needs to be divided into cells. This procedure is called *meshing* and it is common when using numerical methods. Meshing is an important step because, if not performed correctly, it leads to wrong results or unnecessarily long simulations. To prevent these effects, a preliminary test called “convergence test” has to be performed to optimize the simulation parameters. To be clear, let us consider the parameters in the case of the FIMMWAVE simulation tool (for the custom mode-solver the reasoning is analogous). Before starting the simulations, any symmetry of the system is identified to speed up calculations. The simulation window size is chosen to have less than 1% of the maximum power at the edges of the simulation window. Smaller windows decrease the precision while wider windows increase the simulation time, therefore a trade-off needs to be found. The mode-solver numerical method is selected based on the materials and geometry of the structure. For the structures analyzed in this study, the choice was the Non-uniform FDM (Finite Difference Method) solver. Non-uniform refers to the meshing: since the HPWG structure contains a metal-dielectric interface and the field is discontinuous at the interface, the number of mesh nodes in the proximity of the interface should be high. On the contrary, when calculating the field inside a homogeneous material, the simulation mesh nodes can be further apart without drastically affecting the results. As shown in chapter 4, the HPWG structure has surface modes that have abrupt changes at the interfaces thus requiring a high density of calculation points close to the interfaces. This is why the Non-uniform FDM (Finite Difference Method) solver is the chosen solver. The option of the FEM solver is a good candidate. However, we decided to keep the Non-uniform FDM (Finite Difference Method) as the main simulation solver because it has faster simulation time and comparable results in term of precision.

For non-uniform FDM solvers, the convergence parameter is the maximum number of divisions along the  $y$ -axis and the  $x$ -axis, also noted as  $n_x max$  and  $n_y max$ , which is proportional to the precision of the simulation. The convergence study starts with a low number of mesh points, associated with fast simulation times. Afterwards the number of mesh points is progressively increased until the effective refractive index of the mode stabilizes. Convergence is reached and there is no need to further increase the maximum number of divisions  $n_x max$ , avoiding unnecessary long simulations. Figure 3.7 shows the  $n_{eff}$  and its relative error as a function of the maximum number of divisions across the mesh.

In the case depicted in figure 3.7, the optimal tradeoff between speed and precision of the simulation is reached when  $n_{eff}$  stabilizes. This condition is satisfied when  $n_x max = 500$ . Once these parameters are set, the simulation provides reliable parameter estimates of the modes, as explained before ( $n_{eff}$ , filling factor, mode losses).

In this section, we presented the simulation methods and the methodology to perform simulations for 2D cross-section waveguides. The next section is dedicated to examples of more complex structures, such as bent waveguides and directional couplers.

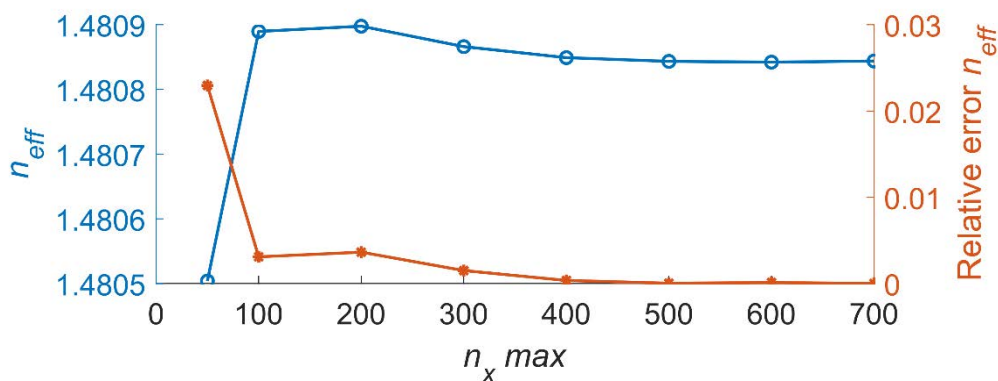


Figure 3.7 the error in the convergence test when changing the maximum number of points of the simulation window  $n_x max$ . The convergence is reached above  $n_x max = 500$  which represents the optimal tradeoff between speed and precision.

### 3.1.3.2 Bent waveguides

When waveguides are not straight, their propagation constant changes along the direction of propagation. This property can be taken into account in the simulation by changing the refractive index with a conformal transformation, as shown in figure 3.8[10]. The problem is expressed in cylindrical coordinates. The result is that the mode's field distribution is modified, as shown in pictures 3.8.c and 3.8.d.

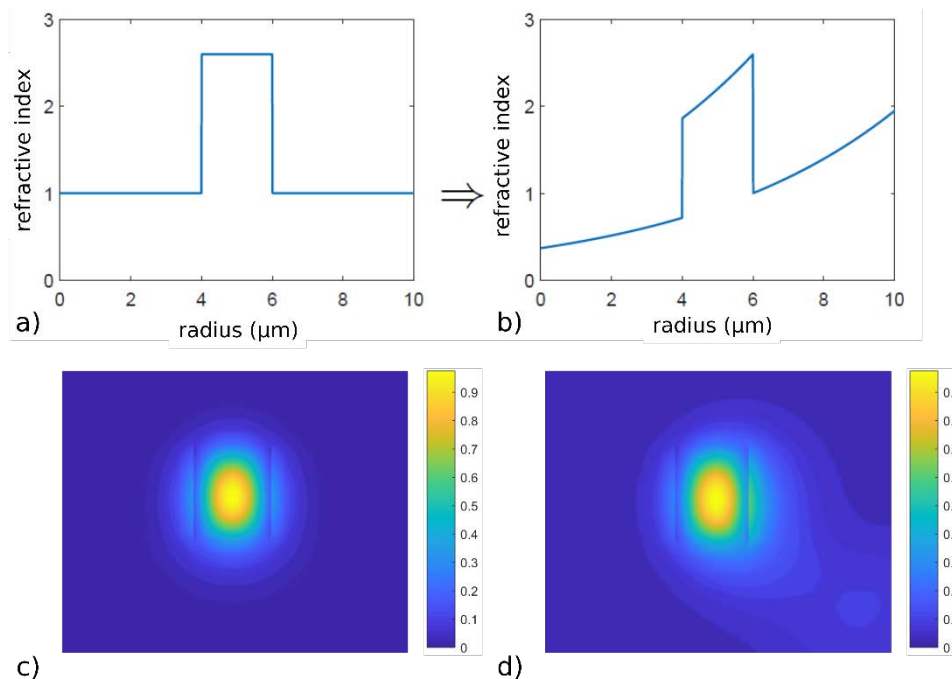


Figure 3.8.a and 3.8.b show the diagram of the conformal transformation from a conventional waveguide profile to a profile with a conformal transformation. 3.8.c and 3.8.d show the final transformation field distribution of the mode when the conformal transformation is applied.

This study did not focus on the optimization of the bend, we just show here that the bending radius ( $5 \mu\text{m}$ ) is a tradeoff between losses and compactness as it has been already proven by previous results using the same industrial platform.

### 3.1.3.3 Coupling between two waveguides—2D analysis

As seen in paragraph 3.1.2.1, modes of different structures can exchange power when the waveguides are placed sufficiently close. This phenomenon is called *coupling*. Coupling is studied to understand and to optimize the interaction between the waveguide modes and it is the phenomenon based on which direction couplers work. To describe coupling between 2D waveguides we can use a 2D mode-solver to simulate the modes of the waveguide. There also exist analytical approximations such as the Coupled Mode Theory (CMT) and the approximated coupling formula for rectangular waveguides[11]. In this section, we will detail the 2D simulation, the CMT and the rectangular waveguide approximation formula. The system under study are two  $Si_3N_4$  waveguides whose geometry is shown in figure 3.9.a and 3.9.b.

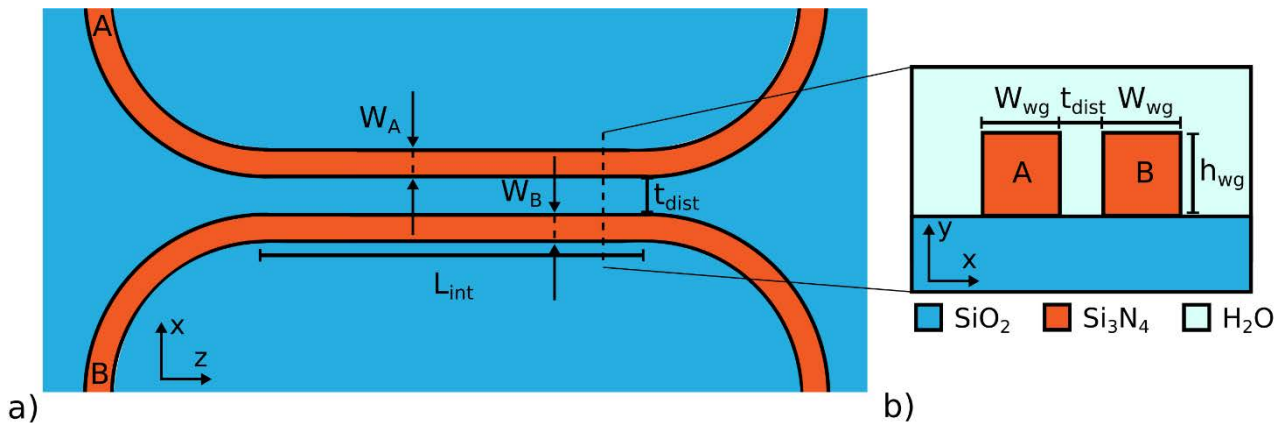


Figure 3.9 Example of coupling geometry between two waveguides. 3.9.a) top view of two dielectric waveguides A and B in proximity to the coupling region  $L_{int}$ . 3.9.b) cross section of the coupling region of the device

The 2D simulation provides the  $n_{eff}$  and the field distribution of the even and odd modes, as shown in figure 3.10.a-b. Like in the 1D case, we can find the coupling coefficient using formula 19.

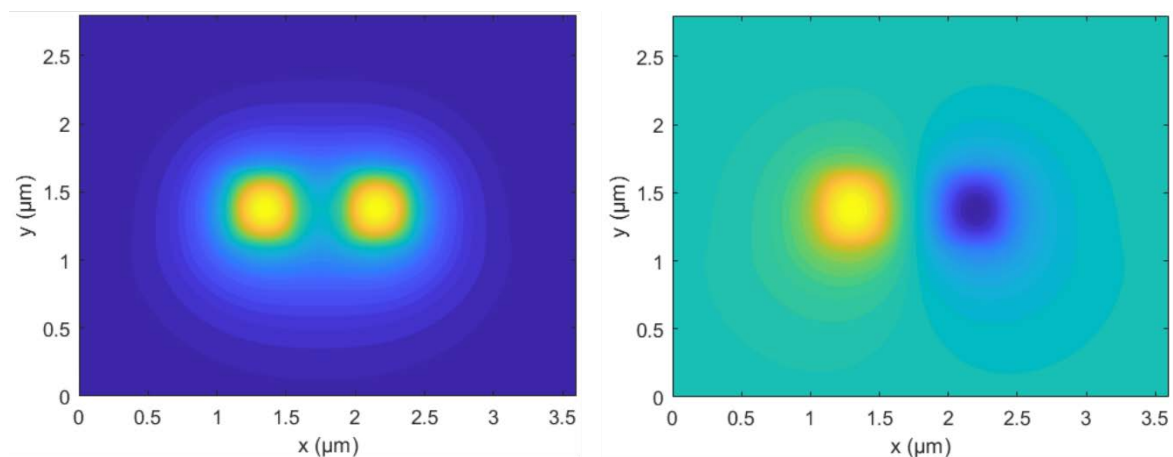


Figure 3.10.a Plot of the field  $E_y$  of the even mode ( $n_{eff} = 1.558$ ). 3.10.b Plot of the field  $E_y$  of the odd mode ( $n_{eff} = 1.513$ ).

Concerning analytical methods to explore the coupling between waveguides, the Coupled Mode Theory (CMT)<sup>6</sup> is well-known in literature [12]. CMT is a perturbation theory that works when the waveguides interact weakly, i.e. without significantly modifying the field distribution of isolated waveguides. The CMT is generally used to find the distance and the length of the coupling region in ring resonators. In the CMT, the coupling coefficient  $k$  defines how much power transfers from one waveguide to the other. For example, in the case of two rectangular waveguides  $A$  and  $B$ , the coupling coefficient  $k_{A,B}$  is calculated using the equation 24 [12].

$$k_{A,B} = \frac{\omega \epsilon_0 \iint_{-\infty}^{+\infty} (\epsilon_{core} - \epsilon_{sub}) \vec{E}_A^* \circ \vec{E}_B \, dx dy}{\iint_{-\infty}^{+\infty} (\vec{E}_A^* \times \vec{H}_A + \vec{H}_A^* \times \vec{E}_A) dx dy} \quad (24)$$

where  $\epsilon_{core}$  the relative permittivity of the core and  $\epsilon_{sub}$  the relative permittivity of the substrate,  $\vec{E}_A$  and  $\vec{E}_B$  the electric field of isolated waveguides A and B respectively,  $\vec{H}_A$  and  $\vec{H}_B$  the magnetic field of the isolated waveguide A and B respectively,  $E_n$  and  $E_n^*$  the electric field of waveguide  $n$  and its complex conjugate,  $H_n$  and  $H_n^*$  the magnetic field of waveguide  $n$  and its complex conjugate. From equation 24, we notice that the value of the integrals depends on the geometry and materials of the waveguides. Since there are no analytical solutions of the spatial electric and magnetic field for a 2D waveguide cross section problem, in practice the integrals are approximated by discrete summations. In case of rectangular waveguides, the coupling coefficient can be estimated by formula 25 without the need of integral calculation [11].

$$K \approx \frac{2k_{x_{core}}^2 \beta_{cladding} e^{-\beta_{cladding} s}}{W \beta (\beta_{cladding}^2 + k_{x_{core}}^2)} \quad (25)$$

where  $K$  is the coupling coefficient,  $k_{x_{core}}$  the wavevector in the core of the waveguide,  $\beta_{cladding}$  the propagation constant in the cladding,  $\beta$  the propagation constant of the mode,  $s$  the distance between the two waveguides and  $W$  the thickness of the waveguides.

This formula was used to have a first estimation of the gap and the length of the coupling region of the racetrack resonator. After the first estimation with the rectangular approximation formula, a validation simulation was performed using the precise mode matching method detailed later in this chapter.

Concerning coupling between the plasmonic mode and the dielectric mode in HPWG structure, the CMT cannot be used because the coupling strongly modifies the shape of the isolated waveguides' modes [13]. The model of the coupling used in this case is detailed in chapter 4.

### 3.1.4 Simulations—3D analysis

To simulate the full behaviour of photonic devices, simulations must be done in 3D. This section shows the two methods used to simulate modes propagation. A table of comparison

---

Since CMT was not the main focus in this thesis, the aim of the following explication is to give the basics information to help the reader understand the design choices. The detailed solution can be found in literature.



at the end of this section compares the different methods and specifies when they were used in this project.

### 3.1.4.1 Mode matching method

The mode matching method is a propagation method that works on a principle very similar to the transfer matrix: The device is segmented into a multilayer stack (figure 3.11.a). The modes are then calculated in each layer along  $z$ . At each interface, both the propagating and the reflected wave are calculated (figure 3.11.b).

In this study, the mode matching method was used to optimize the devices used to route light in the photonic chip, such as multimode interferometers and directional couplers.

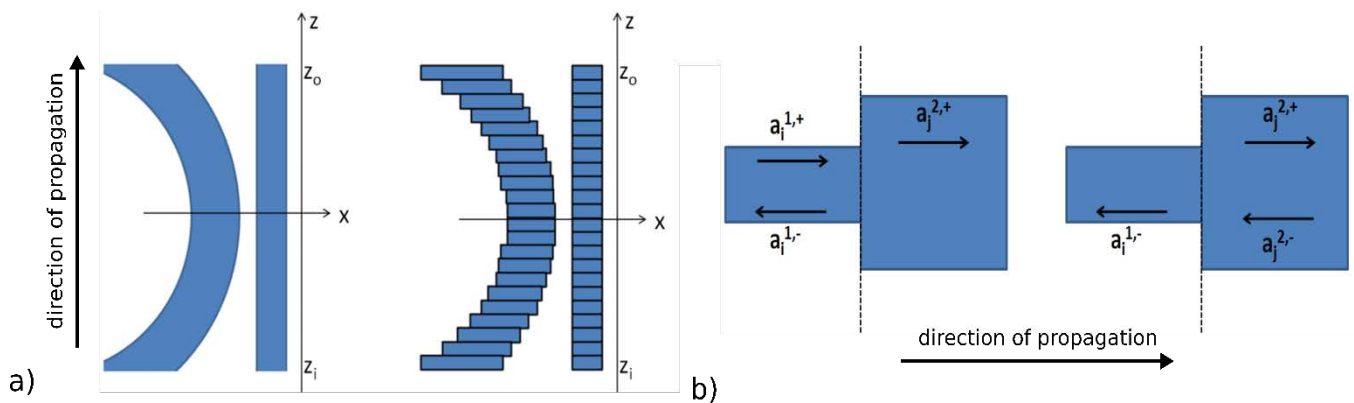


Figure 3.11.a schematic of the coupling waveguides before and after the discretization.  
3.11.b example of interface with the forward and backward waves used for the calculation.

### 3.1.4.2 FDTD simulation

This section describes the features of the Finite Difference Time Domain method (or FDTD) and the process flow for choosing the parameters. A detailed description of the method implementation can be found in literature [14]. The FDTD software used in this project was the Lumerical FDTD: 3D Electromagnetic Simulator.

The Finite Difference Time Domain simulation is part of the family of Finite Difference Methods. Maxwell equations are solved stepping in time. At the beginning, the electric and magnetic fields are zero everywhere. A selected source excites the field and the simulation starts by calculating the electric field change. Then, the magnetic field is calculated from the values of the electric field and the values are stored. A time step later, the fields are recalculated using the previous field values and updating the value of the source. In particular, the mesh size (like the mode-solver), source type, boundary conditions and simulation time depend on the structure geometry and material. The mesh size is estimated taking into account the smallest wavelength and the smallest feature size. The FDTD mesh used in the

Lumerical FDTD commercial software used for simulations is called Yee cell [15], and it is shown in figure 3.12 [16].

In our case, the source type was a “mode source,” i.e. a guided mode calculated with the

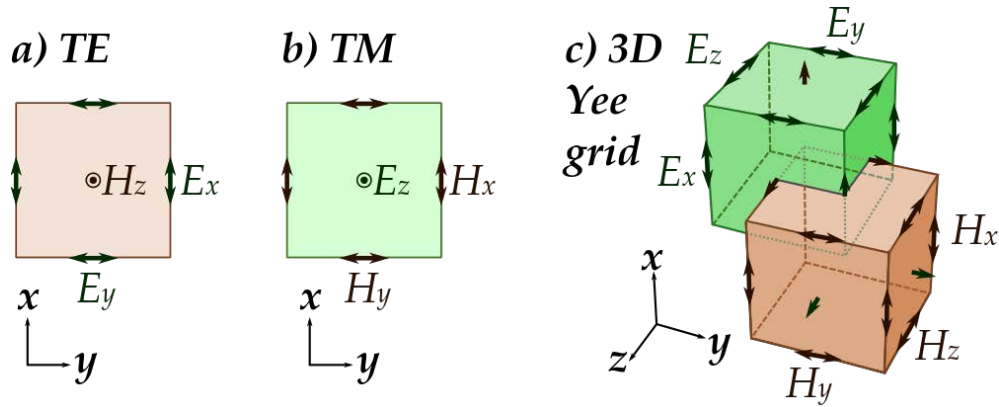


Figure 3.12 Yee unit cell for 2D and 3D meshing. It can be noticed that the points for the calculation of the  $E$  and  $H$  are shifted.

Lumerical mode-solver MODE (see mode-solver section above). This choice is adapted to integrated optics because the light is brought to the device by means of a guided mode.

The boundary conditions were set to a Perfectly Matched Layer (PML) to avoid any reflections from on the computational windows edges. PMLs are absorbing layers at the boundary of the simulation window used to avoid reflections by transforming propagating waves hitting the boundary into decaying exponentials. The thickness of the PML layer is optimized to avoid reflections while keeping simulation times reasonable.

The simulation time depends on the structure. For instance, when the simulations were performed for devices that do not store energy (such as couplers, multiple mode interferometers (MMI), HPWG) the time was estimated taking into account the auto-shutoff parameter. The auto-shutoff parameter is an estimate of the energy in the simulation window. For non-resonant devices, the simulation lasts until the auto-shutoff level is close to one, sign that most of the energy has left the simulation window.

The power monitor or the movie monitor confirms where the light has propagated, been stored or been reflected, as will be shown in the following section. For resonant devices, simulation time must be increased.

One of the advantages of this type of simulation is that it shows the behaviour of the structure over time, giving a very intuitive result. It also finds a solution for multiple frequencies with a single simulation based on the source used. On the other hand, FDTD simulation is time consuming for large simulation domains and thin structures. In this study, the FDTD method allows the verification of the parameters estimated with the approximated analytical formulae, for example the coupling length and coupling coefficient otherwise determined by the approximated equation 25.

### 3.1.5 Table of comparison

To conclude the presentation of the simulation methods used in this project, Table 1 shows a summary of the advantages and drawbacks and when they are used in this study.

Table 3.2 The simulation methods included in this thesis

Method	Advantages	Drawbacks	Use in this study
Transfer matrix	Fast, intuitive results.	Only 1D results are available	Give a simple and intuitive idea of the coupling between the plasmonic and dielectric waveguides in 1D
Mode-solver FDM	2D solver, nonlinear mesh adapted to HPWG	Medium computational time	Used to estimate the parameters for the resonator and to simulate the HPWG cross section
Mode-solver FEM	Meshing well adapted for plasmonic modes	Medium/high computational time	Used to simulate mode field profile when the FDM method fails to converge.
FDTD	Possibility to model 1D, 2D and 3D structures, intuitive results	High computational time	To verify the correctness of the faster methods, simulating the critical points of the devices such as tapers and coupling regions
Mode Matching Method	Fast, 3D simulation	Medium computational time	Rapid verification of basic building block dimensioning
Couple Mode Theory	Immediate solution	Approximated model	To have a first estimate of the coupling region of the ring resonator

## 3.2 Modelling and optimization of the basic building blocks

Before giving the details of the HPWG device in chapter 4, this section describes the basic building blocks of the photonic circuit used to bring light from the input fiber up to the output fiber (the fibers allows to couple light from the source to the chip and from the chip to the spectrometer, as it will be explained in chapter 5). More specifically, we detail the choice of the geometry of the simple waveguides, the multi mode interferometers (MMI) and the ring resonator coupling region. Chapter 4 describes the results concerning the dimensioning the HPWG sections of the ring and the exact dimension of the ring linked to the properties of the HPWG.

### 3.2.1 Multimode and monomode waveguides

The “conducts” that connect the different elements in a photonic chip are known as waveguides. To transport light effectively they must have low losses and preserve the light polarization. The geometry of the cross section of the waveguide is shown in figure 3.13.a, where the thickness of the waveguide is fixed at 600 nm by the industrial DAPHNE environment rules. The DAPHNE process also specifies the materials and their dispersion as mentioned in section 3.1.1.

The only free parameter is the width of the waveguide, as shown in picture 3.13.a. The width of the waveguide is chosen based on its function : the input and output fiber butt coupling, transporting light in the chip and internal coupling between the devices.

Light injection into the chip is performed by *butt coupling*, i.e. using a lensed fiber at the input waveguide. Since the monomode waveguide is too small to perform an efficient coupling and stable alignment, the width was increased to 2  $\mu\text{m}$  where the waveguide is multimode. An adiabatic taper connected the multimode waveguide to the monomode ones to filter all the parasitic higher order modes without increasing the losses of the fundamental one.

To route light in the photonic chip, we used a monomode waveguide called *bus waveguide*. Using a monomode bus waveguide concentrates power in the only existing mode and avoids perturbations due to higher order modes. Concerning the width of the waveguide, figure 3.13.b shows the variation of the effective refractive index of the modes as a function of the width of the waveguide. In this part of the design, the power needs to be concentrated to reduce losses from the side wall rough surface of the waveguide. Since the fabrication parameters become critical for small features, the optimum was chosen to be in the center of the monomode range, at 600 nm reducing the chances of being multimode or not guided. The losses of the bus waveguides are estimated using waveguides of different lengths, as explained in chapter 6 dedicated to characterizations. We used instead a Mach-Zehnder interferometer to experimentally determine their effective refractive index. By fitting the output of the Mach-Zehnder with the analytical formula, we are able to trace back the experimental value of the waveguide effective refractive index. The results of this method are given in chapter 6, dedicated to experimental results.

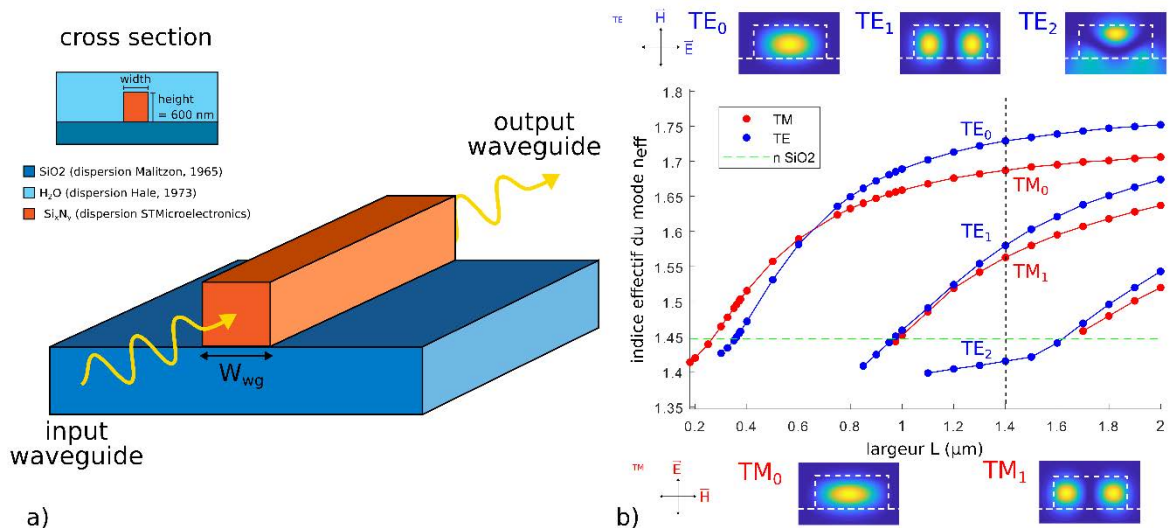


Figure 3.13.a Image of the waveguide, the cross section and 3D view. 3.13.b the  $n_{eff}$  as a function of the width of the waveguide. The power distribution for modes at  $W_{wg} = 1.4 \mu m$  are shown.

Once the light had reached the device (e.g. the ring resonator), the width of the bus waveguides was reduced to the one of the ring resonator (450 nm) to improve coupling. Also in this case, an adiabatic coupler connects the 600 nm bus waveguides to the 450 nm bus waveguides.

When needing a waveguide turn, for example at the output of a multi mode interferometer (MMI), losses can drastically increase and higher order modes can be excited [17]. The value of the bent radius is  $20 \mu m$  to minimize losses and ensure compactness as shown in the section 3.1.3.1.

### 3.2.2. The multimode interferometer coupler modelling

After designing the bus waveguides to transport light, it is possible to split or recombine the injected power between waveguides. There are three very common methods to split a signal: the Y junction, the multi mode interferometer and the directional coupler. While the Y junction, easier to implement, is more affected by reflection losses and fabrication parameters, the multi mode interferometer (or MMI) and the directional coupler have several advantages. This section is dedicated to the MMI coupler, while directional couplers are explained in the next section.

Due to their symmetry and compactness, MMIs work well to equally split light power from a single waveguide to two (for example Mach-Zehnder Interferometers) [18]. MMIs are multimode rectangular waveguides sections with a monomode input and output waveguides at its opposite side (picture 8). The input light excites the modes of the wide central waveguide. When these modes are excited, they interfere with each other and their phases vary along the propagation axis creating particular field distributions. This is called the *self-imaging principle*. It is a property of multimode waveguides by which the input field profile is reproduced in single or multiple images along the propagation direction of the waveguide [19]. The principle can create  $1 \times N$  MMI couplers by accordingly fixing the length of the central waveguide. It is useful to introduce the beat length  $L_{\pi}$  defined in equation 15:

$$L_\pi = \frac{\pi}{\beta_0 - \beta_1} \quad (15)$$

where  $\beta_0$  and  $\beta_1$  are the propagation constants of the first and second modes of the multimode waveguide [19].

Knowing the parameter  $L_\pi$ , it is possible to know the distance at which the images of the MMI appear along the structure. For example, at a distance of  $3L_\pi$  from the input waveguide, the image of the input waveguide is recreated because the interferences of all the modes are out of phase by  $2\pi$ . When designing a 1x2 MMI coupler, the two output waveguides are placed where the double image of the input is created, more precisely at  $L_{MMI} = 3L_\pi/2$ . The width of the MMI is chosen to have at least 5 guided modes, enough to have strong interference and a well-defined image. Compactness of the MMI is important to preserve a large bandwidth.

The width of the output waveguides  $W_{out}$  was increased with respect to the input waveguide to maximize the transmission and decrease parasitic reflections. The dimensions of the MMI were calculated with the MMM modeling software developed at INL and confirmed with FDTD, as shown in figure 3.14.b.

In this study, the 1x2 MMI coupler is used to split light equally between the device under test and to the reference waveguide. It is also used in the Mach-Zehnder interferometer to balance the input of each branch and to recombine the outputs.

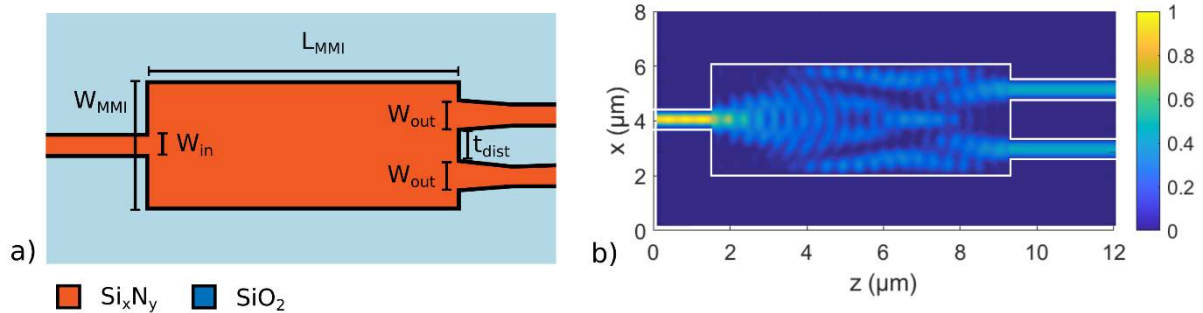


Figure 3.14.a example of the geometry of a MMI. b. Image of the power in the 1x2 MMI coupler with the mode matching solver.

### 3.2.3 Directional coupler

Directional couplers, like MMI, are devices that can split or recombine power from one to two waveguides and vice-versa. The advantage of the directional coupler is that the power percentage in the output branches can be tuned by simply adjusting the length of the coupling region. Figure 3.15.a shows the geometry of a directional coupler: two waveguides of width  $W_{wg}$  in close proximity for a length  $L_{DC}$  exchange power through evanescent coupling (the interaction between the exponential decaying fields external to the waveguides core). In this region, the two modes of the whole structure are not isolated modes of each waveguide but a linear combination of both, called even and odd modes due to their symmetry configuration. Power is periodically transferred from one waveguide to the other with a period  $L_\pi$  very similar to the MMI, where the propagation constants  $\beta_0$  and  $\beta_1$  are the ones of the odd and even modes of the coupler. This phenomenon is called *beating*. If the length  $L_{DC} = L_\pi/2$ , the

coupler will be a 50/50 directional coupler. The main use of the coupler in this work is to couple the right amount of power in the ring resonators. At first the coupling coefficient is

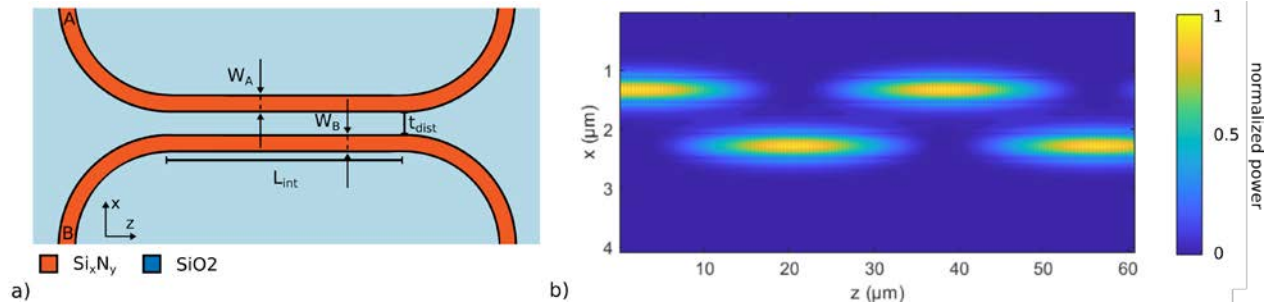


Figure 3.15.a directional coupler schematics,17.b Power distribution calculated with mode matching method.

estimated with the rectangular approximation formula[11] and then the result verified by mode matching solver.

### 3.2.4 Mach-Zehnder interferometer

Often used in literature, a Mach-Zehnder interferometer is a device used to measure the phase shift between two electromagnetic waves coming from a single source. At first, light is split into two waveguide *arms* often using an MMI or a directional coupler. The two signals are then phase shifted and recombined to create interference. The asymmetric Mach-Zehnder interferometer, called asymmetric because the two arms have different lengths,

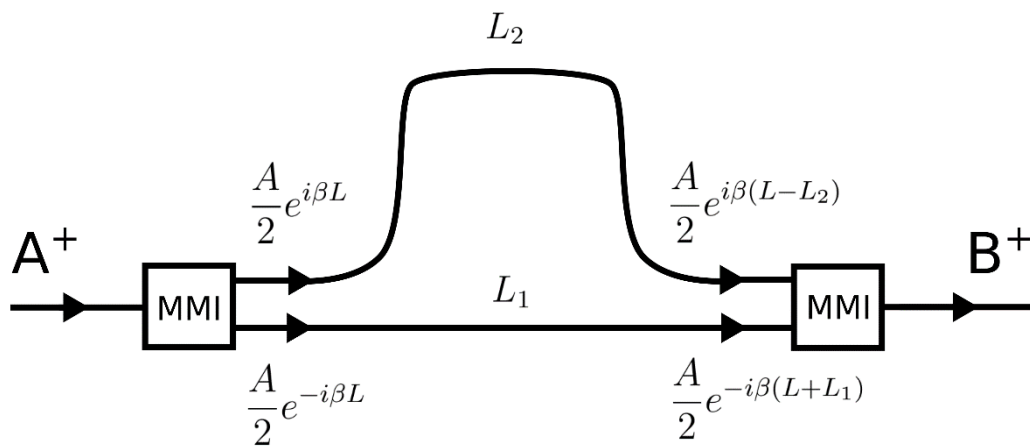


Figure 3.16 Schematics of a Mach-Zehnder interferometer. The input intensity  $A^+$  is split in the two arms of the interferometer. The arms are asymmetric so when the signals recombine in the output MMI they interfere. The interference is quantified by analyzing the output intensity  $B^+$ .

experimentally measures the dispersion law of the effective refractive index of the mode. Its geometry is shown in Figure 3.16.

The amplitude  $A$  at the input waveguide is split up equally by the 1x2 MMI coupler and propagated in the 2 arms of length  $L_1$  and  $L_2$ . At the output of the interferometer, light is

recombined with a 2X1 MMI coupler. Formula 16 represents the output amplitude as the summation of the phase shifted waves:

$$E(z) = \frac{A}{2} (e^{-i\beta \cdot (2L+L_1)} + e^{-i\beta \cdot (2L+L_2)}) \quad (16)$$

where  $L$  is the length of the MMI coupler,  $L_1$  and  $L_2$  the length of the 2 arms of the Mach-Zehnder interferometer and  $\beta$  the propagation constant in the waveguide.

After some algebraic manipulations and applying Euler's equation, from equation 16 we obtain formula 17 for the output amplitude and 18 for the output power:

$$E(z) = A e^{-i\beta \cdot (2L + \frac{L_1+L_2}{2})} \cos\left(\frac{\pi \cdot n_{eff} \Delta L}{\lambda}\right) \quad (17)$$

$$P(\lambda) = \cos^2\left(\frac{\pi \cdot n_{eff} \Delta L}{\lambda}\right) \text{ with } n_{eff} = a_1 + a_2 \lambda + a_3 \lambda^2 + a_4 \lambda^3 \quad (18)$$

where the  $\Delta L = L_1 - L_2$  is the difference of optical paths between the two arms,  $n_{eff}$  the effective refractive index in the arms,  $\lambda$  the working wavelength.

Equation 18 describes the output power as a function of the wavelength, giving an interference pattern that can be compared to the experimental results. In particular, a nonlinear fit determines the dispersion law coefficient of the real part of the effective indices  $a_1$ ,  $a_2$ ,  $a_3$  and  $a_4$ .

Since the goal of this chapter is to provide the model used in the simulation, the characterization results are discussed later, in chapter 6.

### 3.2.5 Ring resonator model

The purpose of this section is to show the reader the basics of ring resonators and the reasoning behind their design. This section presents the models for ring resonators used when studying HPWG, in the next chapter. Although only approximate, these models allow a quick analysis to estimate the geometry of the device and provide fit parameters for the evaluation of experimental results.

The first part of this section gives a general overview of the types of integrated ring resonators. Once the shape and type of ring resonator is chosen, the second part details the reasoning behind the choice of the geometry of the waveguides and gaps constituting the ring resonator. The general expression for the transmission and the main parameters are given (such as resonance wavelength, free spectral range, quality factor). The last part is dedicated to the modification of the transmission model to take into account the parasitic fluctuation observed after the measures.

#### 3.2.5.1 Models for racetrack and ring resonators

Well-known for their use as filters, in nonlinear optics and sensors, *ring resonators* are compact resonant devices widely described in literature [20]. Ring resonators consist of a loop waveguide and one or multiple waveguides feeding and/or collecting light from the loop. Light



injected through the input waveguide circles around the loop and couples to the output waveguide. The ring resonates if the optical path length is a multiple of the excitation wavelength [20].

Two common configurations of ring resonators are *all-pass* or *add-drop*, when having respectively one and two input/output waveguides. Figures 3.17.a and 3.17.b represent all-

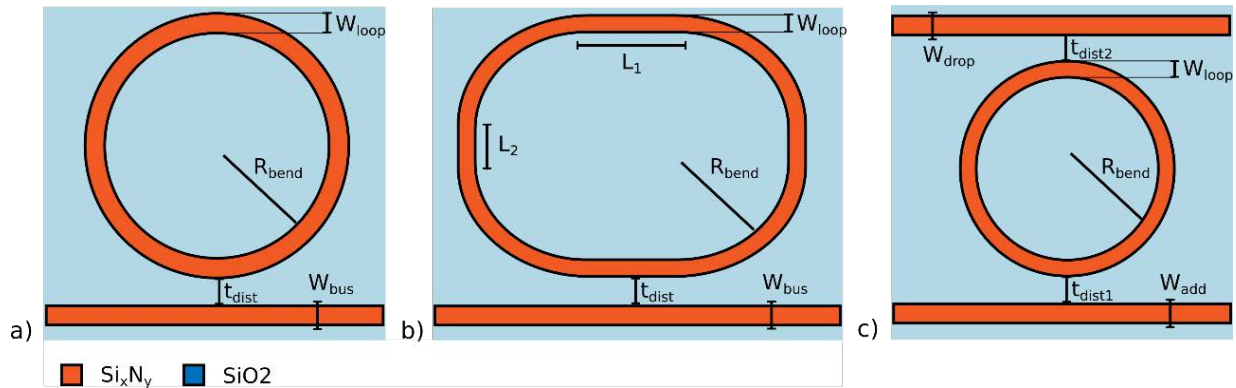


Figure 3.17 Different kinds of resonator existing in literature: (a) all-pass circular ring resonator b) all-pass racetrack ring resonator and c) add-drop ring resonator. The parameters are bent radius  $R_r$ , width of the loop waveguide  $W_{loop}$ ,  $t_{dist1}$  the coupling gap with the waveguide,  $W_{bus}$  the width of the bus waveguide,  $t_{dist2}$  the coupling gap between the loop and the drop waveguide,  $W_{add}$  the width of the add waveguide,  $W_{drop}$  the width of the drop waveguide,  $L_1$  the horizontal length of the straight part of the racetrack and  $L_2$  the vertical length of the straight part of the racetrack.

pass resonators while figure 3.17.c represents an add-drop. When taking a closer look, the all-pass filter ring resonator is essentially a directional coupler where one of its outputs is connected back to its corresponding input. The add-drop resonator is slightly more complicated and it does not add a real advantage compared to the all-pass in this case. Therefore, in this study we focus on the all-pass ring resonators. Concerning the shape of the loop waveguide, a *circular ring resonator* defines a circular resonator (figures 3.17.a and 3.17.c). If the shape is similar to a rectangle with rounded edges, it will be referred to as a *racetrack ring resonator* (figures 3.17.b). To avoid any confusion, the term *ring resonator* is used as a general term including both circular ring resonators and racetrack ring resonators. The racetrack ring resonator represents a good candidate because it HPWG can be inserted into the straight sections, separating them from possible deconfinement effects due to the bending radius.

### 3.2.5.2 Optical response of a ring resonator

To determine the optical response of a ring resonator, different parameters are required such as the coupling efficiency between the straight waveguide and the resonator, the resonator losses and the propagation constants of the modes that propagate in the different parts of the resonator. The formulae that follow are valid for both the racetrack ring resonator and the circular ring resonator, unless stated otherwise.

If the couplers are considered lossless and not subject to backward reflections, the amplitudes of the guided modes in the different arms are related to the matrix system in equation 20:

$$\begin{pmatrix} B^+ \\ b^+ \end{pmatrix} = \begin{bmatrix} t & -ik \\ -ik & t \end{bmatrix} \begin{pmatrix} A^+ \\ a^+ \end{pmatrix} \quad (20)$$

where  $A^+$  and  $B^+$  are the amplitudes at the input and output of the bus waveguide respectively,  $a^+$  and  $b^+$  are the amplitudes in the racetrack ring resonator entering and exiting the coupling region respectively (as shown in figure 3.18), and  $k$  et  $t$  are respectively the cross-coupling factor and the self-coupling coefficient of the directional coupler.

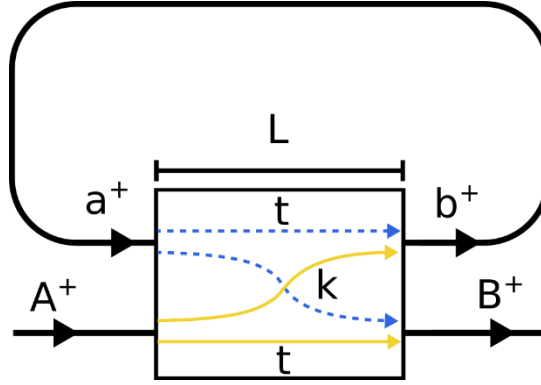


Figure 3.18 racetrack resonator with detail on the coupling section and coupling coefficient  $k$  and transmission coefficient  $t$ .

Since the racetrack feeds back the amplitude  $b^+$  to the waveguide  $a^+$ , their relation can be expressed as formula 21.

$$a^+ = b^+ e^{-(i\beta(p-L) + \alpha(p-L))} \quad (21)$$

where  $\beta$  is the propagation constant of the ring resonator,  $\alpha$  the resonator losses,  $p$  the perimeter of the racetrack and  $L$  the length of the coupling region.

By substituting equation 21 into equation 20, and applying the energy conservation imposing  $|t|^2 + |k|^2 = 1$ , we obtain equation 22 linking the input and output amplitudes.

$$B^+ = \frac{\sqrt{1-|k|^2} e^{-(i\beta+\alpha)p}}{1-\sqrt{1-|k|^2} e^{-(i\beta+\alpha)p}} A^+ = \frac{t e^{-(i\beta+\alpha)p}}{1-t e^{-(i\beta+\alpha)p}} A^+ \quad (22)$$

The transmission of the device is given by multiplying equation (22) with her complex conjugate:

$$T = \frac{|B^+|^2}{|A^+|^2} = \frac{|t|^2 + a^2 - 2a|t|\cos(\phi)}{1 + (a|t|)^2 - 2a|t|\cos(\phi)} \quad (23)$$

where  $a = e^{-\alpha p}$  is the single pass transition coefficient and  $\phi = p\beta$  the single-pass phase shift.

In the case of a circular ring resonator, the single-pass phase shift is simply  $p\beta = 2\pi R_{bend}\beta$ . For a racetrack ring resonator, there are parts of the optical path with different propagation constants. In this case, the global optical path is the weighted average of the effective refractive indices  $p\beta = 2\pi R_{bend}\beta_{bend} + (L_1 + L_2)\beta_{straight}$  where  $\beta_{bend}$  is the propagation constant in the bent and  $\beta_{straight}$  is the propagation constant of the straight parts  $L_1$  and  $L_2$ .

The single pass transmission  $a$  depends on the geometry and losses (material absorption, wall roughness, bending losses). It is difficult to have the exact value before experimental measurements. However, some hypothesis can help to estimate its value. To estimate the losses of the dielectric part of the material, we use experimental results available from existing waveguides of different width (700 nm instead of 450 nm) detailed in chapter 6. We expect this to be an underestimation of the actual losses since the roughness induces greater losses in smaller waveguides since the field discontinuity takes place at a higher field power. To calculate the losses of the plasmonic waveguides, the structure was simulated at first with the materials properties found in the literature (Au complex index and the Cr complex index by Johnson and Christy [6]). Once the fabrication process was finished and the materials were deposited, we substituted the literature values with the experimental one to have a more accurate model. The details of these measurements are given in chapter 6. The value of the losses are around 2 dB/cm for the dielectric waveguides and 1 dB/ $\mu\text{m}$  for the hybrid plasmonic device (for a gap of 600 nm between the dielectric waveguide and the plasmonic surfaces). In other words, the hybrid plasmonic waveguide losses are 3 orders of magnitude higher than the dielectric ones. Once the results were found, the losses were converted from decibels to linear to calculate the single pass transmission  $a$ .

Once the single pass transmission  $a$  is obtained, the coupling coefficient  $k$  is calculated based on the coupling condition. There are three possible conditions for a ring resonator: critical coupling condition, undercoupling condition and overcoupling condition. The critical coupling condition is the condition for which the losses are exactly compensated by the coupling of the bus waveguide so  $t = a$ . The other two conditions are called undercoupling ( $t > a$ ) and overcoupling ( $t < a$ ), defined when the injected power is below or above the loss level. Among these three coupling conditions, the maximum contrast of the resonant peaks is reached when the coupling is at the critical condition. Since the goal of the sensor is to find the position of the peak, the signal to noise ratio needs to be maximized and the amplitude of the signal should be maximized. This is the reason why the coupling is chosen to be critical. The coupling coefficient  $k$  is calculated in order to obtain the critical coupling condition at a wavelength of 1.31  $\mu\text{m}$ . Formula 24 shows the coupling condition used to obtain  $k$  when knowing the parameter  $a$ :

$$1 - a^2 = k^2 \quad (24)$$

Once the coupling coefficient  $k$  is known, we can define the geometry of the coupler injecting energy in to the waveguide. As explained in the previous section dedicated to the directional coupler, the length  $L_1$  and the gap between waveguides  $t_{dist}$  were chosen to obtain the appropriate coupling coefficient. For example, in case of a SiN waveguide with the SiO<sub>2</sub> substrate and a H<sub>2</sub>O cladding yielded a beat length  $L_{ap} = 10\mu\text{m}$  with the approximated formula and yielded a  $L_{MMT} = 18\mu\text{m}$  for the MMT simulation. The approximation gives an order of magnitude of the coupling length but all the results are verified by MMT.  $L_2$  is chosen to respect the FSR of 5 nm according to the dynamic range. All the dimensions of the ring resonator are now defined.

### 3.2.5.3 Models for racetrack and ring resonators—relevant parameters

The important working parameters of the ring resonator are the resonance wavelength, the Q factor, the Full Width Half Maximum (FWHM) and the Free Spectral Range (FSR). Figure 3.19

shows the spectral transmission of the ring resonator and the related parameters discussed in this section.

Resonance wavelength occurs when the optical path is an integer multiple of the working wavelength. From formula 25, the resonance wavelength can be found knowing the azimuthal order  $m$  or, vice-versa, to calculate the azimuthal order knowing the resonance wavelength.

$$\lambda_{res} = \frac{n_{eff}L}{m}, m = 1,2,3 \dots \quad (25)$$

where  $\lambda_{res}$  is the resonance wavelength,  $n_{eff}$  is the effective refractive index of the mode in the ring resonator and  $L$  is the optical path of the resonator (for racetrack resonators the optical length is the weighted average of the different effective indices in the ring), and  $m$  the azimuthal order.

The FSR is the distance between two resonance consecutive peaks. Its first order approximation is formula 26 [13]:

$$FSR = \frac{\lambda^2}{n_g L} \quad (26)$$

where  $\lambda$  is the working wavelength and  $n_g$  the group index. As stated before when justifying the choice of the perimeter of the ring, the parameter  $L$  is inversely proportional to the FSR. The FSR is the free spectral range, a defining parameter for the sensor based on its application. It should be noted that the formula is just a first order approximation and  $n_g$ , not to be confused with the effective index  $n_{eff}$ , is the group index defined as :

$$n_g = n_{eff} + \lambda_0 \frac{\partial n_{eff}}{\partial \lambda} \quad (27)$$

The group index helps describe the behaviour of a propagating pulse (speed of the envelope

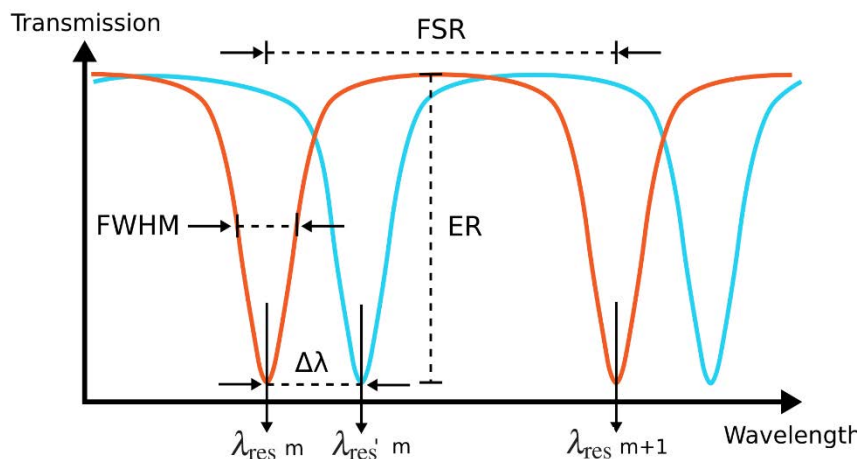


Figure 3.19 Examples of transmission of a ring resonator with significant parameters. The orange curve is the curve at rest and the blue curve represents a shift due to a refractive index change.

and dispersion).

Another parameter is the width of the resonance peak also called 3 dB bandwidth or Full Width Half Maximum (or FWHM) shown in picture 11. It represents the spectral width of the resonance peak and it is calculated with formula 28 [20]:

$$FWHM = \frac{(1 - ta)\lambda_{res}^2}{\pi n_g L \sqrt{ta}} \quad (28)$$

where  $t$  is the transmission coefficient,  $a$  is the single pass transmission efficiency,  $\lambda_{res}$  the resonance wavelength,  $L$  the perimeter of the ring and  $n_g$  the group index.

The quality factor, or Q-factor, approximately represents the number of turns in the resonator made by the light before the energy is reduced to  $1/e$  of its initial value. The Q-factor is expressed in formula 29 :

$$Q = \frac{\lambda_{res}}{FWHM} = \frac{\pi n_g L \sqrt{ta}}{\lambda_{res}(1 - ta)} \quad (29)$$

showing dependence on the physical parameters of the all-pass ring resonator. Often in literature, when trying to build sensors, the Q-factor is chosen to be as high as possible to have a steep slope in the resonance response. The Q factor relates to the smallest detectable shift, also known as the inferior limit of detection and doesn't need to be excessively large. This matter is discussed in chapter 4, paragraph 4.2.1.6, when describing the figures of merit of the resonator.

The contrast of the peaks, or on-off extinction ratio ( $ER$ ), is the difference between the maximum of the transmission  $T_t$  and the minimum of the resonance  $R_{min}$ .

$$ER = \frac{T_t}{R_{min}} = \frac{(t + a)^2(1 - ta)^2}{(t - a)^2(1 + ta)^2} \quad (30)$$

The ER can help us understand how easy it will be to detect the resonance frequency.

When ring resonators are used as sensors, it is important to define how the change in the effective refractive index affects the resonance shift. From equation 25, we can get a formula for  $\Delta\lambda$  assuming that there are no reflections and the phase shift caused by the coupling region is zero :

$$\Delta\lambda = \frac{\Delta n_{eff} L}{m}, m = 1, 2, 3 \dots \quad (31)$$

In chapter 4, formula 31 will be used to extract the wavelength shift from the change in effective refractive index.

### 3.2.5.4 Models for racetrack and ring resonators—parasitic resonances

This section is dedicated to the modeling of parasitic resonances that were observed during characterization. The experimental results show parasitic low Q resonances that were not predicted by the simulations.

Since the parasitic resonances have an FSR corresponding to the mm scale, we suppose that these resonances are due to the reflection at the interface between air, H<sub>2</sub>O and silicone (i.e. polydimethylsiloxane, PDMS) or the interfaces of the photonic chip. PDMS is the material used to fabricate the reservoir above the structure that contains the liquids under analysis (figure 3.20.a). It is important to identify these resonances because they perturb the position

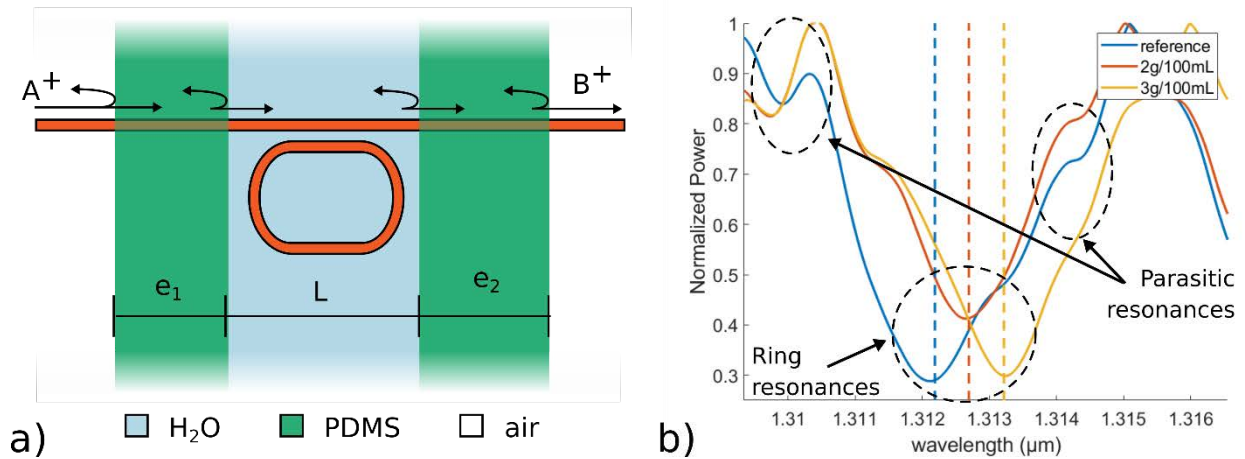


Figure 3.20.a simplified diagram of the device with the PDMS reservoir walls. The PDMS walls are represented in green, the inside of the pool is the light blue region in the center (the sensing liquid in H<sub>2</sub>O in this case) and the outermost regions are air outside the reservoir. 3.20.b example of transmission for a highly perturbed signal with the parasitic interference. The orange circles indicate the parasitic resonances and the blue one the ring resonance peak.

of the resonance peaks of the ring resonator, thus increasing the uncertainty of the measurement, as shown in figure 3.20.b. Once they are modelled, we can isolate and subtract them from the original signal to improve the signal to noise ratio (SNR).

The transmission of the ring resonator is modified to introduce a Fabry-Perrot oscillator in the bus waveguide: we consider an all-pass ring resonator and its optical response  $t_{ap}(\lambda)$  given in the previous section. Figure 3.21.a shows a simplified diagram of the resonator with the Fabry Perrot parasitic interfaces as vertical lines on the bus waveguide and the associated reflection and transmission amplitude coefficients  $r_{FP}$  and  $t_{FP}$ . The  $r_{FP}$  and  $t_{FP}$  can be modelled by the facets of the chip or an element like a PDMS reservoir put on top of the optical device for  $\mu$ -fluidic interconnect based on the situation. The optical response of the all-pass ring resonator with parasitic Fabry-Perrot's reflection can be modelled by writing the output amplitude as the combination of all the possible reflections. By adding all the contributions, as shown in figure 3.22, we can obtain the relation between the input and output amplitudes in formula 32.

$$B^+ = t_{AP}(\lambda)t_{FP}^2 A^+ + t_{AP}(\lambda)^3 t_{FP}^2 r_{FP}^2 e^{i2\beta_g L - 2\alpha_g L} A^+ + \dots + t_{AP}(\lambda)^{2n+1} t_{FP}^2 r_{FP}^{2n} e^{i2n\beta_g L - 2n\alpha_g L} A^+$$

$$n = 1, 2, 3 \dots \quad (32)$$

where  $B^+$  is the output amplitude of the bus waveguide,  $A^+$  is the input amplitude of the bus waveguide,  $\beta_g$  the real part of the propagation constant of the bus waveguide,  $\alpha_g$  its losses and  $L$  the length of the Fabry-Perrot cavity.

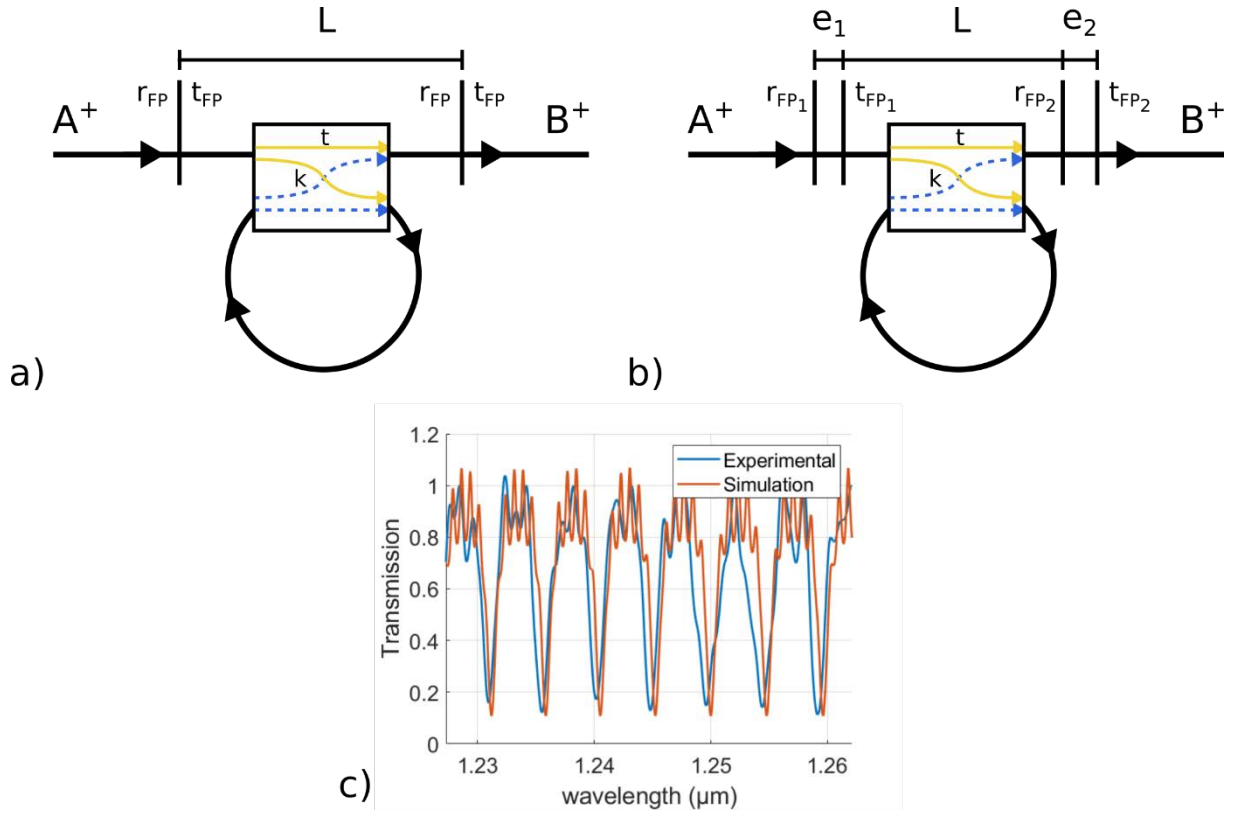


Figure 3.21.a diagram of the ring resonator with a Fabry-Perrot interferometer in the bus waveguides, represented by the vertical bars. 3.21.b modified model to include the thickness of the interfaces. 3.21.c result of the model compared to characterization results (the orange curve represents the simulation and the blue one the characterization).

Generalizing to infinity, we can find a series that represents the behaviour of the parasitic resonances, formula 33:

$$B^+ = t_{AP}(\lambda)t_{FP}^2 A^+ \sum_{n=0}^{+\infty} (t_{AP}(\lambda)^{2n} r_{FP}^{2n} e^{i2n\beta_g L - 2n\alpha_g L})^{2n} \Rightarrow B^+ = \frac{t_{AP}(\lambda)t_{FP}^2}{1 - t_{AP}(\lambda)^2 r_{FP}^2 e^{i2\beta_g L - 2\alpha_g L}} A^+ \quad (33)$$

The global power transmission is the ratio of the output and input amplitude shown in formula 34

$$T(\lambda) = \left( \frac{B^+}{A^+} \right)^2 = \frac{T_{AP}(\lambda)T_{FP}^2}{1 + T_{AP}(\lambda)^2 R_{FP}^2 - 2T_{AP}(\lambda)R_{FP} \cos(2\beta_g L) e^{-2\alpha_g L}} \quad (34)$$

where  $T_{AP}$ ,  $T_{FP}$ ,  $R_{FP}$  are the power transmission for the all-pass resonator, the Fabry-Perot and the reflection of the Fabry-Perot defined as the square of the corresponding amplitude. This model gives us a result closer to the real transmission thanks to the modelling of the parasitic reflections as it can be noticed in Figure 3.21.b.

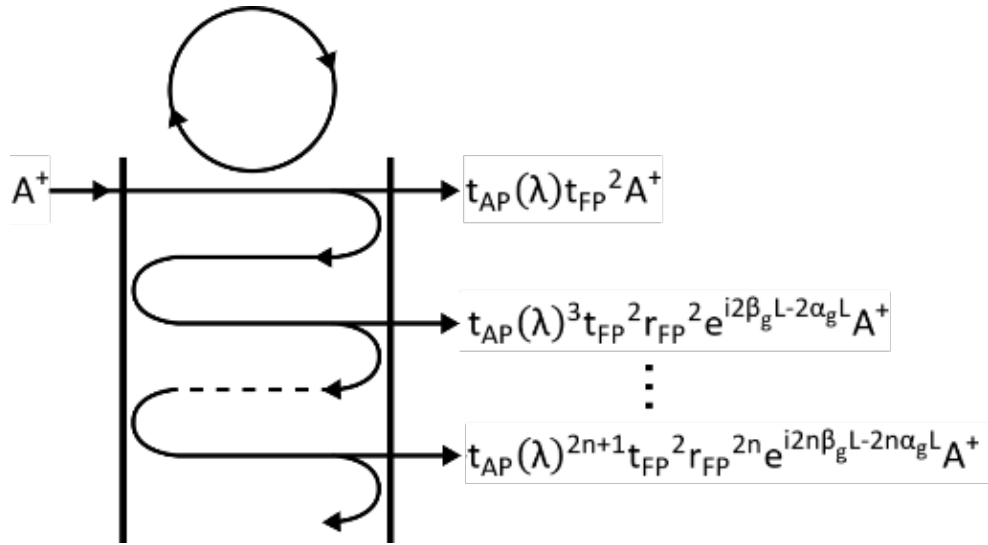


Figure 3.22 the principle of the back and forward reflections in the PDMS reservoir. Each reflection and transmission is accounted for up to infinity, as a series.

However, the modelling can be improved by taking into account the width of the two PDMS walls, as shown in figure 3.21.b. This will cause a modulation of the parasitic fluctuation that we observe in the experimental results.

To include the PDMS walls, we define the reflection and transmission Fresnel coefficients at the interfaces  $r_{\text{PDMS/air}}$ ,  $t_{\text{PDMS/air}}$ ,  $r_{\text{H}_2\text{O}/\text{PDMS}}$  and  $t_{\text{H}_2\text{O}/\text{PDMS}}$ , as shown in formulae 35–38.

$$r_{\text{PDMS/air}} \approx \frac{\beta_{\text{gPDMS}} - \beta_{\text{gair}}}{\beta_{\text{gPDMS}} + \beta_{\text{gair}}} \quad (35)$$

$$t_{\text{PDMS/air}} \approx \frac{2\beta_{\text{gPDMS}} \cdot \beta_{\text{gair}}}{\beta_{\text{gPDMS}} + \beta_{\text{gair}}} \quad (36)$$

$$r_{\text{H}_2\text{O}/\text{PDMS}} \approx \frac{\beta_{\text{gH}_2\text{O}} - \beta_{\text{gPDMS}}}{\beta_{\text{gH}_2\text{O}} + \beta_{\text{gPDMS}}} \quad (37)$$

$$t_{\text{H}_2\text{O}/\text{PDMS}} \approx \frac{2\beta_{\text{gH}_2\text{O}} - \beta_{\text{gPDMS}}}{\beta_{\text{gH}_2\text{O}} + \beta_{\text{gPDMS}}} \quad (38)$$

where  $\beta_{\text{gair}}$  is the propagation constants in a cladding of air,  $\beta_{\text{gPDMS}}$  is the propagation constants in a cladding of PDMS,  $\beta_{\text{gH}_2\text{O}}$  is the propagation constants in a cladding of H<sub>2</sub>O.

Once the Fresnel coefficients are calculated, we calculate the transmission and reflection on each wall:  $r_1$  and  $t_1$  are related to the wall closest to the light source and  $r_2$  and  $t_2$  are related to the wall closest to the output fiber. These parameters are defined as functions of  $r_{\text{PDMS/air}}$ ,  $t_{\text{PDMS/air}}$ ,  $r_{\text{H}_2\text{O}/\text{PDMS}}$ ,  $t_{\text{H}_2\text{O}/\text{PDMS}}$  and the thicknesses of the two walls  $e_1$  and  $e_2$ . Formulae 39–42 shows the relation between the two:



$$t_1 = \frac{t_{\text{air/PDMS}}t_{\text{PDMS/H2O}}}{1-r_{\text{PDMS/air}}r_{\text{H2O/PDMS}}e^{i2n\beta_{\text{gPDMS}}e_1-2n\alpha_{\text{g}}e_1}} \quad (39)$$

$$t_2 = \frac{t_{\text{H2O/PDMS}}t_{\text{PDMS/air}}}{1-r_{\text{PDMS/air}}r_{\text{H2O/PDMS}}e^{i2n\beta_{\text{gPDMS}}e_2-2n\alpha_{\text{g}}e_2}} \quad (40)$$

$$r_1 = r_{\text{H2O/PDMS}} - \frac{t_{\text{H2O/PDMS}}t_{\text{PDMS/air}}r_{\text{PDMS/air}}}{1-r_{\text{PDMS/air}}r_{\text{PDMS/H2O}}e^{i2n\beta_{\text{gPDMS}}e_1-2n\alpha_{\text{g}}e_1}} \quad (41)$$

$$r_2 = r_{\text{H2O/PDMS}} - \frac{t_{\text{H2O/PDMS}}t_{\text{PDMS/air}}r_{\text{PDMS/air}}}{1-r_{\text{PDMS/air}}r_{\text{PDMS/H2O}}e^{i2n\beta_{\text{gPDMS}}e_2-2n\alpha_{\text{g}}e_2}} \quad (42)$$

The expression of the total transmission is modified to formula 43:

$$t(\lambda) = \frac{t_{\text{AP}}(\lambda)t_1(\lambda)t_2(\lambda)}{1-t_{\text{AP}}(\lambda)^2r_1(\lambda)r_2(\lambda)e^{i2\beta_{\text{gH2O}}L-2\alpha_{\text{gH2O}}L}} \quad (43)$$

Thanks to this formula, the fit with the experimental results are more meaningful, as shown in picture 3.21.b.

## 3.3 Conclusion

This chapter provided the basic reasoning and basic building blocks for the design of the integrated photonic components. At first, the simulation methods were described giving a general understanding of their advantages and drawbacks, specifying when the simulations were used throughout the analysis. The goal of this section was to group all simulation explanations in order to understand the results in the following chapters.

Secondly, the analytical and numerical models used in this project were described, followed by the reasoning behind the dimensioning of the components routing light in the chip. From the waveguides to the ring resonator model, the analytical models are provided in this chapter and will be used in chapter 4 and chapter 6. In the last part of this section, we presented the adapted analytical model for a ring resonator to include the parasitic Fabry-Perot interferometer specific to our setup.

In conclusion, this chapter is the reference chapter for the simulation methods and design of the basic blocks with the goal to prepare the reader to one of the core subjects of this PhD project detailed in chapter 4: the simulation of the HPWG sensor.

## 3.4 References

- [1] D. Fleisch, *A Student's Guide to Maxwell's Equations*, 1 edition. Cambridge, UK ; New York: Cambridge University Press, 2008.
- [2] I. H. Malitson, "Interspecimen Comparison of the Refractive Index of Fused Silica\*,†," *J. Opt. Soc. Am., JOS A*, vol. 55, no. 10, pp. 1205–1209, Oct. 1965, doi: 10.1364/JOSA.55.001205.
- [3] S. Kedenburg, M. Vieweg, T. Gissibl, and H. Giessen, "Linear refractive index and absorption measurements of nonlinear optical liquids in the visible and near-infrared spectral region," *Opt. Mater. Express, OME*, vol. 2, no. 11, pp. 1588–1611, Nov. 2012, doi: 10.1364/OME.2.001588.
- [4] T. Tamir, Ed., *Integrated Optics*, 2 edition. Berlin ; New York: Springer-Verlag, 1979.
- [5] Arnold. Sommerfeld, *Partial differential equations in physics.*, Academic press. 1949.
- [6] P. B. Johnson and R. W. Christy, "Optical Constants of the Noble Metals," *Phys. Rev. B*, vol. 6, no. 12, pp. 4370–4379, Dec. 1972, doi: 10.1103/PhysRevB.6.4370.
- [7] C. Grossmann, H.-G. Roos, and M. Stynes, *Numerical Treatment of Partial Differential Equations*. Springer Science & Business Media, 2007.
- [8] D. L. Logan, *A First Course in the Finite Element Method*. Cengage Learning, 2011.
- [9] X. Hu, "Etude et caractérisation de composants d'optique intégrée exploitant les propriétés électro-optiques d'oxydes fonctionnels épitaxiés," p. 189.
- [10] "M. Heiblum, J. H. Harris, Analysis of curved optical... - Google Scholar." [https://scholar.google.fr/scholar?hl=fr&as\\_sdt=0%2C5&q=M.+Heiblum%2C+J.+H.+Harris%2C+Analysis+of+curved+optical+waveguides+by+conformal+transformation%2C+Journ.+of+Quantum+Electr.%2C+1975%2C+11%2C+pp.+75-85&btnG=](https://scholar.google.fr/scholar?hl=fr&as_sdt=0%2C5&q=M.+Heiblum%2C+J.+H.+Harris%2C+Analysis+of+curved+optical+waveguides+by+conformal+transformation%2C+Journ.+of+Quantum+Electr.%2C+1975%2C+11%2C+pp.+75-85&btnG=) (accessed Mar. 20, 2020).
- [11] R. G. Hunsperger, *Integrated Optics: Theory and Technology*, 6th ed. 2009 edition. New York ; London: Springer, 2009.
- [12] H. A. Haus and W. Huang, "Coupled-mode theory," *Proceedings of the IEEE*, vol. 79, no. 10, pp. 1505–1518, Oct. 1991, doi: 10.1109/5.104225.
- [13] M. Z. Alam, J. S. Aitchison, and M. Mojahedi, "A marriage of convenience: Hybridization of surface plasmon and dielectric waveguide modes," *Laser & Photonics Reviews*, vol. 8, no. 3, pp. 394–408, May 2014, doi: 10.1002/lpor.201300168.
- [14] "FDTD Solutions | Lumerical's Nanophotonic FDTD Simulation Software." <https://www.lumerical.com/tcad-products/fdtd/> (accessed Sep. 06, 2018).
- [15] Kane Yee, "Numerical solution of initial boundary value problems involving maxwell's equations in isotropic media," *IEEE Transactions on Antennas and Propagation*, vol. 14, no. 3, pp. 302–307, May 1966, doi: 10.1109/TAP.1966.1138693.

- [16] Kane Yee (1966). "Numerical solution of initial boundary value problems involving Maxwell's equations in isotropic media". *IEEE Transactions on Antennas and Propagation*. 14(3): 302–307
- [17] G. Fan *et al.*, "Optical Waveguides on Three Material Platforms of Silicon-on-Insulator, Amorphous Silicon and Silicon Nitride," *IEEE Journal of Selected Topics in Quantum Electronics*, vol. 22, no. 6, pp. 225–231, Nov. 2016, doi: 10.1109/JSTQE.2015.2494681.
- [18] L. B. Soldano and E. C. M. Pennings, "Optical multi-mode interference devices based on self-imaging: principles and applications," *J. Lightwave Technol.*, vol. 13, no. 4, pp. 615–627, Apr. 1995, doi: 10.1109/50.372474.
- [19] B. J. Zimmerman, A. Bandura, and M. Martinez-Pons, "In recent years, there has been a growing interest in students' self-regulation," *SAGE Directions in Educational Psychology*, vol. 1, no. 3, pp. 231–242, 2010.
- [20] W. Bogaerts *et al.*, "Silicon microring resonators," *Laser & Photon. Rev.*, vol. 6, no. 1, pp. 47–73, Jan. 2012, doi: 10.1002/lpor.201100017.

# CHAPTER 4 - DESIGN OF ROUTING COMPONENTS, HYBRID PLASMONIC WAVEGUIDES AND MACH-ZEHNDER INTERFEROMETER

The objective of this chapter is to explain the dimensioning of the devices used in this project (from the waveguides to the Mach-Zehnder interferometer and the Hybrid Plasmonic WaveGuide, or HPWG). The first part of the chapter is dedicated to dimensioning the basic building blocks of the routing system such as waveguides and multi mode interferometers. The second part details the simulation of the HPWG structure and the Mach-Zehnder Interferometer used to extract the measurement from the sensor. All considerations about the models and simulation techniques used in this chapter were previously explained in chapter 3.

Before going into the design details, it is wise to recall that the dielectric ridge waveguides are fabricated in an industrial environment called Datacom Advanced PHotonic Nanoscale Environment (or DAPHNE). This involves using materials specific to the platform listed in the previous chapter (e.g.  $SiO_2$  and  $SiN$ ) and following design rules (e.g. fixed thickness of the  $SiN$  layer of 600 nm, theoretical minimum feature size of 180 nm, avoid the use of acute angles).

## 4.1 Dimensioning of the basic building blocks for light manipulation

In this section, the basic building blocks are presented. The general goal is to bring light to the desired device with the lowest losses possible without modifying its polarization. In the following section, the design of the waveguides, bends and devices to split and recombine light are detailed.

## 4.1.1 Dielectric ridge waveguides and bend dimensioning

As stated before, the materials and the thickness of the SiN layer are fixed by the industrial platform. The only free parameter for a waveguide is its width and it is chosen based on the purpose of the waveguide. One can identify three main uses:

- the coupling with input and output fibers
- the bus waveguide routing light in the chip
- internal coupling with the bus waveguides and the devices

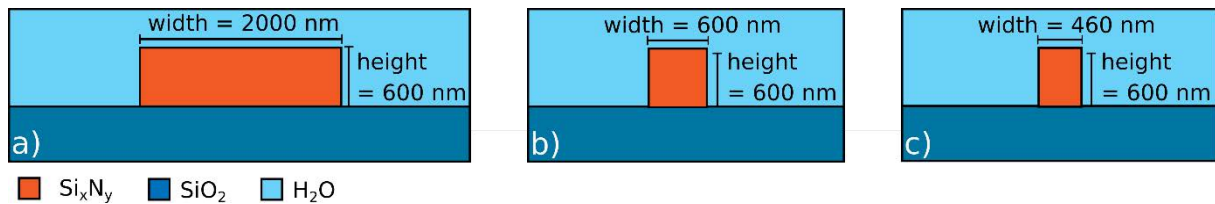


Figure 4.2 a) cross-section of the 2  $\mu\text{m}$  waveguide for input butt coupling, b) cross-section of the waveguide for propagation in the photonic chip and c) cross-section of the waveguide for ring resonators' coupling.

Butt coupling is the method used to perform light injection in the chip. The reason for this choice is detailed in chapter 6 dedicated to characterization. Since the monomode waveguide is too small to perform an efficient coupling and stable alignment of the fiber, the width was increased to 2  $\mu\text{m}$ , as shown in figure 4.1.a. Since the waveguide is multimode, an adiabatic taper filters out the higher order modes while keeping the fundamental one.

A monomode waveguide, called *bus waveguide*, routes light in the photonic chip. Using a monomode bus waveguide concentrates power in the only existing mode and avoid perturbations due to higher order modes. The width of the bus waveguide is optimized to reduce losses from vertical wall surface roughness by choosing the configuration where the power is most concentrated in the core. Since the fabrication parameters become critical for small features, the optimum was chosen to be in the center of the monomode range, at 600 nm, reducing the chances of being multimode or below the cutoff, as shown in figure 4.1.b.

Once the light had reached the device (e.g. the ring resonator), the width of the bus waveguides is reduced to the width of the ring resonator waveguides (460 nm) to improve coupling between the two. In this case, an adiabatic coupler connects the 600 nm bus waveguides to the 460 nm bus waveguides to avoid excitation of higher order modes, as shown in figure 4.1.c. The choice of the width of the ring resonator is chosen from parameters discussed later in this chapter.

Furthermore, inside the photonic chip there is the need to bend waveguides to guide light in other directions. Bends can drastically increase losses and higher order modes can be excited due to the mismatch of the mode between straight and bent parts [1]. The value of the bend radius was chosen to be 20  $\mu\text{m}$  to have low losses while being compact. This result comes from previous studies performed with the same industrial platform [2].

## 4.1.2 Tapers

Tapers are transitions designed to transfer light from two waveguides of different geometry. The most straightforward approach is to gradually reduce (or increase) the width of the waveguide [3], as shown in figure 4.2. As explained before, the taper is chosen to be adiabatic, i.e. the mode is unchanged without losses and without exciting higher order modes. The rule of thumb for adiabatic tapers is to keep a taper angle  $\theta \approx 1^\circ$  as shown in figure 4.2 [3].

All tapers in the design were designed following this rule of thumb and verified by FDTD afterwards. The length of the tapers from the fiber coupling waveguide ( $W_{in} = 2\mu m$ ) to the bus waveguide ( $W_{out} = 0.6\mu m$ ) are of  $L_{MMI} = 40\mu m$  and from the bus waveguide ( $W_{in} = 0.6\mu m$ ) to the device coupling waveguide ( $W_{out} = 0.46\mu m$ ) are of  $L_{MMI} = 7.5\mu m$ .

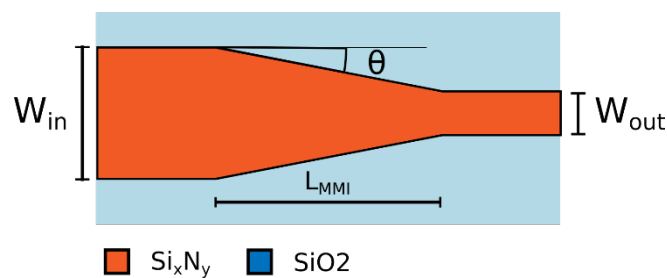


Figure 4.2 Schematics of a taper in SiN that ideally goes from  $W_{in} 2\mu m$  to  $W_{out} 0.6\mu m$ .

## 4.1.3 Multi mode interferometer (MMI)

As explained in chapter 3, the multimode interferometer is a device able to separate power coming from  $N$  input waveguides into  $M$  output waveguides. In this case, for Mach-Zehnder interferometers and power splitters in the reference waveguide, the desired MMIs are the 1X2 and 2X1. Since the devices are reciprocal, once the 1X2 is designed, the 2X1 is just the symmetric structure with two input waveguides and one output waveguide. The design of the MMI begins from the wide central waveguide: the width of the MMI is chosen to be  $W_{MMI} = 3.2\mu m$  in order to have a multimode waveguide with 5 modes for both polarization, enough to have strong interference and a well-defined image at the output. The length of the central part is fixed by calculating the  $L_\pi$  (explained in chapter 3) and taking the distance at which the second image appears, i.e.  $L_{MMI} = 3L_\pi/2 = 7.7\mu m$ , as indicated in picture 3.a. The output waveguides were placed at the maxima of the interference pattern ( $t_{dist} = 0.9\mu m$ ) and  $W_{out}$  was increased with respect to the input waveguide (from  $0.6\mu m$  to  $0.8\mu m$ ) to optimize the transmission and decrease the parasitic reflections. The width of the output waveguides is brought back to  $600\text{ nm}$  by means of  $6\mu m$ —long adiabatic taper. Figure 4.3.b shows the simulation of the MMI.

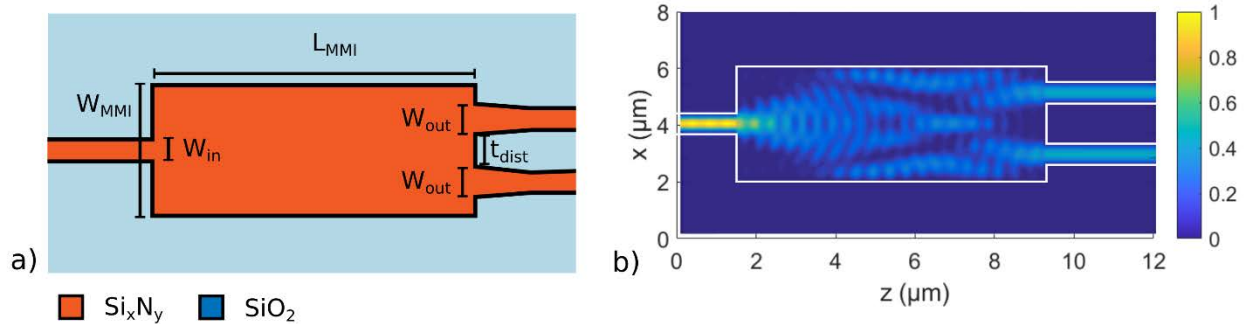


Figure 4.3 a) MMI geometry and b) simulation by means of the mode matching technique.

## 4.2 Dimensioning of the devices

The second section of this chapter is dedicated to the dimensioning of the devices, such as HPWG ring resonators used as sensors and Mach-Zehnder interferometers used to experimentally evaluate the effective refractive index of modes.

### 4.2.1 Hybrid plasmonic waveguides (HPWG) as biosensors

This section is dedicated to the optimization of the HPWG used as a sensor. Before optimization, it is fundamental to identify the parameters of interest for the sensor to compare with existing sensors, strongly linked to the ones previously defined when exploring the literature. In case of a biosensor, 5 parameters taken into account in this study:

- *Sensitivity*: represents the slope of the linear region of the calibration curve of the sensor. Based on the experiment, it can be a bulk sensitivity (when the refractive index of the overall fluid changes) or surface sensitivity (when the refractive index change is only at the surface of the sensor, for example in molecules or particles detection). For the same analyte variation, a high sensitivity enhances the output signal.
- *Limit of detection*: there are two limits of detections. The superior limit of detection, that represents the highest interpretable signal, and the inferior limit of detection, that represents the smallest interpretable signal [4].
- *Repeatability*: reveals if the sensor gives the same result for the same situations. The repeatability has various interpretations: it can be relative to multiple measures with the same sensor tested with the same liquid, multiple measures with the same sensor tested with different liquids or multiple measures with different sensors tested with different liquids.
- *Specificity*: This parameter describes the detection of the specific target phenomenon (index change or specific analyte) with respect to other possible phenomena that can cause a change in the measures signal. For example, in case of this study, a variation of temperature can be confused with an intrinsic change of refractive index of the target liquid or molecule.



- *Accuracy*: describes whether the response of the sensor returns the correct value. To evaluate the accuracy, the measurement has to be compared to other reliable measurement methods.

With these parameters in mind, the working principle of the HPWG and their simulations are described below. The repeatability, specificity and accuracy are discussed in chapter 6 since they strongly depend on the setup and the manufacturing process.

In the first part of this section, the choice of the metal is explained. Secondly, the problem is analyzed in 1D to understand the working principle of HPWG. Thirdly, the 2D simulation results show the analysis in a more realistic case, since the manufactured devices have a 2D cross section. Lastly, integration of the HPWG in a ring resonator is studied to define the geometry of the fabricated devices.

#### 4.2.1.1 The choice of the metal

The choice of the plasmonic material has to respect the following characteristics:

- Compatible with biosensing applications
- Compatible with the STMicroelectronics platform
- Have plasmonic behavior (plasma frequency above the working telecom wavelength – 1.31 $\mu\text{m}$  and 1.55 $\mu\text{m}$ )
- Compatible with the microfabrication methods (e.g. Chemical Mechanical Polishing or CMP, cleanroom deposition)

Table 4.1 shows the compatibility for the metals available at STMicroelectronics and their characteristics. In particular the compatibility with the CMP fabrication method is underlined because it is an important equipment for the fabrication, as shown later in chapter 5.

Table 4.1 Metals available at STMicroelectronics and their characteristics that helped to choose the most appropriate metal: the plasmonic behaviour in the infrared, the compatibility with the biology test existing and the compatibility with nano-patterning fabrication constraints.

	<b>STMicroelectronics</b>	<b>Plasmonic</b>	<b>Bio-compatible</b>	<b>CMP compatible</b>
Au	Yes	Yes	Yes, well-known	Yes
Ag	yes	Yes	No	-
Al	Yes	Yes	Yes	Yes
Cu	Yes	Yes	No	Yes
Ti	Yes	No	-	-
W	Yes	No	-	-

The two straightforward choices are Au and Al and simulations were performed with both metals. For the fabrication, only Au was used because it is well known in biology for functionalization.

### 4.2.1.2 1D Results — Plasmonic waveguides and HPWG simulations

The goal of this first section is to understand the coupling between the plasmonic and the dielectric ridge waveguides that compose the hybrid plasmonic waveguide, as explained in chapter 2. This section describes the exact solution of the 1D HPWG structure using the transfer matrix method. Although the transfer matrix method is just one-dimensional, it is useful to explain the coupling principle of plasmonic and dielectric modes. Once the coupling between the two waveguides is roughly estimated, the following section analyzes the problem with 2D methods.

The first step to understand a complex problem is to separate it in smaller parts and understand each one separately. With this philosophy in mind, figure 4.4.a shows the geometry of a planar waveguide (top left) and of a plasmonic waveguide (bottom left) as well as their effective refractive index  $n_{eff}$  (right). The abscissa coordinate  $gap$  represents the gap in the structure: in figure 4.4.a the  $n_{eff}$  of the dielectric ridge waveguide and the plasmonic waveguide are independent of the gap.

It is useful to consider the interaction between the two plasmonic waveguides without the dielectric ridge waveguide in between. Figure 4.4.b shows the geometry of two plasmonic modes coupled with each other. As explained in chapter 3, the two modes deriving from the coupling of two waveguides are called even and odd super-modes, the name deriving from the symmetry of their fields. The  $n_{eff}$  of the even and odd modes split from the value of the isolated waveguide modes and they are increasingly different when the coupling gets stronger between the waveguides, as shown in figure 4.4.b (right). Furthermore, the  $n_{eff}$  of the even mode is always higher than the  $n_{eff}$  of the odd mode. The even plasmonic mode crosses the horizontal line associated with the dielectric mode of the first example (the blue dashed line in the picture).

Figure 4.4.c shows the geometry of the dielectric ridge waveguide and the two plasmonic waveguides (left) as well as the  $n_{eff}$  of its odd and even modes (right). The even supermode of (light green line in plot 4.4.c) approaches the dielectric mode (the blue dashed line in plot 4.4.c) when the plasmonic waveguides are far apart. However, when the gap is extremely small, the even supermode follows the even mode of the two coupled plasmonic waveguides (the yellow dashed line in plot 4.4.c). Between these two extrema, the behaviour of the even supermode is a mix between the dielectric and the plasmonic modes. For this reason, this waveguide is called *Hybrid Plasmonic WaveGuide* or HPWG. Coupled mode theory (CMT) analysis cannot be used in this case because the waveguides are strongly coupled and have a high index contrast between core and cladding [5].

In the discussion below, the focus is on the sensitivity and the limit of detection since the other three quantities (repeatability, specificity and accuracy) are related to the measurement setup and will be discussed in chapter 6.

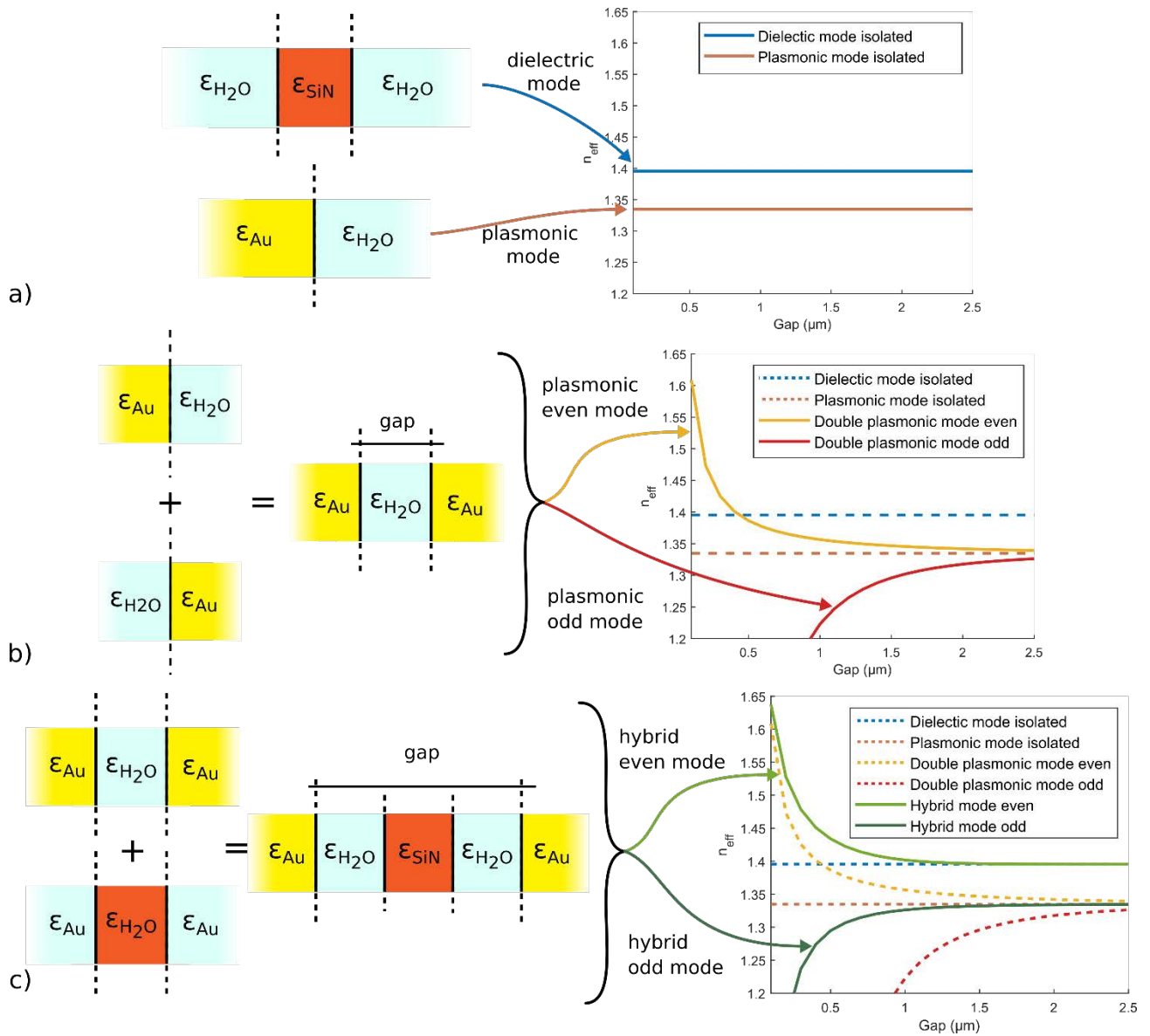


Figure 4.4 a) geometry and effective refractive index of 1D dielectric waveguides and the plasmonic waveguides, b) coupling between two plasmonic waveguides divided in even and odd modes as a function of the distance between the two plasmonic interfaces, c) coupling between the even and odd plasmonic modes and the dielectric mode, also divided between the hybrid even and odd modes.

Bulk sensitivity relates to the change  $\Delta n_{eff}$  of the mode to a change in fluid refractive index, in this case  $H_2O$ . The effective index is essentially a weighted average of the field and the materials surrounding it. As confirmed later by the simulations, the  $n_{eff}$  is more influenced when the power is concentrated in the target liquid for a given change in fluid refractive index. The filling factor, introduced in chapter 3, reveals the percentage of the power in a specific region of the simulation region, in this case the sensing region. Thus, the filling factor is an indication of the behaviour of sensitivity.

As shown before, the HPWG geometry includes a metal with plasmonic properties in the infrared, in our case either Au or Al. Its modes are lossy modes, associated with a complex  $n_{eff}$ . In order to calculate the losses of the mode in dB/cm the following formula is used:

$$losses_{dB/cm} = \frac{2 k_0 \alpha}{\log(10)}$$

where  $k_0$  is the free space wavevector at the working wavelength  $\lambda$  ( $k_0 = 2\pi/\lambda$ ) expressed in  $cm$ , and  $\alpha$  is the imaginary part of the  $n_{eff}$ . Losses are important because they are related to the limit of detection, as it will be explained later in this chapter when introducing the final device.

To estimate the effect of the filling factor on performances, 4.5.a and 4.5.b show the filling factor and the losses for 1D structures with varying the gap and the width of the central

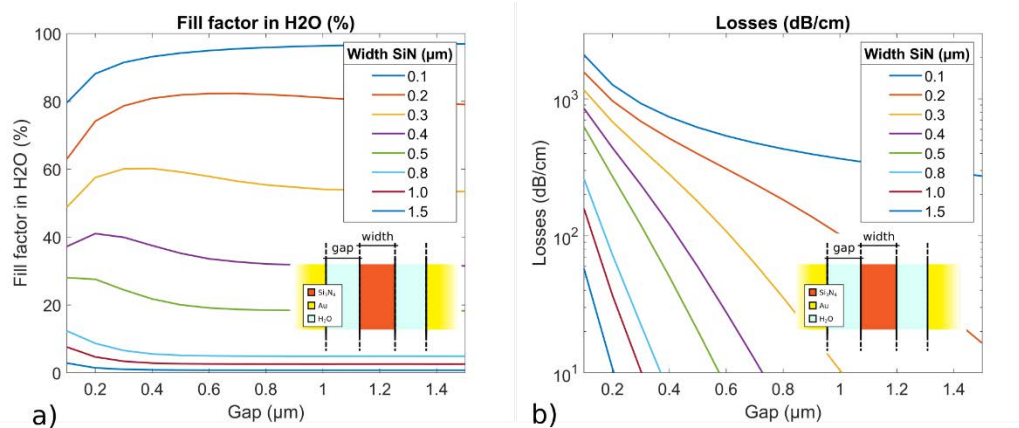


Figure 4.5.a) Simulation of the filling factor, i.e. the percentage of the field in the target liquid (water) for different gaps and core widths. b) Losses in dB/cm of the structures for different gaps and core widths. Insets: geometry of the structures.

waveguide. As explained in the paragraph before, the filling factor influences sensibility and the losses influence limit of detection. To optimize the sensor, the filling factor should be maximized and the losses minimized.

For large core widths, power is confined to the SiN waveguide core and less in the liquid. Thus, the interaction between the dielectric and the plasmonic modes is weak leading to a low filling factor (below 10%). However, for small gaps, the filling factor increases due to the enhancement of coupling while losses increase due to the proximity of the metal.

When the width of the SiN core decreases, the effective refractive index of the dielectric modes decreases, approaching that of the plasmonic waveguide, improving the hybridization between the two. The mode is deconfined in the liquid, increasing the filling factor and the sensitivity.

Furthermore, for small widths and gaps, the effective refractive index of the hybrid mode increases, slightly confining the mode back into the dielectric ridge waveguide. This results in a decrease of the filling factor for very small gaps. The best compromise is to have thin waveguides cores with large gaps. As shown later, in 2D simulations the filling factor decreases for large gaps because the dielectric mode is not able to confine light without the plasmonic modes. The optimization of 2D waveguides is explained in the next section.

The 1D simulations show the dynamics of the coupling between dielectric and plasmonic modes. Based on the filling factor and the losses, the best structure has a large gap that would result in lower losses and enhanced sensitivity. The next section is dedicated to the more realistic 2D problem, where the fundamental mode has a cutoff frequency, significantly changing the behaviour of the figures of merit.

#### 4.2.1.3 2D Results — Plasmonic waveguides and HPWG simulations—Bulk sensitivity modeling results

It is fundamental to analyze the structure in 2D, where the approximations of a planar waveguide are not true anymore and there is no analytical solution. The structure is the one in figure 4.6, showing the geometry from the 1D analysis to the 2D cross-section analysis.

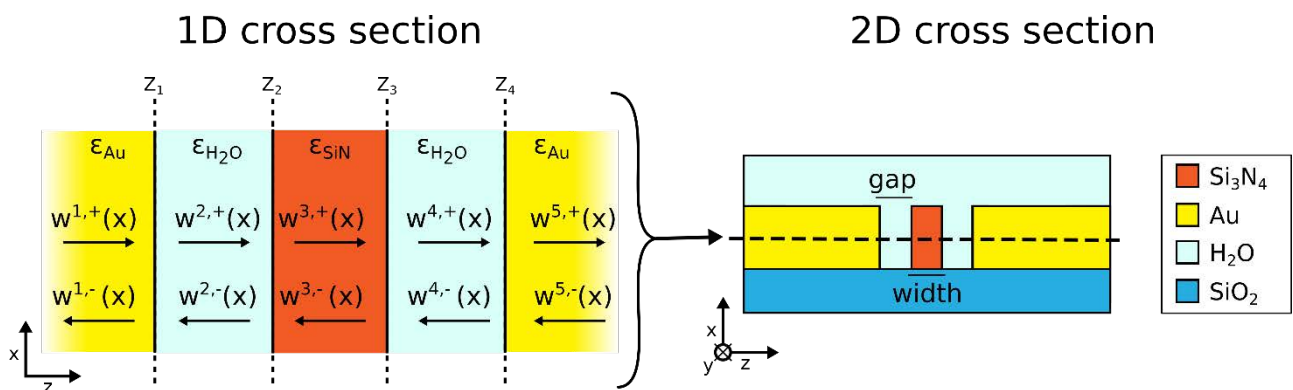


Figure 4.6 From the 1D simulation to the 2D cross section simulation

Solving for the electromagnetic field profiles in 2D does not have an analytic solution. As explained in the 1D simulations, in our case CMT cannot be applied because the coupling is strong. As shown by the 1D analysis of the previous section the dielectric and plasmonic modes are strongly coupled because the  $n_{eff}$  of the even and odd modes are not symmetric with respect to the isolated  $n_{eff}$ . A mode solver was used to simulate the 2D cross section. The cross section is shown in the inset of figure 4.7.a and 4.7.b for simulations of Au and Al. The materials used for the simulation have been selected for the DAPHNE industrial environment, as explained earlier. The thickness of the waveguide is fixed at  $0.6 \mu\text{m}$ , whereas the gap (the distance between the SiN waveguide and the metal) and the width of the SiN waveguide core are free parameters of the simulation.

As explained in chapter 3, both a custom-designed mode solver and the commercial tool FIMMWAVE (Photon Design) were used to simulate the 2D cross sections and calculate the mode  $n_{eff}$ .

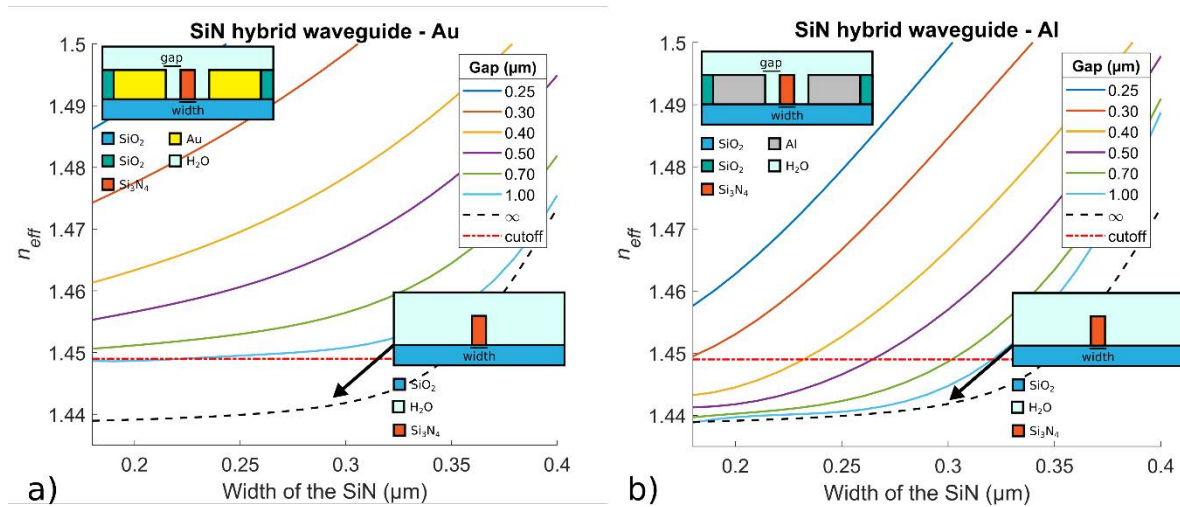


Figure 4.7 Study of the SiN hybrid waveguide with Au (a) and Al (b). The multiple lines represent different gaps between the metal surface of the plasmonic waveguide and the SiN dielectric waveguide core. The black dotted line shows the  $n_{eff}$  as a function of the width of the dielectric waveguide. The red dotted line is the index of the  $SiO_2$ , in other words, the limit above which the waveguides support guided modes.

It is interesting to compare the effective index of a SiN dielectric ridge waveguide with the one of a SiN dielectric ridge waveguide coupled with surface plasmon modes, as a function of their core width. The black dashed line in figure 4.7.a and 4.7.b represent the index of SiN waveguides modes with a fixed thickness of  $0.6 \mu\text{m}$  and variable width. For widths smaller than  $0.36 \mu\text{m}$  the mode is below cutoff (leaky) because the effective refractive index of the mode passes below the refractive index of the substrate (the red dashed line).

When adding the vertical metal walls (waveguides for plasmonic surface modes) on the sides of the SiN waveguide, the effective index curve is shifted upwards. This means that the surface modes can increase the refractive index of the leaky waveguide modes resulting in an overall

guided mode. As stated before, the filling factor, is a useful indication of the sensitivity of the device. Figure 4.8.a-f show the filling factor, the change in the effective refractive index of the mode in nm per Refractive Index Unit (abbreviated to RIU—dimensionless units) and the

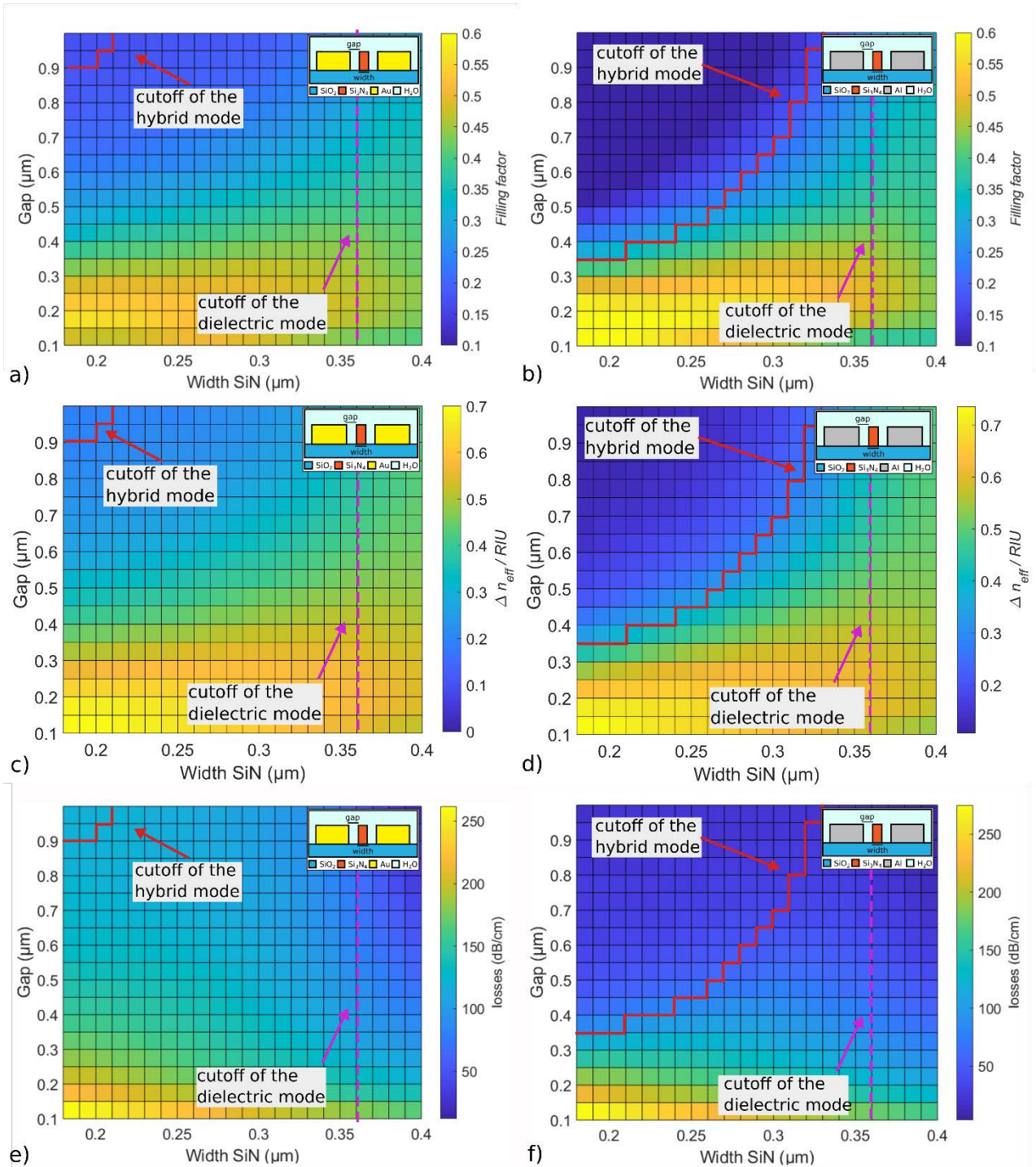


Figure 4.8: Fill factor (a, b), difference of effective refractive index when changing the liquid by one refractive index unit (c, d) and losses in dB/μm (e, f). The red continuous line represents the limit beyond which the hybrid mode is below the cutoff. The purple dashed line represents the limit beyond which the dielectric mode is below the cutoff. (RIU stands for Refractive Index Unit.)

losses of the mode for both Au and Al as a function of the gap and the width of the core waveguide. Both filling factor and refractive index change graphs have the same trend,

increasing for small widths and gaps. This shows that the filling factor is indeed an indication of the amplitude of effective refractive index change. Particular attention is given to the cutoff of the dielectric ridge waveguide isolated and the cutoff of the hybrid super-mode: unlike the 1D case, for big gaps and small waveguide widths the super-mode is below cutoff because the mode leaks to the substrate from the waveguide core (figure 4.8.g and 4.8.h). By reducing the gap, the coupling becomes stronger and the mode is guided (figure from 4.8.a and 4.8.f). For wider waveguide core width, the sensitivity decreases because the power is concentrated in the core of the central dielectric ridge waveguide, thus being less exposed to the target liquid.

The highest sensibility is achieved when the SiN waveguide is below cutoff and the overall

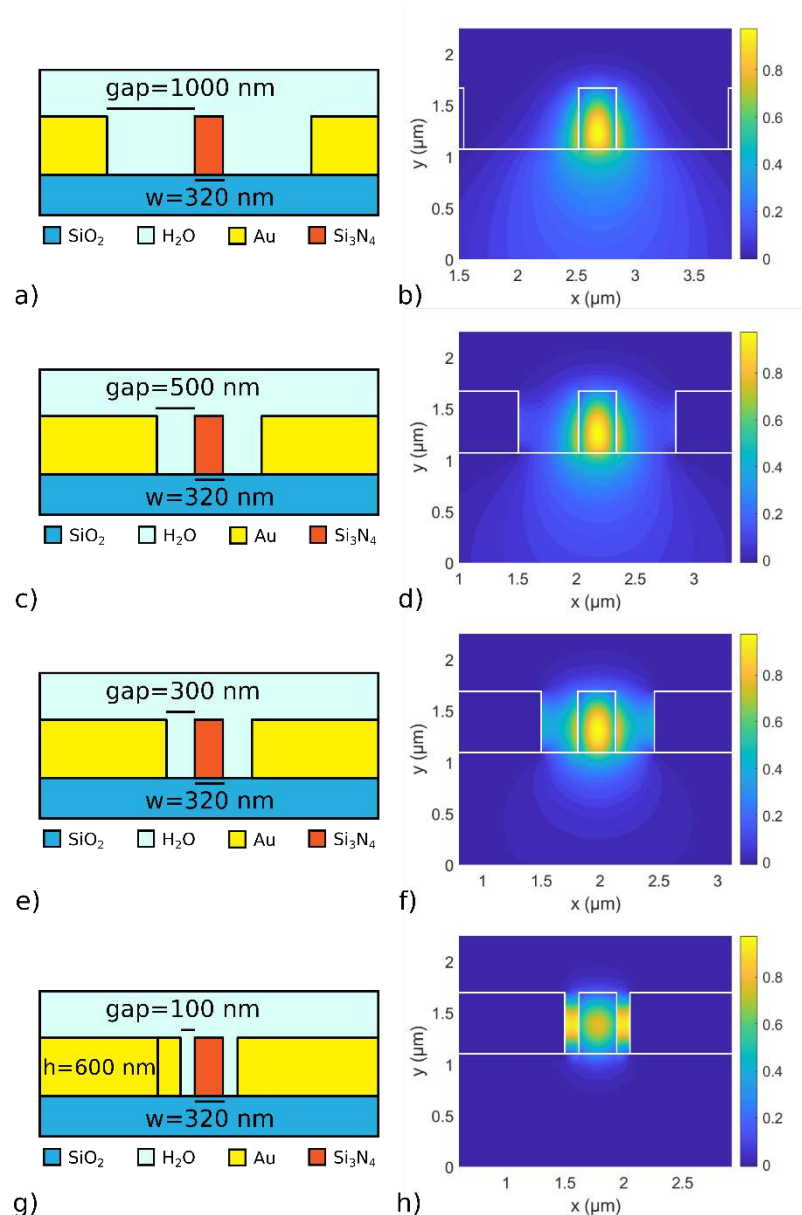


Figure 4.9 Field distribution of the mode for different geometries: a-b) gap = 100 nm, c-d) gap = 300 nm, e-f) gap = 500 nm, g-h) gap = 1000 nm. When the metal is close to the SiN waveguide, the mode is confined in the gap while, for large gaps, the mode is deconfined towards the substrate.

super-mode is guided. This principle is termed “mode lift,” as patented during this thesis. Both Al and Au are valid for HPWG. For this study we began with Au because of its affinity with



biosensing and because it is less likely to oxidize than Al. For the remainder of this document, only Au is considered for the plasmonic waveguides.

The field distribution of the modes changes based on the geometry. Figure 4.9 shows the field distributions for different gaps. When the gap is large, the ridge waveguide mode is not guided and it leaks to the substrate (figure 4.9.a-d). However, when the plasmonic waveguides are close to the ridge waveguide, the supermode is guided and the energy is concentrated in the gap between the two (figure 4.9.e-h). The detection of molecules takes place because their presence changes the field distribution of the mode that propagates in the waveguide (and therefore its effective index). Therefore, the majority of the field should be where the molecules will be. Figure 4.10.a and 4.10.b show a cross section view of the structure showing the desired light energy distribution (red shade) according to the size of the molecules. In the first case, the detection is said to be a volume detection, because it takes place in the volume between the walls of Au and SiN. In the second case it is said to be surface detection, because it takes place only at the surface.

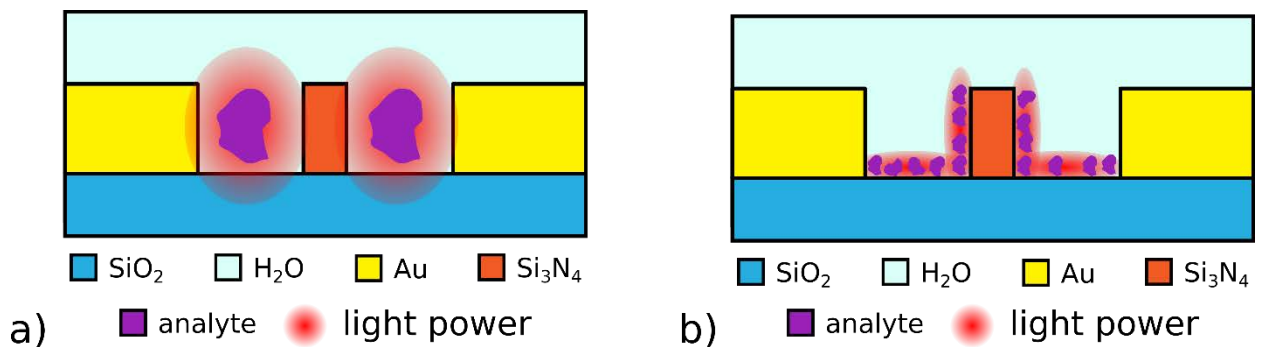


Figure 4.10 Two examples of the desired distribution of power to maximize sensitivity in the case of: a) large molecules and b) small molecules.

The HPWG field can be modulated by changing the geometry of the structure based on the target molecules (in particular the width and the gap between the metal and the dielectric). Depending on the application, the bioreceptor layers and the size of the analytes, the geometry will be optimized to better collocate the electric field at the position of the molecules. As shown later in this chapter, the example used for simulation is a monolayer of proteins.

Figure 4.11 shows an example of a structure of 340 nm of SiN width and a gap of 300 nm. On the left, the schematic of the cross section. The study is performed by changing the position of a square with sides of 5 nm having the refractive index of the adlayer, as depicted in figure 4.11 by the purple square and the arrow. On the right, the variation of the effective refractive index of the mode as a function of the position of the adlayer square. With this method we are capable to understand the sensitivity of the device as a function of the position of the adlayer in the gap and adapt it to the target molecule.

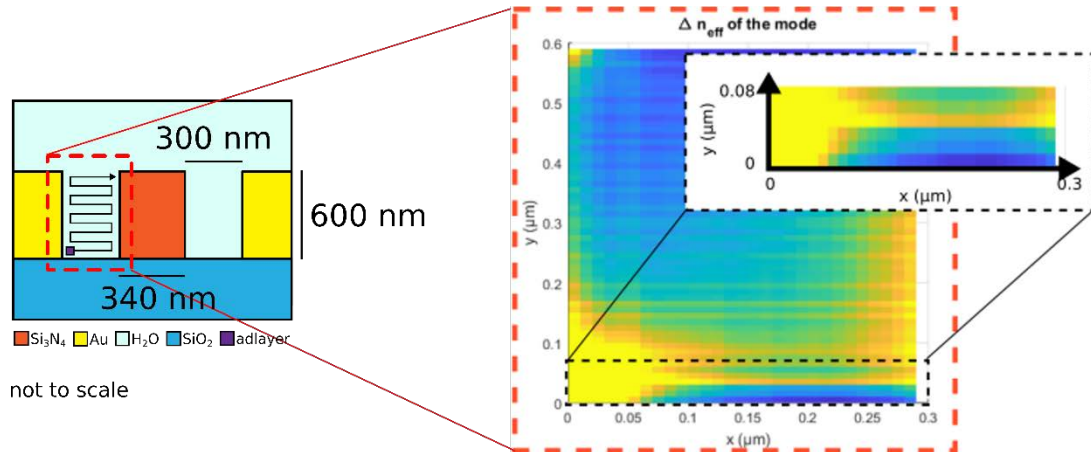


Figure 4.11 the study of the sensitivity of the device as a function of the location of a square of biological material with a side of 5 nm. The detection is not done at the surface of the SiO<sub>2</sub> but around 5nm above. This can be an advantage because in most cases the target molecules are not located on the surface but on a layer of bio-receptors which is about ten nanometers.

#### 4.2.1.4 Integration of the HPWG in a ring resonator

To detect the optical phase change induced by a change in the sensing liquid refractive index, a ring resonator is often used because of its compactness and high light-matter interaction [6]–[8]. The modelling methodology is a combination of analytical methods, a mode solver [8]–[11], and FDTD (Lumerical) [13] as explained in chapter 3.

The resonator is a racetrack resonator with its cross-section defined by the 2D simulations performed in the previous section. Being less time consuming than a full FDTD simulations, the mode solver calculates the effective refractive index of the modes in the ring resonator. Once the effective refractive index is known it is used in the analytical formula for the transmission of a ring resonator expressed by formula 1, derived in chapter 3:

$$T = \frac{|t|^2 + a^2 - 2a|t|\cos(\phi)}{1 + (a|t|)^2 - 2a|t|\cos(\phi)} \quad (1)$$

where  $t$  is the self-coupling coefficient,  $a$  is the single pass transition coefficient and  $\phi$  the single-pass phase shift. Coupling was chosen to be critical in order to maximize the SNR ( $t = a$ ) [13]. Since the ring losses depend on the gap size, the coupling was optimized to be in critical coupling condition for each modeled case.

By simulating a change in refractive index of the liquid, the bulk sensitivity can be calculated. As in the 2D case, the limit of detection is linked to losses. In a resonator, the losses, and

therefore the minimum detectable signal, are linked to the quality factor Q, shown in Figure 4.12.b. Figure 4.12.a and 4.12.b show the resonance wavelength shift and the quality factor as a function of the width of the core waveguide and the gap between the core waveguide and the wall of the plasmonic waveguide. For every data point, the coupling gap is optimized for critical coupling.

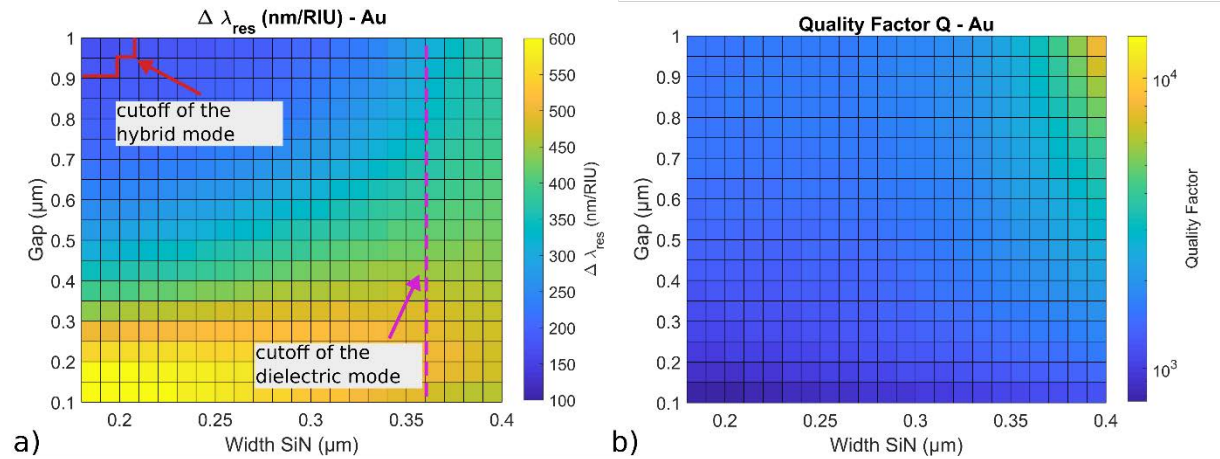


Figure 4.12 a) Bulk sensitivity of the HPWG ring resonator and b) Q factor as a function of the width of the core waveguide and the gap between the core and the metallic walls

As expected, the sensitivity changes with the same trend as the previously calculated  $\Delta n_{eff}$  (increasing for small width and small gaps). This is coherent because, for a constant length of the ring resonator, the highest change in the effective refractive index will result in a high phase shift and, by consequence, a high resonant wavelength shift.

The goal of the devices fabricated in this project is to study the sensitivity as a function of the coupling between the plasmonic and the dielectric waveguides. In order to avoid the possible parasitic effects caused by the bends, only the straight parts of the racetrack resonator have a cross-sections of HPWG geometry.

As shown later, in the HPWG sections of the ring resonator the width of the dielectric ridge waveguide is below cutoff to improve the sensitivity. In the bend parts, the ridge waveguides are thicker to have a guided mode and avoid radiation losses. Picture 4.13 shows the schematics of a ring resonator with three sensing zones and thicker bends to confine light during turns. The choice of the widths is given later in this section.

In the racetrack ring resonator, there are two different sections : the HPWG and the bend sections. The single-pass phase shift inside a racetrack ring resonator with different sections is defined as:

$$\phi = (L_1 + 2L_2)n_{eff_{HPWG}} + 2\pi R_{bend}n_{eff_{bend}} \quad (2)$$

where  $n_{eff_{HPWG}}$  is the effective refractive index of the HPWG section and  $n_{eff_{bend}}$  is the effective refractive index of the bend section.

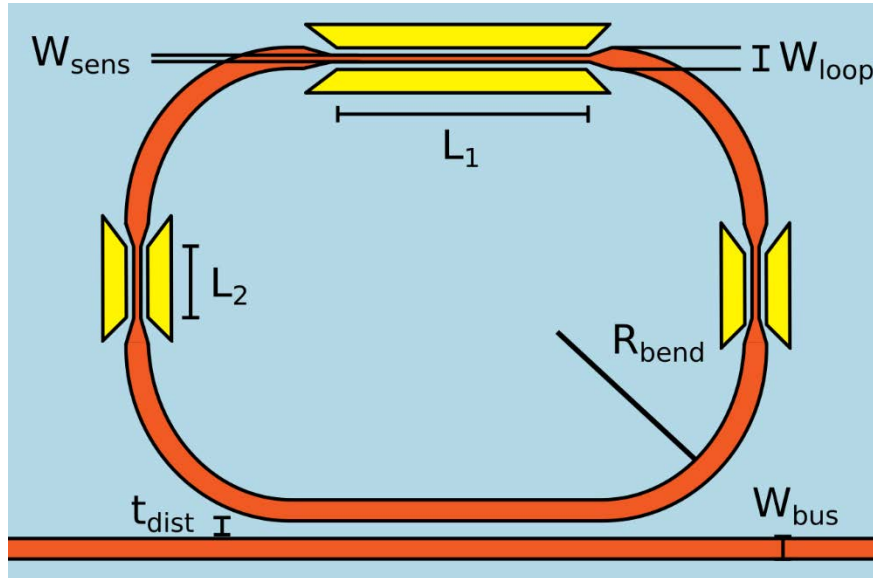


Figure 4.13 Schematics of the hybrid plasmonic ring resonator

The first parameter is  $W_{loop}$ , chosen to be 460 nm to minimize losses and ensure that the mode is guided. The width of the bus waveguide is equal to  $W_{loop}$  to have a more efficient coupling.

Concerning the perimeter of the resonator,  $R_{bend}$  was chosen to have low losses (20  $\mu\text{m}$ )—as described in chapter 3.

The directional coupler injecting light in the ring from the bus waveguide dictates the choice of  $t_{dist}$  and  $L_1$ , based on the estimated losses of the ring resonator. The length  $L_1$  and  $t_{dist}$  were chosen to obtain the coupling coefficient in order to satisfy the critical coupling condition  $t = a$ , as explained in chapter 3. In the case of a SiN waveguide with SiO<sub>2</sub> substrate and H<sub>2</sub>O cladding, the power coupling coefficient is  $K = 0.0849$  for the mode matching simulation, as

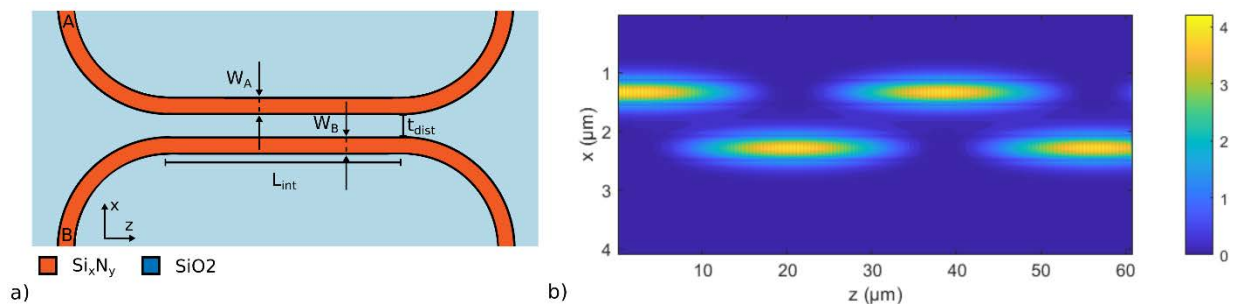


Figure 4.14.a) Directional coupler schematic b) field distribution calculated with mode propagation.

shown in figure 4.14. The dimensions of the manufactured devices at the critical coupling are  $L_1 = 6 \mu\text{m}$ ,  $8 \mu\text{m}$  and  $9 \mu\text{m}$  and  $t_{dist} = 0.4 \mu\text{m}$ ,  $0.6 \mu\text{m}$  and  $0.8 \mu\text{m}$ , depending on the HPWG losses and to take care of the possible fabrication tolerances.

The length of the HPWG is chosen to provide the sensitivity and the dynamic range adapted to the experimental setup. In the case of a ring resonator, the distance between the resonance peaks, also known as Full Spectral Range (FSR), is often chosen higher than the desired dynamic range to avoid confusion with peaks of different order. Keeping in mind that the FSR is inversely proportional to the perimeter of the ring resonator, this creates a tradeoff between the sensitivity of the resonator (increasing when the HPWG length of the ring increases) and the dynamic range (decreasing when the HPWG length of the ring increases). In order to evaluate the tradeoff, the refractive index difference for five glucose monohydrate concentrations in water was measured with the device. Glucose monohydrate was chosen for its low evaporation rate and effective rinse, as explained in chapter 6. The maximum shift of the resonant peak due to the highest glucose monohydrate concentration  $\Delta\lambda_{max}$  was simulated. Once  $\Delta\lambda_{max}$  was known, the perimeter of the ring resonator was chosen to have an FSR of at least twice  $\Delta\lambda_{max}$ , in order to avoid shift exceeding the dynamic range considering fabrication tolerances. The perimeter was chosen to be 150  $\mu\text{m}$  corresponding to an FSR of 5 nm and a  $\Delta\lambda_{max}$  of 2 nm.

For this reason,  $L_2$  was defined to be 0  $\mu\text{m}$ , 7  $\mu\text{m}$  and 14  $\mu\text{m}$ . All the dimensions of the ring resonator are now defined. A schematic of the photolithography mask is shown in picture 4.15, not to scale. It can be noticed that the signal from the input waveguide (on the left) is split in two to form a reference branch and a sensing branch.

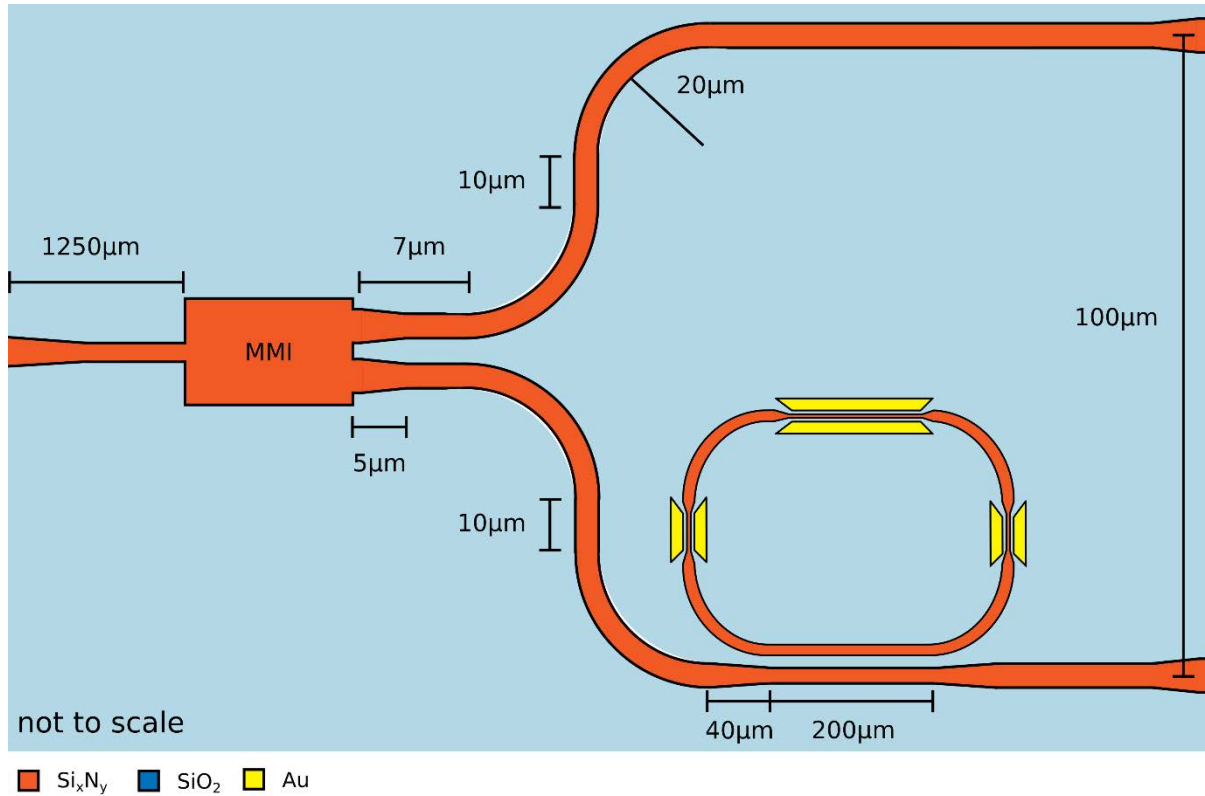


Figure 4.15 Plan of the complete circuit of the racetrack ring resonator. The parameters chosen for the ring resonator and the MMI are explained in the dedicated sections. All the bend radii are  $20 \mu\text{m}$ .

The performance of the device depends on the gap between the plasmonic and the dielectric ridge waveguides constituting the HPWG. We will now discuss in detail the sensitivity and the limit of detection.

#### 4.2.1.5 Sensitivity

The bulk sensitivity of the device, expressed as a shift of the resonant wavelength per change of refractive index of the liquid (measured in  $\text{nm}/\text{RIU}$ ), is calculated with Equation 3:

$$\Delta \lambda_{res} = \frac{\Delta n_{eff} L}{m} \quad (3)$$

where  $\Delta n_{eff}$  is the change in effective refractive index of the mode,  $L$  the diameter of the resonator and  $m$  the mode number of the resonator. In the case of a racetrack resonator, the formula is modified to take into account the propagation constants of the different regions:

$$\Delta \lambda_{res} = \frac{\Delta n_{eff_{HPWG}}(L_1 + 2L_2) + \Delta n_{eff_{bend}} 2\pi R_{bend}}{m}. \quad (4)$$

In other words,  $\Delta\lambda_{res}$  is the weighted average by length of the phase shift divided by the order of the ring resonator. Figure 4.16.b shows sensitivity as a function of the width of the waveguide and the gap between the metal and the dielectric ridge waveguides around working wavelength  $\lambda = 1.31\mu m$ . As expected, the behaviour of the sensitivity is similar to the behaviour of  $\Delta n_{eff}$ , shown in section 4.2.1.3. We decided to work with the parameters presented in the green dashed box of figure 4.16.b (SiN width from 300 nm to 340 nm and variable gap). This region represents a tradeoff between the “mode lift” concept and keeping low losses in case experimental imperfections worsened the SNR unacceptably.

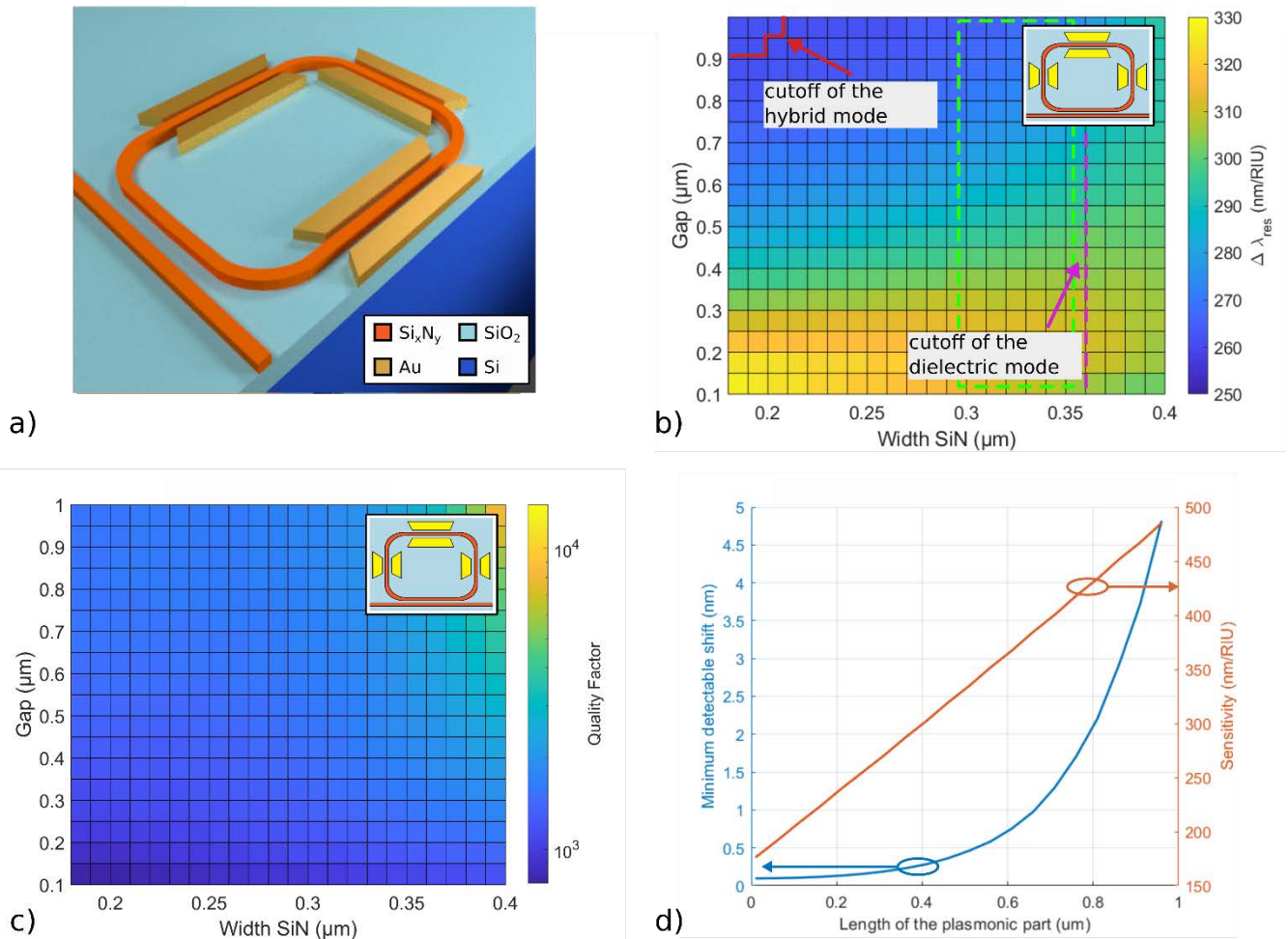


Figure 4.16: a) Schematics of the device, a racetrack resonator hybridized with Au. The sensitive area is between the SiN waveguide (in orange) and the metallic sides (in yellow). b) Shift of the resonance peak as a function of the gap size and the width of the core waveguide for a racetrack with 20  $\mu m$  radius bends, coupling length  $L_{coup} = 10 \mu m$  and vertical length  $L_v = 20 \mu m$ . The lines represent the limits beyond which the hybrid mode and the dielectric mode are below the cutoff. The green dashed box is the area corresponding to the geometry of the fabricated devices in this project. c) Quality factor as a function of the gap and the width of the central waveguide. d) Graph of the minimum detectable shift and the bulk sensitivity as a function of the HPWG percentage occupation of the ring circumference.

#### 4.2.1.6 The Limit of detection

The lower and upper limits of detection are the minimum and maximum quantities that the sensor is able to reliably measure. In this case, the *upper limit of detection* is roughly the concentration that causes a wavelength shift close to the FSR of the resonator.

*The lower limit of detection* is harder to define because it strongly depends on the quality of the signal (the signal to noise ratio and therefore the Q factor of the resonator, see figure 4.16.c) and method to detect the peak shift. The most intuitive method used in literature is the *peak search method*. This method consists in determining the wavelength of the resonance peak. Among all the methods to find this position, from the simple position of the minima to more complicated solutions, the most robust is defined by Claes [14] and White [15] (fitting the peak with a Lorentzian function). This method shows that the limit of detection for a resonant system is linked to the capability of fitting its transmission curve with its theoretical model. The fit of a function is related to the noise of the system thus to the SNR. The noise is assumed to have a Gaussian distribution, common in optical setups [15], with a standard deviation determined by the experimental setup (the details of the setup will be given in chapter 6, dedicated to characterization). Once the system noise characteristics are known, the noise effects on the limit of detection can be simulated by adding the measured noise to the transmission curve of the racetrack resonator. It is known in literature that the resonance peak of an optical resonator has a Lorentzian distribution [14]. The Lorentzian fit, performed using the Levenberg-Marquardt method, will provide the standard deviation of the resonant peak position.

As it is common for biosensors ([14], [16]), the smallest detectable peak is defined as 3 standard deviations of the noise on the resonant peak position [16]. Figure 4.16.d shows a simulation of the smallest detectable peak change as a function of the percentage of the metallized ring in the case of a structure with a gap and width of 0.3  $\mu\text{m}$ . If the ring is fully hybrid plasmonic, the losses limit the detectable peak change. Instead, if the ring is almost completely dielectric, the ring has a lower sensitivity even though the detection limit is small. The optimal compromise for sensitivity and detection limit strongly depends on the measurement setup and therefore on the application. We chose the percentage (from 10 to 30%) of the total length to be HPWG as a safe option in case the fabrication process introduced more losses than expected.

Another interesting method to calculate the resonance shift other than the peak search method is the Fast Fourier Transform method (or FFT), being particularly efficient for low Q factor resonators.

Since the context of this study is lab-on-chip compatible devices, a low quality factor ( $Q < 10^4$ ) means relaxed conditions on the frequency resolution scan and therefore on the light source and detection scan resolution [16]. The FFT is the method chosen to detect the limit of detection and the sensitivity. Since it is more complicated than a simple fit, it will be detailed in chapter 6 when explaining the characterization and data treatment [16].

From the smallest detectable peak change  $\Delta\lambda_{min}$  to the LoD, the following formula is used [14]:



$$LoD = \frac{\Delta\lambda_{\min}}{S} \quad (2)$$

where  $\Delta\lambda_{\min}$  is the smallest detectable peak shift and  $S$  the bulk sensitivity of the sensor. The LoD has the dimensions of the target unit, in this case the refractive index unit RIU.

The calculation of the final LoD is more complex than a simple simulation because of its dependence on the setup. Further details are discussed in the characterization chapter, after presenting the setup and the noise calculation.

This paragraph concludes the simulation of the device parameters to bulk changes. The following paragraph focuses on the simulations in case of the adlayer measurements.

#### 4.2.1.4 Results 2D—Plasmonic waveguides and HPWG simulations—Adlayer measures

The previous section discussed the simulations of the HPWG sensor for a refractive index change of the overall sensing liquid. However, sensors can be destined to detect small local changes of refractive index at the sensor surface, for example caused by molecules on the surface of the sensor. In cases where the concentration of the analyte is low, the sensitivity can be improved by encouraging molecules towards the sensitive site of the sensor. Differential functionalization concentrates molecules on the sensitive areas of the sensor, as shown in pictures 4.17.a and 4.17.b. [18]

To study the response of our device, simulations were performed with a layer of proteins called (Bovine serum albumin, BSA). There are two main aspects that are needed to perform the simulation: the refractive index of the layer and the thickness.

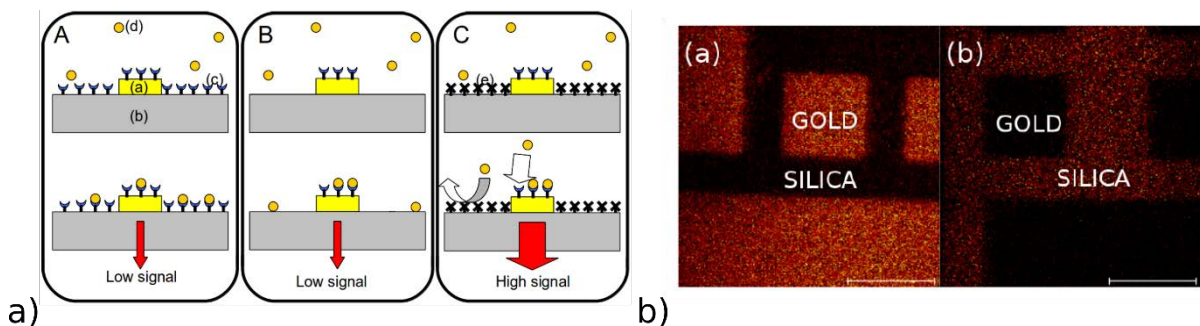


Figure 4.17.a concept of orthogonal differential functionalization to improve high signal in a low concentration regime. 18.b differential functionalization in the article by Palazon, 2015 (scale bar is 100  $\mu\text{m}$ ).

It is hard to define the index of biological material since it changes depending on the concentration and dimensions of the biological species, the temperature and the solvent. The refractive index of BSA can be modelled with a Cauchy dispersion and in the infrared is around 1.45 [19], [20].

The thickness and shape of the most common molecules can be found in literature. Depending on the solvent, the substrate, the configuration of the molecule, the target molecules spread and change their volume. Figure 4.18 shows the shape of Bovine Serum Albumin described by different models based on the conditions of the solvent (e.g. pH) [22], [23].

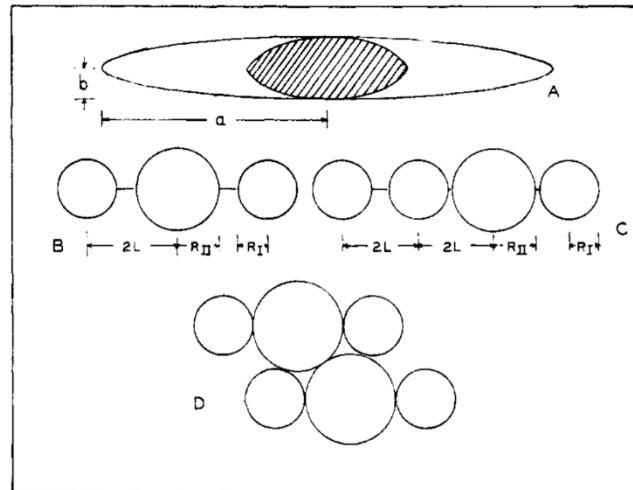


Figure 4.18 Model of Bovine Serum Albumin or BSA by Bloomfield. Structure A is the model of the protein divided in a compact core (central dashed part) and a less dense envelope (approximate values of  $a = 30$  nm and  $b = 3$  nm). B, C and D show the spherical model of the protein.

As shown in Table 4.2, the thickness of the BSA molecule varies by about 0.7 nm in height. We can therefore simulate a variation of  $\pm 0.7$  nm to get an idea of the influence of the resonance peak. When carrying out a quantitative measurement, this is more critical: it would be necessary to make a statistical analysis in order to know the average height.

Table 4.2 Dimensions of the BSA protein in different studies [24]

Study	Dimensions in liquid medium
Different physical techniques—Squire et al. (1968) [25]	4 x 14 nm
Birefringence in an electrical field—Wright and Thompson (1975) [26]	4.16 x 14.09 nm
Viscosity—C. Tanford and G. Buzzell (1956) [27]	3.8 x 15 nm
Chatterjee (1965) [28]	$4.1 \pm 0.7$ x $13.4 \pm 2.2$ nm

Before starting the simulation, there is another question concerning the adlayer: in case of differential functionalization, the surface is engineered to define zones attracting and repulsing the target molecules. Differential functionalization is effective when these zones are constituted by extremely different surfaces, for example a dielectric and a metal [18]. In the case of HPWG, molecules can be selectively bound exclusively either to metal or to dielectric surfaces. The best way to assess which surface is best to functionalize is to simulate the two cases for a HPWG cross-section of SiN, SiO<sub>2</sub> and Au.

Figure 4.19 shows the result of peak shift for a fully plasmonic ring resonator when the adlayer is only on the dielectric (figure 4.19. a) and only on the metal (figure 4.19.b). Different thicknesses are taken into account.

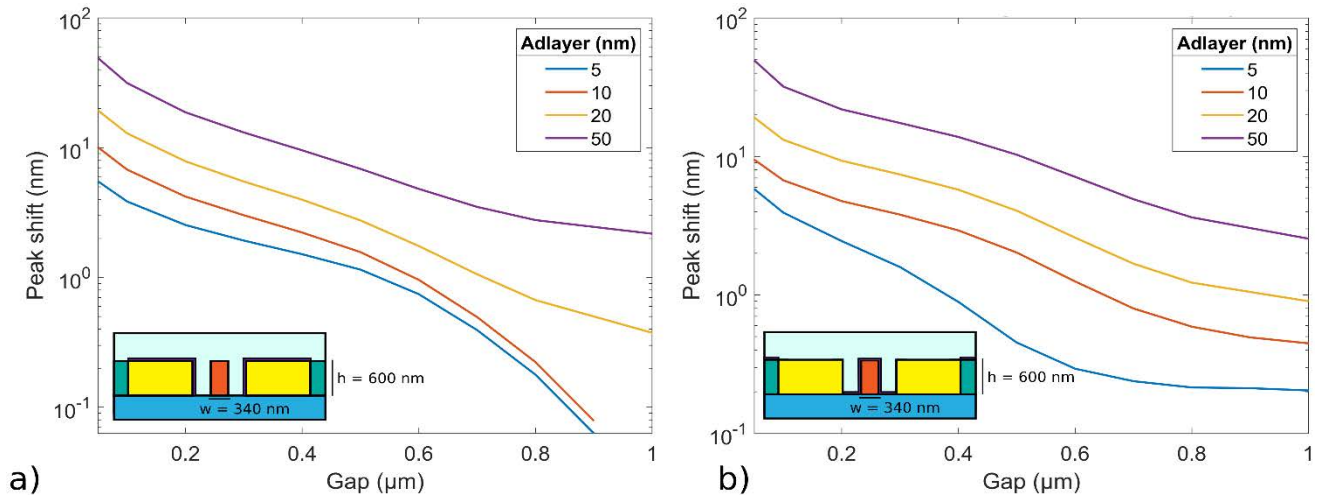


Figure 4.19 adlayer simulations a) when functionalizing Au or b) the dielectrics (SiO<sub>2</sub> and SiN).

The performance for small gaps is slightly better when the dielectric is functionalized. However, practically speaking it would imply a more complicated surface treatment process: since also the fluidic channels and most of the chip are dielectric (glass or plastic), the analytes have a higher probability to fix far from the sensor unless all the rest of the dielectric is passivated. This is why the metallic part of the device is functionalized, increasing the probability of molecules in the sensitive region.

## 4.2.2 Asymmetric Mach-Zehnder Interferometer

An asymmetric Mach-Zehnder interferometer was used to measure the refractive index of the bus waveguide to compare with the simulation. The device is composed of two MMI couplers 1x2 and 2x1 connected with two monomode waveguides of different lengths, as shown in Figure 4.20. The power output as a function of the wavelength is the following cosine function:

$$P(\lambda) = \cos^2\left(\frac{\pi \cdot n_{\text{eff}} \Delta L}{\lambda}\right) \quad (20)$$

depending on the refractive index of the monomode waveguide mode  $n_{eff}$ , the difference of the path lengths  $L$  and the wavelength  $\lambda$ . The experimental transmission is fitted with the nonlinear Levenberg-Marquart method to equation 20 to extract the value of the  $n_{eff}$ , as it is shown in chapter 6.

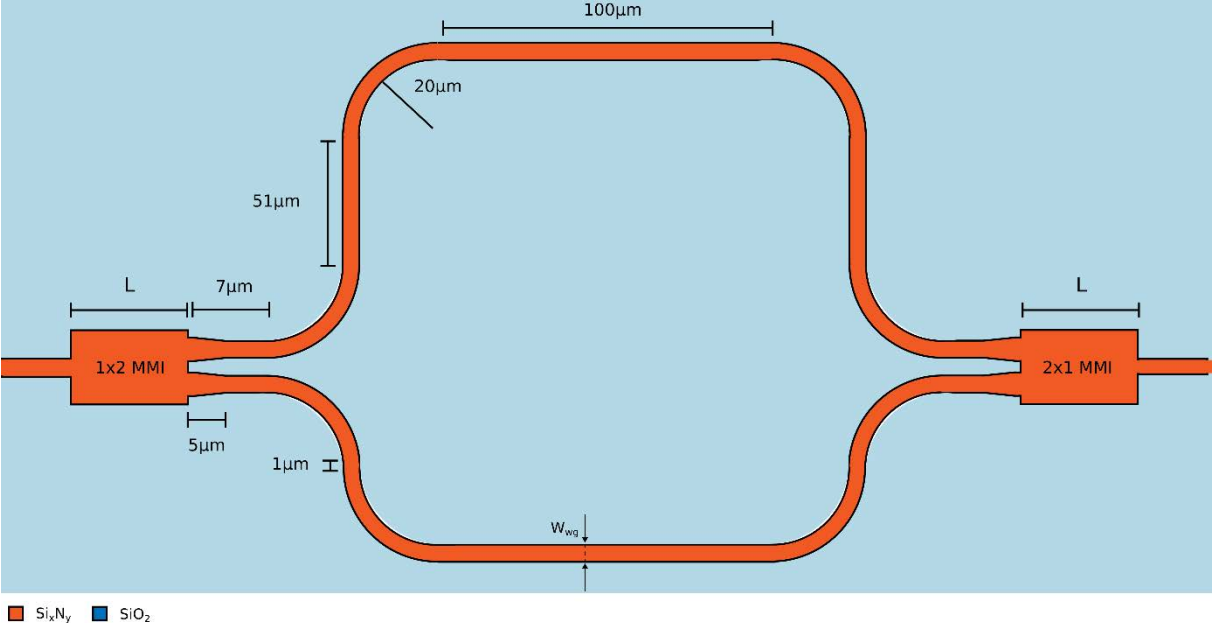


Figure 4.20 Mach-Zehnder interferometer dimensions of the final design

## 4.3 Conclusion

This chapter shows the simulation results obtained with the methods detailed in chapter 3. The HPWG device was analyzed in detail from the 1D structure all the way to the simulation of the 3D device. The simulation results show the sensitivity and the limit of detection when varying the width of the dielectric ridge waveguide and the gap between the plasmonic and the dielectric ridge waveguides. In particular, the simulation of the 2D structure provided an original sensitive geometry, where the dielectric ridge waveguide is below the cutoff. Afterwards, the complete device was designed based on the simulations of the HPWG as well as the simulation of the other light routing components and considerations on the characterization setup (in particular input and output coupling with the setup light source and spectrometer). In conclusion, this chapter explained the simulation results that will be compared in chapter 6 with the experimental results.

## 4.4 Bibliography

- [1] G. Fan *et al.*, “Optical Waveguides on Three Material Platforms of Silicon-on-Insulator, Amorphous Silicon and Silicon Nitride,” *IEEE Journal of Selected Topics in Quantum Electronics*, vol. 22, no. 6, pp. 225–231, Nov. 2016, doi: 10.1109/JSTQE.2015.2494681.
- [2] S. Guerber, “Intégration d’un deuxième niveau de guidage photonique par dépôt de SiN au-dessus du SOI traditionnel,” phdthesis, Université Paris-Saclay, 2019.
- [3] T. Tamir, Ed., *Integrated Optics*, 2 edition. Berlin ; New York: Springer-Verlag, 1979.
- [4] “Coupling Characteristics of an Asymmetric Rectangular Core Optical Wave-guide Coupler: IETE Journal of Research: Vol 51, No 5.” [Online]. Available: <https://www.tandfonline.com/doi/abs/10.1080/03772063.2005.11416419>. [Accessed: 29-Feb-2020].
- [5] M. Z. Alam, J. S. Aitchison, and M. Mojahedi, “Theoretical Analysis of Hybrid Plasmonic Waveguide,” *IEEE Journal of Selected Topics in Quantum Electronics*, vol. 19, no. 3, pp. 4602008–4602008, May 2013, doi: 10.1109/JSTQE.2013.2238894.
- [6] M. A. Butt, S. N. Khonina, and N. L. Kazanskiy, “Hybrid plasmonic waveguide-assisted Metal—Insulator—Metal ring resonator for refractive index sensing,” *Journal of Modern Optics*, pp. 1–6, Jan. 2018, doi: 10.1080/09500340.2018.1427290.
- [7] X. Sun, D. Dai, L. Thylén, and L. Wosinski, “Double-Slot Hybrid Plasmonic Ring Resonator Used for Optical Sensors and Modulators,” *Photonics*, vol. 2, no. 4, pp. 1116–1130, Nov. 2015, doi: 10.3390/photonics2041116.
- [8] C. Ciminelli, F. Dell’Olio, D. Conteduca, F. Innone, T. Tatoli, and M. N. Armenise, “New microphotonic resonant devices for label-free biosensing,” in *2016 18th International Conference on Transparent Optical Networks (ICTON)*, 2016, pp. 1–4, doi: 10.1109/ICTON.2016.7550326.
- [9] M. Masi, R. Orobtcchouk, G. Fan, J.-M. Fedeli, and L. Pavesi, “Towards a Realistic Modelling of Ultra-Compact Racetrack Resonators,” *J. Lightwave Technol., JLT*, vol. 28, no. 22, pp. 3233–3242, Nov. 2010.
- [10] X. Hu, S. Cueff, P. R. Romeo, and R. Orobtcchouk, “Modeling the anisotropic electro-optic interaction in hybrid silicon-ferroelectric optical modulator,” *Optics Express*, vol. 23, no. 2, p. 1699, Jan. 2015, doi: 10.1364/OE.23.001699.
- [11] G. Fan, R. Orbtchouk, B. Han, X. Liu, and Z. Zhen, “Improved coupling technique of ultracompact ring resonators in silicon-on-insulator technology,” *Applied optics*, vol. 51, no. 21, pp. 5212–5215, 2012.
- [12] “FDTD Solutions | Lumerical’s Nanophotonic FDTD Simulation Software.” [Online]. Available: <https://www.lumerical.com/tcad-products/fDTD/>. [Accessed: 06-Sep-2018].

- [13] Linjie Zhou, Xiaomeng Sun, Xinwan Li, and Jianping Chen, "Miniature Microring Resonator Sensor Based on a Hybrid Plasmonic Waveguide," *Sensors* (14248220), vol. 11, no. 7, pp. 6856–6867, Jul. 2011, doi: 10.3390/s110706856.
- [14] T. Claes, J. G. Molera, K. D. Vos, E. Schacht, R. Baets, and P. Bienstman, "Label-Free Biosensing With a Slot-Waveguide-Based Ring Resonator in Silicon on Insulator," *IEEE Photonics Journal*, vol. 1, no. 3, pp. 197–204, Sep. 2009, doi: 10.1109/JPHOT.2009.2031596.
- [15] I. M. White and X. Fan, "On the performance quantification of resonant refractive index sensors," *Optics Express*, vol. 16, no. 2, p. 1020, 2008, doi: 10.1364/OE.16.001020.
- [16] L. Gounaridis, P. Groumas, E. Schreuder, R. Heideman, H. Avramopoulos, and C. Kouloumentas, "New set of design rules for resonant refractive index sensors enabled by FFT based processing of the measurement data," *Optics Express*, vol. 24, no. 7, p. 7611, Apr. 2016, doi: 10.1364/OE.24.007611.
- [17] Y. Ghallab and W. Badawy, "Sensing methods for dielectrophoresis phenomenon: from bulky instruments to lab-on-a-chip," *IEEE Circuits and Systems Magazine*, vol. 4, no. 3, pp. 5–15, 2004, doi: 10.1109/MCAS.2004.1337805.
- [18] F. Palazon *et al.*, "Orthogonal chemical functionalization of patterned gold on silica surfaces," *Beilstein Journal of Nanotechnology*, vol. 6, pp. 2272–2277, Dec. 2015, doi: 10.3762/bjnano.6.233.
- [19] A. Scarangella *et al.*, "Adsorption properties of BSA and DsRed proteins deposited on thin SiO<sub>2</sub> layers: optically non-absorbing versus absorbing proteins," *Nanotechnology*, vol. 29, no. 11, p. 115101, Mar. 2018, doi: 10.1088/1361-6528/aaa68b.
- [20] L. M. Karlsson, M. Schubert, N. Ashkenov, and H. Arwin, "Protein adsorption in porous silicon gradients monitored by spatially-resolved spectroscopic ellipsometry," *Thin Solid Films*, vol. 455–456, pp. 726–730, May 2004, doi: 10.1016/j.tsf.2004.01.062.
- [21] H. Zhao, P. Brown, and P. Schuck, "On the Distribution of Protein Refractive Index Increments," *Biophysical Journal*, vol. 100, no. 9, pp. 2309–2317, May 2011, doi: 10.1016/j.bpj.2011.03.004.
- [22] V. Bloomfield, "The Structure of Bovine Serum Albumin at Low pH \*," *Biochemistry*, vol. 5, no. 2, pp. 684–689, Feb. 1966, doi: 10.1021/bi00866a039.
- [23] "An electron microscope study of the conformational change in bovine serum albumin at low pH," *Journal of Molecular Biology*, vol. 14, no. 2, pp. 443–IN14, Dec. 1965, doi: 10.1016/S0022-2836(65)80194-2.
- [24] T. L. McMEEKIN, M. L. Groves, and N. J. Hipp, "Refractive Indices of Amino Acids, Proteins, and Related Substances," in *Amino Acids and Serum Proteins*, vol. 44, J. A. Stekol, Ed. WASHINGTON, D.C.: AMERICAN CHEMICAL SOCIETY, 1964, pp. 54–66.
- [25] P. G. Squire, Peter. Moser, and C. T. O'Konski, "Hydrodynamic properties of bovine serum albumin monomer and dimer," *Biochemistry*, vol. 7, no. 12, pp. 4261–4272, Dec. 1968, doi: 10.1021/bi00852a018.

- [26] A. K. Wright and M. R. Thompson, "Hydrodynamic structure of bovine serum albumin determined by transient electric birefringence.," *Biophys J*, vol. 15, no. 2 Pt 1, pp. 137–141, Feb. 1975.
- [27] C. Tanford and J. G. Buzzell, "The Viscosity of Aqueous Solutions of Bovine Serum Albumin between pH 4.3 and 10.5.," *J. Phys. Chem.*, vol. 60, no. 2, pp. 225–231, Feb. 1956, doi: 10.1021/j150536a020.
- [28] A. Chatterjee, "Intrinsic Viscosity Measurements of Bovine Serum Albumin at Different Temperatures," *Nature*, vol. 205, no. 4969, pp. 386–386, Jan. 1965, doi: 10.1038/205386a0.



# CHAPITRE 5 - FABRICATION

The goal of this chapter is to detail the manufacturing process of devices, from the cleanroom to the supporting material for characterization setup. At first, the industrial cleanroom fabrication is described. The Datacom Advanced PHotonic Nanoscale Environment (DAPHNE) platform is presented as well as its design rules. All the SiN waveguides are manufactured in this phase, following the design dimensions explained in chapter 4.

The second part of this chapter focuses on the university cleanroom fabrication. Since adding metals in an industrial process is complicated (because of contamination), a proof of concept needs to justify it. For this reason it was necessary to develop the metal patterning in the university cleanroom facilities. However, the process flow must be compatible with the DAPHNE platform for future integration.

For this reason two methods are used, *lift-off*, only compatible with the university cleanroom, and *Chemical Mechanical Polishing* (or *CMP*), compatible with industry. The lift-off process, although imperfect, delivered the devices that were characterized as detailed later in this chapter. On the other hand, CMP produces devices 100% compatible with the industrial environment. However, the fabrication process is more complicated, and it is still under development. Since a lot of effort was put into this method, the details are given in the annex.

The third part focuses on the support devices for characterization, such as microfluidic channels and reservoirs.

## 5.1 The device: from design to characterization

This section is dedicated to describe the manufacturing choices concerning the fabrication of the device. At first, the industrial platform used to build the dielectric parts of the device is presented. The second part of this section concerns the method to add the plasmonic metal waveguides on the sides of the dielectric waveguides to constitute the Hybrid Plasmonic WaveGuide (HPWG).

### 5.1.1 The Datacom Advanced PHotonic Nanoscale Environment platform and design rules

Datacom Advanced PHotonic Nanoscale Environment (or DAPHNE) is an industrial environment, originally thought for Datacom applications, compatible with biosensing applications [1].

The substrate is made of  $750\mu\text{m}$  of Si covered by  $2\mu\text{m}$  of  $\text{SiO}_2$ . Firstly, a layer of  $\text{Si}_x\text{N}_y$ <sup>7</sup> (or simply *SiN*) of  $630\text{nm}$  is deposited by Plasma-Enhanced Chemical Vapour Deposition then patterned with deep UV photolithography. The characteristics of the materials, such as dispersion and absorption, are measured by ellipsometry (HORIBA spectroscopy ellipsometry

---

<sup>7</sup> The index X and Y means that the percentage of Si and N in silicon nitride are not known. It is a slightly different material than stoichiometric  $\text{Si}_3\text{N}_4$ . The details of these processes are part of a confidential cleanroom recipe and will not be described in this document.

[2]). The dispersion of the materials is given at the beginning of chapter 3 as a starting point of the simulations and models analysis. The losses of the waveguides, caused by the wall roughness and absorption by the material, are experimentally evaluated during characterization and are shown in chapter 6.

Once the materials are deposited, the patterning is performed with a photolithography mask. The nominal resolution of the photolithography mask is 180 nm. Other design rules impose limits on angles (over 90°) and distances between structures (greater than 200 nm). The

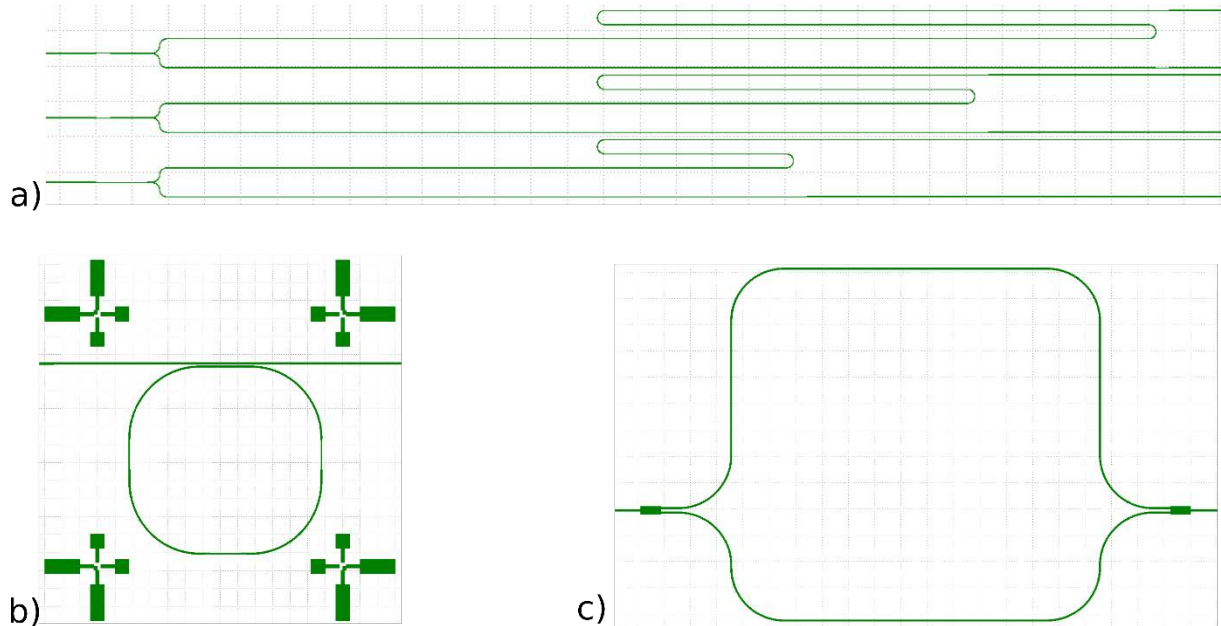


Figure 5.1 Graphic Data System (GDS) of the industrial photolithography mask. a) devices to calculate the losses in the waveguides. b) dielectric part of the HPWG ring with the alignment marks to align the Au plasmonic waveguides. c) Mach-Zehnder interferometer use to experimentally measure the effective refractive index.

photolithography mask was designed with MATLAB by means of the generation tool embedded in CleWin software. The mask contained the waveguide pattern as well as the alignment crosses to place precisely the plasmonic waveguides added later by electron beam lithography (also known as e-beam lithography, electro-lithography or EBL) in the university cleanroom. The GDS file is generated with MATLAB containing all the basic optical test devices needed (HPWG ring resonators for sensing, bends and Mach-Zehnder interferometers for determining the dispersion of the real part of the effective refractive index, directional couplers with different coupling distances). GDS file use for the optical test is given in figure 5.1.

Technological steps such as chemical mechanical polishing (CMP),  $SiO_2$  deposition and inductively coupled plasma (ICP) etching are performed based on the features of the final waveguide (e.g. exposed to air or buried in  $SiO_2$ , thickness of 600 nm or 350 nm). Figure 5.2 shows the schematics of the three main steps (deposition, patterning and the possible final waveguide configuration depending on the final deposition step).

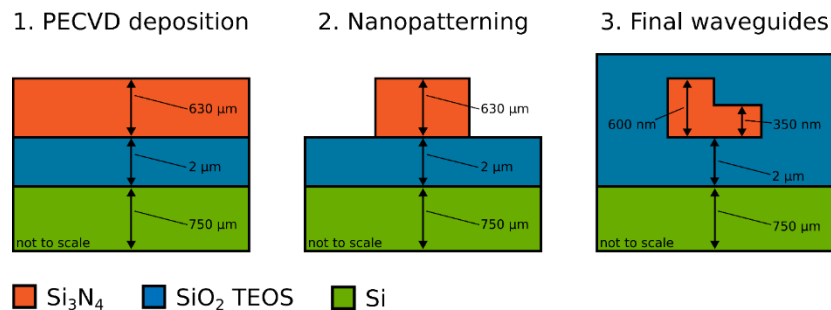


Figure 5.2 Schematics representing the geometry and the materials of the DAPHNE platform

The third step depicted in figure 5.2 can be one of the 6 shown in figure 5.3 based on the thickness of the  $SiN$  layer (600 nm or 350 nm) and the surrounding material ( $SiO_2$ , air or a mix of the two). From the first step (1-NITW) the sample is covered with 1.3  $\mu m$  of  $SiO_2$  on top of the  $SiN$  waveguide, 2-NITW\_EN. The sample is then polished down to the  $SiN$  level giving rise to the 3-NITW\_EN\_CMP configuration. Since in the DAPHNE platform there is an option to partially etch the waveguides to 350 nm, the lithography, the  $SiO_2$  deposition and CMP etching are repeated again, resulting in configurations 5-NITP\_EN and 6-NITP\_EN\_CMP. In the context of this thesis, the choice of the substrate depends on the process used to add the metallic patches to create the Hybrid Plasmonic WaveGuide (or HPWG). More precisely, for the lift-off process NITW level was used while for the CMP process the 3-NITW\_EN\_CMP, 4-NITP or 6-NITP\_EN\_CMP were used.

The result of the industrial process is shown in figure 5.4.a: a TEM image of the cross section of the waveguides is used to calculate the characteristics of the etched  $SiN$  waveguides, in particular the etching angle of the  $SiN$  waveguides and the statistics on the top and bottom width. The standard deviation of the width is 11 nm and the angle of the sides is  $85^\circ$ . Figure 3.b shows the distribution of the thickness of  $SiN$  for the whole 300 mm wafer. The mean is 608 nm with a confidence interval of 3 standard deviation of 21.6 nm.

The roughness of SiN and SiO<sub>2</sub> was experimentally measured with AFM and the RMS value was found to be 0.6 nm for both SiO<sub>2</sub> and SiN, as detailed in next chapter.

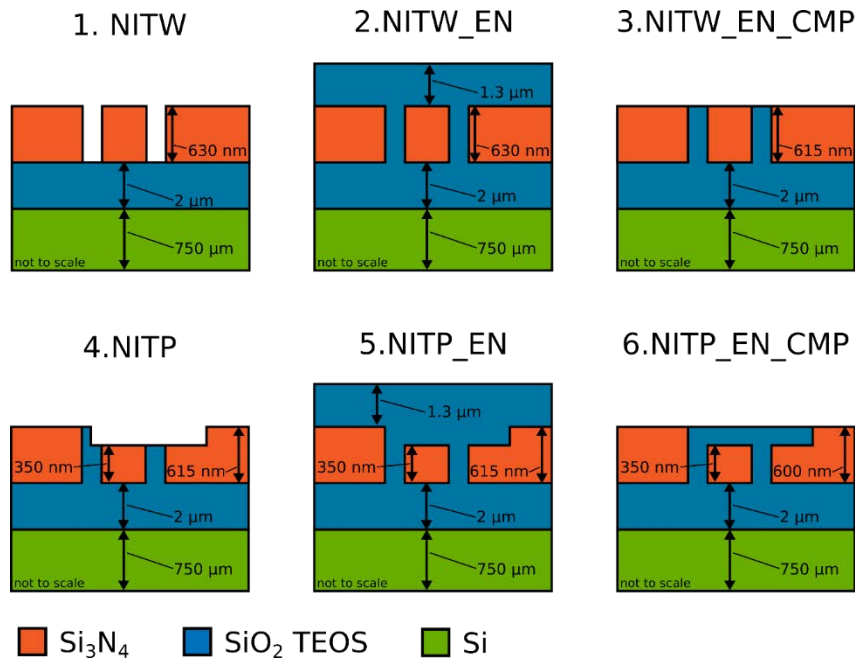


Figure 5.3 possible geometries of the devices at the end of the industrial fabrication process

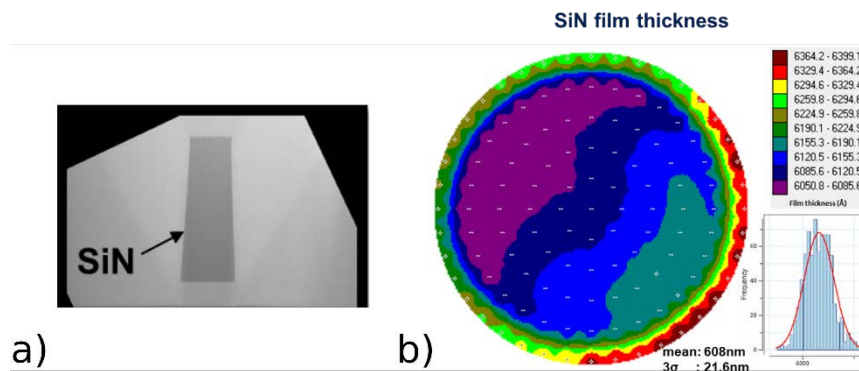


Figure 5.4 a) Transmission Electron Microscopy (TEM) image of a SiN waveguide. b) test of reproducibility on the waveguide core layer thickness.

Once the dielectric waveguides were built, the 300 mm wafers were delivered either complete (Figure 5.5.a) or diced with a method combining a laser and a high precision saw (Figure 5.5.b).

Since the characterization is performed by *butt coupling* techniques, dicing is a delicate operation. Butt coupling consists in placing a fiber in front of the input or output waveguide of the chip to inject or collect the light coming from the source. If the cut is not performed properly, the facet of the waveguide can be rough increasing losses or even, in extreme cases, preventing light to access or exit the waveguides.

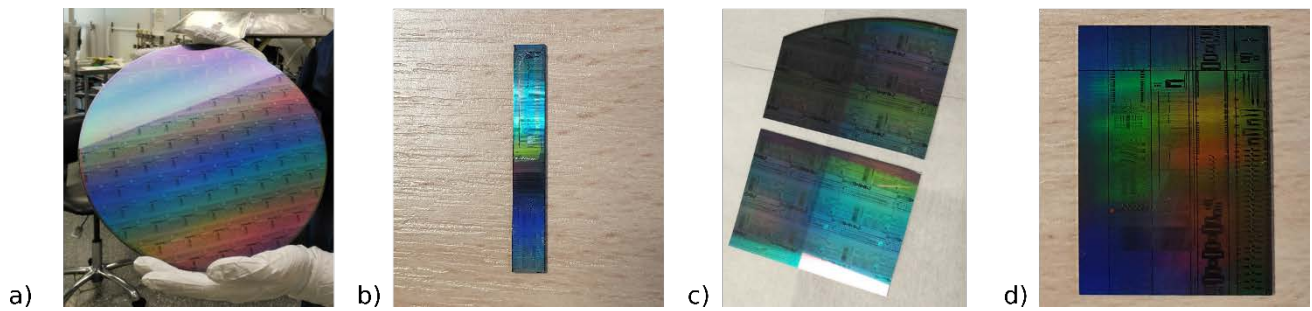


Figure 5.5 a) the full wafer and b) the wafer after cleaving with the diamond pen c) after the dicing of the Université de Sherbrooke d) sample from STMicroelectronics.

The 300 mm wafers were cut in the university facilities using a dicer Disco DAD-320 [3]. Since the maximum wafer size for the dicer is 100 mm, the 300 mm wafer was cleaved in four parts by means of a diamond pen along the crystalline plane of Si (figure 5.5.c) and then diced (figure 5.5.d).

### 5.1.2 Designing a method to add the metal on the sides of the waveguides

As previously explained, to optimize the coupling between the dielectric and the plasmonic modes, the overlap of the field distributions between the two has to be as high as possible given other constraints. That happens when the height of the SiN waveguide and the metal side are the same. The SiN waveguide has a thickness of around 600 nm. The challenging part of the fabrication is to place a 600 nm thick metal layer on the sides of the waveguide with an alignment precision of approximately 10 nm. The alignment is critical because if the metal is too close or touches the SiN waveguide, the losses inside the ring resonator are too high. Thus the quality factor decreases and the coupling condition becomes non-critical, making resonance peaks hard to detect. Indeed, devices with Au on the SiN waveguides of the ring did not have any detectable resonant peak.

Since a standard photolithography process does not have the required alignment precision, patterning is performed by electron beam lithography (EBL) in the university cleanrooms (the process was optimized for both cleanrooms, for the lift-off process at the Institute of Nanotechnologies of Lyon, and for the CMP process at the Université de Sherbrooke). In order to perform the alignment with EBL, the *alignment marks* are fundamental: they are patterns close to the waveguides helping to place and orient Au patches. The more the alignment marks are visible, the more precise the alignment. However, on an insulating substrate it is hard to visualize the alignment marks because the electrons accumulate on the surface, degrading the quality of the image (also known as *charging effect*). Unfortunately, the effect worsens when the electron resist used for EBL is thick because the marks are further from the surface than the resist. It is preferable to work with a thin resist to improve alignment.

Based on the fabrication methods available at the Université de Sherbrooke and the Institute des Nanotechnologies de Lyon, many propositions were made to solve this problem. Of the many propositions, two solutions were explored in the cleanrooms. Since the results presented in this manuscript were obtained with devices using the *lift-off* method, this one will be explained in detail. Although very promising, the second method requires more steps

than the lift-off method. This method, called the *CMP method*, is explained in detail in annex 1 and it is still under development.

### 5.1.3 The lift-off method

Probably one of the most straightforward methods to pattern metals is called lift-off. It consists of depositing metal on a patterned resist that will be subsequently dissolved. If the resist sides have the right inclination, the metal is removed from the substrate where the resist is dissolved while it stays where the resist was removed by lithography. Figure 5.6 shows the process flow for the lift-off from the substrate to the final result.

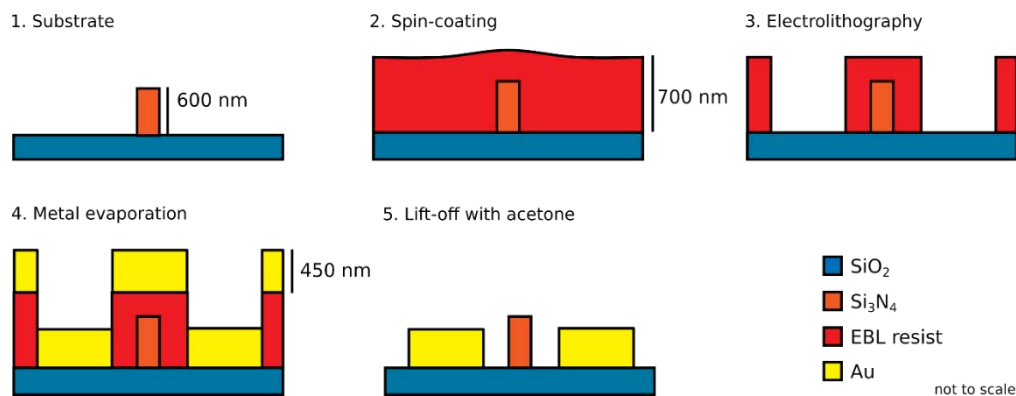


Figure 5.6 the main steps of the lift-off process from the substrate coming from the STMICROELECTRONICS cleanroom to the final device with the lift-off.

Before detailing the process, it should be noted that the drawback of using lift-off is that resist has to be at least 2 times thicker than the metal. As stated before, the thickness of the  $\text{SiN}$  is fixed to 600 nm. Thus, to have a metal thickness of 600 nm, resist should have a thickness of at least 1.2  $\mu\text{m}$ . With such thickness, the alignment would be extremely hard to perform in electrolithography. Although there are complicated methods to improve the alignment<sup>8</sup>, the lift-off was performed with a thinner layer of Au. With a 700 nm thick resist, a 400 nm thick Au was patterned successfully, allowing proof of concept devices to be fabricated while developing the CMP method.

The lift-off process was performed in the NanoLyon cleanrooms, at the Institut des Nanotechnologies de Lyon. As shown in figure 5.3, the 1-NITW level of the industrial process is the most compatible with the lift-off method and it is taken as the starting point.

The first step is to clean the substrate to avoid any organic contamination. This was done using the Piranha solution, a mixture of hydrogen peroxide  $\text{H}_2\text{O}_2$  and sulfuric acid  $\text{H}_2\text{SO}_4$  in proportion 1:3, followed by acetone and ethanol rinsing. This thorough cleaning is necessary because multiple times the resist cracked when baked, probably due to organic contaminants that degraded adherence.

<sup>8</sup> An example is to build metal alignment marks from the dielectric alignment marks thanks to a thin resist lift-off and then perform the thick lift-off with the metal marks. This method should improve the alignment but it complicated the process a lot.

The following step is to spin-coat resist on to the sample with the spin-coater (LabSpin) and the digital hotplates (Stuart), shown later in Figure 5.9.a. To improve adherence, the adherence promoter AR300-80 was added before (speed 2000 rpm, acceleration 900 rpm/s, time 30s). The resist used is the ARP200 (speed 2000 rpm, acceleration 900 rpm/s, time 30s). As the data sheet suggests, the resist is baked at 150 °C for 60s. In order to improve visibility during the EBL, a thin layer of Al was deposited by Joule evaporation (10 nm Al at  $10^{-6}$  mbar). The metal is able to prevent electron charging effects and improve the imaging contrast of the alignment marks.

After spin-coating, the electro-lithography was performed with the scanning electron microscope (SEM) (Inspect F). The acceleration voltage was 30 kV and the current 10  $\mu$ A. The magnification was chosen to be 1100x to have a 100 $\mu$ m $\times$ 100 $\mu$ m scanning field. The electro-lithography was both optimized at the Université de Sherbrooke and in the Nanolyon platform in Lyon. After adjustment of the parameters of the SEM (e.g. focus, astigmatism and angle rotation of the sample), the system follows the position of the alignment marks and it scans around them. The method to detect the alignment marks consists of scanning the marks the first time to identify roughly the position of the marks. Once the marks are found, only the center of the alignment cross is scanned to improve precision. The scan is more precise because the scan window is smaller, reducing the size of the pixels. To clarify how the thick resist can make alignment difficult, Figure 5.7.a shows the SEM image of a ring resonator with the alignment crosses right before exposure. It should be noted that the problem is not just seeing the crosses, but to perform an accurate alignment. By optimizing the scan speed and contrast of the lithography software, the crosses shapes were better defined, as shown in figure 5.7.b. The red pattern are the alignment marks and the blue pattern is the SiO<sub>2</sub> background. The goal of the first scan is to have a quick idea of where the alignment marks are located without scanning for too long. This would cause the development of the resist, which means having Au in those parts of the chip. After the rough scan of the alignment crosses, the center was scanned, as shown in figure 5.7.c. Thanks to this method, the precision of the alignment, measured as the size of the pixel of the precise scan, is around 10 nm. Since it is not always possible to position the center of the design within the precision of one pixel due to the blur of the image, the overall precision is slightly more than 20 nm.

After the electro-lithography, the resist development was performed following the protocol:

- i. Resist remover MIF726 is used to remove the Al or Al etch for 45s.
- ii. Resist developer AR600-546 to develop ARP6200 for 1 minute
- iii. Developer stopper AR600-60 for 30s
- iv. Rinsing with  $H_2O$  for 120s

Sometimes during this process the resist showed cracks and inhomogeneity. We believe that this was due to adherence problems caused by organic contamination. This problem was solved by adding a piranha solution step to the cleaning protocol.

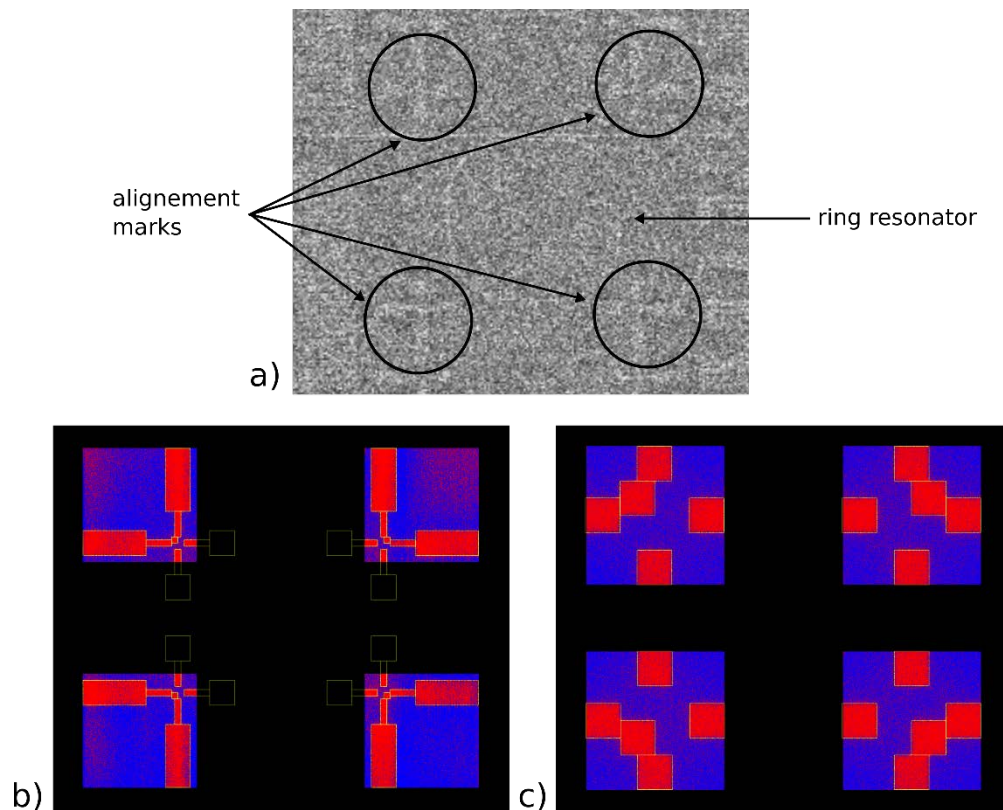


Figure 5.7 a) the electron beam microscopy image of the ring resonator before lithography, b) the center of the alignment marks (add the picture of the dielectric waveguide).

The next step consists in the anisotropic, i.e. directional, deposition of the metal performed with the electron beam evaporator (Leybold). The deposition is anisotropic to avoid the metal sticking to the resist sidewalls, preventing the lift-off from succeeding. The thickness of the

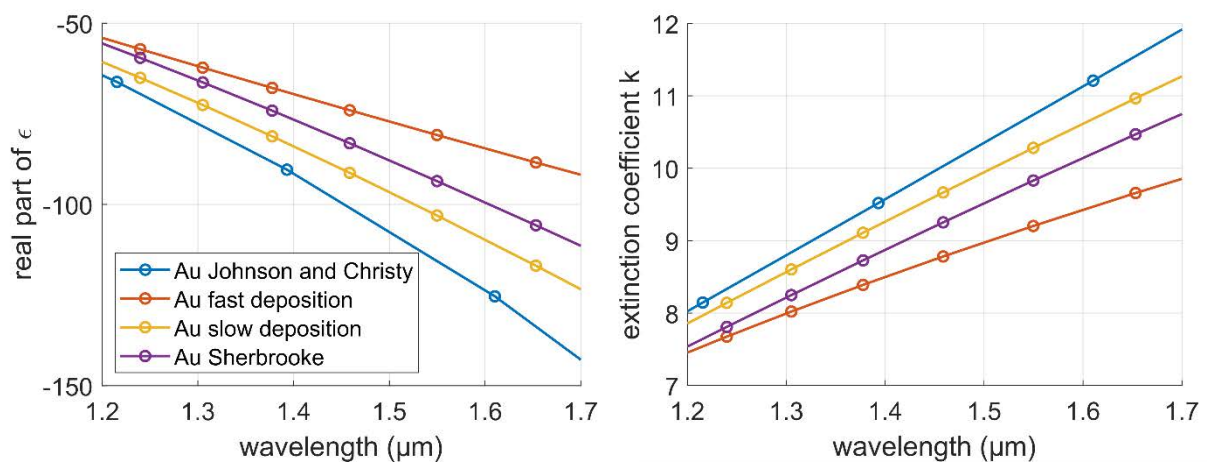


Figure 5.8 Ellipsometry measurements of a) the real part of the relative permittivity and b) the extinction coefficient  $k$  as a function of the wavelength. The curves represent different deposition speeds and the comparison with the Johnson and Christy data.



deposited layer is 2 nm of Cr and 400 nm of Au at  $10^{-6}$  mbar. The deposition speed impacts the characteristics of the deposited material. At first, since the Au thickness is considerable, the deposition rate was high (8 Å/s) to avoid heating the sample: heating the sample could deform the resist and since the deposition chamber is not provided with a temperature measurement of the sample, it is preferable to keep the temperature as low as possible. However, the ellipsometry data in figure 5.8.a and 5.8.b, shows that the real part of the relative permittivity of Au was decreased by 25% in absolute value. This is because when the deposition is faster, the atoms of Au deposit in a less organized structure leading to a less dense layer. Thus, the relative permittivity, and by consequence the refractive index, is an average of air and Au (light blue curve in graphs 5.8.a and 5.8.b). As mentioned in chapter 4, the more the relative permittivity is negative, the stronger the plasmonic effects are. This is why deposition is slowed to 0.7 Å/s (orange curve in graphs 5.8.a and 5.8.b). The values of slow depositions are closer to the measurements of Johnson and Christy (dark blue curve in graphs 5.8.a and 5.8.b) [4]. Before the Au deposition, Cr is added to improve the adherence of Au on the SiO<sub>2</sub> substrate. The Cr layer was reduced from 5 nm to 2 nm to minimize Cr intrinsic losses.

The last step is to dissolve the resist left below the metal in order to lift the Au and Cr layers. The sample was immersed in Remover AR600-71 for approximately 1 hour while in the mixer RotoMix type 48200 at 60 rpm. Once the unwanted metal was separated from the chip, the sample was rinsed in IPA while in an ultrasonic bath.

Figure 5.9 shows the process flow, the machines and the results of this method. Figure 5.9.c and 8.f show the device before and after the lift-off. In figure 5.9.c, the trapezoidal shapes along the straight parts of the ring are the holes in the resist. Figure 5.9.f shows the successful lift-off, leaving the Au only at the bottom of the resist holes.

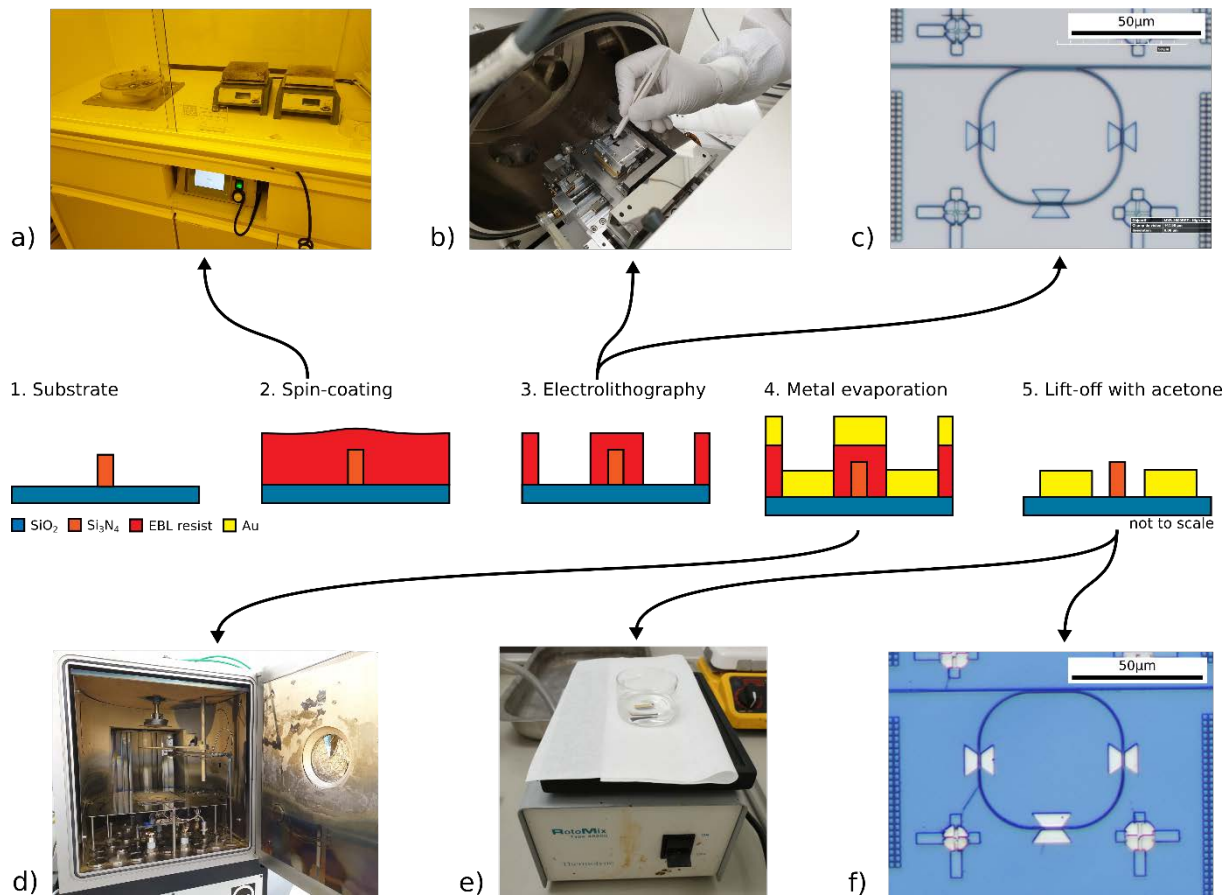


Figure 5.9 fabrication steps associated with the cleanroom images of the process. a) spin-coater, b) the sample inside the scanning electron microscope c) image of the sample after the development. The trapezoidal marks are the hole is the resist. d) The machine for electron beam evaporation Leybold, e) mixer RotoMix type 48200 on which the sample is immersed in acetone, f) final devices with Au patches successfully left of the substrate in correspondence of the holes in the resist.

The lift-off method, although straightforward has two main disadvantages: the first one is that the thickness of the Au layer is lower than the dielectric ridge waveguide core layer, slightly decreasing the sensitivity (around 5%) and the second one is that the lift-off is not compatible with the industrial process.

### 5.3.5 The CMP method

The alternative to the lift-off method is the CMP method, named after the core technique of this method called chemical-mechanical polishing (CMP). The substrates compatible with this method are the 3-NITW\_EN\_CMP, 4-NITP and 6-NITP\_EN\_CMP. Although promising, the CMP method is not yet completed, due to its complexity. The process flow is presented below while more details can be found in annex 1.

Essentially, the CMP method consists in selectively etching the oxide on the sides of the  $Si_xN_y$  waveguides and filling the resulting gaps with metal. This method allows the Au to be thicker, improving the overlap between the core waveguide and the plasmonic modes.

Furthermore, the EBL resist can be thinner than the lift-off method, improving the quality of the image, leading to an easier alignment. The schematics of the process is shown in figure 5.10.

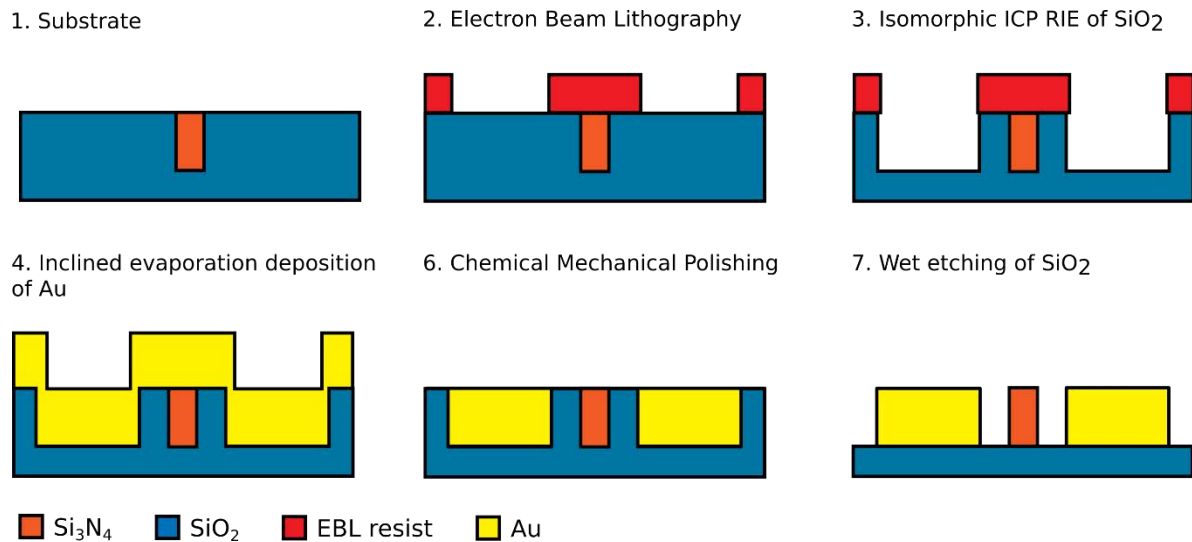


Figure 5.10 Process flow of the CMP method.

## 5.2 PDMS fabrication and bonding

After fabrication, a microfluidic structure must be added atop the optical device to perform measurements into a liquid environment. For this reason, reservoirs and microfluidic channels were built and integrated with the chip and the characterization setup.

In order to characterize the sample, the fluid under test needs to be confined above the ring resonator. One of the most common techniques is to create a reservoir from a polymer called polydiméthylsiloxane (PDMS). PDMS is a chemically inert hydrophobic silicone elastomer commonly used in microfabrication for biological applications.

The first step is to define the mold to shape the PDMS. From the dimension of the chip (5 mm x 45 mm), it was possible to design the desired shape with the Blender software. Figure 5.11.a shows the rendered image of the mold and figure 5.11.b the printed mold. It can be noticed that the mold has a deeper and wider part used to start pouring the PDMS. This is done because PDMS is viscous and, to avoid bubbles in the reservoir walls, it is poured first in the wider and deeper zones and slowly leaks to the useful mold. The thinner parts are the final reservoirs that will be glued onto the chip. They are designed to have a smaller width compared to the photonic chip, not to cover the input and output waveguides from the IR camera, because it would make otherwise complicated to align the input and output fibers. Furthermore, some of the reservoirs are separated in half in order to inject two different

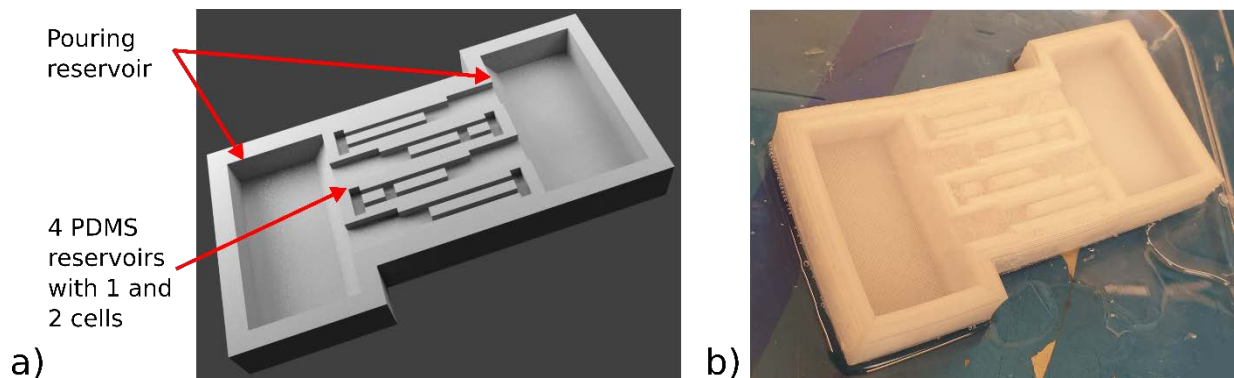


Figure 5.11 Image of the mold for the PDMS and for the sample holder liquids on the same chip.

Once the mold was manufactured, the PDMS was prepared with the following recipe: PDMS is supplied in viscous form (Sylgard 184 Silicone Elastomer Base). By adding a curing agent (Sylgard 184 Silicone Elastomer Curing Agent), the PDMS solidifies becoming more or less rigid based on the curing agent to PDMS ratio. Furthermore, all air bubbles should be avoided to prevent the weakening of the structure. The fabrication protocol is the following:

- a. Mix of PDMS and curing agent (ratio 10:1)
- b. Centrifuge Eppendorf 5702 for 1.5 min at 1500 rpm to remove bubbles
- c. Fill the 3D printed mold
- d. Vacuum bell jar for 10 min to remove residual bubbles
- e. Oven at 70 °C for 1h

Figure 5.12.a shows another example of PDMS mold (with one reservoir instead of 4) and 5.12.b shows the results after taking off the mold. Figure 5.12.c shows the chip and the PDMS reservoir glued after the process.

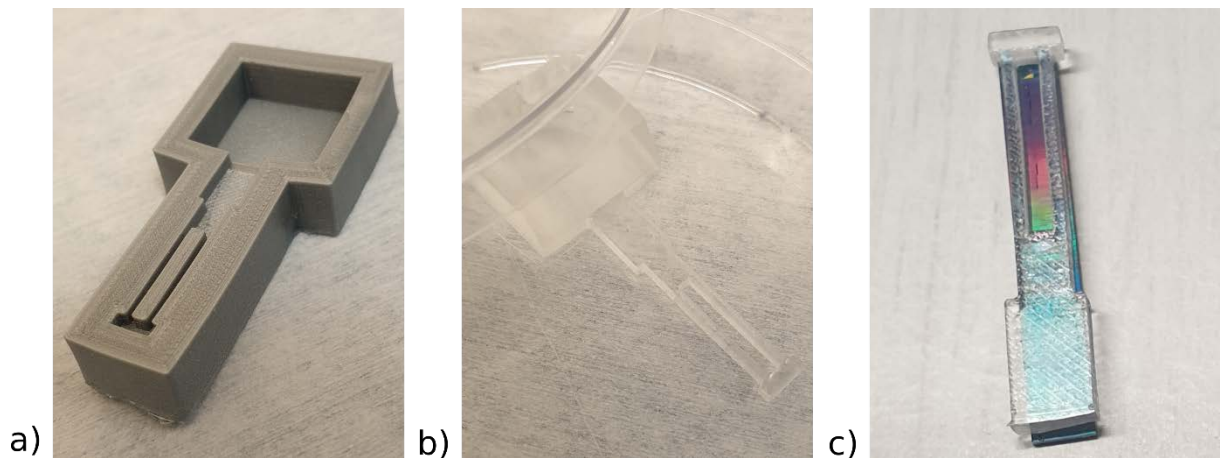


Figure 5.12 a) PDMS mold b) PDMS shaped c) PDMS pool on the sample glued with plasma bonding.

After the PDMS solidified, it was necessary to glue it onto the substrate. Using an oxygen plasma, the surface molecular bonds of PDMS are broken and they react with a silica surface. Thanks to this reaction, the PDMS reservoir sticks to the chip. The plasma  $O_2$  is performed at 900mTorr, 40 sccm  $O_2$ , 29.6 W for 2 min (not more because that would cause a degradation of the PDMS) with the plasma cleaner (Harrick Plasma). After bonding, the samples are put in the oven for 15 min at 70 °C. Once the process is finished, the sample and the PDMS are left to rest and dry for 30 min to solidify the bonding.

By using a similar process, microfluidic channels were made. The mold was done by using a photosensitive film that dissolves after exposure to ultraviolet light on a glass slide (figure 5.13.a). The PDMS is poured on the mold in a Petri dish and follows the same procedure as for the PDMS reservoir. Figure 5.13.b shows the final device with the microfluidic system.

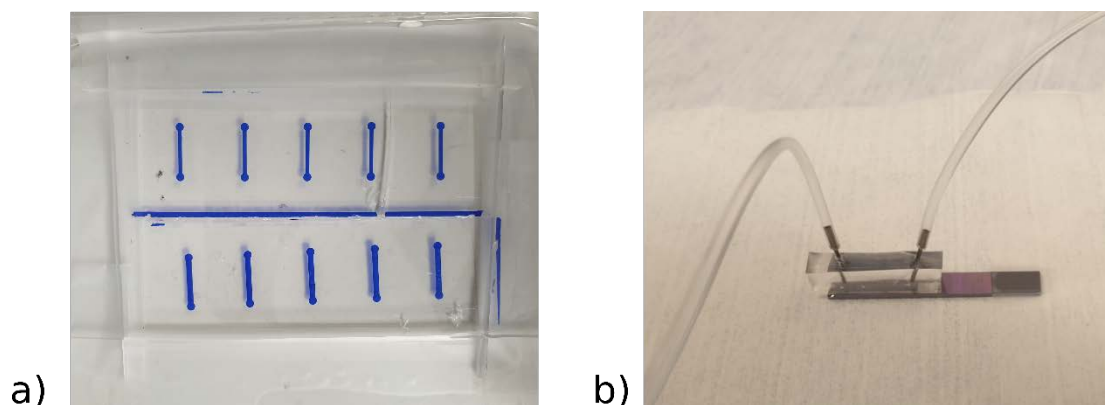


Figure 5.13.a image of the microfluidic mold .b Image of the mold glued to the sample

As shown in the next chapter, the microfluidic channels provide great advantages, such as better visibility of the ring resonator during injection, fast and easier realignment of the fibers with the chip, easier liquid injection. However, measurements with microfluidic channels are

not reproducible. Since this problem is still not solved, the measurements shown in the next chapter are performed with the PDMS reservoir under static fluid conditions.

## 5.3 Conclusion

This chapter describes how the devices were manufactured.

The details of the industrial process were presented. One of the advantages of industrial production is the statistic measurements of the DAPHNE platform, used to give an idea of the variation of the fabricated geometry. Once the wafers were patterned, the university cleanroom fabrication process was designed to add the plasmonic waveguides. Among the many propositions, two methods were explored: the *lift-off* method and the *CMP* method. While the *CMP* method gives a result closer to the simulation geometry, the *lift-off* method is easier to implement and it is the one that provided the devices characterized during this project. For this reason, the *lift-off* method is explained in detail while the *CMP* method is detailed in annex.

In addition, the protocol for shaping a PDMS reservoir and bonding with the chip are given. The PDMS was shaped both as a reservoir and as a microfluidic channel. Despite their many advantages, the final measurements were not performed with microfluidic channels because of repeatability problems.

## 5.4 Bibliography

- [1] M. Calvo *et al.*, “Ring Resonator Designed for Biosensing Applications Manufactured on 300 mm SOI in an Industrial Environment,” *Solid States Devices and Materials 2018*, vol. Solid States Devices and Materials 2018, p. 2.
- [2] “UVISEL : Ellipsomètre Spectroscopique couvrant la Gamme 190 – 2100 nm - HORIBA.” [Online]. Available: <https://www.horiba.com/fr/scientific/products/ellipsometers/spectroscopic-ellipsometers/uvisel/uvisel-plus-640/>. [Accessed: 15-Mar-2020].
- [3] “Disco DAD-320 Dicing Saw—GTS, Giorgio Technology Sales/Service.” [Online]. Available: <http://www.gtsaz.com/equipment/dicing-saw-dad320.php>. [Accessed: 20-Mar-2020].
- [4] P. B. Johnson and R. W. Christy, “Optical Constants of the Noble Metals,” *Phys. Rev. B*, vol. 6, no. 12, pp. 4370–4379, Dec. 1972, doi: 10.1103/PhysRevB.6.4370.



# CHAPTER 6 - CHARACTERIZATION

After the details of the fabrication process of chapter 5, this chapter details the characterization setup and the experimental results. Firstly, the details of the setup and the coupling with the photonic chip are provided to justify some of the design choices detailed in previous chapters. Secondly, before discussing the results, the methods to calculate the figures of merit (such as sensitivity and limit of detection or LoD) and their uncertainty measures are detailed as a fundamental step to interpret the results shown after. Lastly, the experimental results and their discussion is provided, leading to the next chapter on conclusion and perspectives.

## 6.1 Setup

In this section both the optical and the fluidic setups are shown. Furthermore, the following sections also describes the possible upgrades to have faster and easier measurements.

### 6.1.1 Optical setup hardware

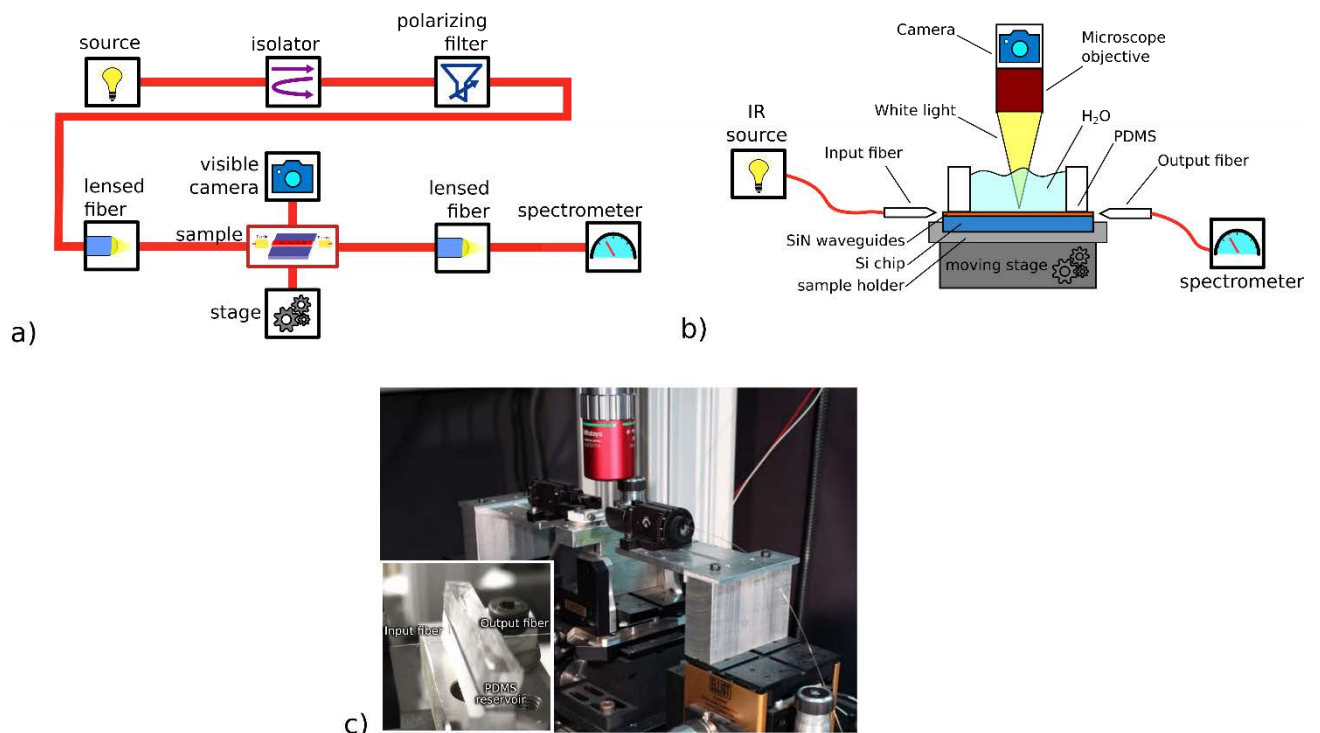


Figure 6.1 a) schematic of the optical set up from the source to the spectrometer b) sketch of the cross section of the stage with the PDMS reservoir and the input and output fibers, c) picture of the setup and the sample.

As shown in the schematic of figure 6.1.a, the components of the optical setup are the following: source, isolator, polarizing filter, input and output lensed fiber and spectrometer.

The first block of the characterization setup is the source: the center wavelength is in the infrared, in particular around  $1.31 \mu\text{m}$  because of the low losses of the SiN waveguides [1].

Two sources corresponded to this requirement: an SLD source from 1.2  $\mu\text{m}$  to 1.4  $\mu\text{m}$ , (nominal average output power of 14.56 mW) from THORlabs and another from 1.2  $\mu\text{m}$  to 1.7  $\mu\text{m}$  from BestSLED (5 LEDs with nominal average output power 30 mW). The output of both sources is oriented in transverse electric (TE) polarization.

After the source, an isolator was placed to avoid back reflection that might damage or influence the source output.

A polarization filter was put after the isolator in order to ensure only TE polarization to pass. All the photonic fibers used are polarization maintaining.

The ellipticity and the polarization state were verified with a THORlab polarimeter PAX1000IR2/M from 900 to 1700nm. A maximum of transmission is noted when the polarizing filter was set to  $0^\circ$  corresponding to the TE polarization. The ellipticity was below  $1^\circ$ , indicating linearly polarized light.

There are mainly two methods to transfer light from a fiber to a chip with this film integrated photonic waveguides: *grating coupling* and *butt coupling* [2].

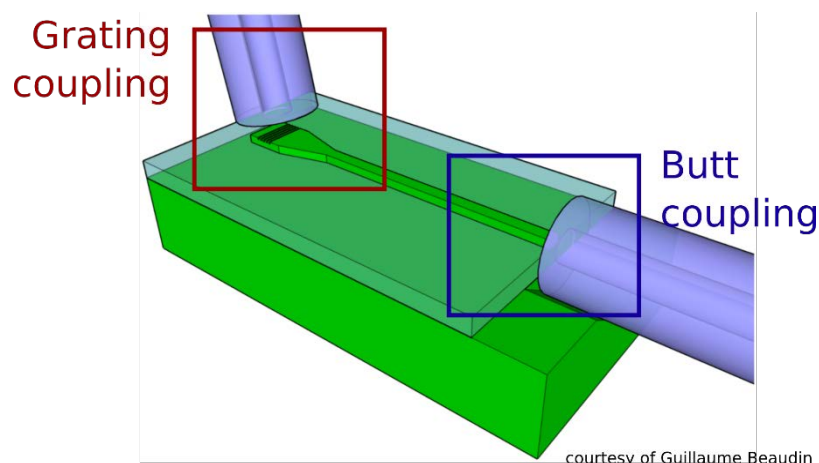


Figure 6.2 Example of two coupling methods on a photonic chip from a fiber: grating coupling in the red square and butt coupling in the blue square

Depicted on the left of Figure 6.2, *grating coupling* is a coupling method that uses gratings to inject light from an inclined fiber onto the waveguide. Grating coupling is sensitive to polarization and has a limited bandwidth (typically around 50 nm). During development, it is preferable to test a wide bandwidth (for example from 1.2  $\mu\text{m}$  to 1.7  $\mu\text{m}$ ) both TE and TM polarizations. For the final device, the grating coupling will be used because it is easier to integrate in a lab-on-chip (or LoC) system.

*Butt coupling* method, shown on the right of figure 6.3, is a coupling method where the fiber is put in front of the cross section of the waveguide, as if it was a prolongation. The light reaching the end of the fiber couples in the waveguide. Lensed fibers can be used to concentrate light in a smaller spot. With micro-positioners, it is possible to place the fiber in front of the waveguide with a precision around one micron. Butt coupling has less constraints in terms of polarization and bandwidth compared to grating coupling, thus making this method better suited to test devices. Butt coupling is therefore the chosen method for testing the device and study its performance.

Once light passed through the desired device, the light is collected by a second lensed fiber. Also in this case, butt coupling is the chosen method to transfer light from the waveguide to the output fiber.

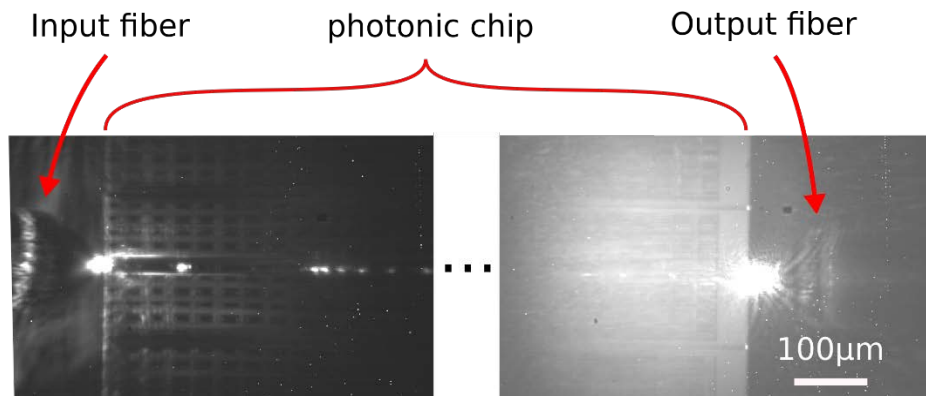


Figure 6.3 top view of the chip while injecting and collecting light by the butt coupling method for the input waveguide (left side) and output waveguide (right side).

Above the chip, a white light source (Fiber-Lite DC-950) and a camera ranging from the visible to the infrared (THORLABS) enable the visualization of the chip and the fibers. Picture 3 shows the input and the output top view of the butt coupling injection and collection.

The power collected is transferred to the spectrometer, model Agilent 86140B. The minimum frequency resolution of 70 pm is low enough to observe the resonance peaks of the ring resonator which, according to the simulations, have a full width at half maximum (FWHM) between 0.2 and 1 nm. The scan time is set accordingly the number of points (10001) and the resolution. For long scans the scan time is 65 sec. A measurement is taken 10 times and then averaged to reduce the high frequency noise of the signal (changing the RMS noise from 40pW to 10pW). The average is done 10 time as a trade off between the measurement time and the improvement of the signal quality.

### 6.1.1.1 Consideration on the type of measurement

With the set up described above, 2 types of measurements can be performed: at fixed and variable wavelengths.

For the final device, the option to work at a single wavelength is interesting, because it would imply a less expensive integration (one wavelength source and a single photodetector). In this case, the working range is more limited and the device has to be extremely stable because the resonance wavelength could vary for other reasons (e.g. temperature changes, fabrication tolerances).

The other option is to excite the device over a range of wavelengths. This enables the detection of the shape of the complete transmission peak and have a larger dynamic range: in this case the working range is the full spectral range (or FSR) of the ring resonator. The disadvantage of this method is the need for a more complex system (such as a wide or tunable source and multiple detectors). The choice will depend on the sensitivity requirements of the final device and the needed working range, in other words on the intended application.

## 6.1.2 Fluidic setup

The optical characterization setup was adapted to allow fluidic reservoirs and microfluidic channels to be integrated on the chip during the measurement. This section is dedicated to the fluidic aspects of the setup.

### 6.1.2.1 Fluidics

There are two main components : a reservoir for static measurements and a microfluidic channel for flow-through measurements.

The first approach involved shaping a reservoir using a 3D printed mold, as explained in chapter 5. The printer is a Ultimaker 3 with a precision of 20 $\mu$ m, using a Chlorinated Polyethylene (CPE) copolymer to withstand heat and solvents.

With the same 3D printer, a sample holder was manufactured so that the sample and the reservoir would fit into it, holding into place. The sample should not move especially when injecting or removing liquids from the reservoir because it might break the optical fibers, close to the sample. Figure 6.4 shows the sample holder model in the digital software Blender (4.a), the printed sample holder with the PDMS reservoir glued to the sample (4.b) and the sample holder while placing the sample inside (4.c).

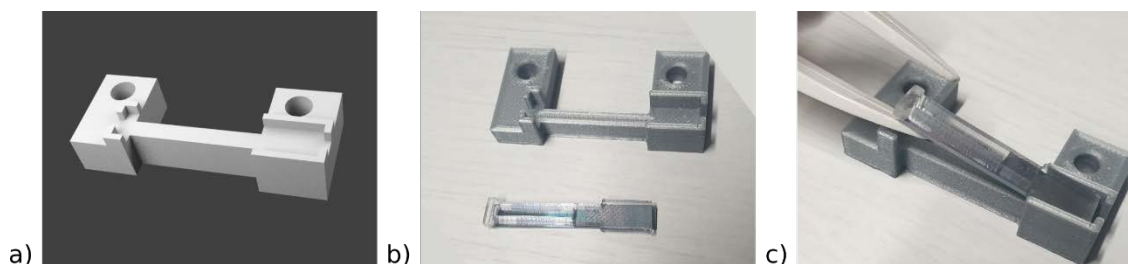


Figure 6.4 a) Sample holder design with the software Blender b) printed sample holder and sample glued with the PDMS reservoir c) loading the sample with the PDMS reservoir on the sample holder. The two fit together to keep the sample in place

This method is produce highly reproducible results and was therefore used to obtain the experimental results presented in this study. However, it has several drawbacks: first of all, it requires important quantities of fluid compared to a microfluidic channel. Furthermore, the injection is done with a syringe by hand, with the risk of hitting the surface and damaging the devices and the fibers. To reduce the chances of the sample touching the fibers during injection, they are pushed back and realigned each time the liquid is changed, increasing sensibly the measurement time. Moreover, to visualize the device under test with this method it is suboptimal because the water meniscus distorts the image. Thus a glass slide is placed on the reservoir to flatten the water surface. This complicates the setup considerably, enhancing the risk of damaging the input and output fibers and further increasing the measure time.

The other method was to place a microfluidic channel on top of the photonic chip. Microfluidic channels come with great advantages: the sample does not move during the injection and the fibers can be kept aligned through the procedure. The signal processing can be performed in real time, giving access to the dynamics of analyte reactions. Furthermore the volume needed for experiments is really small compared to the reservoir system. Another interesting point is that the device is visible at all times thanks to the flat surface of the fluidic channel. Figures 6.5.a and 6.5.b show the microfluidic channel on the sample after the binding in the cleanroom (see chapter 5 for details) and the sample mounted on the setup with the input and output fluidic tubes.

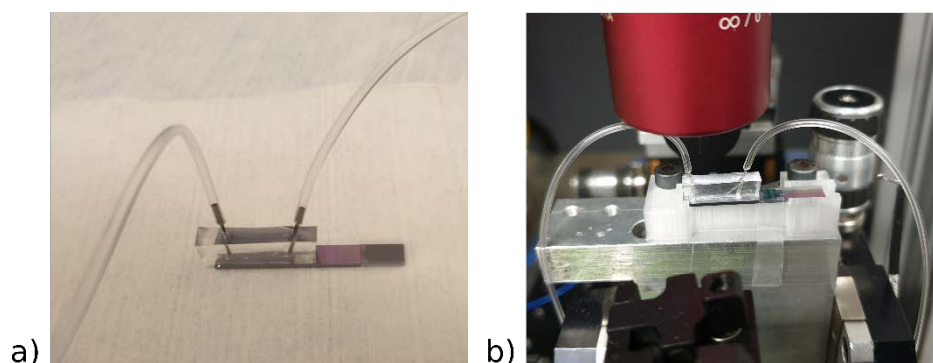


Figure 6.5 a) Microfluidic channel on the sample during the waterproof test in the cleanroom, b) sample on the set up with the input and output channels

Unfortunately this solution, although more advantageous in general, did not succeed in generating reproducible results. For example, when injecting pure water, the response of the ring resonator changed. It is possible that the tubes connecting to the chip with the syringe contained particles that stuck to the device changing the response. Due to lack of time, this problem was not studied in detail.

Table 6.1 Advantages and drawbacks of each method

	<i>Reservoir</i>	<i>Microfluidic channel</i>
<i>Advantages</i>	Measurements were reproducible	<ul style="list-style-type: none"> <li>- Small volume</li> <li>- Compatible with Lab-On-Chip</li> <li>- Faster measurements</li> <li>- No need to realign fibers</li> <li>- Device is easily visible</li> <li>- higher interaction with species</li> </ul>
<i>Drawbacks</i>	<ul style="list-style-type: none"> <li>- High risk of damaging the devices and the setup</li> <li>- Long and more complicated to change the fluids</li> </ul>	<ul style="list-style-type: none"> <li>- Problem with reproducibility in our setup</li> </ul>

### 6.1.2.2 Bulk sensing liquid decision

One of the crucial choices of the characterization was the choice of the fluid to evaluate the bulk performance. The fluid should have a stable refractive index through time and should not change the response of the system (e.g. liquids that leave traces behind). The first idea was to test water with different percentages of ethanol. Since the reservoir is opened, ethanol evaporated over time shifting the device response during the measurement. The second fluid used was glycerol mixed in water. Glycerol is stable and the evaporation is low. To test the reproducibility of the sensor, a first measurement was performed with pure H<sub>2</sub>O, then the test solution was injected (in this case 5% glycerol diluted in H<sub>2</sub>O) and then rinsed with pure H<sub>2</sub>O. If the glycerol left a clean surface, the resonance peak of the resonator should go back to the initial position during the H<sub>2</sub>O rinsing. However, for glycerol the peak did not go all the way back, a sign that some glycerol was left in the reservoir. This hypothesis was proved by the SEM images in figure 6.6, taken after glycerol injection on the chip.

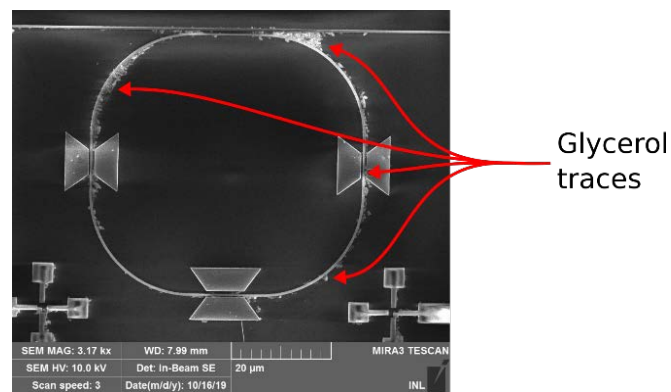


Figure 6.6 HPWG ring resonator after exposure to glycerol. The residues of organic material stick to the surface, changing the response of the device.

Another option is to use a salt and water mix. The solution is stable but if the fluid evaporates, the salt creates salt crystals that are hard to clean. Furthermore, salt solutions slightly etch SiO<sub>2</sub> (10pm/hour) [3]. The best solution was to use water and a glucose monohydrate (sugar) mix. Not only is it easy to clean, but it reduces the evaporation rate of water making the measurement stable. In calibration measurements, 6 concentrations were tested: 0g/100mL, 2g/100mL, 3g/100mL, 4g/100mL, 5g/100mL and 6g/100mL.

## 6.2 Considerations on the uncertainty of the measurements

Regarding the uncertainty of measurements, it is necessary to take into account factors likely to influence the result of the measurement. This paragraph is dedicated to explaining which phenomena were taken into account and how the uncertainty was calculated. In this study, the main sources of uncertainty are the variation of the refractive index of the materials, the variation of the geometry of the device and the temperature.

### 6.2.1 Geometry and refractive indices

This section details the fabrication uncertainties on the refractive indices of the materials and the geometry of the devices.

#### 6.2.1.1 Geometry

Uncertainty on manufacturing process results in an error in the geometry and therefore an error in the parameters of the waveguiding components, such as the coupling devices, the length of the ring, the distance between the plasmonic and the dielectric waveguides and the width and thickness of the waveguides.

A large variation in the coupling zone can bring the ring resonator into overcoupling and undercoupling conditions which reduce the depth of the resonance peak. Furthermore, the length of the ring can vary, changing the FSR and by consequences the dynamic range of the measurement.

These considerations concern the dielectric mask that was used in the DAPHNE environment. Being an industrial platform, the DAPHNE platform has the great advantage of reproducibility of the geometry and the possibility of a statistical study. The standard deviation on the height and the width on a whole 300mm wafer are characterized at STMicroelectronics and the values are:

- Top width of the waveguides: 3nm rms
- Bottom width of the waveguides: 10nm rms
- Thickness: 7nm rms

In the worst case, with one standard deviation on all three values, the resulting change in the sensitivity was simulated. The effective refractive index variation was below  $10^{-5}$ , which means that the main parameters of the ring resonator were minimally affected. The radius of the racetrack was measured with the scanning electron microscope (SEM) and the change was of 0.5%. It is considered not significant because the corresponding variation of the FSR, around 2% of the simulated FSR, does not prevent the measurements to be performed.

The other sources of uncertainty affecting the geometry come from the university cleanroom process. The main geometrical uncertainties are the position of the Au plasmonic waveguides

and their thickness. The uncertainty on the position depends on the alignment during the electrolithography. As explained in chapter 5, after the optimization of the alignment the uncertainty was of about 20 nm, based on the quality of the image of the alignment marks. The impact on the sensitivity is around 0.5 nm/RIU.

The thickness of Au was measured by AFM at  $370\text{nm} \pm 10\text{ nm}$ . Simulations show that this uncertainty on the Au thickness corresponds to a sensitivity variation of 1 nm/RIU.

### 6.2.1.2 Refractive indices

The refractive indices of the materials of the structure were measured with the ellipsometer (HORIBA) [4]. For the ellipsometry, the precision is  $10^{-3}$  on the measured refractive index. The measures were presented at the beginning of chapter 3 to justify the choices on the simulation methods and design.

Concerning the refractive index of the testing liquid, it was possible to test the liquids with a refractometer (Schmidt Haensch [5]). The uncertainty on the refractive index of the refractometer is  $4 \times 10^{-5}$ . The heating stage stabilizes the temperature with a precision of  $\pm 0.03^\circ\text{C}$ . However, the refractometer does not reach wavelengths in the infrared but only from 400nm to 950nm. In order to obtain the values around 1.31 and  $1.55\mu\text{m}$ , two expression for the dispersion were tested (Cauchy and Sellmeier) and compared to experimental results found in literature[6]. The Cauchy expression is the following:

$$n(\lambda) = A + \frac{B}{\lambda^2} + \frac{C}{\lambda^4} + \dots \quad (1)$$

where  $n$  is the refractive index,  $\lambda$  the wavelength and  $A, B$  and  $C$  are the Cauchy coefficients. The degree of the equation is determined by the highest exponent of the parameter  $\lambda$ . The Sellmeier equation, a particular type of Cauchy equation, is expressed as:

$$n^2(\lambda) = 1 + \frac{A_1\lambda^2}{\lambda^2 - A_2} + \frac{B_1\lambda^2}{\lambda^2 - B_2} + \frac{C_1\lambda^2}{\lambda^2 - C_2} + \dots \quad (2)$$

where  $A_1, A_2, B_1, B_2, C_1$  and  $C_2$  are the Sellmeier coefficients.

The Cauchy and Sellmeier coefficients are the parameters optimized during the nonlinear fit with the experimental results.

In order to understand which expression works better, the following method was used: in the literature the refractive index of H2O can be found for a wide range of wavelengths [7]. Both expressions are fit with these data in the range between 400nm to 950nm (Figure 6.7, shows the result of both Cauchy and Sellmeier equations fits when using the data in the range of the refractometer, represented by the red dots. The purple dotted curve represents the fit from the Cauchy curve and the blue one represents the fit using Sellmeier. The green circles represents the experimental data taken from experimental results in literature from [7], from  $0.5\mu\text{m}$  to  $1.6\mu\text{m}$ .



The Sellmeier equation predicts the experimental data from 1 $\mu\text{m}$  to 1.6 $\mu\text{m}$  with higher accuracy. Therefore, Sellmeier equation was used to fit the experimental data coming from the refractometer and estimate the refractive index at 1.31 $\mu\text{m}$ .

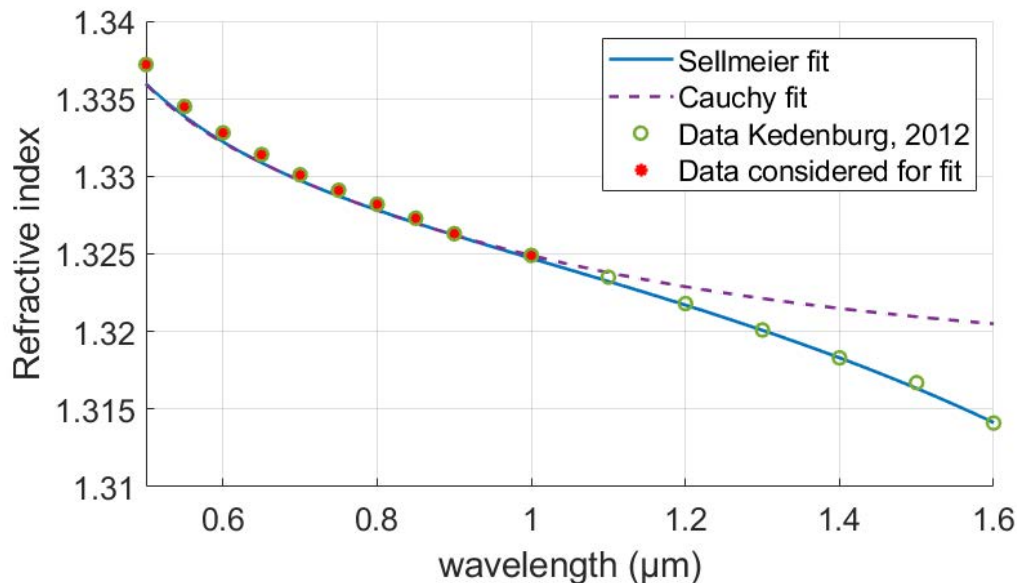


Figure 6.7 Comparison of Sellmeier and Cauchy equations fitted to the experimental data from Kedengurg 2012. Kedengurg’s data are shown in red and green dots. The fits with Cauchy and Sellmeier are performed only with the data shown in red (0.4 $\mu\text{m}$  – 1 $\mu\text{m}$ ). Sellmeier equation gives a better estimate at wavelengths outside the fitting

## 6.2.2 Temperature

Temperature is an important variable because it influences both the dimensions and the optical indices of the materials. The setup described before does not have an integrated control on temperature. However, room temperature is controlled and set around 23 $^{\circ}\text{C}$ . To quantify the possible influence on the measurements, the temperature is measured before, during and after each experiment with the AideTek thermometer (precision of  $\pm 0.5$   $^{\circ}\text{C}$ ). The highest temperature change measured was 0.5  $^{\circ}\text{C}$  (0.5  $^{\circ}\text{C}$  is taken as worse case).

Existing dielectric ring resonators manufactured with the DAPHNE platform have been tested previously to this study in a setup with temperature control and they showed a variation of the experimental resonance peak of 10 pm/ $^{\circ}\text{C}$ . In order to evaluate the dependence on temperature when adding Au, the variation on temperature of relative permittivity and absorption coefficient of Au was measured with the temperature controlled stage of the HORIBA ellipsometer (HORIBA spectroscopy ellipsometry - precision 0.5  $^{\circ}\text{C}$  [4]). The variation of relative permittivity and absorption coefficient were  $\epsilon_{real} = \pm 0.0037$   $^{\circ}\text{C}^{-1}$  and  $k = \pm 0.0002$   $^{\circ}\text{C}^{-1}$ . With this data, the simulations could be performed to estimate the variation of the resonance peak. The result is of the order of 1 pm/ $^{\circ}\text{C}$ .

Concerning the temperature variation of the refractive index of the testing liquid, it was possible to test the liquids at different temperature with the refractometer. The refractive index variation as a function of the temperature was  $10^{-4}$  RIU/°C.

Furthermore, temperature also affects the dimensions of the materials. By taking the coefficient of thermal expansion  $\alpha_{th}$  for each material in the device, shown in table 6.2, the effects can be evaluated. In order to evaluate this influence, the formula :

$$\Delta L = \alpha_{th} \Delta T L$$

is used, where  $\Delta L$  is the variation along one dimension,  $\Delta T$  is the temperature variation and  $L$  the length of the considered geometry [8].

Table 6.2 Coefficients of thermal expansion for SiN, Au and SiO<sub>2</sub>

Material	Coefficient of thermal expansion
	$\alpha_{th}$
SiN	$7.5 \times 10^{-6}$ /°C (source)
Au	$23 \times 10^{-6}$ /°C (source)
SiO <sub>2</sub>	$0.65 \times 10^{-6}$ /°C (source)

Considering in the worse case a temperature change of 0.5°C, the geometrical changes are well below the atomic scale, so the structure is considered invariant to this parameter.

### 6.2.3 Uncertainty calculation

Once that all the uncertainty contributions are identified, it is possible to estimate their impact on the performance of the sensor. The uncertainty is defined by the International Organization for Standardization (ISO) as:

“parameter, associated with the result of a measurement, that characterizes the dispersion of the values that could reasonably be attributed to the measurand” [9] .

In other words, the uncertainty of a measurement characterizes the expected variation of the result. The straightforward way to have a good estimation of the uncertainty is to fabricate a large number of identical devices and perform a statistical study on them. Unfortunately, in this study the devices are few so the uncertainty is calculated in an indirect way.

The main idea is to add all the uncertainty contributions measured with distinct methods (ellipsometry, refractometer, AFM, SEM images) into one uncertainty. The mathematical tool is called the *combined standard uncertainty* defined as [10]:

$$u_{tot}(x) = \sqrt{u_1(x)^2 + u_2(x)^2 + u_3(x)^2 + \dots} \quad (3)$$

where  $u_{tot}$  is the uncertainty,  $u_n(x)$  with  $n = 1, 2, 3 \dots$  are the different uncertainties linked to the different effects (temperature, geometry, refractive indices) and  $x$  the parameter under consideration (resonant wavelength shift or sensitivity).

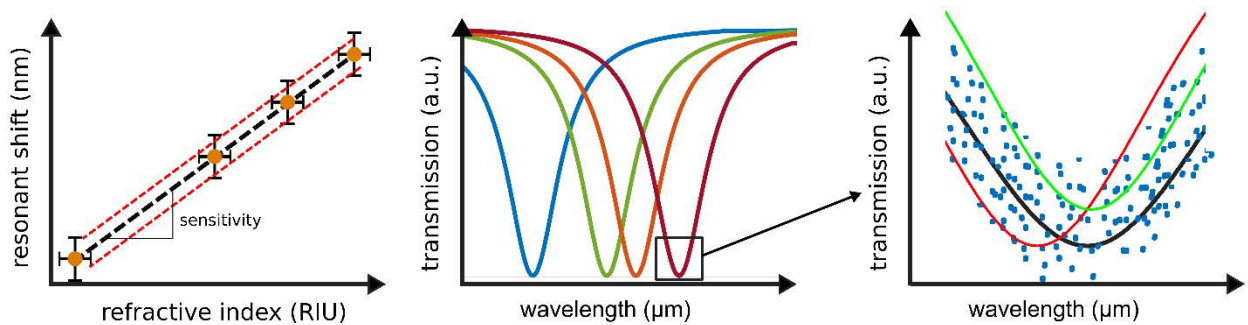


Figure 6.8 a) example of calibration curve with the error bars along X and Y representing the uncertainty. The dotted red lines represents the uncertainty interval on the fit of the straight line. The slope is the sensitivity. b) Example of transmission curve for different concentrations of analyte, c) zoom on the transmission curve where the blue points are an example of the measurement points, the green curve represents an error on the intensity and the red curve an error on the resonance wavelength.

In our case, the relevant properties of the sensor are the shift of the resonance peak (in nm) as a function of the refractive index of the sensing liquid (in refractive index unit or RIU). The slope of the calibration curve shows the sensitivity of the sensor, as shown in figure 6.8.a. Each point has an error bar along the x and y axis. The uncertainty along x (the horizontal error bar) is given by the uncertainty on the measurement of the refractive index liquid. The uncertainty along y (the vertical error bar), depends on the capability of defining the position of the resonant peak. Figures 6.8.b and 6.8.c show respectively the transmission of the device for different fluids and the uncertainty on the peak position. The black curve represents the ideal solution while the green and the red ones represent respectively errors in amplitude and spectral resonance shift due to noise.

### 6.2.3.1 Uncertainty along the horizontal axis

The main sources of uncertainty on the refractive index of the fluid along the x axis of the calibration curve are the uncertainty of the refractometer, the temperature of the measurement and the evaporation rate of the liquids both during the measurement and the storage.

The precision of the refractometer on the index of refraction is of  $4 \times 10^{-5}$  RIU while the variation due to the temperature of the characterization room is of  $5 \times 10^{-5}$  RIU, considering a worse case variation of  $0.5^\circ\text{C}$ , worse case. The refractive index change due to the evaporation rate of the solutions while in storage is of  $10^{-7}$  RIU/day (value extracted over a time range of 2 months).

### 6.2.3.2 Uncertainty along the vertical axis

The main sources of uncertainty along the y axis are the ones that influence the uncertainty of the position of the peak. These uncertainties depend on the temperature variation and the method used to find the peak shift, which in turn depends on signal to noise ratio (SNR) of the

signal. In addition, the hysteresis linked to the quality of the cleaning of the PDMS reservoir when changing liquid can influence the position of the peak. The hysteresis due to the cleaning is around 10 pm but it can be improved by using other products than H<sub>2</sub>O (for example Tween soap). The temperature-related variation of the peak was both simulated and measured experimentally. Its value is around 10 pm/°C, so 5pm for our system. The last uncertainty to evaluate is the one caused by the method used to find the peak shift: since it is a rather complex problem, the next section is dedicated it.

### 6.2.3.2.1 Methods to define the peak shift – peak search

The method to find the peak shift should be chosen carefully since it determines the uncertainty on the measurement, thus influencing the smallest detectable change  $\Delta\lambda_{\min}$  and the limit of detection or LoD. A well known family of methods to find the resonance peak are called *peak-search* methods. Probably the simplest peak-search method consist in identifying the minimum of the resonance peak. However, for systems where noise is important and the quality factor is low, this method generates important uncertainty [11]. A more refined method used by Claes[12] and White[13] consists in fitting the curve with a Lorentzian. Moreover, the limit of detection for a resonant system is strictly linked to the capability of fitting its transmission curve with its theoretical model. This method, although more complex, consist in fitting the transmission peak with a Lorentzian curve whose expression is the following:

$$L(\lambda) = \frac{1}{\pi\gamma \left[ 1 + \left( \frac{\lambda - \lambda_0}{\gamma} \right)^2 \right]} \quad (4)$$

Where  $\lambda$  is the wavelength,  $\gamma$  is defined as the scale parameter specifying the FWHM and  $\lambda_0$  is the location parameter indicating the position of the central peak. Thanks to the nonlinear curve fitting function *lsqcurvefit* of MATLAB, the fit could be found using Levenberg-Marquardt method. Furthermore, MATLAB allows the calculation of the *standard error* in the least squared sense of each fitting parameter by giving the residuals  $r$  and the estimation of the Jacobian matrix  $J$ . The *mean squared residual*  $s$  is defined as [14]:

$$s^2 = \frac{1}{n - p} \sum_{i=1}^n r_i^2 \quad (5)$$

where  $n$  is the number of data points and  $p$  the number of parameters. The covariance matrix  $\hat{\Sigma}$  can be approximated as follows:

$$\hat{\Sigma} = [J^T J]^{-1} s^2 \quad (6)$$

The last step is to find the vector of standard error  $\hat{a}$  from  $\hat{\Sigma}$ :

$$\hat{a} = \sqrt{\text{diag}(\hat{\Sigma})} \quad (7)$$

where *diag()* is the function extracting the elements of the diagonal of a matrix. As is common for biosensors ([11], [12]), the smallest detectable peak is defined as 3 standard

deviations[11] above the noise floor. The smallest detectable peak shift ranges from 5 to 0.5 pm, depending on the wavelength and the noise of the system. These fluctuations of one order of magnitude are caused, as explained in chapter 3, by the parasitic noise due to the Fabri-Perrot cavity interference between the input and output interfaces. Concerning higher frequency noise of the system from the photodetector, the SNR (signal to noise ratio) also influence the quality of the fit. It can be assumed that the noise of the characterization setup has a Gaussian distribution, common in optical setups [15]. The measured standard deviation of the setup used in this project is of 10pW. Once the system noise characteristics are known, the noise is added to the transmission curve for different Q factors to study the relation between the two.

Although the Lorentz method is simple, there is another method able to reduce noise and perform when the quality factor of the resonant system is below  $Q < 10^4$ , explained in the next section.

### 6.2.3.2.2 Methods to define the peak shift – Fast Fourier Transform method

The FFT method is applied when the shift needs to be found in high noise and low Q factor systems ( $Q < 10^4$ )[11]. It is able to calculate the shift without the need of finding the peak position. Furthermore, this method is against the general belief that resonance-based sensors with high Q factors are always preferable[11].

The FFT method is divided in two main parts. The first one is a rough estimate of the shift and the second one is a refinement.

The first part consists in calculating the cross correlation between the different shifted signals related to distinct measurements. The cross correlation measures how similar two functions are by shifting them one relative to the other. The maximum of the cross correlation function is obtained when the two functions overlap in the best way.

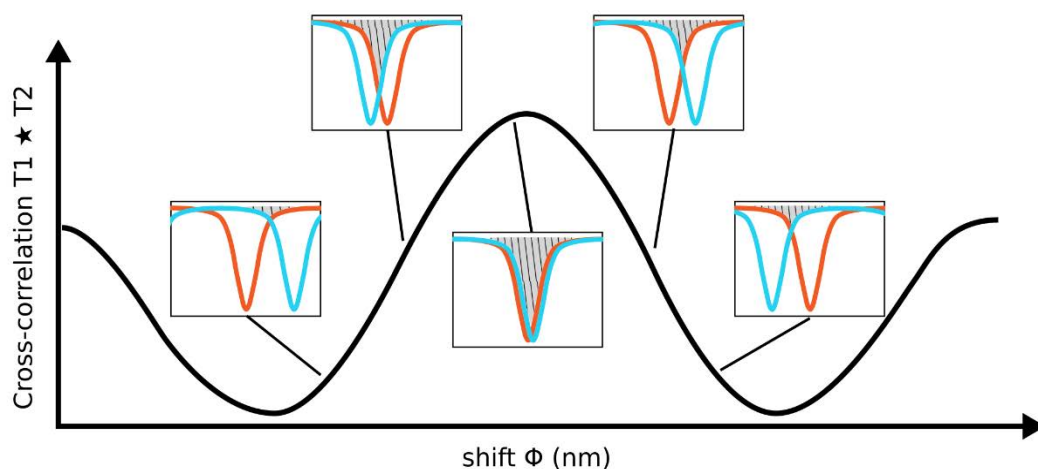


Figure 6.9 Picture of the cross correlation. The insets show the two functions of which on calculate the cross-correlation. The gray hatched area is the overlap of the two curves. Cross-correlation is proportional to the area of the overlap: when the two curves are perfectly overlapped, cross correlation is maximal.

In formula, the cross-correlation  $\star$  is defined as

$$(f \star g)(\phi) = \int_a^b f(\lambda) \star g(\lambda) d\lambda$$

where  $f$  and  $g$  are the two functions two compare,  $\star$  represents the complex conjugate and  $\lambda$  the wavelength. In the case of this study,  $f$  and  $g$  are respectively the transmission spectra of the reference with  $H_2O$  and of a known concentration (from 2g to 6g/100ml). The position of the maximum of the cross correlation corresponds to the shift difference between the two transmission spectra. At this stage the calculated root mean square error, calculated from the residuals from the linear fit of the calibration curve, is of  $10^{-4}$  nm.

To further decrease the error, there is a second procedure to refine the shift search, which is the core of the FFT method.

Let us suppose that the function  $f(n)$  is a signal and its discrete time Fourier transform is  $F(\omega)$  such that

$$F(\omega) = \sum_{n=0}^{N-1} f(n) \times e^{-i\omega n}$$

where  $n$  is the discrete time variable,  $\omega$  the normalized frequency and  $N$  the number of points in the sample.

The function  $g(m)$  is the function  $f(n)$  delayed in time by an integer delay  $\Delta$ .

The shift theorem [15] states that a delay in time domain corresponds to a linear phase term in the frequency domain. This means that the two Fourier transforms are linked by the following formulas:

$$f(n) \leftrightarrow F(\omega)$$

$$f(n - \Delta) = g(m) \leftrightarrow G(\omega') = e^{-j\omega\Delta} F(\omega)$$

It is interesting to express the evolution of the phase of the added term  $e^{-j\omega\Delta}$  as a function of:

$$\angle e^{-j\omega\Delta} = -\omega\Delta$$

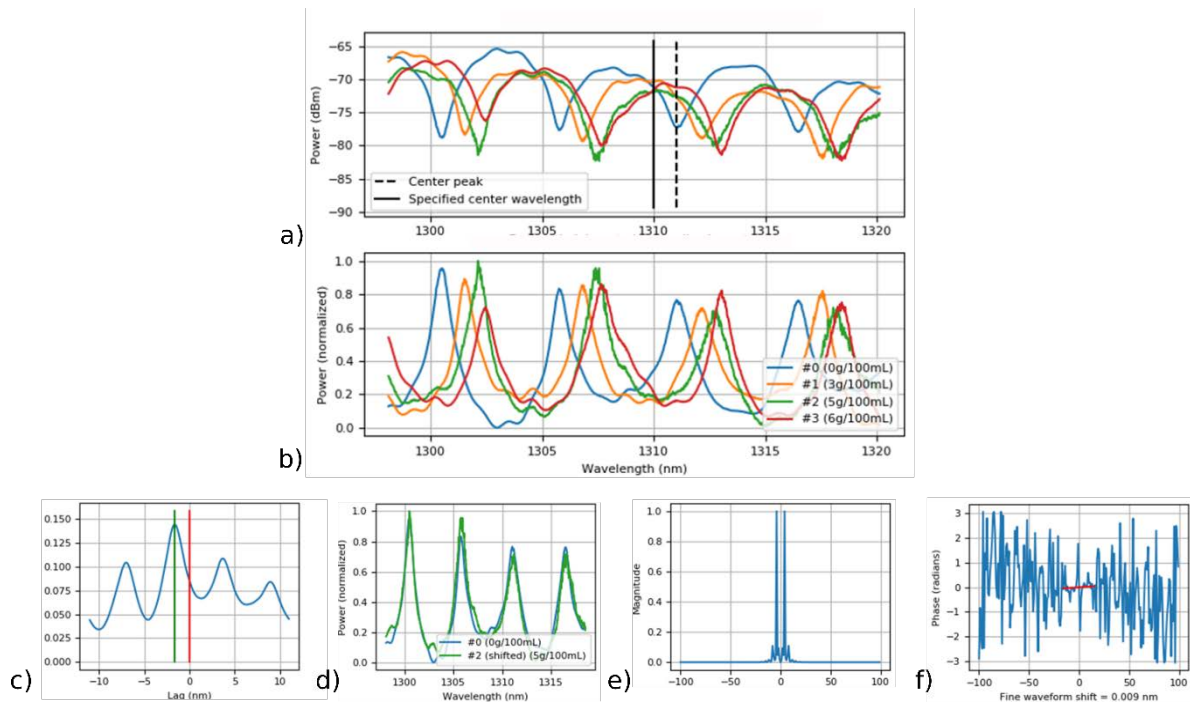


Figure 6.10 illustrates the FFT method: a) the reference and the measurement spectra and b) transmission spectra after normalization and inversion. c-d) Example of result of the cross-correlation. e-f) Example of the amplitude of the Fourier transform and linear fit of the phase to estimate the delay.

Thus, the delay between the two curves in the time domain corresponds to a linear phase term in the frequency domain, whose slope represents the delay value,  $\Delta$ .

When considering the application to the problem of finding the shift of the resonance peak, the time delay in the previous paragraph becomes a “wavelength delay” or shift. The FFT method calculates the Fourier transform of the reference signal and the measurement signal. The phase difference is fitted with a linear model and its slope represents the delay. This method can improve the precision on the detection of the resonance frequency up to  $5 \times 10^{-4}$  nm.

Table 6.3 Advantages and drawbacks of the two main methodologies

	<i>Peak search methods</i>	<i>Fast Fourier Transform method</i>
<i>Advantages</i>	<ul style="list-style-type: none"> <li>• More intuitive</li> </ul>	<ul style="list-style-type: none"> <li>• Precise (<math>\approx 0.5\text{pm}</math>)</li> <li>• No need to have a perfect peak form</li> <li>• No need of high SNR</li> <li>• low quality factor (<math>Q &lt; 10^4</math>) means large scanning steps which make the device compatible with the low-cost aspect of the lab-on-chip[11].</li> </ul>
<i>Drawbacks</i>	<ul style="list-style-type: none"> <li>• Need of high SNR</li> </ul>	<ul style="list-style-type: none"> <li>• More complex to implement</li> </ul>

Another table showing the calculation of the uncertainty along the two axes with the standard combined uncertainty shown in formula (3) and it is represented as error bars in the calibration curve of the sensor.

Table 6.4 Table of uncertainty along the horizontal and vertical axis

Uncertainty in horizontal axis	Uncertainty along vertical axis
<ul style="list-style-type: none"> <li>• Measurement refractometer : <math>4 \cdot 10^{-5}</math> RIU</li> <li>• Temperature refractometer : <math>3,5 \cdot 10^{-6}</math> RIU</li> <li>• Total uncertainty along horizontal axis <math>\approx 4 \cdot 10^{-5}</math> RIU</li> </ul>	<ul style="list-style-type: none"> <li>• Temperature measurement : measurements on other devices <math>10\text{pm}/^\circ\text{C} = 5 \text{ pm}</math></li> <li>• Fit error = <math>0.5 \text{ pm}</math></li> <li>• Total uncertainty along vertical axis <math>\approx 5 \text{ pm}</math></li> </ul>

### 6.2.3.3 The limit of detection (LoD)

Once the uncertainties are identified, the inferior limit of detection can be calculated. Thanks to the previous calculations on uncertainty of the peak position, the minimum detectable wavelength shift  $\Delta\lambda_{\min}$  is defined as:

$$\Delta\lambda_{\min} = 3 * u_y$$

where  $u_y$  is the uncertainty on the peak position. In literature usually 3 standard deviations are used in order to have a range of plausible values of 99.9% probability [11].

From the minimum detectable peak shift, the LoD is found using the following formula [12]:

$$LoD = \frac{\Delta\lambda_{\min}}{S} \quad (2)$$

where  $\Delta\lambda_{\min}$  is the smallest detectable peak and  $S$  the sensitivity of the sensor.



## 6.3 Experimental results

The experimental results are described in this section. Firstly the method to calculate the losses of the waveguides is described. Secondly the results of the HPWG ring are compared with the simulations shown in chapter 4. Lastly, the results of the Mach-Zehnder interferometer are given.

### 6.3.1 Waveguide losses

The losses of a waveguide are important to know in order to estimate performance. Furthermore, such a study provides information about the losses as a function of the wavelength, important to validate the choice of the working wavelength. The study was performed with waveguides of 600nm widths and different lengths. Each waveguide was coupled with a reference waveguide through an multimode interferometer (MMI), as shown in figure 6.11.a. The length difference between the different waveguides are of 1mm, 2mm and 3mm. After obtaining the power transmission of each waveguide, a linear regression of the losses as a function of the length was performed in the least squared sense. The slope of the linear fit represents the losses per unit length of a 600 nm wide waveguide. Figure 6.11.b shows the transmitted power of the different waveguides and figure 6.11.c shows the calculated losses and the errors.

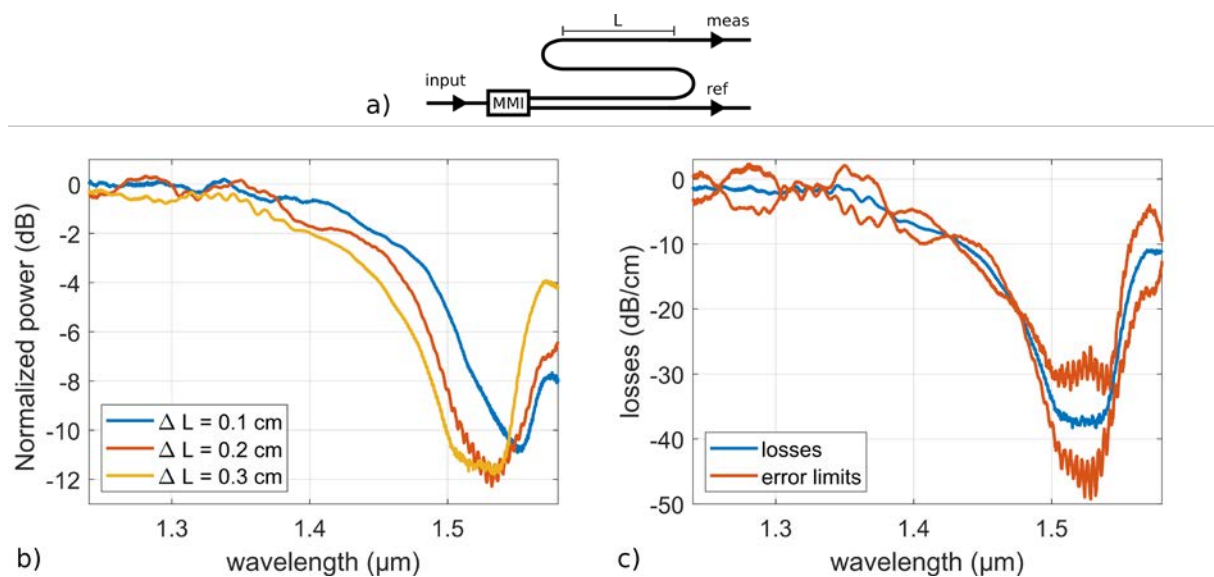


Figure 6.11.a) schematic of the layout of the device to test linear losses. b) losses in waveguides of different lengths as a function of the wavelength. c) losses (blue) with error bounds (red) as a function of wavelength.

Losses are on average  $1.63 \text{ dB/cm}$  from  $1.25 \mu\text{m}$  to  $1.35 \mu\text{m}$ . Figure 6.11.c shows that the error has a large standard deviation in the examined range, and this is due to the small length difference between waveguides ( $\approx 8 \text{ dB/cm}$ ). To have a better estimation of the waveguides' losses, the optical path difference should be increased. In the same industrial lithography mask, spirals with larger different length ( $4.24 \text{ cm}$ ,  $6.00 \text{ cm}$  and  $9.76 \text{ cm}$ ) allowed to experimentally calculate the losses of  $700 \text{ nm}$  wide waveguides. Although they do not have the same width, the spirals underwent the same cleanroom process as the  $600 \text{ nm}$

waveguides. The larger length difference between the spirals decreases the uncertainty on the measured losses. Therefore, the losses measured for these devices have a smaller standard deviation ( $\approx 0.07$  dB/cm). Figure 6.12.a shows the transmitted power of each waveguide. The transmitted power could not be normalized because the spirals didn't have a reference waveguide. The losses are calculated as before, in the least square sense, are shown in figure 6.12.b.

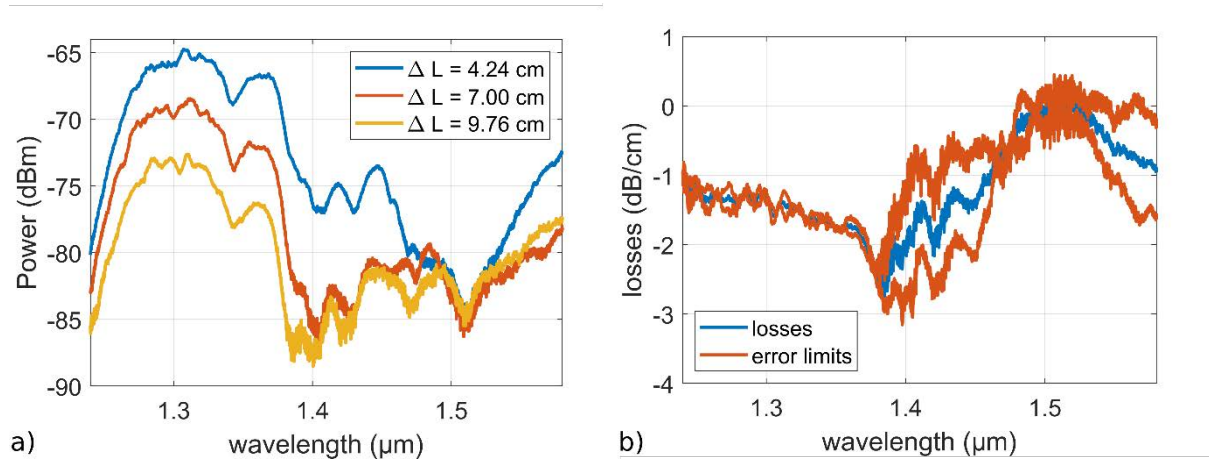


Figure 6.12.a) Transmitted power for the spirals of 700nm width. b) losses (blue) with error bounds (red) as a function of the wavelength

Losses of the 700nm waveguides are in average  $1.44 \pm 0.07$  dB/cm from  $1.25 \mu\text{m}$  to  $1.35 \mu\text{m}$ . As expected, the losses are slightly lower for the 700nm wide waveguides. Furthermore, Figure 6.12.a shows that the highest power transmission is in the wavelength range from  $1.25 \mu\text{m}$  to  $1.35 \mu\text{m}$ , which includes the working wavelength around  $1.31 \mu\text{m}$ .

In the range above  $1.4 \mu\text{m}$  it is hard to conclude on the losses of the waveguide: the strong decrease in the signal seen in figure 6.12.a is due to a peak of absorption due to the composition of the SiN material. Figure 6.12.b shows a decrease of losses in this range: when the power transmission of the three spirals are all close to zero, the regression line is almost flat, giving the impression of low losses. This is why it is important to take into account both the power transmission and the calculated losses to conclude.

### 6.3.2 HPWG results

Testing a sensor goes beyond just finding the calibration curve. For example, the signal must be stable and reproducible to draw a conclusion on the sensitivity. For this reason, calibration tests validate the measurement protocol before testing liquids. Once the protocol is validated, the calibration curve is determined by subsequent measurements changing the target fluid or molecular concentration. The results are compared with the simulation to validate the hypothesis made in chapter 4. This section is divided in two parts, the bulk measurements and the adlayer measurements.

## 6.3.2.1 Bulk measurements – preliminary measurements

### 6.3.2.1.1 Repeatability measurements

Repeatability is tested by measuring multiple times the response to under the same conditions. This procedure is important to define the correct cleaning protocol and the procedure to change fluids in the PDMS reservoir. Before the test, the sample is cleaned in a laminar flow chamber with ethanol to remove dust particles. The sample is then rinsed with deionized H<sub>2</sub>O (or DI H<sub>2</sub>O) to ensure that no ethanol is left in the porous walls of PDMS. Afterwards, the sample is located in the sample holder and the sensing fluid (in this case DI H<sub>2</sub>O) is injected via a syringe or a micropipette. When changing the sensing fluid, the PDMS reservoir is emptied with a syringe (or a micropipette) and rinsed with the new fluid 5 times to ensure that any remaining of previous fluids are highly diluted and do not influence the following measurement.

Figure 6.13 shows the repeatability measurements when replacing 5 times DI H<sub>2</sub>O during the same day. The range between the minimum and maximum change of the resonance peak is around 10 pm.

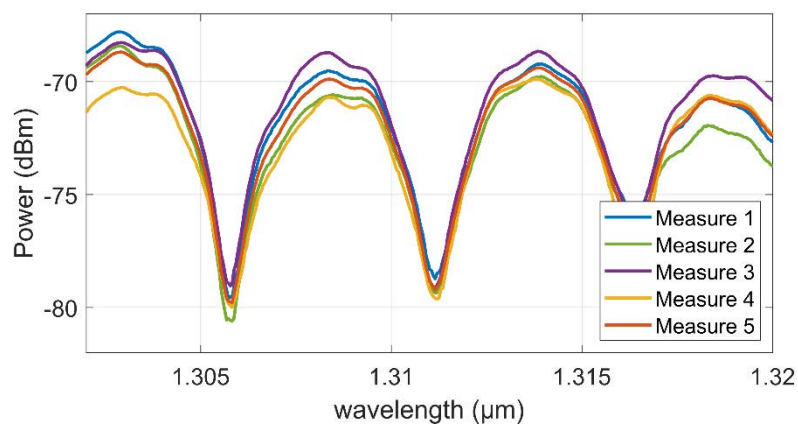


Figure 6.13 transmission of 5 measurements after changing the DI H<sub>2</sub>O to validate the cleaning procedure and the procedure to change fluids. The maximum resonance peak change is around 10pm.

### 6.3.2.1.2 Evaporation measurements

Once the repeatability with DI H<sub>2</sub>O is measured, the next step is to measure the stability of the chosen bulk fluid. As explained before in this chapter, the chosen testing fluid is glucose monohydrate in different concentrations. In order to test the evaporation rate, multiple measurements of the same glucose concentration are taken over time for different configurations: without the PDMS reservoir, with the PDMS reservoir and with the PDMS reservoir covered by a glass slide. A measurement is considered stable when the peak change stays in the uncertainty interval defined, below (10 pm).

Without the PDMS reservoir, the signal was considered unstable because the resonance peak change was above the uncertainty range (around 100pm). With the PDMS pool the peak was stable at least up to 36 min, more than 3 times the length of a standard measure ( $\approx$

10 min as seen in section 6.1.1). With the PDMS pool and the glass slide, the peak was stable at least up to 1h, 6 times the length of the usual measurement. In conclusion, both configurations with PDMS reservoir show a sufficiently stable response. Since the glass slide complicates the setup, the final protocol uses a PDMS reservoir without the glass slide unless there is a need to visualize the ring resonator, in which case the glass slide is added.

### 6.3.2.1.3 Linearity of the response

From theory and simulation, the device should have a linear response to the index changes in glucose in concentration. The devices were tested with glucose concentration varying from 2 to 6 g/100 mL. Figure 6.14.a shows an example of the power transmission of the devices. Figure 6.14.b shows an example of the calibration curve with the error bars calculated as stated in the previous section. The fit of the calibration data with a straight line confirms that the response is indeed linear.

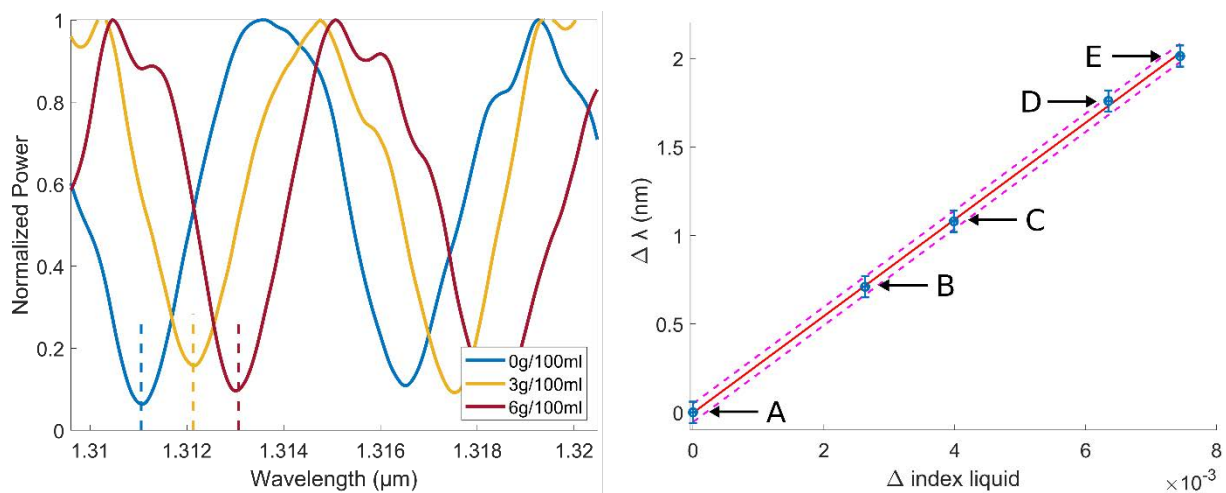


Figure 6.14 a. Transmission spectra of the HPWG device for different glucose monohydrate dilutions in H<sub>2</sub>O. 6.14.b Calibration curve to calculate the sensitivity as the slope of the linear fit of the peak shift as a function of the difference of refractive index of the fluids: “A” represents the reference measurement in pure water, “B”: 2g/100 mL, “C”: 3g/100 mL, “D”: 5g/100 mL and “E”: 6g/100mL. The slope of the fitted line, the sensitivity, is 275 nm/RIU.

### 6.3.2.2 Bulk measurements – sensitivity measures

The experimental results are presented and compared with the previous simulations. This section is divided in three parts. The first details the first HPWG devices tested. The difference with the simulations are shown, leading to further investigations of the geometry and refractive index of the devices. The second part shows the supplementary characterizations and the decision leading to a second fabrication run of devices. The third part shows the results of the second set of devices and the conclusions on the bulk measurements.

#### 6.3.2.2.1 Bulk measurements – first generation devices

Figure 6.15 shows the schematics of the cross sections of the three ring resonator configurations considered in this section. The geometries were measured with the scanning electron microscopy (SEM - 10nm of uncertainty)<sup>9</sup>. We recall that at this point the Au was deposited with a deposition rate of 8 Å/s and a Cr adherence layer of 5nm.

The sensitivity was extracted with both the peak-search and FFT methods, in order to compare them. Furthermore, measuring the geometry of the cross section allowed to adjust simulations taking into account the fabrication alignment and thicknesses. Simulations were performed taking the literature values of refractive index of Au from Johnson and Christy (from now on Au JC) [16] and the experimental geometry. Figure 6.16 compares the simulated sensitivity (Au JC) with the experimental values extracted using both peak-search and FFT methods.

The comparison with the simulation results shows that the sensitivity is lower than expected, except for the peak-search method of sample PR22\_4G, which is associated with a great uncertainty.

Furthermore, as shown in figure 6.16, the peak-search method holds a similar or higher uncertainty than the FFT method as stated in the literature. This comparison confirmed this hypothesis, thus FFT method is the one preferred in this work.

---

<sup>9</sup> For these samples, the alignment of the Au around the SiN was not yet fully optimized (the Au has a shift of 170nm, 130nm and 65nm with respect to the core SiN waveguide, as shown in picture 15).

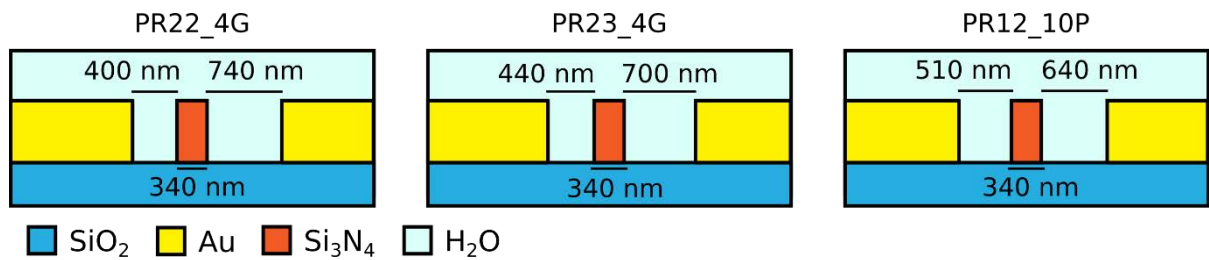


Figure 6.15 cross section of the three considered samples with the gap measured at the Electron Scanning Microscope.

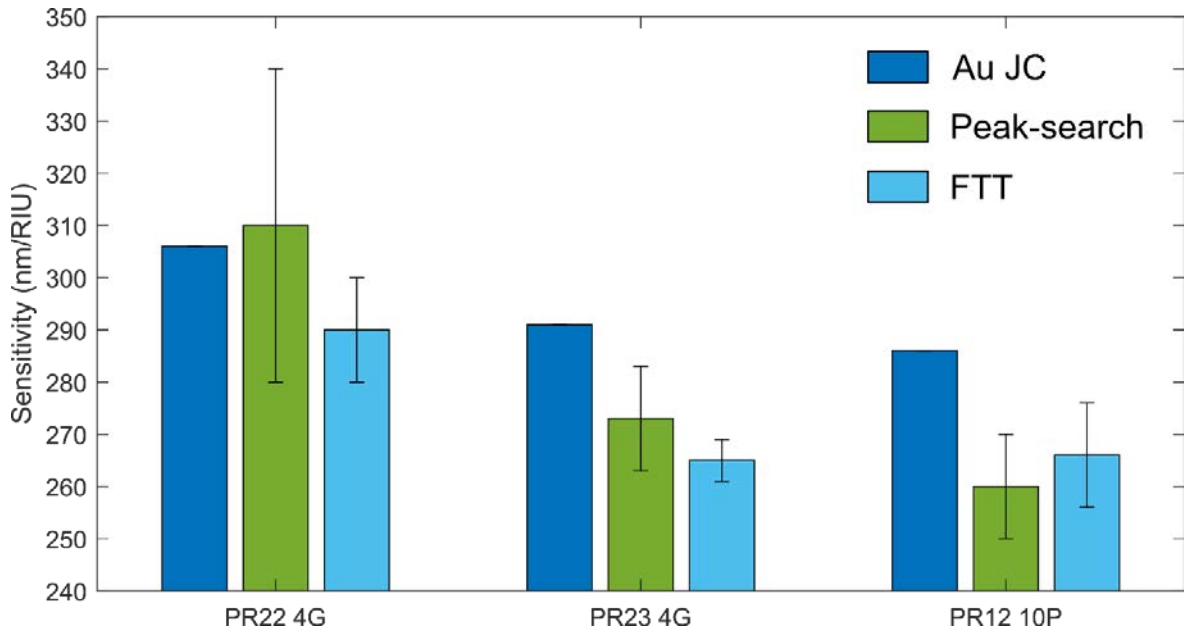


Figure 6.16 Comparison between simulation with the Jonhson and Cristy Au (Au JC - dark blue bars) and experimental results with peak-search (green) and FFT (light blue). The lower sensitivity of the experimental results with respect to the simulations required further analysis, in particular the geometry and refractive index of the materials.

### 6.3.2.2.2 Bulk measurements – further characterization measurements

In order to better understand the differences between the simulation and the experimental results, further physical characterizations were performed. In particular, the atomic force microscopy (or AFM) was used to find the topology and the ellipsometry to find the refractive index of the deposited Au.

#### Atomic Force Microscopy measurements

AFM is an imaging method with a resolution below one nanometer [17]. By means of a sharp tip, like the one shown in picture 6.16.a, the information is collected by touching the surface of the sample. AFM is a useful method to measure the topography of a surface, such as the thickness of a waveguide or the surface roughness of materials. However, because of the angle of the AFM tip, AFM is not adapted to measure the inclination of the sidewalls of a waveguide. Surface roughness was measured using the transmission electron microscopy (TEM) as shown in chapter 5.

Figure 6.17.b and 6.17.c shows the comparison between the first simulated waveguide without Au and the profile measured with the AFM. The height and the width of the waveguide are slightly bigger than the one simulated. No conclusion can be made on the inclination of the sidewalls. To prove the “mode lift” process, the waveguide should be below cutoff. Simulations show that a waveguide of width 360 nm and 670 nm of height is above cutoff. In case the fabrication tolerances were not as expected, thinner waveguides were built with thinner widths (300 nm and 320 nm), as explained in chapter 5.

AFM also enabled the calculation of the flat surface roughness of the materials as a root mean square (RMS) value: 8 nm for Au, 0.6 nm for SiO<sub>2</sub> and 0.6 nm for SiN. However, we do not expect a noticeable influence of this roughness on the performance of the device because the waveguide modes mostly interact with the sidewalls of Au. Simulations are ongoing to quantify the influence of Au roughness.

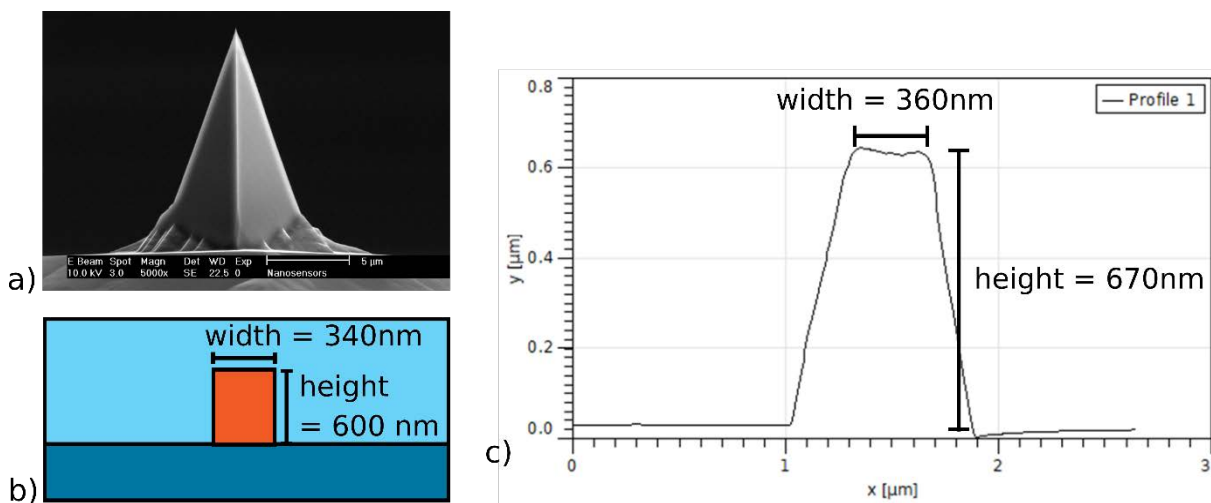


Figure 6.17.a) image of the AFM tip, inclination of 20°. b) Cross section of the simulated waveguides. c) Average profile over a SiN waveguide.

## Ellipsometry

Ellipsometry was used to calculate the refractive index of Au for different deposition recipes, as shown in chapter 5. In particular, the deposition speed played an important role for the enhancement of the plasmonic effect. This effect is discussed in chapter 4 and later in this chapter when commenting on the experimental results. For future reference, the Au deposited at 8 Å/sec is labeled as “Au INL fast”, the one deposited at 0.7 Å/sec is labeled as “Au INL slow”.

### 6.3.2.2.3 Bulk measurements – comparison between the first and second generation devices

Based on the geometry and refractive indices detailed in the previous section, simulations were adjusted in order to study the influence of fabrication parameters on the performance.

Figure 6.18, compares the simulation results using the different Au (Au JC and Au INL fast) and the influence of the Cr adhesion layer. As before, these simulations were also compared to the measurements of the three HPWG ring resonators previously analyzed. It can be noticed

that the experimental sensitivity is closer to the simulations using Au INL fast and the 5nm Cr adhesion layer.

Losses were also simulated: figure 6.19 shows the comparison between the losses of the different configurations for the three samples.

These results rise three main considerations:

1. The first consideration is that the SiN waveguide is not actually below cutoff based on the AFM measurements. As shown in chapter 4, the sensitivity of the HPWG decreases when the SiN waveguide is above cutoff.
2. The second point concerns the dielectric constant of Au: when Au deposition rate is faster, the material is less dense due to the less organized distribution of Au grains. This means that the absolute value of the real part of the dielectric constant is lower due to the air inside the material and by consequence reduces the interaction between the plasmonic and dielectric waveguides.
3. The third consideration is that Cr decreases the sensitivity and introduces losses. This is due to the low real part of its relative permittivity and the high imaginary part of the relative permittivity ( $\epsilon_{Cr} = -0.347 + 27.439i$ ). However, the presence of Cr is necessary because without it Au will not adhere to the substrate.

Next paragraph describes the solutions to optimize the manufacturing of the plasmonic patches taking into account the aforementioned consideration.

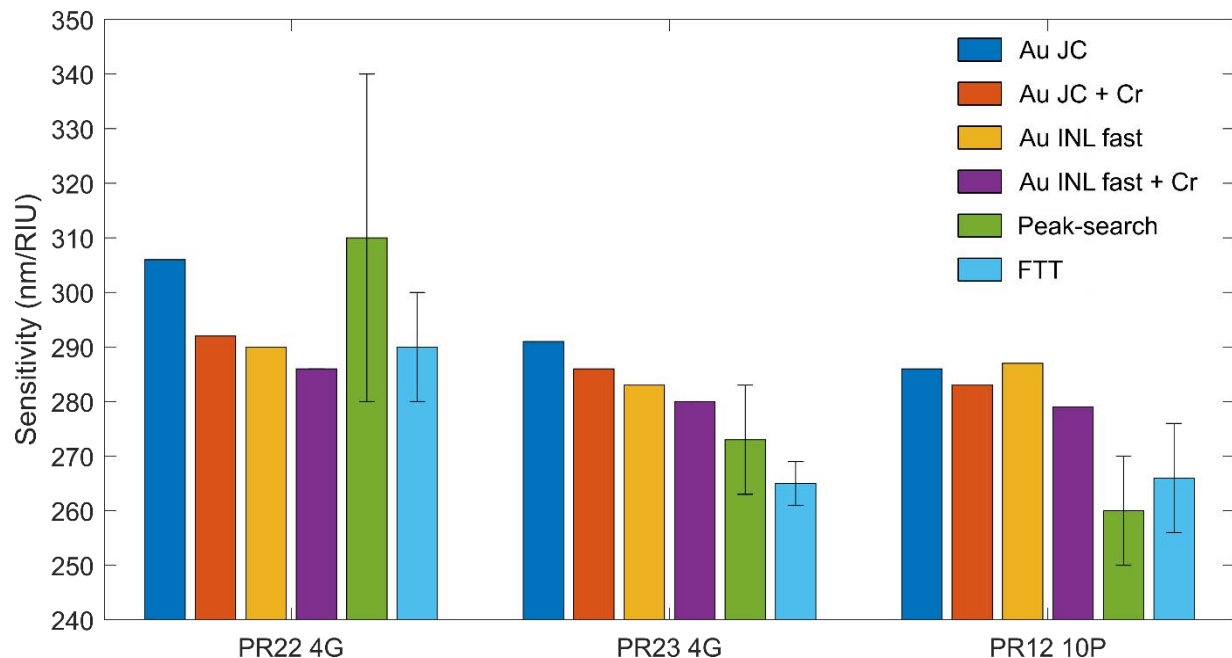


Figure 6.18 comparison of the sensitivity for simulated devices and the experimental results for three samples, PR22\_4G, PR23\_4G and PR12\_10P.



In the second fabrication run of devices characteristics were optimized based on the previous considerations: Au was deposited at a slower rate to improve the interaction between the plasmonic and dielectric ridge waveguide (“Au INL slow”); the Cr adhesion layer thickness, fundamental for Au deposition, was reduced from 5nm to 2nm after testing the adherence through ultrasonic bath in acetone.

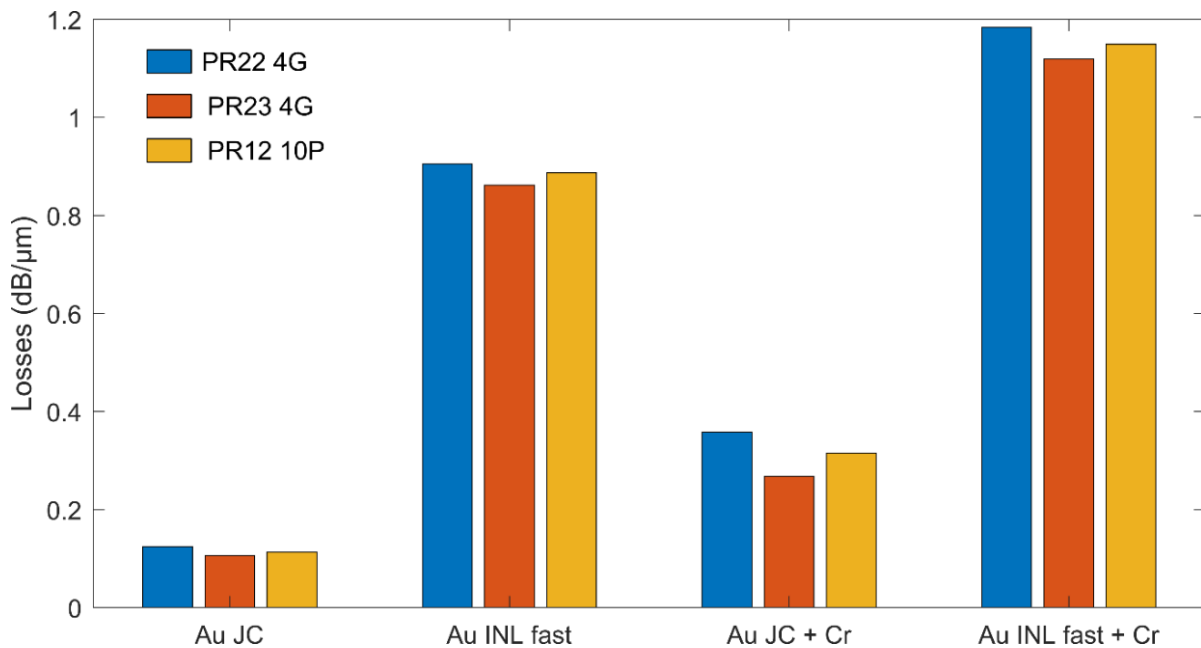


Figure 6.19 simulation of the losses of three samples, PR22\_4G, PR23\_4G and PR12\_10P, with different types of Au and Cr. The Cr and the Au INL both contribute to increase losses.

Furthermore, the SiN waveguides of 340nm nominal width on the lithography mask, are actually manufactured thicker and wider. It is interesting to consider and compare the response of thinner waveguides of 300nm width. The new devices cross sections are shown in figure 6.20. We can see the improvement of the alignment process of the electron beam lithography by looking at the lateral shift of the plasmonic waveguides ( $\approx 10\text{nm}$ ).

Figure 6.20 compares the experimental results between the SiN waveguides with and without Au both 300 nm and 340 nm in width, when 10% of the ring is a HPWG (the rest is purely dielectric). It is important to recall the principle of “mode lift” we are studying: simulations suggest that sensitivity improves when the plasmonic modes have a strong interaction with a dielectric waveguide below cutoff (see chapter 4 for more details).

The first remark concerns the HPWG resonators with SiN width of 300 nm: the improvement in the sensitivity (from 210 to 320 nm/RIU) suggests that the mode is correctly lifted above the cutoff while concentrating the energy in the sensing fluid. Moreover, the resonator is even more sensitive compared to the results at 340nm. The second remark concerns the waveguide at 340nm: adding the Au at 340nm does not affect much the sensitivity. This fact supports the hypothesis that the waveguides at 340 nm are actually guiding and they do not interact enough with the plasmonic modes. The Q factor of these resonators are in the same range of

values, around  $1000 \pm 200$ , as expected for the different sources of losses (plasmonic or radiation losses for dielectric waveguides below cutoff).

We are aware that to validate the concept a statistical analysis must be performed with multiple devices, to verify the repeatability of these results. This was not possible due to time limitations. However, the combined uncertainty (shown by the error bars in figure 6.20) suggests that fabrication uncertainty, temperature uncertainty and refractive index uncertainty should not significantly change the trend of the results.

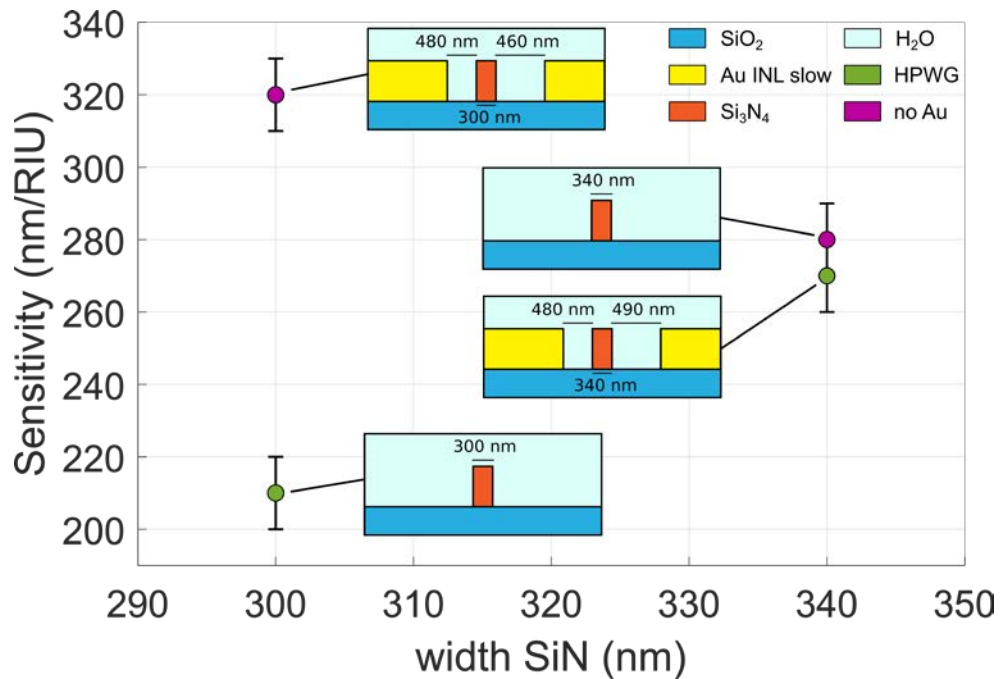


Figure 6.20 Experimental sensitivity of the resonators for two SiN waveguide widths and two configurations (Au INL slow deposition compared with the ring resonators without Au).

### 6.3.2.3 Adlayer measurements

Adlayer tests are performed with Bovine Serum Albumin (BSA). As explained in chapter 3, BSA is a good candidate for testing the surface based response because it adheres to most surfaces and it has a thickness adapted to HPWG sensing (approximately 4 nm). The buffer solution is phosphate-buffered saline (or PBS). The sensing protocol consists in exposing the sample to increasing concentrations of BSA, from 20 to 50  $\mu\text{mol/mL}$ . Although the preliminary tests performed on dielectric samples showed a response to the deposition, we cannot yet draw a conclusion of the sensitivity because of lack of repeatability of the measurements. The tests are still ongoing to finalize the repeatability tests and the following step will be to test the HPWG samples.

### 6.3.2.4 Differential functionalization

Once the BSA tests provide results for a homogeneous functionalization, the next step is to consider the advantages of differential functionalization. Differential functionalization enables the selective localization of particles in well-defined parts of the sensor. When these parts are the sensitive sites of the sensor, the probability of molecule detection increases. Therefore, the advantage of differential functionalization is the enhancement of the signal for low concentrations of analyte[18]. Differential functionalization is particularly stable between metallic and dielectric surfaces. In particular, Au is known in biology for its affinity with the S atom in organic compounds called thiols. However, the affinity between Au and thiols strongly depends on the quality of the Au surface, thus on its deposition and the previous fabrication steps. It is then fundamental to verify that the differential functionalization works on the Au deposited at INL after all the fabrication steps.

To verify the selectiveness of the differential functionalization, one sample on which the lift off did not completely work was used. This ensured that the sample underwent the exact same procedures as a full ring resonator device. Fluorescent nanoparticles were attached to the thiols via a biotin-streptavidine interaction for visualization with a microscope. The fluorescent compound used was rhodamine, inside  $\text{SiO}_2$  50nm diameter nanoparticles. The location of the nanoparticles (and by consequence of the thiols) can be verified with the fluorescent microscope to conclude on the specificity of the functionalization. The schematic of the chemical functionalization is shown in figure 6.21.

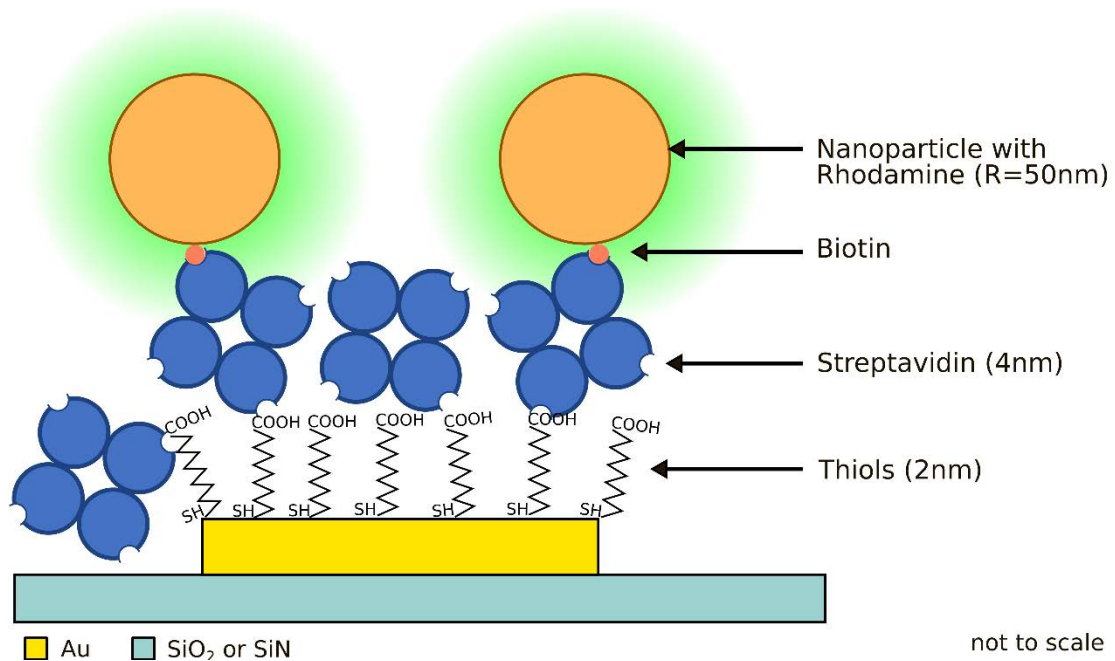


Figure 6.21 schematic of differential functionalization for thiols, streptavidin, biotin and nanoparticles with rhodamine and the different estimated thicknesses

### 6.3.2.5 Functionalization procedure

The first step is to clean the samples. All the possible organic contaminants are cleaned by means of a Piranha solution and plasma cleaning:

1. Piranha solution 1:3 H<sub>2</sub>O<sub>2</sub>:H<sub>2</sub>SO<sub>4</sub> for 1 min
2. Rinse with ultra-pure H<sub>2</sub>O for 15 min
3. Plasma cleaning with O<sub>2</sub> under 0.7 mbar pressure with 29.6 W for 3 min
4. Plasma cleaning with H<sub>2</sub> under 1 mbar pressure with 22.2 W for 5 min

Thiol functionalization is performed immediately after cleaning the sample, with the following protocol:

1. Immersion in the acid thiol (11-Mercaptoundecanoic acid, MUA) solution in ethanol 99% (C=1mM, pH=2) for 12h at 4°C.
2. Rinse with ethanol
3. Rinse with ultra-pure H<sub>2</sub>O

Once the thiols are on the Au surface, the acid group COOH on top of the thiols is activated to bond with the streptavidine:

1. Deposit the solution 0.2M EDC (1-Ethyl-3-(3-dimethylaminopropyl) carbodiimide) /0.05M NHS (N-hydroxysuccinimide) in the buffer solution MES 5 mM (2-(N-morpholino)ethanesulfonic acid - pH ≈ 6) for 2 hours at room temperature (≈ 70 μl).
2. Rinse with 1ml de MES 5mM.
3. Rinse with H<sub>2</sub>O UP.

4. Dry with Ar or N
5. Deposit 50  $\mu\text{l}$  of streptavidine solution (1 mg/mL) on the surface incubate overnight at room temperature.

Once the streptavidine is bound to the thiol, the biotin-streptavidin interaction protocol to immobilize nanoparticles is:

1. Rinse with 1 ml of MES 5 mM solution
2. Incubation in 2 ml of ethanolamine 10 mM in ultra pure  $\text{H}_2\text{O}$  for 15 min in order to passivate the active thiols that did not react.
3. Rinse with 1 ml of MES 5mM solution.
4. Immersion in the solution of nanoparticles in ultra pure  $\text{H}_2\text{O}$  for 1h (concentration 5.2 nanoparticules/mL).

The results of the functionalization is observed with the fluorescent microscope to confirm that the nanoparticles are localized on the Au. In order to keep track of all the steps, a control sample was tested in a surface plasmon resonance (or SPR) instrument.

Figure 6.22.a shows the fluorescent image of the nanoparticles. Figure 6.22.b shows the visible light image, where the light color is the Au and the darker color is the  $\text{SiO}_2$  and SiN. Figure 6.22.c is a superposition of the two, with the fluorescent image of nanoparticles is shown in red.



Figure 6.22 result of the differential functionalization. a) image of the fluorescent light, b) image of the visible light where the lighter part is the Au, superposition of the two where the red points are the fluorescent light of the nanoparticles.

### 6.3.3 Mach-Zehnder results

The Mach-Zehnder device is used to compare the theoretical and the experimental results for the effective refractive index of the modes in the 600nm bus waveguide, to have an estimate of the difference between the simulated effective refractive index and the experimental one. The model of the Mach-Zehnder transmission, presented in chapter 3, is adapted to take into account the amplitude modulation of the source. The theoretical formula is modified by an offset parameter  $P_{offset}$  and an amplitude parameter  $P_{max}$  to best fit the curves.

$$P(\lambda) = P_{max}(\lambda) \cdot \cos^2\left(\frac{\pi \cdot n_{eff} \Delta L}{\lambda}\right) + P_{offset}(\lambda) \quad (19)$$

where  $\lambda$  is the wavelength,  $n_{eff}$  is the effective refractive index of the mode and  $\Delta L$  is the difference in length between the two arms. The effective refractive index is approximated by a 3<sup>rd</sup> degree polynomial :

$$n_{eff} = a_1 + a_2\lambda + a_3\lambda^2 + a_4\lambda^3.$$

To find  $P_{max}(\lambda)$  as a function of wavelength, the maxima of the transmission curve are fitted with a polynomial of 4<sup>th</sup> degree.  $P_{offset}(\lambda)$  is calculated by averaging the values of the maxima and minima of the transmission and fitting the result with a polynomial of 4<sup>th</sup> degree as well. After obtaining  $P_{offset}(\lambda)$  and  $P_{max}(\lambda)$ , the coefficients  $a_1$ ,  $a_2$ ,  $a_3$  and  $a_4$  were found with a nonlinear fit in the least squared sense with the Levenberg-Marquardt algorithm. Figure 6.23 shows the comparison between the power transmission of the experimental setup and the nonlinear fit.

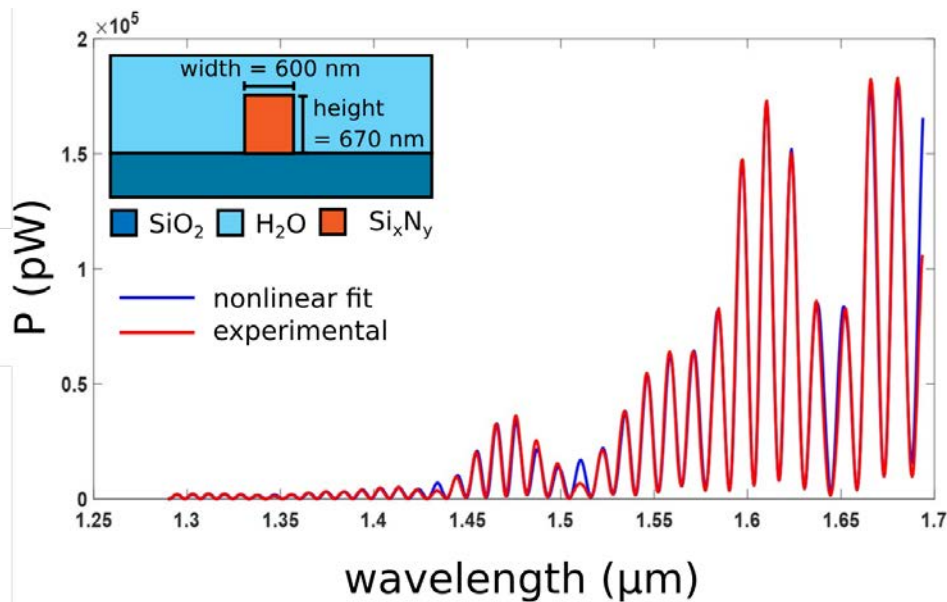


Figure 6.23 Mach-Zehnder interferometer - comparison between the experimental results (red curve) and the nonlinear fit (blue curve). The inset shows the cross section of the waveguide.

Table 6.4 shows the values of the coefficient of the fit for the  $n_{eff}$  after the mode solver simulation (P8\_600nmth) and after the fit with the experimental results (P8\_600nmexp). The

variation of  $\Delta L$  of  $1.5 \mu m$  is it compatible with the expectation on the fabrication tolerances. The experimental values of the coefficients differ by around 2% from the theoretical ones, confirming the simulation calculations and providing the order of magnitude of the error on the estimated  $n_{eff}$  caused by the roughness and fabrication tolerances.

Table 6.5 comparison of the coefficients of the fitting  $n_{eff}$  model found by theoretical simulation and the experimental values found with the nonlinear fit.

	<b>a1</b>	<b>a2</b>	<b>a3</b>	<b>a4</b>	<b><math>\Delta L</math></b>
<b>P8_600nmth</b>	<b>2,034062</b>	<b>-0,207522</b>	<b>-0,128849</b>	<b>0,049706</b>	<b>100</b>
<b>P8_600nmexp</b>	<b>2,031722</b>	<b>-0,207645</b>	<b>-0,1373</b>	<b>0,050496</b>	<b>98,54</b>

## 6.4 Conclusion

This chapter presented the characterization setup, the experimental results and their comparison with the simulations.

First, the characterization setup was described (e.g. PDMS pool, glucose as sensing fluid, butt coupling for light injection). Samples were characterized and the results indicated that the experimental sensitivity is lower than the simulations. The reasons were analyzed by physical characterizations such as AFM and ellipsometry: the Au used at first was deposited too fast (8 Å/s) with a Cr adhesion layer that was too thick (5 nm). Furthermore, the SiN waveguides were wider than the simulations. A comparison between the experimental geometry and the updated simulations showed similar trends, suggesting that to improve both sensitivity and losses Au must be deposited more slowly (0.7 Å/s) and the Cr layer thickness must be reduced (from 5 nm to 2 nm).

The second generation devices indicated that the plasmonic effect of HPWG (called “mode lift”) improved the sensitivity for waveguides of nominal width of 300 nm (from 210 nm/RIU to 320 nm/RIU when only 10% of the ring is a HPWG). This result were also compared to waveguides above cutoff (360nm, nominal 340nm), where the increase in sensitivity was 40nm/RIU, suggesting that the mode lift improves the performances even compared to guiding dielectric waveguides. The perspectives are to fabricate other devices with the same geometry to confirm the results. Afterwards, the percentage of the HPWG section of the ring will be increased to further enhance the sensitivity.

Adlayer functionalization is ongoing with BSA. The repeatability test are being performed. Differential functionalization essays were performed on test samples to verify the compatibility with thiols of the Au INL surface. The results show a good selectivity of thiols for Au against dielectric surfaces (SiN and SiO<sub>2</sub>). Future functionalization will be performed on the HPWG ring resonator with measurements on the integrated optic setup.

The last part of this chapter showed the results of the Mach-Zehnder interferometer used to determine the experimental refractive index of the waveguides. The comparison with the theoretical results showed a good agreement between the effective refractive indices, with an error below 2%.



## 6.5 Bibliography

- [1] S. Guerber, "Intégration d'un deuxième niveau de guidage photonique par dépôt de SiN au-dessus du SOI traditionnel," phdthesis, Université Paris-Saclay, 2019.
- [2] T. Tamir, Ed., *Integrated Optics*, 2 edition. Berlin ; New York: Springer-Verlag, 1979.
- [3] S. Ahn, P. S. Spuhler, M. Chiari, M. Cabodi, and M. Selim Ünlü, "Quantification of surface etching by common buffers and implications on the accuracy of label-free biological assays," *Biosensors and Bioelectronics*, vol. 36, no. 1, pp. 222–229, Jun. 2012, doi: 10.1016/j.bios.2012.04.020.
- [4] "UVISEL Spectroscopic Ellipsometer from VUV to NIR - HORIBA." <https://www.horiba.com/uk/scientific/products/ellipsometers/spectroscopic-ellipsometers/uvisel/uvisel-plus-640/> (accessed Mar. 15, 2020).
- [5] "ATR-L refractometer," *SCHMIDT+HAENSCH*. <https://schmidt-haensch.com/products/laboratory-instruments/refractometer/atr-l/> (accessed Mar. 15, 2020).
- [6] "OSA | Optical Constants of Water in the 200-nm to 200- $\mu$ m Wavelength Region." <https://www.osapublishing.org/ao/abstract.cfm?uri=ao-12-3-555> (accessed Feb. 02, 2020).
- [7] S. Kedenburg, M. Vieweg, T. Gissibl, and H. Giessen, "Linear refractive index and absorption measurements of nonlinear optical liquids in the visible and near-infrared spectral region," *Opt. Mater. Express, OME*, vol. 2, no. 11, pp. 1588–1611, Nov. 2012, doi: 10.1364/OME.2.001588.
- [8] P. A. Tipler and G. Mosca, *Physics for Scientists and Engineers*. W. H. Freeman, 2007.
- [9] I. ISO and B. OIML, "Guide to the Expression of Uncertainty in Measurement," *Geneva, Switzerland*, vol. 122, 1995.
- [10] S. A. Teukolsky, B. P. Flannery, W. H. Press, and W. T. Vetterling, "Numerical recipes in C," *SMR*, vol. 693, no. 1, pp. 59–70, 1992.
- [11] L. Gounaridis, P. Groumas, E. Schreuder, R. Heideman, H. Avramopoulos, and C. Kouloumentas, "New set of design rules for resonant refractive index sensors enabled by FFT based processing of the measurement data," *Optics Express*, vol. 24, no. 7, p. 7611, Apr. 2016, doi: 10.1364/OE.24.007611.
- [12] T. Claes, J. G. Molera, K. D. Vos, E. Schacht, R. Baets, and P. Bienstman, "Label-Free Biosensing With a Slot-Waveguide-Based Ring Resonator in Silicon on Insulator," *IEEE Photonics Journal*, vol. 1, no. 3, pp. 197–204, Sep. 2009, doi: 10.1109/JPHOT.2009.2031596.
- [13] I. M. White and X. Fan, "On the performance quantification of resonant refractive index sensors," *Optics Express*, vol. 16, no. 2, p. 1020, 2008, doi: 10.1364/OE.16.001020.
- [14] Seber, G. A. F., and C. J. Wild. "Nonlinear Regression New Jersey." (2003).

- [15] R. N. Bracewell and R. N. Bracewell, *The Fourier transform and its applications*, vol. 31999. McGraw-Hill New York, 1986.
- [16] P. B. Johnson and R. W. Christy, "Optical Constants of the Noble Metals," *Phys. Rev. B*, vol. 6, no. 12, pp. 4370–4379, Dec. 1972, doi: 10.1103/PhysRevB.6.4370.
- [17] "True Atomic Resolution by Atomic Force Microscopy Through Repulsive and Attractive Forces | Science." <https://science.sciencemag.org/content/260/5113/1451> (accessed Mar. 15, 2020).
- [18] F. Palazon *et al.*, "Orthogonal chemical functionalization of patterned gold on silica surfaces," *Beilstein Journal of Nanotechnology*, vol. 6, pp. 2272–2277, Dec. 2015, doi: 10.3762/bjnano.6.233.

# CHAPTER 7 - CONCLUSIONS AND PERSPECTIVES

## 7.1 Conclusion

This PhD project's goal was to design, build and test a photonic transducer compatible with Lab On Chip systems. The main goals we focused on were: sensitive biological transduction, compatible with industrial manufacturing in large volumes and at low cost, compact and versatile for different biological targets. In other words, the goal of this research was to answer the following research question:

“How to design and produce a compact biosensor based on a transducer in integrated photonics, simple to functionalize, compatible with an industrial platform and lab-on-chip, having a sensitivity equal or superior to the state of the art?”

To answer this question, the state of the art was analyzed and we found that the hybrid plasmonic waveguide (HPWG) was the most compatible with our objectives. Furthermore, based on a principle called “mode lift,” a new geometry of HPWG was patented and will be the subject of an article. The simulation of the HPWG structure allowed us to understand the coupling mechanisms of the modes inside the structure (more specifically the plasmonic and the ridge waveguide modes). The original contributions of this project can be summarized in two main points:

- Design and fabrication of a HPWG sensor, using industrial manufacturing in large volumes and at low cost (DAPHNE platform).
- The sensitivity of the sensor can be improved by increasing the coupling between the dielectric and plasmonic modes of the HPWG.

The design and fabrication process were made possible thanks to the collaboration between the STMICROELECTRONICS industrial cleanroom and the two university cleanrooms of the Institut des Nanotechnologies de Lyon and l'Université de Sherbrooke. The advantages of industrial manufacturing are the low-cost manufacturing per device and the high reproducibility of the devices: statistic measurements of the DAPHNE platform quantified the variations in the fabricated geometry, as shown in chapter 5. Once the wafers were patterned, the university cleanroom fabrication process was designed to add the metallic waveguides. Among the many propositions, two methods were explored: the lift-off method and the CMP method. While the CMP method gave a result closer to the simulation geometry, the lift-off method was easier to implement and it is the one that provided the devices characterized during this project.

Once the devices were fabricated, the characterization was possible: the preliminary measurements defined the optimal testing fluid and the uncertainty of the measures. The HPWG were characterized and it was found out that the experimental sensitivity is lower than the devices expected from the simulations. After adjusting the fabrication parameters (mainly Au and Cr deposition rates and thicknesses), the second-generation devices indicated that the plasmonic effect of HPWG (called “mode lift”) improved the sensitivity for dielectrics waveguides below cutoff (from 210 nm/RIU to 320 nm/RIU when only 10% of the ring has a

HPWG section). This result was also compared to purely dielectric ridge waveguides above the cutoff: the increase in sensitivity was 40 nm/RIU, suggesting that the mode lift improves the performance even compared to ridge waveguides above the cutoff. We also showed the compatibility of the fabricated devices with differential functionalization, by means of fluorescent nanoparticles.

## 7.2 Perspectives

### 7.2.1 Bulk measurements

The perspectives for the bulk measurements are to fabricate other devices with the same geometry and increase the percentage of the HPWG section of the ring from 10% to 30% to test the effect of the performance of the device.

### 7.2.2 Adlayer measurements

For the adlayer measurements the final geometry of the HPWG section will be optimized to hide the Au not involved with the coupling with the SiN waveguide, to make the differential functionalization more effective. On the one hand this would require other fabrication steps but on the other hand it would increase the probability of trapping analytes in the sensitive region. An example of the final cross section is shown in figure 7.1, where the top and external sides of the Au patches are covered with SiO<sub>2</sub>. This modification would increase the useful fraction of Au surface from 14% to approximately 98%.

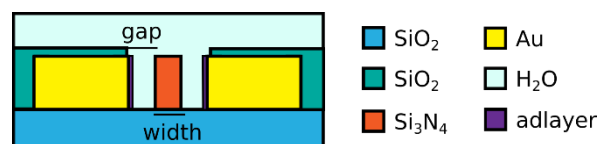


Figure 7.1 schematic of an improved plasmonic waveguide configuration for a more efficient functionalization

### 7.2.3 Integration—towards a Lab on Chip device

When thinking of the Lab on Chip applications, it is important to evaluate the perspectives of what should be added to the HPWG transducer to achieve a complete chip integration on the DAPHNE platform to replace the bulky optical setup. In particular the source and the detection mechanism should be integrated.

### 7.2.3.1 Photonic integration

The main challenges of photonic integration are the light source and detection. To simplify the discussion, we can divide the discussion into three configurations: a) source and detection not integrated, b) integrated detection and c) source and detection integrated, as shown in the diagram in Figure 7.2.

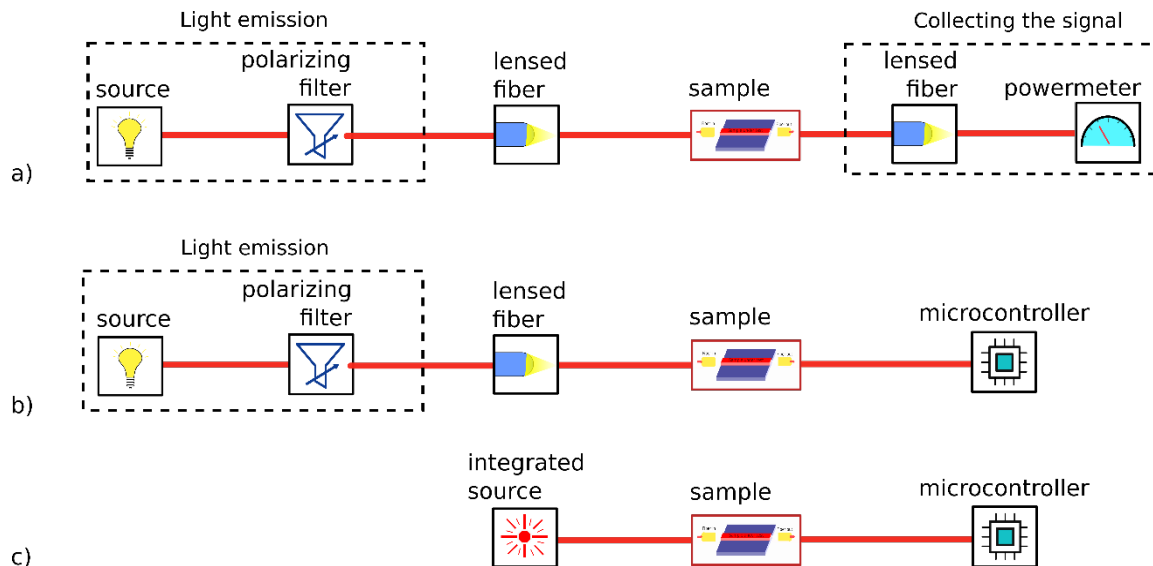


Figure 7.2 a) setup where neither the source nor the detection are integrated, b) setup where the detection is integrated, c) setup where both the source and the detection are integrated.

Before going into the details of the setups, we would like to recall that the choice of the type of analysis (if the signal is examined at a fixed wavelength or multiple wavelengths) strongly influences the choice of the source. If we have a fixed wavelength, we need only one narrow laser and therefore only one photodetector at the output. The price to pay for a simple detection is the stability of the measurement: the resonance peak can vary for a parasitic effect (e.g. a temperature variation) and the signal could easily saturate or change sensitivity. On the other hand, a system with several wavelengths is undoubtedly more complex because it requires the excitation of several wavelengths (which can be obtained by the use of several lasers in parallel, by a tunable laser or by a broad source e.g. supercontinuum generation) and an integrated spectrometer. In this study we consider that the detection is performed at multiple wavelengths because it is the most reliable method.

Considering the first setup of figure 7.2.a, the non-integrated sources have three disadvantages: size, price and the coupling to the photonic chip. Compact sources on the market are a 10<sup>th</sup> of centimeter size and extremely expensive (thousands of euros). External spectrometers are of the same order of size and price. Even if the prices and dimensions were accessible, there would still be the problem of coupling with the photonic chip with the transducer. We could imagine that the source and detection are not disposable but the photonic chip is. This implies that the alignment must be extremely simple, repeatable and effective. One option is the V groove: the fiber is kept in place by a V-shaped trench. In addition, to facilitate coupling, reverse tapers could be used [1]. Another technique is that of coupling in a relatively wide guide in polymer for then coupling it in the bus guide of the ring

resonator [2]. Probably the best option would be to change the coupling method to grating couplers, which require a less critical alignment precision. However this would imply only the use of one polarization: this could be a problem in case a double detection with both TE and TM polarizations is needed for example to detect both thickness and refractive index of a adlayer.

If we consider the circuit in figure 7.2.b, the detection is integrated. Detection can be done using integrated photodetectors, compatible with the DAPHNE platform. In the case of detection with multiple wavelengths, a fairly simple solution is the use of an AWG. There are several types: AWG 256 channels (0.2 nm spacing), AWG 16 channels (1 nm spacing) 1–2 cm<sup>2</sup> area (photon design website, 2018). They are relatively bulky but completely integrated into a chip. Another option is to use spectrometers based on a disordered photonic chip. The spectral resolution is 0.75 nm at a wavelength of 1500 nm in a radius structure of 25 μm [3]. For these two methods, the choice between the best resolution or the smallest footprint depends on the application.

For all the integrated configuration of figure 7.2.c, it is necessary to integrate the lasers. A semi-integrated technique allows injection into a chip manufactured by the DAPHNE platform: it is a coupling between a 250 μm Reflective Semiconductor Optical Amplifier (RSOA) and Bragg gratings [4].

Another type of integrated lasers are based on integrated micro-disk resonators. An example of these laser was fabricated with the INL cleanroom in 2008 [5]. In this configuration, the laser could be integrated directly onto a chip. The problem is compatibility with the DAPHNE platform, which for now does not include InP.

### 7.2.3.1 Fluidic integration

For now the microfluidic part is made in PDMS. Studies have shown that the photoresist KMPR can be used as well and promotes a more efficient functionalization since it can be passivated [5]. The structure of the fluidic system depends as well on the final application. For now, two options were considered: a reservoir and microfluidic channels. The advantages of microfluidic channels are a small volume of target analyte required, higher interaction with biological species and compatible with other microfluidic systems (e.g. for cell separation). However, they require a microfluidic circuit and a pumping system (external pump or syringe). The concept of the reservoir is simpler but requires a high volume and the interaction with the biological material is less important. The final decision strongly depends on the application.

## 7.3 Bibliography

- [1] R. Marchetti, C. Lacava, L. Carroll, K. Gradkowski, and P. Minzioni, “Coupling strategies for silicon photonics integrated chips [Invited],” *Photon. Res.*, vol. 7, no. 2, p. 201, Feb. 2019, doi: 10.1364/PRJ.7.000201.
- [2] G. Beaudin, E. Grondin, A. Belarouci, P. G. Charette, and V. Aimez, “Evanescent Field Coupler Optimized for High Refractive Index Differences (ECHRID)—A Platform for a SOI Photonics Optical Interface,” *IEEE Journal of Selected Topics in Quantum Electronics*, vol. 22, no. 6, pp. 434–442, Nov. 2016, doi: 10.1109/JSTQE.2016.2553451.
- [3] Xiao Ma, Mingyu Li, and Jian-Jun He, “CMOS-Compatible Integrated Spectrometer Based on Echelle Diffraction Grating and MSM Photodetector Array,” *IEEE Photonics Journal*, vol. 5, no. 2, pp. 6600807–6600807, Apr. 2013, doi: 10.1109/JPHOT.2013.2250944.
- [4] S. Iadanza *et al.*, “Thermally stable hybrid cavity laser based on silicon nitride gratings,” *Applied Optics*, vol. 57, no. 22, p. E218, Aug. 2018, doi: 10.1364/AO.57.00E218.
- [5] J. Van Campenhout *et al.*, “A Compact SOI-Integrated Multiwavelength Laser Source Based on Cascaded InP Microdisks,” *IEEE Photonics Technology Letters*, vol. 20, no. 16, pp. 1345–1347, Aug. 2008, doi: 10.1109/LPT.2008.926857.

# ANNEX A - CMP METHOD

In this annex, the CMP method is shown as a compatible method with the industrial environment to build HPWG.

The main goal of this method is to pattern thick gold (600 nm), hard to do with the lift off method. Figure A.1 shows the final process flow of this method.

## Electron beam lithography

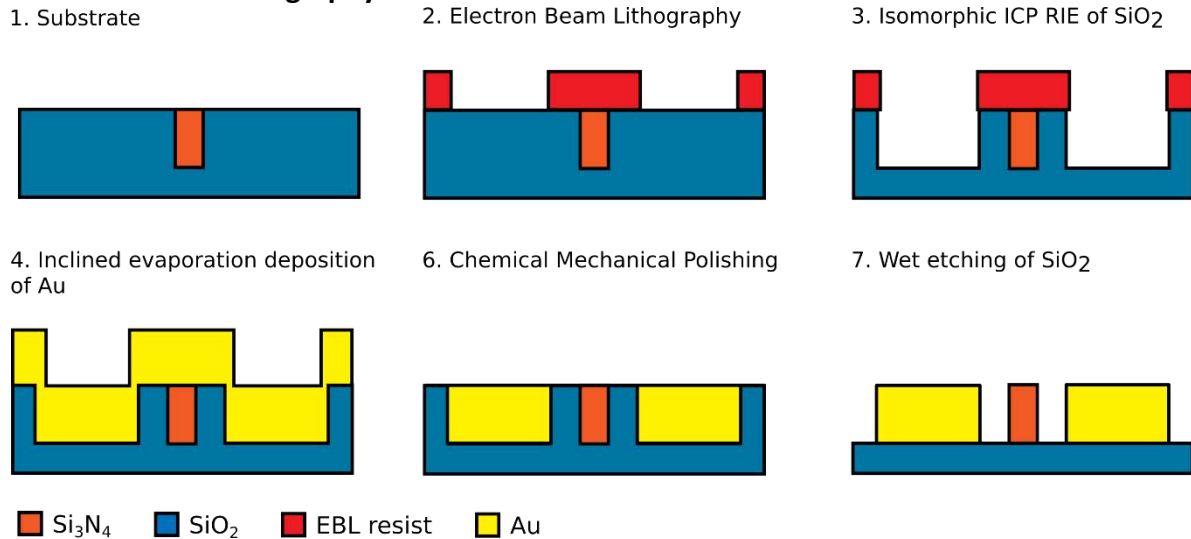


Figure A.1 Process flow of the CMP method.

The electron beam lithography step is similar to the one of the lift off method: thanks to the alignment marks, the resist is patterned to remove resist where the Au patches will be positioned. The process flow for electron beam lithography is the following:

1. MCC Primer (5000 rpm, 30 s)
2. Spin-coating of ZEP520A (5000 rpm, 60 sec)
3. Bake (180 C°, 5 min)
4. Electron beam lithography, dose (36  $\mu\text{C}/\text{cm}^2$ )
5. Development (2.5 min in Oxylene)
6. Rinsing (30 s in MIBK, 1 min in H<sub>2</sub>O)

The main difference with the lift off method is the resist (ZEP520A) of 450 nm thickness.

## Inductively Coupled Plasma - Reactive Ion Etching of SiO<sub>2</sub>

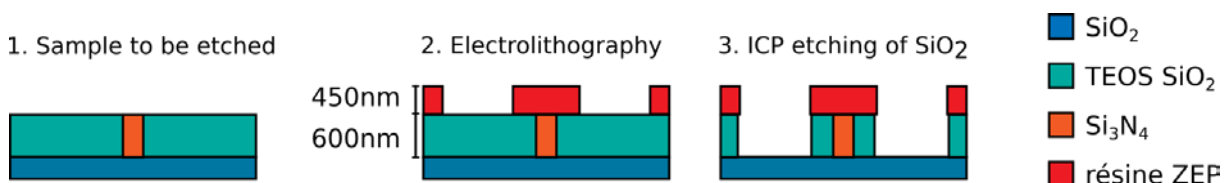


Figure A.2 schematic of the ICP etching

After that, an Inductively Coupled Plasma (or ICP) etching is performed to etch at least 600nm of SiO<sub>2</sub>. The selectivity between the SiO<sub>2</sub> and the ZEP520A resist should be at least 1.7 to leave 100nm of ZEP520A resist in case of process fluctuations.



The first etching recipe, called Si3N4\_T because originally used to etch Si3N4, had the following parameters:

Table A.1 Parameters of the ICP etching recipe Si3N4\_T

Parameter	Value
He (sccm)	140
CF4 (sccm)	10
H2 (sccm)	25
RFlload (W)	1000
RFbias (W)	300

We observed after etching is that the selectivity between the resist ZEP520A and the SiO2 was too low (around 1.2) etching all the resist and part of the surface underneath it. Moreover, the etching process drastically increases the roughness of the resist. The roughness is transferred to the substrate and the results are shown in Figure A.3.a and A.3.b, two pictures of the SiN samples after Si3N4\_T recipe for 2min50sec.

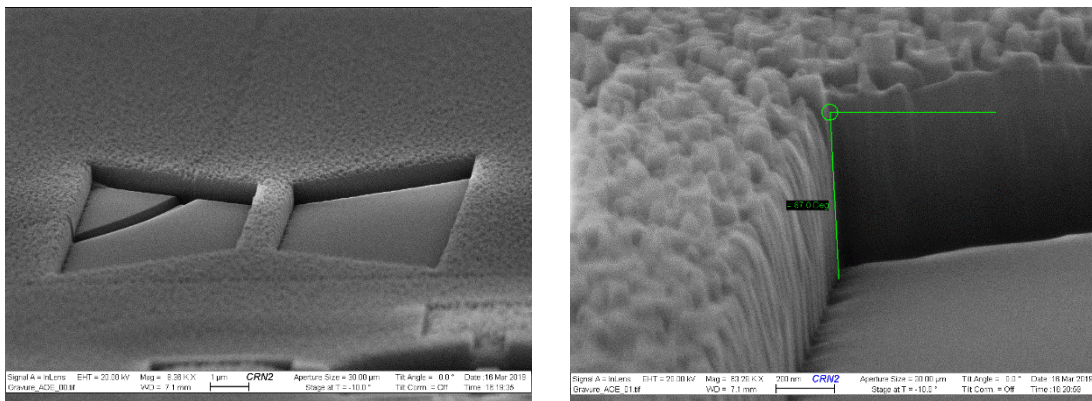


Figure A.3.a side view of the etched patch. We can notice that there is no more resist present that the roughness is rather high. A.3.b Side view of the etched patch

Due to the high roughness of the surface, the losses of the waveguides would skyrocket because of light diffusion. We then need to increase the selectivity of the etching process.

One of the options we considered was to increase the temperature to 60°C. It is shown in literature that an increase in temperature increase the selectivity [1]. Furthermore, due to a shortage of ZEP resist, test about the selectivity were done also with another resist called CSAR. These new resist will be the one used for future devices with the CMP method. The results of the selectivity at 60° increased to 1.7. However, the roughness of the resist still influenced the sidewalls of the etched SiO2.

We realized that increasing the temperature the selectivity of the Si3N4 recipe improved, but it also increased the roughness of the resist and therefore the roughness of the SiO2 sidewalls. We are currently testing working at -20°C to improve the roughness while changing the etching recipe (gas composition and power) to have a higher selectivity (currently 1.2).

## Au inclined evaporation

A planetary rotation evaporation allows depositing the Au isotopically to have thick vertical walls. The sample is inclined with an angle  $\phi$  with respect to the source and it turns along the axis perpendicular to the sample holder, as shown in figure A.4.a. The deposition was performed at different angles with a nominal deposition thickness of 400nm. We compare the thickness of the Au layer against the sidewalls: for  $\theta = 20^\circ$  the Au walls were 20 nm thick,  $\theta = 30^\circ$  and  $\theta = 45^\circ$  both showed a thickness of around  $70 \text{ nm} \pm 10 \text{ nm}$ . A cross section of the three angle deposition is shown in figure A.4.b, A.4.c and A.4.d. To have a continuous layer of Au, the deposition was performed at  $45^\circ$ .

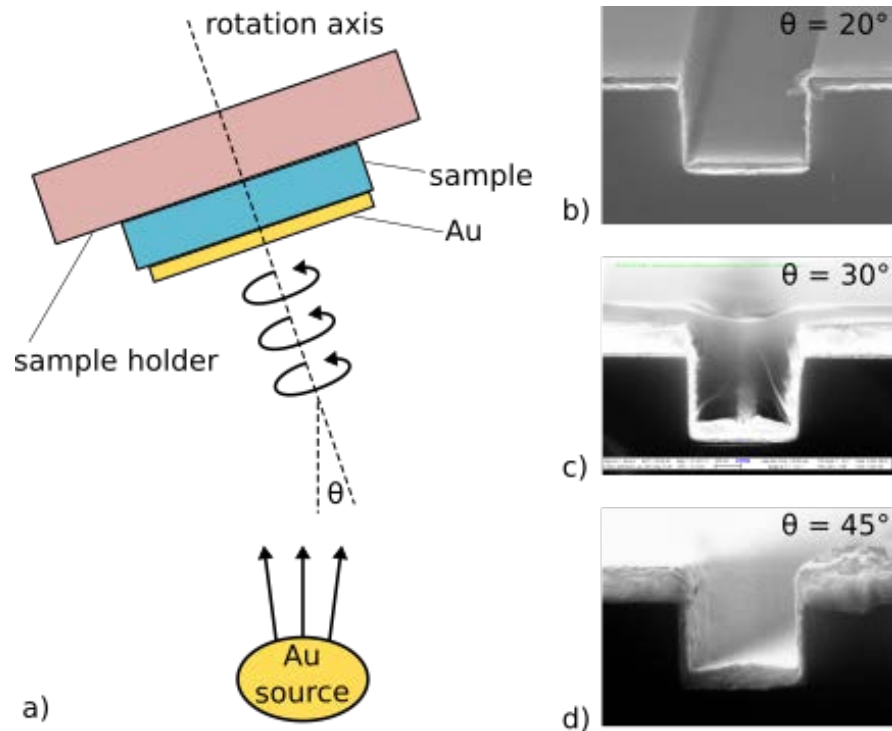


Figure A.4.a schematics of the deposition process. A.4.b-d SEM cross-sections of depositions at different angles ( $\theta = 20^\circ$ ,  $\theta = 30^\circ$  and  $\theta = 45^\circ$ ).

## Chemical Mechanical Polishing

After the Au deposition, the CMP was performed to remove the Au external to the  $\text{SiO}_2$  holes.

Figure A.5 shows the results of the complete device and a zoom of the Au patches. The SEM images are colored with a semi-transparent color to distinguish the different materials: the yellow represents the Au and the orange the SiN waveguide. It can be noticed that the alignment is working well (alignment error of 10nm) thanks to the thin resist (compared to the more complicated alignment of the lift-off method).

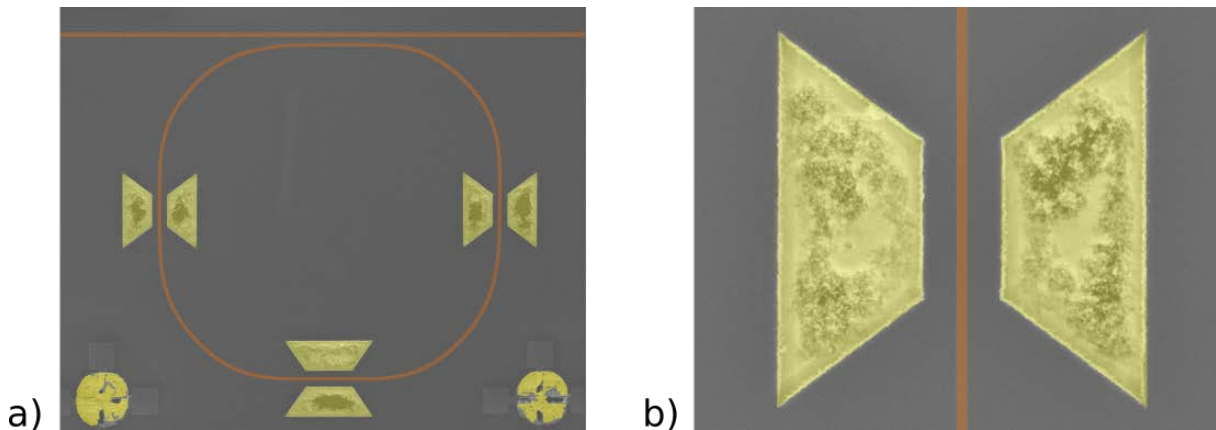


Figure A.5 Result of the CMP of one ring resonator and one Au patch. The pictures were colored to underline the different materials. The yellow is the Au and the orange is the SiN while the rest is SiO<sub>2</sub>.

### SiO<sub>2</sub> wet etching

To finish the process, the SiO<sub>2</sub> was etched using Buffered oxide etch (BOE). BOE is a mix of hydrofluoric acid (HF) and a buffering acid. In this case, the dilution was 6:1. In order to calculate the etching rate of SiO<sub>2</sub> TEOS, test samples were submerged in BOE for different

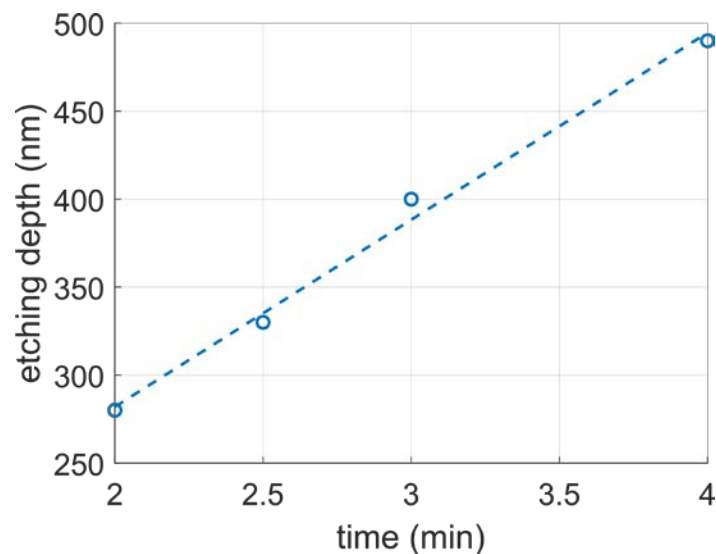


Figure A.6 etching rate. Each point is an average of three SEM measures. The calculated etching time is 110 nm/min

time. Figure A.6 shows the results of the experiment and the trend suggesting an etching time of 110nm/min.

## Conclusion

These tests show that the CMP method is a real alternative to the lift-off method. Furthermore, in order to be completely compatible with the DAPHNE environment, the electrolithography step should be replaced with the STMicroelectronics deep UV lithography, with a resolution of 180nm. These steps were performed in Sherbrooke's cleanroom and show the basic results for a complete optimization of the process.

## Bibliography

[1] M. Guilmain, A. Jaouad, S. Ecoffey, and D. Drouin, "SiO<sub>2</sub> shallow nanostructures ICP etching using ZEP electroresist," *Microelectronic engineering*, vol. 88, no. 8, pp. 2505–2508, 2011.

# ANNEX B – Higher order mode sensors

Besides hybrid plasmonic waveguides, a new type of sensor was tested with the DAPHE platform: the *higher order mode* ring resonators.

The higher order mode sensing approach consists in selectively exciting a mode other than the fundamental mode of the ring resonator waveguide, typically the second mode (called the first order mode as opposed to the fundamental). An example of waveguide cross section is shown in figure B.1.b, where the higher order mode is designed to be close to its cutoff. Thanks to their greater exposure to the sensing fluid compared to the fundamental mode, the higher order modes are more sensitive. Furthermore, the waveguide is multimode, thus wider than a monomode one (1  $\mu\text{m}$  and 0.5  $\mu\text{m}$ , respectively). This greater width reduces the constraints on fabrication especially concerning the lithography resolution.

The proof of concept shown in this annexe, the first order mode is selectively excited by using a monomode bus waveguide with a fundamental mode having the same effective refractive index. The monomode and the multimode waveguides couple generating even and odd modes.

The photonic devices are simulated using the same custom design mode solver used for HPWG modes. Once the modes of the waveguides and their effective refractive index are found, the ring resonators operating parameters are calculated using analytical expressions. The modes of both monomode and multimode waveguides are shown in figures B.1.a and B.1.b. The first order mode has two power maxima and the proportion of mode power in the sensing liquid is more important compared to the fundamental mode. This shows that the first order mode is more sensitive with respect to the fundamental.

However, simply increasing the width of a waveguide brings up another problem: the first order mode has to be selectively excited because the fundamental is guided as well. The system avoids excitation of the fundamental mode through asymmetrical directional couplers: the bus waveguide is single mode and the ring waveguide is multimode, where the first order

mode has the same effective index as the fundamental mode in the bus waveguide. Figure B.1.c shows how the electric field of the two waveguides is influenced by the presence of the other one. Like with HPWG, a racetrack ring resonator is used to change the phase shift caused by refractive index change in the fluid medium into an intensity change at the output of the bus waveguide. Critical coupling conditions are achieved by choosing the distance between the waveguides. The sensitivity calculated from the simulation is 250 nm/RIU.

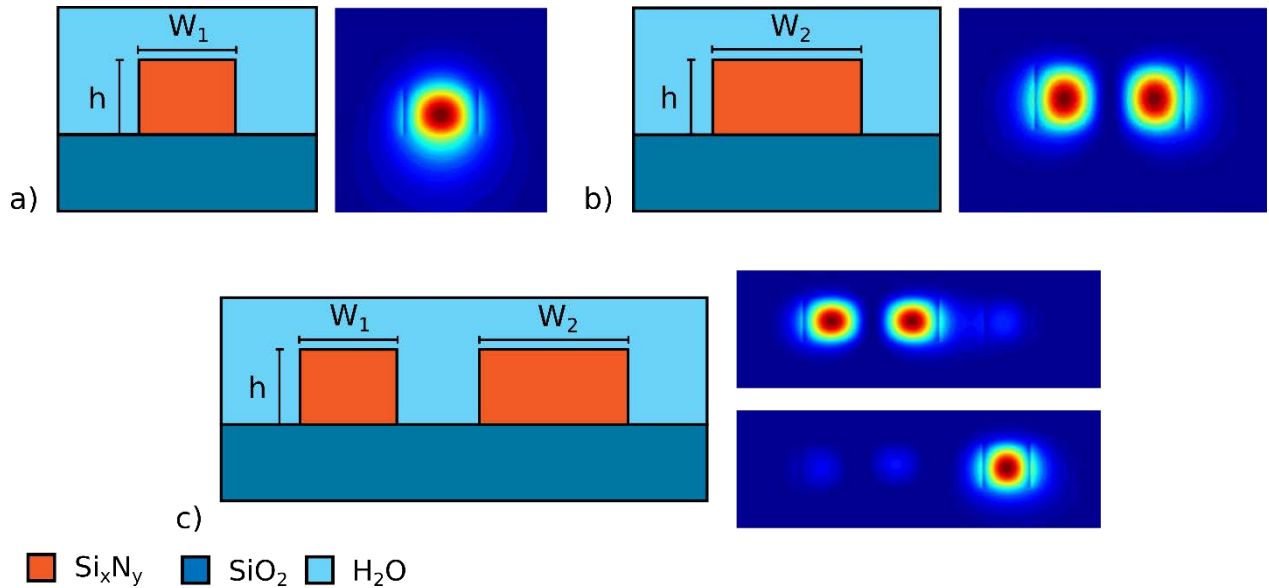


Figure B.1.a single mode bus waveguide and mode profile. 1.b two-mode waveguide where the first order mode profile is shown (effective index is 1.45, close to the cutoff). 1.c shows the two waveguides close to each other and the coupling between the two modes.

The fabrication is performed on the Datacom Advanced PHotonic Nanoscale Environment or DAPHNE platform, an industrial 300 mm SOI platform. Figure B.2 shows the fabricated devices and the inset shows the coupling region of the ring resonator.

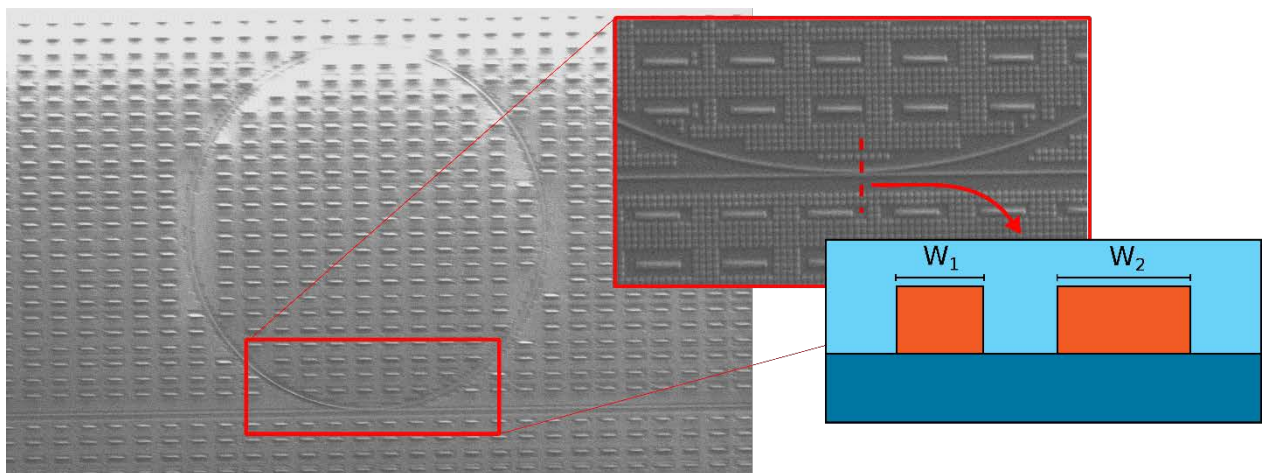


Figure B.2 Scanning electron microscope image of the higher order mode ring resonator. A zoom on the coupling section is shown as well as the schematic showing the cross section.

Once the sensors were manufactured at STMicroelectronics, a polydimethylsiloxane (PDMS) reservoir was glued to the device surface to contain the fluids used during measurements. Glucose monohydrate was used in different concentrations to estimate the sensitivity (from 0 to 6g/100mL).

The experimental results are compared to a conventional dielectric waveguide ring resonator, built with the same DAPHNE platform with a rib waveguide. The reference ring has a sensitivity of 120 nm/RIU around 1.30  $\mu\text{m}$ .

The transmission spectra of the higher order mode ring resonator are shown in figure B.3.a. The quality factor is higher than in the case of HPWG (around 4000) because there is no absorbing metal. The sensitivity of the sensor was found to be around 212 nm/RIU. This value is slightly lower than the simulation because of fabrication tolerances.

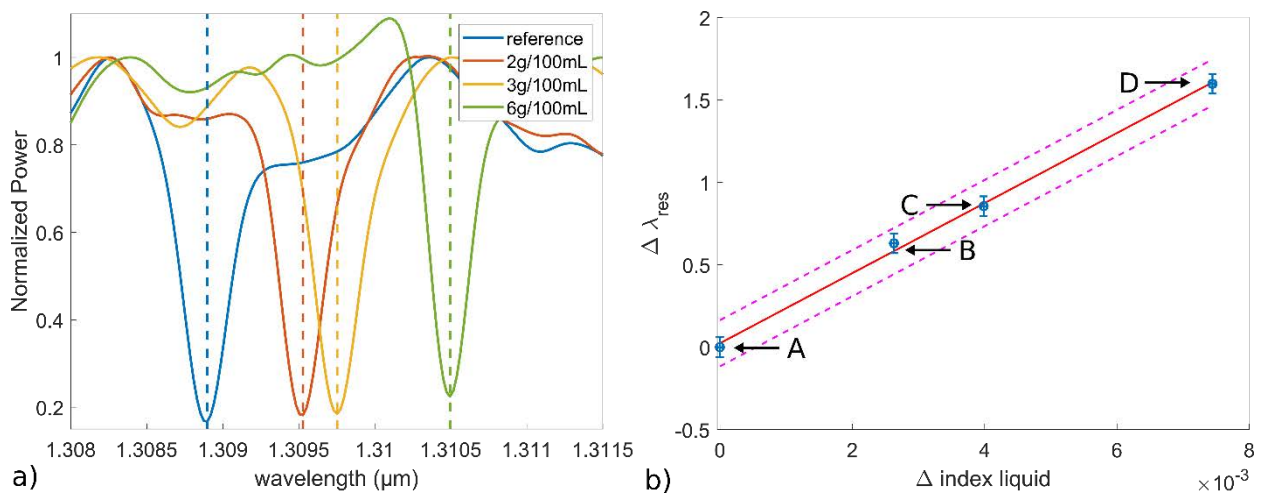


Figure B.3.a transmissions spectra for the higher order mode device for different glucose monohydrate dilutions in H<sub>2</sub>O. 3.b Calibration curve to calculate the sensitivity as the slope of the linear fit: “A” represent the reference measurement in water, “B”: 2g/100mL, “C”: 3g/100mL and “D”: 6g/100mL. Sensitivity is of 212 nm/RIU.

In conclusion, another approach to improve the sensitivity of a silicon nitride waveguide ring resonator sensor is shown. Compatible with an industrial fabrication platform, higher order modes ring resonators show a higher sensitivity compared to a conventional dielectric waveguide ring resonator sensor (210nm/RIU for the higher order modes compared to the 120 nm/RIU of the rib waveguide).

The perspectives for this device is to test the response to an adlayer of proteins in order to evaluate the surface sensitivity. Differential functionalization will not be tested for this structure because, to our knowledge, the surfaces of SiN and SiO<sub>2</sub> are very similar and they functionalize with the same molecules.



# RÉSUMÉ LONG EN FRANÇAIS

## Introduction

L'identification ou la détection de molécules biologiques spécifiques dans un appareil portable et réutilisable présente un intérêt majeur dans différents domaines comme la santé publique, le contrôle de qualité alimentaire, de la nutrition animale, la défense militaire. Un tel système, capable de fournir un diagnostic rapide, est normalement hétérogène, car il intègre plusieurs technologies différentes, par exemple l'électronique, la photonique, la microfluidique et la biologie.

Tel que schématisé dans la figure R1.1, les deux principales fonctions qu'il faut maîtriser pour la réalisation d'un biocapteur sont : le « test biochimique » et la « transduction ». Le test biochimique est une procédure de biochimie analytique (réactifs, cinétique, etc.) qui permet de détecter/quantifier la présence d'une cible d'intérêt (analyte), idéalement avec une grande sélectivité relativement aux autres espèces en présence. Dans les biocapteurs photoniques, elle consiste à préparer sa surface par une étape dite de fonctionnalisation et de mise en forme de l'échantillon à analyser. Dans le cas d'un système réutilisable, elle inclue également les étapes de nettoyages du capteur qui ne doivent pas entraîner de dérive de la mesure. Le transducteur permet de convertir la résultante de la réaction biochimique en un signal mesurable électriquement.

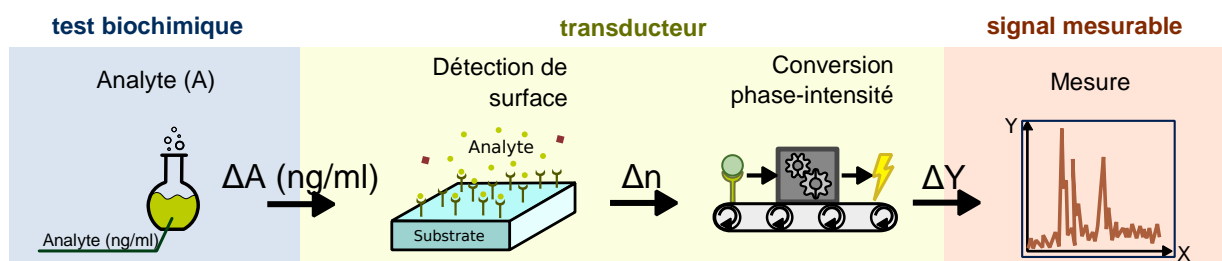


Figure R1.1 Schéma du fonctionnement d'un biocapteur : deux composantes principales (le test biochimique et le transducteur) qui donnent comme résultat un signal mesurable.

Dans le cas d'une détection surfacique, le processus de détection commence avec l'exposition de l'analyte en solution aux récepteurs de la surface du biocapteur. Du point de vue de la photonique intégrée, soit d'un guide d'onde fabriqué par un empilement de couches minces d'indices de réfraction optique distincts, l'attachement d'analytes aux récepteurs en surface est équivalente au dépôt d'une couche mince d'un nouveau matériau auquel on peut associer une constante diélectrique. La lumière transitant dans le guide d'onde verra en conséquence sa phase modifiée, laquelle pourra ensuite être mesurée par un interféromètre ou un résonateur par exemple. Le dispositif interférométrique transforme la variation de phase optique en une variation d'intensité du signal lumineux mesurable par une photodiode. La figure R1.2 schématise le fonctionnement de la détection surfacique par



un résonateur en anneau : solution retenue dans cette étude aux vues de sa compacité et de sa sensibilité vis-à-vis des autres interféromètres optiques.

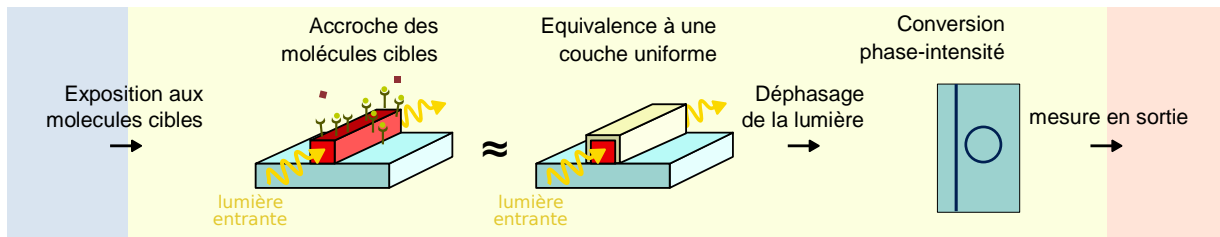


Figure R1.2 Schéma du fonctionnement de la détection de surface.

L'objectif de ce doctorat est de démontrer la faisabilité d'un système intégrée sur puce possédant toutes les briques de bases nécessaires à la détection de l'espèce chimique ou biologique spécifique (circuit fluidique, circuit photonique de routage de l'information optique, source de lumière et photodiode pour la conversion optique/électrique) dans une technologie compatible CMOS favorisant une fabrication industrielle en large volume et à faible coût. Ce travail est le fruit d'une collaboration entre ST Microelectronics, leader européen de la fabrication de composants pour les datacoms en photonique sur silicium avec sa central de fabrication 300 mm DAPHNE (Datacom Advanced PHotonic Nanoscale Environment), l'Institut des Nanotechnologies de Lyon (INL) et l'université de Sherbrooke au travers du LN2 (université mixte internationale Nanotechnologies et Nanosystèmes) qui toute les deux ont une expertise en photonique et en intégration de nouveaux procédés pour la preuve de concept. Un grand nombre de briques de base tel que les photo-détecteurs et les sources de lumière sont disponible sur la plateforme DAPHNE et ne seront pas étudiées dans ce travail de thèse. Il se focalisera sur l'intégration de nouveaux capteurs bio-photoniques sur des guides d'onde en nitrure sur silicium et de circuits fluidiques, éléments non disponibles sur la plateforme DAPHNE.

La première partie de ce manuscrit est consacré à une étude bibliographique des différents capteurs bio-photoniques réalisés en optique intégrée et de leurs performances. Cette étude a permis d'isoler une ligne directrice qui se résume en une phrase : L'augmentation de la sensibilité d'un détecteur en optique guidée nécessite une maximisation de l'interaction lumière matière à l'extérieur du cœur du guide d'onde si on veut améliorer ses performances vis-à-vis de l'état de l'art. Cette maximisation n'est possible que dans des structures guidantes dites « creuses » telles que des guides à fente appelés « SLOT » ou des guides métalliques dans lesquels se propagent une onde de surface appelé « plasmon » ou des modes guidés proche de la condition de coupure.

Les principes physiques et la conception théorique des solutions innovantes envisagées dans ce travail de thèse que sont les guides d'onde diélectrique-métal (Hybrid Plasmonic Waveguide ou HPWG) seront détaillés dans les chapitres suivants. Leurs réalisations et caractérisations optique en milieu liquide fera l'objet du dernier chapitre.

# Etat de l'art

Un biocapteur en photonique intégrée permet de mesurer un changement d'une grandeur expérimentale d'intérêt (par exemple la concentration surfacique d'une espèce biomoléculaire) par la modification de l'épaisseur ou de l'indice de réfraction du milieu adjacent au coeur du guide d'onde. Ces modifications sont mesurable uniquement si un dispositif complet comme un interféromètre ou un résonateur est réalisé à partir d'un assemblage de guides d'onde. La revue de l'état de l'art est séparée en deux parties : (1) les différents types de guides d'onde et (2) les dispositifs complets.

Avant de rentrer dans les détails de l'état de l'art, il est nécessaire de définir les paramètres considérés pour l'évaluation comparative des différents dispositifs existants.

**Sensibilité volumique (bulk sensitivity)** : pour un biocapteur à base de résonateur, elle est généralement définie comme le décalage de la longueur d'onde de résonance ( $\delta\lambda_0$ ) en fonction du changement d'indice de réfraction du milieu ( $\delta n_{\text{bulk}}$ ), soit ( $\delta\lambda_0/\delta n_{\text{bulk}}$ ) en nm/RIU<sup>10</sup>. Dans le cas d'une détection sur une surface bio-fonctionnalisée, il est plus pertinent de parler de sensibilité surfacique, définie généralement comme le décalage de la longueur d'onde de résonance ( $\delta\lambda_0$ ) en fonction du changement d'épaisseur de la couche,  $\delta a$  ( $\delta\lambda_0/\delta a$  en nm/nm) ou du changement de densité surfacique de l'espèce détectée,  $\delta\rho$  ( $\delta\lambda_0/\delta\rho$  en nm).

**Limite inférieure de détection (Limit Of Detection, LOD)** : C'est la plus petite quantité d'espèce cible détectable selon certaines conditions expérimentales spécifiques (par exemple l'intervalle temporel de mesure). Son unité de mesure change selon l'analyte et la méthode de détection (il peut être en RIU pour les mesures de liquides d'indice de réfraction ou en g/L pour les mesures avec fonctionnalisation de surface).

**Compatibilité avec le milieu industriel** : les matériaux et les techniques de fabrication doivent être compatibles avec les plateformes existantes. Dans le cadre de ce projet, la plateforme DAPHNE (Datacom Advanced PHotonic Nanoscale Environment) de STMicroelectronics est prise comme référence.

**Fonctionnalisation de surface** : Elle représente la facilité, robustesse, spécificité surfacique/chimique de la chimie d'accroche de surface de l'espèce à détecter.

**Dimensions du dispositif** : On souhaite avoir une puce intégrée où plusieurs fonctionnalisations peuvent être testées la fois.

---

<sup>10</sup> Refractive Index Unit, unité de l'indice de réfraction, adimensionnelle

## Guides d'onde

Dans cette partie, les principaux types de guides d'onde utilisés pour la fabrication de biocapteurs en photonique intégrée sont détaillés.

### Guide d'onde ruban (ridge waveguide)

L'exemple le plus simple de guide d'onde en optique intégrée est le guide d'onde ruban, constitué de deux matériaux ou plus : un premier avec un indice de réfraction plus élevé, le cœur (core) du guide, et un deuxième (ou plus) avec un/des indice(s) de réfraction plus faible(s), la/les gaines (cladding). La figure R1.3.a est un schéma d'un guide d'onde ruban avec un cœur en nitrure de silicium ( $Si_xN_y$  : indice de réfraction de  $n = 1.9$  à  $\lambda = 1.31\mu m$ ) et des gaines en dioxyde de silicium ( $SiO_2$  :  $n = 1.44$  à  $\lambda = 1.31\mu m$ ) et d'eau ( $H_2O$  :  $n = 1.32$  à  $\lambda = 1.31\mu m$ ).

L'onde électromagnétique se propage dans le guide d'onde selon des distributions de champ bien définies qu'on appelle des modes guidés. Chaque mode guidé est caractérisé par un indice effectif donné par le rapport entre la vitesse de phase du mode et celle du vide. Le nombre de modes guidés dans un guide dépend de la géométrie du cœur et des indices de réfraction des matériaux. Dans le cas d'un guide d'onde asymétrique, en dessous de certaines dimensions critiques de cœur il n'y aura aucun mode guidé, le guide est dit sous la coupure (cutoff). Selon la composante principale du champ magnétique et électrique d'un mode dans le plan normal au sens de la propagation, celui-ci est caractérisé par sa polarisation transverse magnétique (TM) ou transverse électrique (TE). La figure R1.3.b montre un graphique des indices effectifs des modes guidés pour les 2 polarisations. Dans le cas d'un guide d'onde où tous les matériaux sont des diélectriques, soit un guide d'onde diélectrique, la plus grande proportion de l'énergie lumineuse est normalement localisée dans le cœur, à moins que le mode ne soit très près de la coupure. Le champ dans la gaine s'appelle champ évanescent et décroît exponentiellement en amplitude en fonction de la distance.

Dans le cas d'un capteur en photonique intégrée, le milieu fluide sondé (liquide ou gaz) est typiquement en contact avec le cœur du guide et fait donc office de gaine. Un changement d'indice de réfraction dans le milieu fluide occasionné par un changement de sa composition chimique modifiera les propriétés du guide d'onde et de ses modes guidés

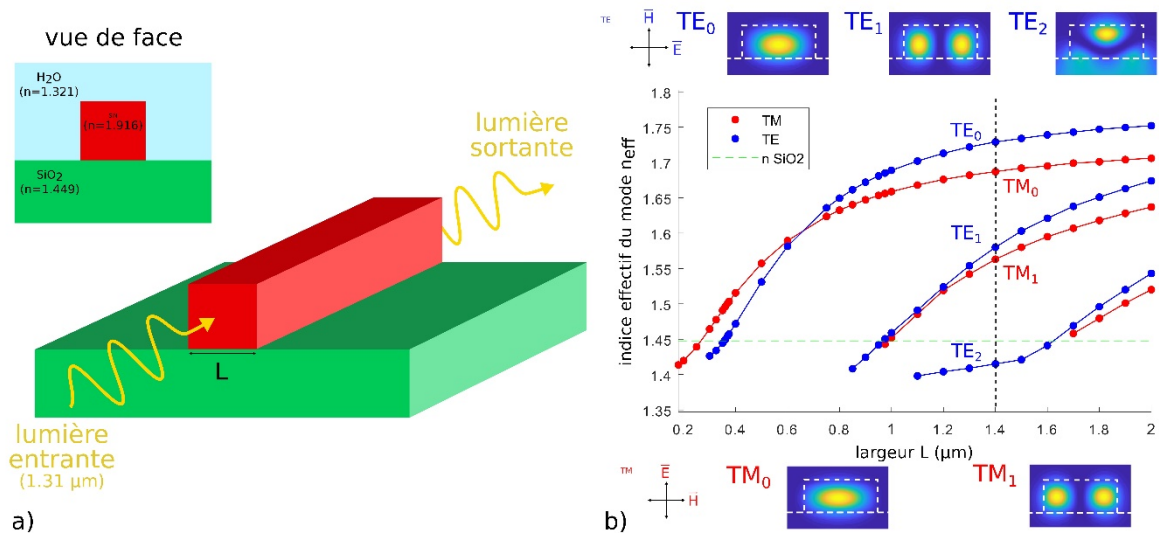


Figure R1.3 a) Schéma d'un guide d'onde avec un cœur de  $Si_3N_4$  et une gaine composée en partie par du  $SiO_2$  et de l' $H_2O$ . b) Distribution des modes et leur cartographie de champ : les modes A, B, D et E sont des modes guidés, par opposition à C qui est un mode radiatif car son indice effectif est inférieur celui du  $SiO_2$ , représenté par une ligne horizontale verte sur la figure.

Les capteurs en photonique intégrée révèlent donc les changements dans le milieu fluide par des changements dans les propriétés des modes guidés au niveau de leurs indices effectifs. Plus la portion d'énergie lumineuse totale dans le milieu fluide sondé est grande, plus le capteur sera sensible.

## Guides d'onde fente (slot waveguide)

Les guides fente sont des guides ruban qui ont la particularité d'avoir une portion de matériau faible indice au milieu du cœur. Dans le cas d'un capteur, ceci permet de rendre les zones de fort champ électrique accessibles au milieu fluide sondé. Découverts en 2004 à l'Université de Cornell [4], les guides d'onde fente ont eu un certain succès dans le domaine de la bio-détection [9]. Le principe physique derrière ce concept est la discontinuité de la composante normale du champ électrique à une interface entre 2 matériaux. Si on approche suffisamment 2 interfaces, les discontinuités vont créer un mode guidé avec un maximum de champ dans la fente.

Les Figure R1.4.a et Figure R1.4.b montrent la géométrie et la distribution de champ des guides fente.

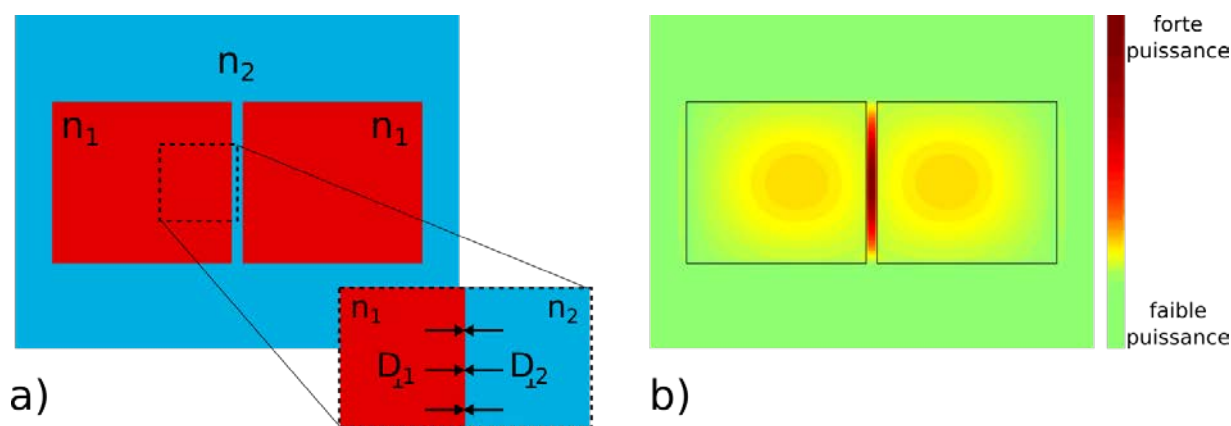


Figure R1.4 : a) Schéma d'un guide fente avec un matériau d'indices de réfraction  $n_1 > n_2$ . L'agrandissement montre la direction de l'induction électrique normale la surface. b) Distribution de la puissance lumineuse dans un guide fente. L'intensité maximale du champ est localisée dans la fente de faible indice de réfraction qui pourrait être, par exemple, le milieu liquide de détection.

Étant donné que l'énergie se situe majoritairement dans le matériau de faible indice de réfraction au centre du cœur, un changement d'indice de réfraction y entrainera un changement d'indice effectif plus important que dans le cas d'un guide d'onde ruban. L'avantage des capteurs à guides d'onde à fente par rapport aux guides ruban est donc leur plus grande sensibilité.

Cependant, il est important de noter ici que la fente est généralement de très petite dimension. L'effet de localisation du mode guidé dans la fente est limité à de faibles largeurs inférieures à 100 nm (environ 40 nm pour un guide d'onde où le matériau fort indice de réfraction est du  $Si_xN_y$  et celui faible est de l' $H_2O$ ,  $1.31\mu m$  [24]). Ceci amène la fois un problème d'accès pour les molécules et un défi de fabrication.

## Guides purement plasmoniques

Plusieurs biocapteurs sont conçus avec des guides d'onde plasmons-polaritons de surface (surface plasmon polariton ou SPP), ou plus simplement guides d'onde à plasmons de surface ou guides d'onde plasmoniques. La structure qui supporte ces modes de surface est une interface entre un matériau avec un comportement métallique<sup>11</sup> et un matériau avec un comportement diélectrique. Quand un photon possédant assez d'énergie arrive en contact avec l'interface métallique, il excite le nuage électronique du métal. De manière similaire aux vagues dans l'océan, les électrons se déplacent localement grâce à l'excitation électromagnétique; un quantum de ces oscillations collectives s'appelle plasmon. Étant donné que le champ électrique n'arrive pas à pénétrer dans le métal, la vague électronique reste en surface. Ce phénomène prend le nom de plasmons-polaritons de surface car le phénomène a lieu à la surface du métal et il est produit grâce à l'interaction entre une onde électromagnétique et un plasmon<sup>3</sup>, comme montré la Figure R1.5.a.

<sup>11</sup> . Il est préférable de parler de matériau avec un comportement métallique plutôt que de métal, car, selon la longueur d'onde d'excitation, un métal peut se comporter comme un milieu transparent.

La distribution du champ électromagnétique a la forme de deux exponentielles décroissantes de part et d'autre de l'interface, comme un guide sans cœur. La figure R1.5.b montre la distribution de l'intensité du champ du mode plasmonique à l'interface entre l'or et l'eau à  $1.31\mu m$ . Notez que comme le profil exponentiel décroissant du champ dans le métal est beaucoup plus rapide que dans le diélectrique, seul le profil décroissant dans ce dernier est visible avec l'échelle horizontale choisie.

Les guides d'onde plasmoniques sont très intéressants pour la bio-détection vu la proportion importante d'énergie lumineuse dans le milieu fluide et leur facilité de fabrication. Plusieurs publications (citées dans le tableau 1 de l'article de synthèse [20]) montrent des capteurs performants avec des valeurs de sensibilité volumique expérimentale jusqu' 10 fois plus élevées que des structures diélectriques (par exemple  $32000\text{ nm}/\text{RIU}$  par rapport  $2169\text{ nm}/\text{RIU}$  pour des résonateurs en anneau diélectriques).

Un des inconvénients des guides plasmoniques est au niveau des dimensions relativement importantes qui sont requises pour obtenir une sensibilité élevée [5-6]. De plus, par rapport aux guides diélectriques diélectriques qui peuvent fournir deux mesures simultanées (TE et TM) permettant plus de flexibilité dans les mesures, seul le mode de propagation transverse magnétique (TM) est utilisable [3].

Par exemple, un guide diélectrique peut détecter l'épaisseur d'une couche biologique grâce au mode TE et son indice de réfraction en utilisant le mode TM. Dans le cas d'un guide purement plasmonique, une seule des deux informations est obtenue.

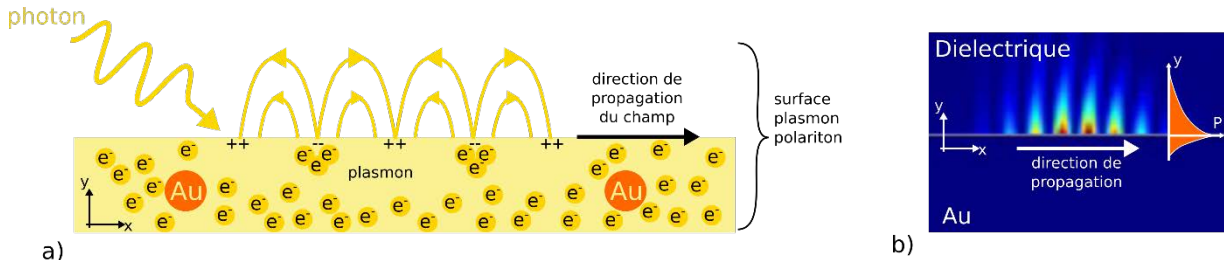


Figure R1.5 a) Schéma du mécanisme de guidage d'un plasmon-polariton de surface entre un diélectrique et un métal (dans cet exemple de l'or) b) Distribution de l'intensité lumineuse d'une impulsion électromagnétique dans un guide plasmon de surface. Le champ est très intense dans le matériau diélectrique, par exemple le milieu liquide d'intérêt, près de l'interface métal/diélectrique et négligeable dans l'or. La simulation a été faite avec un moteur FDTD à  $\lambda = 1.31\mu m$ .

## Guides hybrides plasmoniques-diélectriques (Hybrid plasmonic waveguides, HPWG)

Les guides d'onde hybrides plasmoniques-diélectriques (en anglais hybrid plasmonic waveguides) combinent les deux types précédents : créés à la base pour diminuer la taille des dispositifs optiques en télécommunications [17], les guides d'onde HPWG sont le résultat d'un couplage entre un mode guidé diélectrique et un mode guidé plasmonique. Si un guide d'onde diélectrique et un guide d'onde plasmonique sont suffisamment proches, la structure supporte des supermodes TE et TM dont les propriétés sont un amalgame des profils des modes guidés propres aux deux guides d'onde séparés, ayant des propriétés

intéressantes pour la bio-détection. Cependant, par opposition aux modes dans des guides diélectriques dont les caractéristiques peuvent être estimées par des méthodes analytiques approximatives comme la théorie des modes couplés (coupled mode theory ou CMT), les HPWGs requièrent l'utilisation d'outils de modélisation numérique [1-2].

Les applications pour ce type de guide d'onde sont variées : dispositifs de contrôle de polarisation, coupleurs directionnels, pinces optiques, dispositifs non linéaires et bien sûr les biocapteurs. Les géométries possibles pour atteindre ces objectifs sont illustrées sur la figure R1.6.a [1]. En particulier, une géométrie intéressante est celle qui combine les concepts des guides d'onde à fente et les modes guidés plasmoniques. Ce type de dispositif s'appelle guide d'onde double-slot hybrid plasmonic (DSHP). La Figure R1.6.b montre la géométrie d'un guide DSHP utilisé comme capteur et son champ fortement localisé dans le liquide de faible indice de réfraction [23]. Le guide d'onde DSHP peut être interprété comme un mélange entre un guide d'onde hybride plasmonique et à fente.

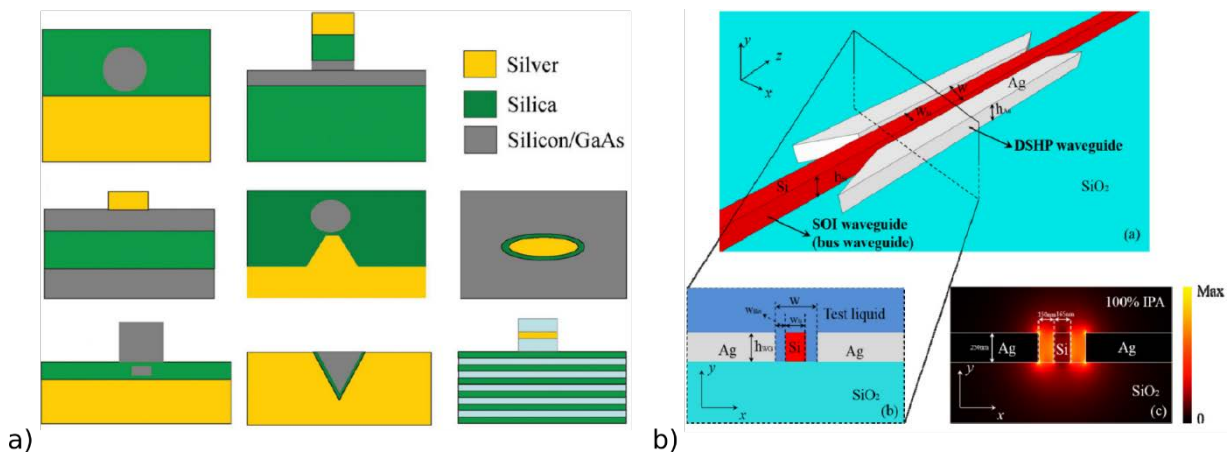


Figure R1.6 a) Différentes géométries de guides d'onde plasmonique hybrides (image modifiée pour améliorer la lisibilité) [1], b) Géométrie, coupe transversale et profil du mode guidé double fente hybride plasmonique [23].

Un autre aspect qui rend le HPWG prometteur pour un biocapteur est la facilité de la fonctionnalisation de surface : étant constitué d'une partie diélectrique et d'une partie métallique, les méthodes de fonctionnalisation différentielles peuvent être utilisées. L'inconvénient principal est la fabrication diélectrique/plasmonique avec les plateformes industrielles à cause de la nature du métal utilisé (or ou aluminium).

## Conclusion

Tableau R1.1 Guides d'onde pour la détection photonique intégrée : avantages et inconvénients

Dispositif	Avantages	Inconvénients
Guides d'onde ruban	Faibles pertes Facile à réaliser Modes TE/TM	Faible sensibilité Fonctionnalisation de surface différentielle difficile
Guides d'onde fente [4],[9]	Très sensible (interaction élevée entre la lumière et l'environnement) Modes TE/TM	Accès difficile pour les grosses molécules Difficile à fabriquer en raison du faible espacement Fonctionnalisation de surface différentielle difficile
Guides plasmoniques [5],[6],[20]	Très sensible Fonctionnalisation de surface différentielle simple	Pertes élevées (qui peut être aussi un avantage selon la méthode de détection) Taille grande (millimétrique) Mode TM seulement
Guides HPWG [1],[2]	Sensible (plus sensible qu'un guide d'onde diélectrique, mais moins qu'une guide plasmonique) Modes TE/TM Fonctionnalisation de surface différentielle simple	Compromis au niveau des pertes et sensibilité entre le mode plasmonique et le mode diélectrique

Le Tableau R1.1 résume les avantages et les inconvénients des différents types de guides d'onde analysés dans cette section. Les données indiquées ne sont pas quantitatives car dans la plupart des cas la performance du capteur complet dépend des caractéristiques du dispositif complet.



## Dispositifs complets

Dans cette section, des exemples de capteurs complets en photonique intégrée seront décrits.

### Surface Plasmon Resonance

Les capteurs résonants de plasmon de surface (Surface Plasmon Resonance ou SPR) sont souvent utilisés pour la détection surfacique. Plusieurs dispositifs, portatifs ou non, ont été conçus avec cette méthode qui exploite la variation du pic de résonance du plasmon de surface ([14], [13] et [25]). Toutefois les SPR ne sont pas pris en considération comme dispositif possible car ils ne sont pas compatibles avec la plateforme industrielle considérée dans cette étude.

### Interféromètre Mach-Zehnder asymétrique

Le principe de l'interféromètre Mach-Zehnder (Mach-Zehnder interferometer or MZI) est de faire interférer la lumière qui passe à travers le parcours de détection où l'élément mesurer se situe, avec celle du parcours de référence (Figure R1.7). Selon l'interférence obtenue, il est possible de déduire les propriétés optiques de l'élément en question. La sensibilité étant en fonction de la longueur du parcours optique, un dispositif sensible (5027 rad/RIU [7]) occupe typiquement une longueur supérieure au *mm*. Des interféromètres de Mach-Zehnder ont été réalisés avec des guides d'onde à fente [8] et des HPWG [23].

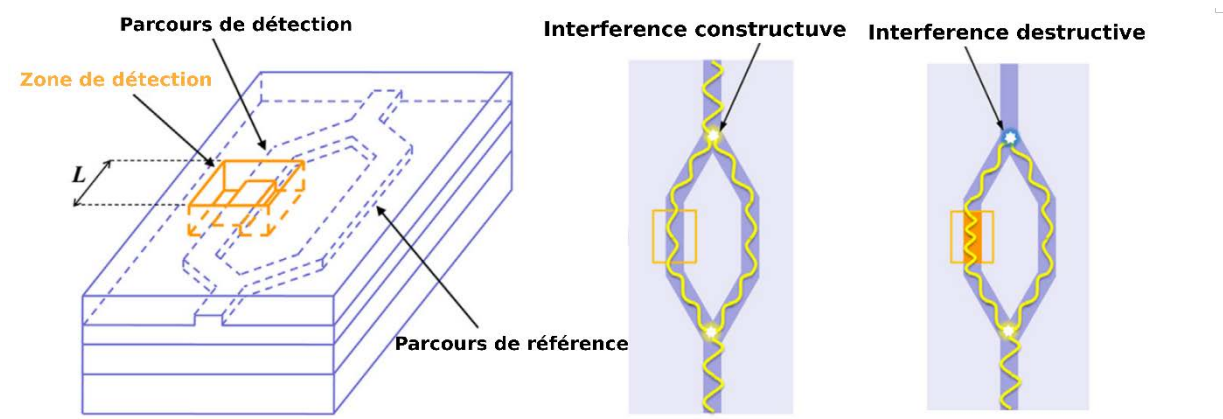


Figure R1.7 Schéma d'un interféromètre Mach-Zehnder utilisé comme capteur [7].

### Résonateurs en anneau à guides diélectriques simples

Les résonateurs en anneau, où anneaux résonants, permettent de réaliser des dispositifs plus compacts qu'avec des interféromètres. Dans le cas le plus simple, ils sont constitués d'un guide d'injection/collection (guide bus ou bus waveguide) et d'un guide en forme d'anneau comme montré la figure R1.8.a. La lumière est injectée dans le guide bus, puis dans la zone de couplage indiquée dans la figure R1.8.a, il y a transfert d'énergie lumineuse par couplage direct entre les deux guides d'onde (voir les figure R1.8.b et Figure R1.8.c où la

coupe transversale et la vue de dessus montrent la distribution de puissance lumineuse dans la zone de couplage).

La proportion d'énergie transférée du guide bus vers l'anneau est calculée grâce au coefficient de couplage  $\kappa$ , qui dépend de la géométrie du dispositif et des matériaux. La proportion de lumière qui n'est pas transférée dans l'anneau reste dans le guide bus et continue vers la sortie. Après avoir fait le tour de l'anneau, la lumière se propageant dans le résonateur atteint à nouveau la zone de couplage où elle se divise entre une première composante qui repart dans l'anneau et une deuxième qui repasse dans le guide bus où il y aura interférence avec la lumière qui s'y trouve. Ce mécanisme est illustré dans la figure R1.8.d, où la zone de couplage est représentée par une boîte de 4 ports. Avec un choix judicieux des paramètres de couplage, il y aura extinction totale de la lumière en sortie du guide bus. C'est le couplage critique, lequel est très sensible aux changements de propriétés optiques du milieu fluide en contact avec le cœur du guide.

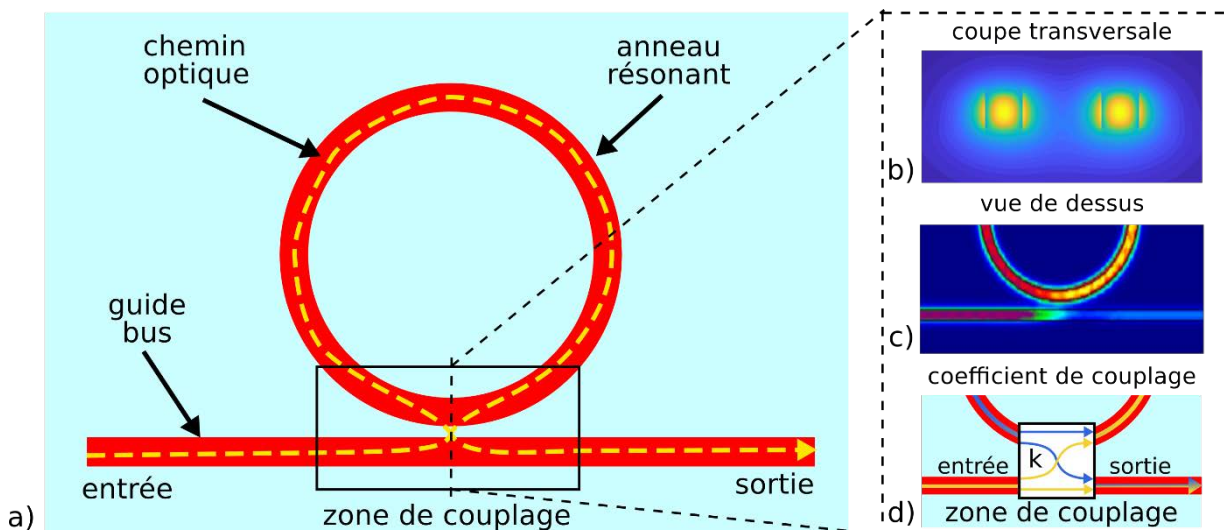


Figure R1.8 a) Schéma d'un anneau résonant, b) distribution de la puissance dans la zone de couplage entre le guide bus et l'anneau, c) vue de dessus de la puissance lumineuse dans la zone de couplage et d) schéma de couplage entre l'anneau et le guide bus

Les résonateurs en anneau sont d'un grand intérêt pour les biocapteurs car ils sont compacts, sensibles à l'environnement fluide sondé et relativement simples à réaliser. Ils ont une valeur typique de sensibilité bulk d'environ 100 nm/RIU<sup>12</sup> [8] [19] [15]. Un premier anneau peut être combiné avec un deuxième anneau résonant de référence ce qui permet d'augmenter la sensibilité du capteur (2169 nm/RIU [10]). C'est l'équivalent de l'effet Vernier utilisé à l'origine pour améliorer la précision des mesures de longueur dans les pieds à coulisse.

Les inconvénients de cette structure sont une fonctionnalisation de surface relativement compliquée et le possible besoin d'intégrer une source accordable en entrée ou un

<sup>12</sup>. Comme expliqué au début de cette section, la sensibilité bulk indique de combien la résonance de l'anneau se décale, en longueur d'onde, avec un changement d'indice de réfraction du milieu environnant d'un.

spectromètre en sortie, par rapport à une source monochromatique et un simple photodétecteur dans le cas d'un interféromètre.

## Résonateur en anneaux avancés

**Résonateurs avec guides d'onde à fente** Les résonateurs en anneau peuvent être conçus avec des guides d'onde à fente, ce qui améliore la sensibilité en rendant accessible la cible d'intérêt dans un volume contenant une plus forte proportion de l'énergie lumineuse. Plusieurs géométries ont été étudiées dans la littérature où les guides d'onde à fente sont utilisés dans une partie de l'anneau (106 nm/RIU en Si) [21], dans la totalité de l'anneau (141 nm/RIU en SiN) [24], ou bien la fois dans l'anneau et dans le guide bus (298 nm/RIU en Si) [11]. La Figure R1.9 montre des images prises au microscope électronique des trois types d'anneaux comprenant des guides d'onde à fente.

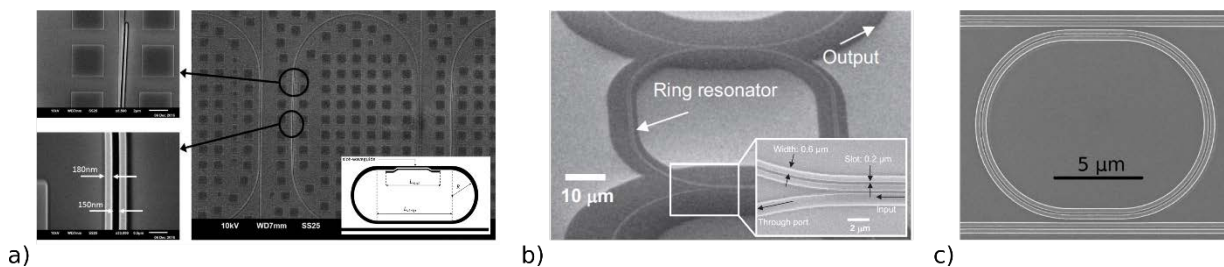


Figure R1.9 Images MEB des différentes structures en anneau résonant combinées avec des guides d'onde à fente : a) anneau avec une portion de guide d'onde à fente [21], b) anneau totalement à fente [24], c) anneau et guide d'onde bus à fente [11].

Aussi, la forme des fentes des guides d'onde peut être modifiée pour optimiser le confinement dans le liquide d'intérêt. Un exemple est le guide T inversé. En plus de la fente verticale au milieu, il y a une deuxième horizontale, comme décrit la figure R1.10 [12]. Dans l'article concerné, les auteurs ne mentionnent pas d'indice RIU, mais ils définissent la sensibilité comme  $(\delta n_{eff}/\delta a)$ , où  $n_{eff}$  est l'indice effectif du mode guidé et  $a$  est l'épaisseur de la couche de fonctionnalisation. Avec cette structure, une valeur de sensibilité théorique de  $S = 0.0011 nm^{-1}$  peut être atteinte.

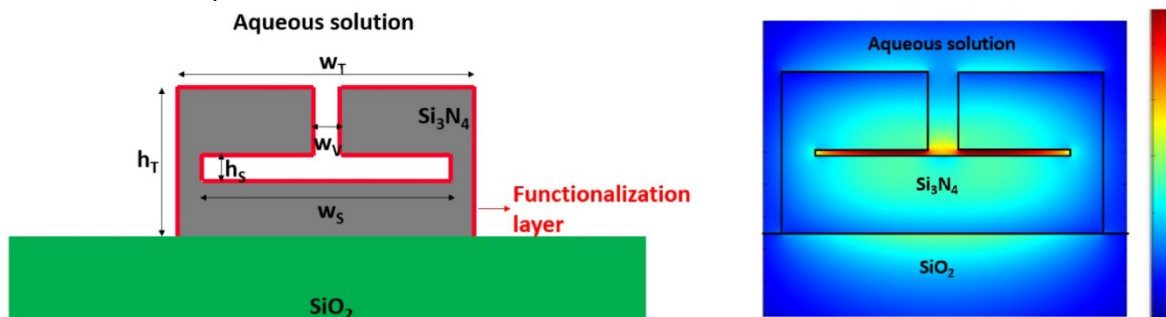
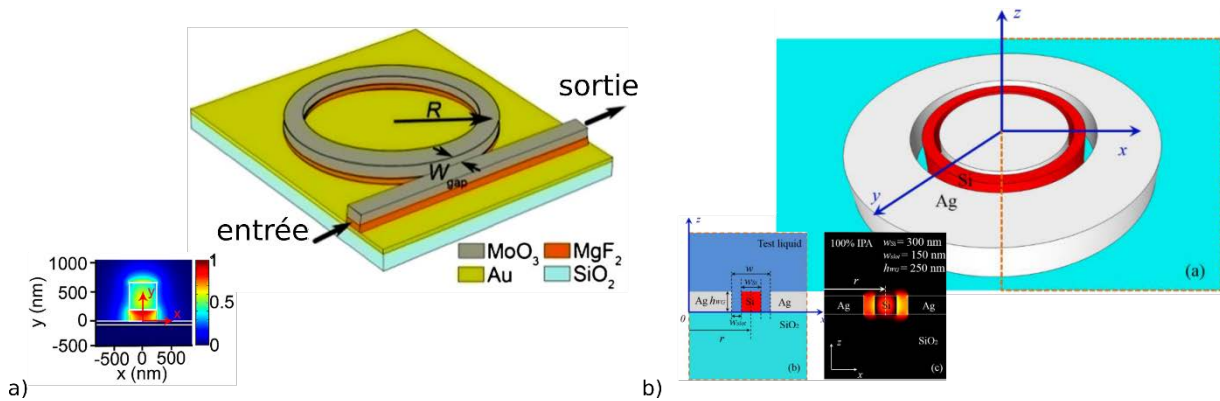


Figure R1.10 a) Schéma de la configuration fente en T inversé et b) distribution de champ dans la configuration inversée [12].

**Résonateurs en anneau et HPWG** Les résonateurs en anneau peuvent aussi être réalisés avec des guides d'ondes hybrides plasmoniques. Il y a principalement 2 géométries qui ont été étudiées : un substrat métallique (408 nm RIU théoriques) [16] et un guide d'onde double-slot hybrid plasmonic (DSHP) (688 nm/RIU expérimentale) [22]. Les figures R.11.a et figure R.11.b montrent les géométries de ces 2 configurations. La présence du métal permet une fonctionnalisation de surface différentielle métal/diélectrique.



## Conclusion

Dans le Tableau R1.2, les performances des dispositifs mentionnés plus haut sont résumées afin de pouvoir mieux les comparer.

Tableau 2.2 Récapitulatif des performances de chaque dispositif

Méthode de détection	Type de guide	Sensibilité (bulk ou surfacique)	Limite de détection	Plateforme industrielle	Fonctionnalisation différentielle métal/diélectrique	Dimension (footprint)
SPR	Systèmes non portables [14], [25]	10–300ng/mL	10pg/mm	-	-	-
	Systèmes portables [13]	316nm/RIU	4.2×10 <sup>-6</sup> RIU	-	-	-
Interféromètre MachZehnder	Diélectrique [7]	1600 πrad/RIU		OUI	NON	Large (> 1 mm <sup>2</sup> )
	Fente [8]	2663 πrad/RIU	5.4×10 <sup>-6</sup> RIU	OUI	NON	Large (> 1 mm <sup>2</sup> )
	Double slot hybrid plasmonic [23]	1061 nm/RIU		OUI	OUI	Large (> 4000 μm <sup>2</sup> )
Anneau résonant	Diélectrique [8],[15],[19]	163 nm/RIU	7.6×10 <sup>-7</sup> RIU	OUI	NON	compact (226 μm <sup>2</sup> )
	E et Vernier (2 anneaux) [10]	2169 nm/RIU	8.3×10 <sup>-6</sup> RIU	OUI	NON	large (> 30000 μm <sup>2</sup> )
Anneau résonant slot	Partial slot [21]	106 nm/RIU		OUI	NON	acceptable (2720 μm <sup>2</sup> )
	Full slot [24]	141 nm/RIU 50 ng/mL (PSA <sup>5</sup> )	10 ng/mL (PSA)	OUI	NON	compact (< 1000 μm <sup>2</sup> )
	Full slot et guide bus [11]	298 nm/RIU	4.2×10 <sup>-5</sup> RIU	OUI	NON	compact (130 μm <sup>2</sup> )
	T inversé[12]	0.0011 nm <sup>-1</sup>	1 ng/mL (cancer du poumon <sup>6</sup> )	OUI	NON	acceptable (2200 μm <sup>2</sup> )
Anneau résonant HPWG	Substrat métallique [16]	408.7 nm/RIU	2.13×10 <sup>-4</sup> RIU	NON	OUI	compact (< 200μm <sup>2</sup> )
	Double slot hybride plasmonique 2.9	687.5 nm/RIU	5.37×10 <sup>-6</sup> RIU	OUI	OUI	compact (< 200 μm <sup>2</sup> )

5. PSA est l'antigène prostatique spécifique (prostate-specific antigen en anglais)

6. Dans cette étude 5 protéines du sérum humain liées au cancer du poumon ont été testées : Alpha-1 antitrypsin (A1AT), cytokeratin fragment 21-1 (Cyfra 21 1), insulin-like growth factor 1 (IGF1), regulated upon activation normal T cell expressed and secreted (RANTES), and alpha-fetoprotein (AFP)

# Problématique et objectifs

**Problématique** Les biocapteurs sont des dispositifs qui intègrent une ou plusieurs fonctionnalités d'analyse qui sont utilisées dans des contextes où l'étude d'espèces moléculaires biologiques est nécessaire (la santé, le contrôle de qualité des aliments et l'analyse environnementale). Les technologies qui peuvent être impliqués dans un tel dispositif sont multiples : de la biologie, de l'électronique, de la photonique et de la microfluidique. Cependant, les dispositifs sont rarement conçus en considérant tous les éléments permettant d'aboutir à un produit final qui peut être produit commercialement. L'intérêt de ce projet n'est pas seulement d'identifier, concevoir et fabriquer un transducteur qui arrive à convertir efficacement la présence biologique de l'analyte en information optique, mais dont le design est compatible avec la production industrielle.

Plusieurs contraintes sont prises en compte dans notre analyse :

- 1) Du point de vue optique, il faut veiller à obtenir une transduction photonique sensible aux molécules cibles et obtenir un signal traitable en sortie.
- 2) Pour la partie biologique, 2 facteurs sont à considérer : la molécule d'intérêt doit être capable d'atteindre la zone de détection et doit s'y accrocher de manière préférentielle par rapport aux zones mortes du dispositif. La zone de détection doit donc être suffisamment accessible pour satisfaire la première contrainte et doit posséder une chimie différentielle pour la deuxième.
- 3) Le circuit microfluidique impose que le substrat utilisé doit être compatible avec un collage de microcanaux fabriqués par exemple avec du polydiméthylsiloxane (PDMS).
- 4) Enfin les matériaux et les dimensions du dispositif doivent être adaptés aux procédés de fabrication industriels. En considérant les infrastructures du partenaire industriel STMicroelectronics, le dispositif doit être conçu avec les matériaux déjà disponibles dans l'usine, de dimensions non inférieures à la limite de la lithographie optique (environ 180nm).

La problématique se résume en une question : Comment concevoir et réaliser un biocapteur compact à base de transducteur en photonique intégrée, simple, fonctionnaliser, compatible avec une plateforme industrielle et ayant une sensibilité égale ou supérieure à l'état de l'art?

**Objectifs** L'objectif est d'identifier et d'évaluer les performances d'un transducteur en photonique intégrée qui satisfait au mieux les caractéristiques décrites dans la problématique. De plus, il faudra démontrer le fonctionnement du dispositif et son potentiel. Le premier dispositif dont les performances seront analysées est l'anneau résonant à base des guides d'onde hybrides plasmoniques. Afin d'atteindre ce but, il faudra :

1. Comprendre et modéliser numériquement les mécanismes physiques à la base du transducteur lors d'une interaction avec l'espèce biologique, afin de bien cerner les applications possibles du dispositif et d'optimiser le design.
2. Choisir un procédé de fabrication en tenant compte de l'objectif final de fabriquer en milieu industriel, permettant d'atteindre des coûts de production et un niveau de fiabilité requis pour le marché.
3. Concevoir un système pour la caractérisation : montage optique pour tester les puces (source, détection et filtres optiques) incluant les aspects multiphysiques (canaux micro fluidiques, fonctionnalisation étalon, intégration sur support).

## Hypothèses et approche proposée

Puisqu'il est souhaitable d'avoir un capteur polyvalent, il doit permettre une chimie de surface générique, stable, reproductible et simple. De plus, une caractéristique importante pour la fonctionnalisation de surface est d'être sélectif spatialement, soit de pouvoir positionner les cibles sélectivement sur la surface sensible du capteur et non sur les zones mortes afin de maximiser l'efficacité de la mesure. Dans le cadre de ce projet, l'expertise de l'équipe de chimie et nano-biotechnologies de l'Institut de Nanotechnologies de Lyon (INL) dans la chimie différentielle entre un diélectrique et un métal [18] a naturellement orientée vers une solution qui intègre les diélectriques et métaux, comme par exemple les guides plasmoniques.

Comme souligné précédemment, un des objectifs est de réduire la taille du dispositif afin d'augmenter la quantité de transducteurs par unité de surface et également de minimiser le volume de réactifs nécessaire pour le fonctionnement du capteur. Le résonateur en anneau a été sélectionné car il est sensible et compact, permettant ainsi d'atteindre cet objectif.

Toutefois, le résonateur en anneau est un dispositif dans lequel les métaux sont rarement intégrés, car pour que le résonateur soit performant, les pertes dans l'anneau doivent être faibles. Les guides d'onde plasmonique ont des pertes de l'ordre de 1000 dB/cm tandis que les guides d'onde diélectrique ont des pertes de l'ordre de 1 dB/cm. Un anneau complètement plasmonique serait donc peu performant. Les guides d'onde hybride plasmonique offrent une solution à ce dilemme. Ces guides d'onde, semblables à des guides d'onde à fente, sont constitués par deux guides d'onde parallèles, l'un diélectrique et l'autre plasmonique, séparés par une fente ou slot. Les modes de ces guides ont des pertes plus faibles que les modes purement plasmoniques bien que plus importantes que les guides diélectriques. Cependant, les pertes peuvent être modulées en modifiant la distance entre le métal et le diélectrique, ce qui permet de les adapter pour la structure en anneau résonant.

De plus, la capacité d'accorder une large gamme de dimension pour la fente sera évaluée pour les guides double-slot HPWG. Comme le montre l'image 5.2 dans le chapitre 5, les paramètres tel que la distance entre le métal et le diélectrique (ou gap), la longueur de l'anneau, le choix du matériau conducteur, la largeur du guide diélectrique centrale affectent

les performances d'un tel guide d'onde. Ceux-ci influencent d'un côté les pertes et de l'autre la sensibilité du dispositif, ce qui implique que, pour une application donnée, les paramètres doivent être optimisés. Cette propriété est importante car elle pourrait être limitante selon la taille des molécules cibles. Les guides d'onde hybrides plasmonique représentent une bonne configuration de guide d'onde pour un biocapteur compact et sensible en photonique intégré [22] [1].

Enfin, pour que le biocapteur soit fabricable à bas coût, sa réalisation doit être compatible avec une plateforme de production de masse. La plateforme DAPHNE, développée pour les télécommunications par le partenaire industriel du projet STMicroelectronics, répond à ce besoin. Un document détaillé définit les règles de design des motifs et les disponibilités des matériaux de la plateforme. La fabrication des guides d'onde hybride plasmonique est majoritairement compatible avec la plateforme DAPHNE, mis part les étapes de fabrication des parties métalliques par lift off utilisé dans le cadre de cette étude. Au stade de production, le lift off sera remplacé par un procédé compatible avec la plateforme DAPHNE.



# Méthodologie et conception

Ce paragraphe décrit la méthodologie qui sera utilisée qui se divise en trois parties, soit la conception du dispositif, la fabrication et la caractérisation.

**Conception** La première étape est de comprendre les phénomènes physiques derrière les modes hybrides plasmoniques. La revue de la littérature, l'étude théorique et la simulation sont les trois éléments mis à profit pour la compréhension du phénomène.

En ce qui concerne l'étude théorique, les principaux concepts considérés sont les suivants : l'optique guidée pour les guides d'onde diélectriques, les plasmons de surface et les modes hybrides diélectrique-plasmonique.

Etant donné que le premier dispositif considéré est un résonateur en anneau, la théorie des résonateurs en anneau doit être étudiée en détail (par exemple, le couplage dans l'anneau, le calcul des figures de mérite de l'anneau tel que le facteur de qualité, la largeur à mi-hauteur, l'intervalle spectral libre). Afin d'explicitier la forme du signal de sortie et les figures de mérite intéressantes, la figure R1.12 montre la transmission typique d'un anneau résonnant en fonction de la longueur d'onde.

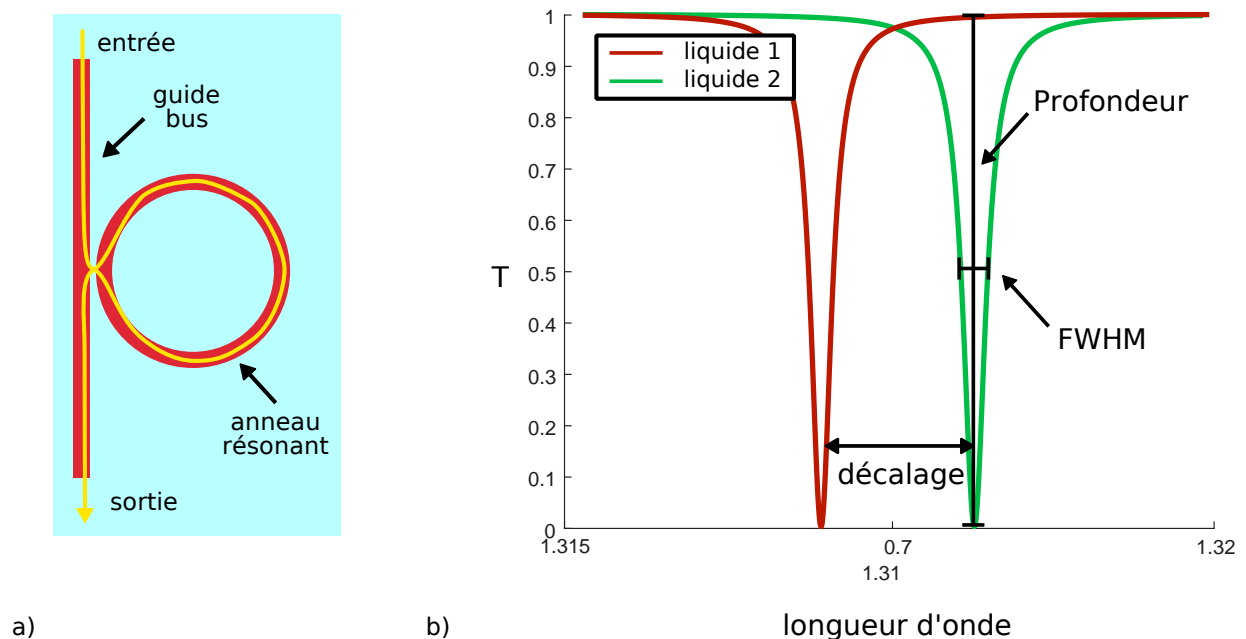


Figure R1.12 Exemple de la géométrie d'un résonateur en anneau et de sa transmission

Le logiciel MATLAB sera utilisé pour tous les calculs et les résolutions d'équations qui ne requièrent pas un logiciel dédié.

Concernant la simulation, 2 méthodes seront utilisées pour comprendre et concevoir le dispositif : la méthode de finite-difference time-domain (ou FDTD) et la détermination de modes guidés (mode-solver).

Bien que la méthode FDTD permet d'obtenir la distribution spatiale et temporelle de la lumière qui se propage dans le composant, il est parfois difficile de comprendre les

phénomènes physiques à partir des résultats de simulation. Après une discrétisation de l'espace et du temps, la FDTD montre la propagation de la lumière à partir d'une source polychromatique. Le principal point négatif de la méthode FDTD est le temps de calcul qui varie beaucoup selon la discrétisation et les dimensions de l'espace considérées (1D, 2D ou 3D). Dans le cas présent, le logiciel utilisé pour ce type de simulation sera Lumerical FDTD.

La résolution de modes est une méthode pour calculer la distribution spatiale du champ d'un mode guidé dans une structure photonique dans le plan perpendiculaire la propagation. Après avoir défini la géométrie, les matériaux et le maillage de la section transversale de la structure, le logiciel formule les équations de Maxwell sous forme d'un problème matriciel aux valeurs propres. Pour effectuer ce type de simulations, un outil développé à l'INSA de Lyon par Régis Orobitchouk est utilisé basé de la méthode des différences finies (finite difference method) et permet d'obtenir des résultats avec des temps de calcul inférieurs aux logiciels commerciaux. Il est aussi possible d'utiliser le logiciel de résolution de modes commercial FIMMWAVE où on peut choisir entre une résolution avec la méthode des différences finies ou la méthode des éléments finis (finite element method ou FEM). L'inconvénient d'un logiciel de calcul de modes est que, contrairement aux simulations FDTD, l'on ne considère qu'une seule longueur d'onde et uniquement des modes résonnants. Par contre, en termes de temps de calcul, le logiciel de calcul de modes est beaucoup plus rapide. Un autre avantage du logiciel de calcul de mode est qu'il est possible d'observer les modes de la structure séparément alors que dans une simulation FDTD une réponse optique complète est obtenue, où il n'est pas possible de distinguer les modes individuellement.

Dans le cadre de mon projet, je vais utiliser un logiciel de calcul de modes pour étudier, en fonction des matériaux et de la géométrie des guides d'onde, les propriétés des modes présents dans les guides d'onde hybride plasmonique. La simulation FDTD sera utilisée pour confirmer les calculs concernant le fonctionnement des dispositifs de routage de la lumière et pour une vérification des principes théoriques à l'origine des guides d'onde hybride plasmonique.

La géométrie proposée des guides d'onde hybride plasmonique à fente ainsi que la cartographie de l'intensité du mode guidé sont illustrées sur la figure R1.13.a. La majorité de l'intensité lumineuse (environ 60%) est confinée dans le milieu biologique, soit entre le métal et le diélectrique. La figure R1.13.b montre une image du transducteur, soit un anneau résonnant couvert de récepteurs (des molécules qui ancrent l'analyte sur le détecteur). Le fait de ne pas avoir des récepteurs ailleurs que sur les guides  $S_iN_y$  est préférable, car il faut positionner les analytes dans la zone sensible.

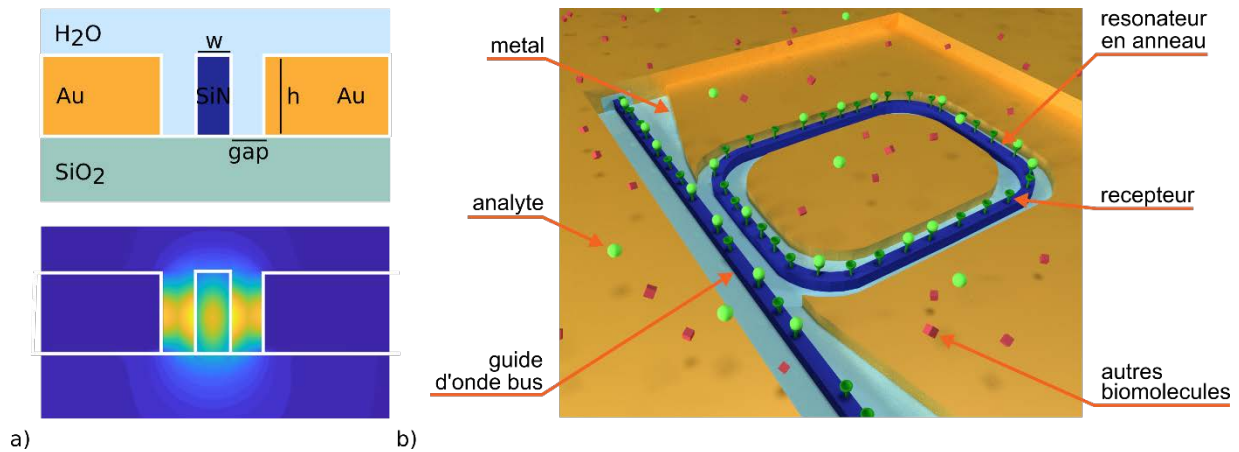
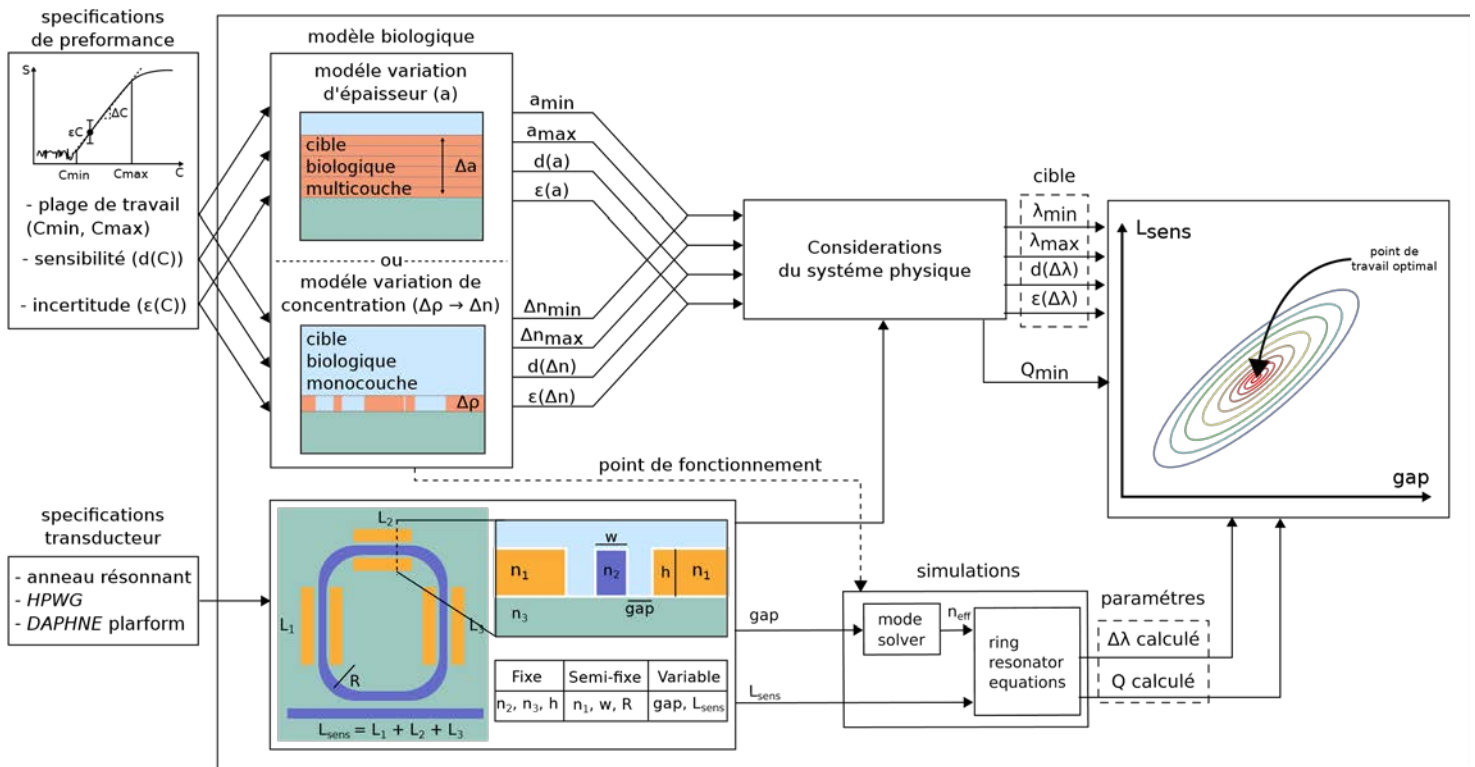


Figure R1.13 a) Schéma de la coupe transversale du guide d'onde et de la distribution de la puissance lumineuse calculée par l'outil de calcul de modes ( $w = 300\text{nm}$ ,  $h = 600\text{nm}$ ,  $\text{gap} = 300\text{nm}$ ). b) Schéma du dispositif en 3D avec les interactions biologiques. Le rayon de courbure des virages est de  $20\mu\text{m}$ , assez grands pour considérer les pertes nulles dans ces zones.

La figure R1.14 montre le schéma simplifié du processus d'optimisation de la géométrie du dispositif, notamment la distance entre le métal et le diélectrique (gap) et la longueur de l'anneau. La cinétique d'intérêt est décrite par un modèle biologique (multicouche ou monocouche, selon la dynamique d'accroche de la molécule cible), menant à un changement des paramètres mesurables du transducteur choisi (dans le cas d'un anneau résonnant un décalage en longueur d'onde et du facteur de qualité de la résonance). Le graphique de la figure de mérite, obtenu grâce à des simulations en fonction des paramètres, permettra de trouver une zone de compromis entre la performance du capteur et les contraintes technologiques, autrement dit les dimensions physiques pour lesquelles la figure de mérite est maximale. Le choix de la largeur du guide d'onde en nitrure est faite pour que le mode guidé soit en limite de coupure lorsqu'on enlève le métal à côté. En faisant cela, la puissance lumineuse sera d'avantage concentrée dans la fente.



Considerations du système physique

Définition des paramètres dans le graphique :

- resolution spectrometre (0.1 pm)
- $\Delta\lambda_{min}$  - Q suffisant (SNR et  $Q_{min}$ )
- $Q_{min}$  - bruits (thermique, etc...)
- geometrie du capteur
- bande passante du detecteur
- $\Delta\lambda_{max}$  - modèle biologique
- Supposant que le pic est detectable (Q et SNR suffisants) le paramètre qui influence principalement est  $\Delta\lambda$
- $d(\Delta\lambda)$
- positions des molecules
- $\epsilon(\Delta\lambda)$  - incertitude spectrometre
- bruits (thermique, etc...)

- C = concentration en volume de l'espèce d'intéret (i.e. le paramètre à déterminer)
- a = épaisseur de la couche du matériau cible
- $\Delta n$  = variation d'indice de réfraction de la couche dans le modèle biologique
- $\Delta\rho$  = variation de la densité de la couche cible
- $\lambda$  = longueur de résonance de l'anneau
- $L_{sens}$  = longueur des parties droites HPWG de l'anneau résonnant
- $n_1$  = indice de réfraction du métal - dans un premier temps fixé à l'indice de l'or
- $n_2$  = indice de réfraction du guide centrale - fixé à l'indice du SiN
- $n_3$  = indice de réfraction du substrat - fixé à l'indice du SiO<sub>2</sub>
- w = largeur du guide en nitrure - dans un premier temps fixée à 340 nm
- h = épaisseur du guide en nitrure et du métal - fixée à 600 nm
- R = rayon des parties courbes - dans un premier temps fixé à 20  $\mu m$
- gap = distance entre le guide en nitrure et le métal
- Q = facteur de qualité du résonateur en anneau
- $n_{eff}$  = indice effectif du mode dans le résonateur en anneau

Figure R1.14 Processus d'optimisation des paramètres géométriques selon les besoins de performances.

# Fabrication

La fabrication est faite en partie chez le partenaire industriel STMicroelectronics sur la plateforme DAPHNE et en partie dans les salles blanches universitaires (l'INL de Lyon ainsi qu'à l'Université de Sherbrooke). Pour obtenir un dispositif le plus compatible possible avec la plateforme industrielle, la plupart des étapes seront faites dans la salle blanche industrielle. L'objectif est de fabriquer le biocapteur en tenant compte des contraintes de cette plateforme. Plus en détail, le dispositif doit être conçu avec les matériaux déjà disponibles dans l'usine, des dimensions supérieures à la limite de la lithographie optique (180 nm environ) et des épaisseurs fixées par la production (choix entre 600 et 350 nm pour le guide d'onde de  $\text{Si}_3\text{N}_4$ ).

La seule étape qui pour l'instant n'est pas compatible avec la plateforme DAPHNE est la réalisation des parties métalliques du dispositif. Deux procédés ont été développés. Le premier utilise une lithographie électronique et un procédé de lift off qui permet d'ajouter des papillons de métal sur les puces de nitrure de silicium réalisés sur la plateforme DAPHNE. Ce procédé a été développé à l'INL par Pedro Rojo Romeo et a permis de fabriquer des premiers échantillons pour la caractérisation optique. Afin de pouvoir intégrer l'étape de métallisation à la plateforme DAPHNE, un procédé auto-aligné utilisant des étapes de polissage mécano chimique (chemical mechanical polishing - CMP) est en cours de validation à l'université de Sherbrooke. Les détails du procédé sont donnés en annexe.

Concernant le choix du métal, plusieurs facteurs sont considérés : la disponibilité dans la plateforme industrielle, la stabilité et les propriétés optiques. Les deux candidats principaux sont l'or et l'aluminium. L'or est plus stable que l'aluminium car il ne s'oxyde pas au contact avec un liquide. Par contre, l'aluminium a des propriétés optiques plus intéressantes : la partie réelle de la permittivité diélectrique de l'aluminium  $\epsilon_{\text{Al}}$  (-242.68 à  $\lambda = 1.55 \mu\text{m}$ ) est plus négative que celle de l'or  $\epsilon_{\text{Au}}$  (-115.13 à  $\lambda = 1.55 \mu\text{m}$ ). La relation d'existence d'un plasmon de surface indique que plus la partie réelle du métal est négative, plus la constante de décroissance du profil exponentiel dans le diélectrique diminue. Or, l'interaction entre le mode plasmonique et le mode diélectrique dans les guides HPWG est plus prononcée pour un matériau dont la partie réelle de la permittivité est plus négative, ce qui permet de maximiser la proportion de l'énergie lumineuse dans le slot.

L'or sera testé en premier pour assurer la stabilité de la chimie différentielle. Une fois que le dispositif sera validé avec l'or, on pourra essayer l'aluminium pour avoir une comparaison des performances et de la chimie différentielle.

La figure R1.15 montre le procédé de fabrication avec lift off ainsi que les images des différentes étapes.

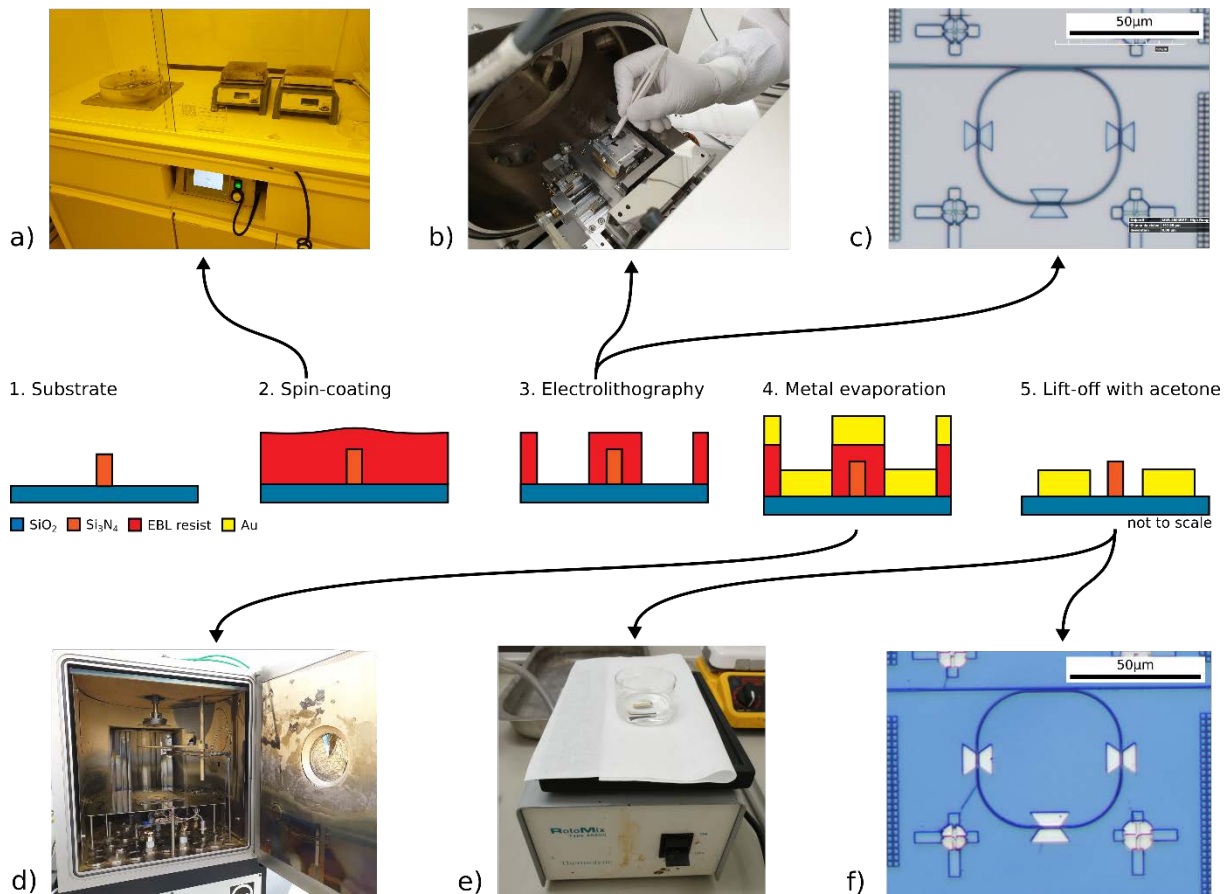


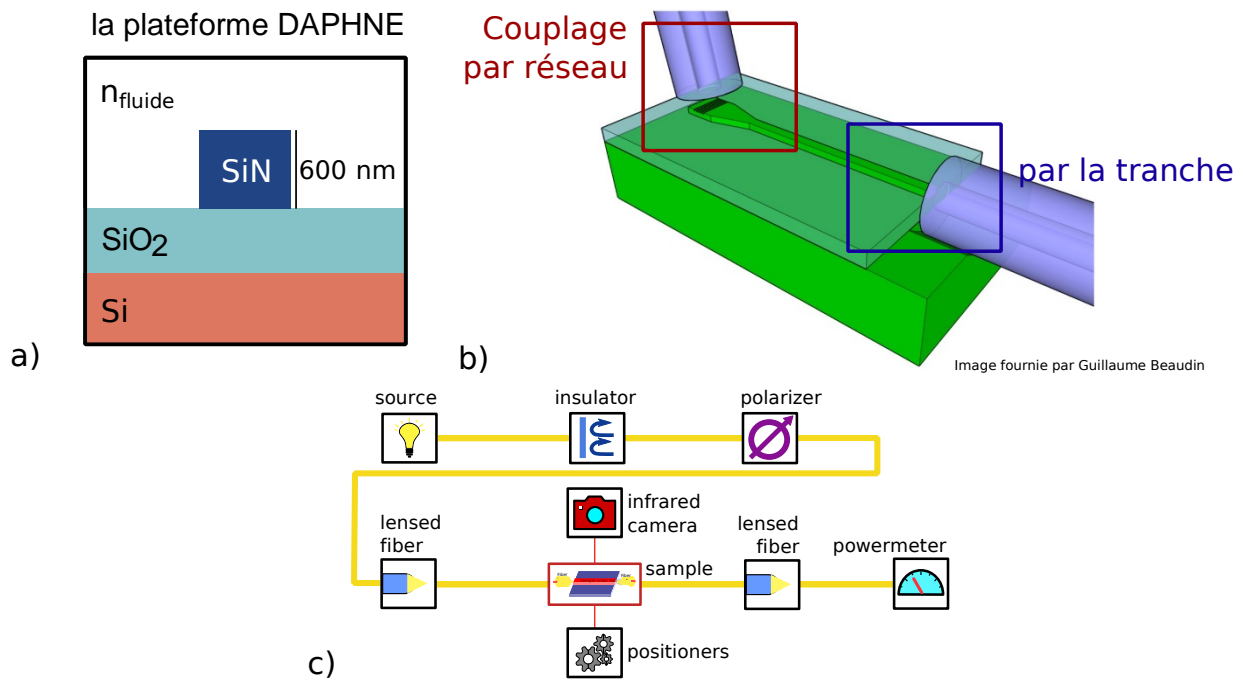
Figure R1.15 Etapes de fabrication du procede Lift off illustrées par des images prises en salle blanche durant la réalisation. a) dépôt de la résine à la tournette, b) Lithographie électronique c) image d'un échantillon après le développement. Les papillons trapézoïdaux représentent les trous dans la résine. d) Evaporation du metal par canon à electron Leybold, e) Lift off dans le mixer RotoMix type 48200 où l'échantillon est immergé dans l'acétone, f) Echantillon en fin de procédé.

Une fois que les dispositifs ont été fabriqués, la caractérisation a lieu. Les résultats de caractérisation seront présentés dans la prochaine section.

## Caractérisation

En ce qui concerne l'injection de lumière dans ce dispositif, 2 configurations sont possibles : un couplage par réseau de diffraction ou un couplage par la tranche. Le premier type de couplage, schéma 1 de la Figure R1.16.b, est sensible à la polarisation et possède une bande passante limitée (typiquement autour de 50 nm). Dans ce projet, il est préférable dans un premier temps d'avoir la possibilité de tester 2 longueurs d'onde dans l'infrarouge (1,31  $\mu\text{m}$  pour la faible absorption du SiN et 1,55  $\mu\text{m}$  pour être compatible avec les lasers déjà présents dans les bancs de caractérisation) et d'observer le comportement dans les 2 polarisations TE et TM pour obtenir un maximum d'information. Le couplage par la tranche est une méthode ayant moins de contraintes au niveau de la polarisation et au niveau de la bande passante. Le couplage par la tranche est donc la méthode privilégiée pour tester le fonctionnement du dispositif et l'améliorer. Lorsque le design du capteur sera terminé, le couplage par réseau pourra être envisagé pour rendre le dispositif plus compatible avec l'industrie.

Pour l'instant, le banc de couplage par la tranche est optimisé pour les besoins du dispositif. Le chemin optique commence par un laser accordable émettant entre 1,46 et 1,58  $\mu\text{m}$  (ceci est suffisamment large pour observer des pics de résonance qui ont une largeur d'environ 10 nm), possédant une résolution fréquentielle de 0,1 pm (ceci est suffisamment faible pour observer les pics qui, selon les simulations, sont entre 0,2 et 1 nm de largeur à mi hauteur (Full Width at Half Maximum ou FWHM)). Avant d'effectuer la mesure, un balayage en longueur d'onde est réalisé avec le laser et la puissance en sortie est mesurée avec un photodétecteur à la sortie du parcours optique. Une fibre à maintien de polarisation relie le laser à un contrôleur de polarisation. Lorsque la polarisation souhaitée est choisie, une fibre lentillée amène la lumière jusqu'à une facette de l'échantillon (taille du spot d'environ 2,5  $\mu\text{m}$ , distance de travail de 14  $\mu\text{m}$ ). Une caméra infrarouge permet de vérifier l'alignement de la fibre d'entrée. Dans cette configuration, il est aussi possible de vérifier si la polarisation est bien celle souhaitée avec un analyseur de polarisation. Lorsque le signal de sortie est optimisé, la caméra est remplacée par une fibre lentillée qui récolte le signal et le dirige vers un photodétecteur. Le contrôleur du laser et du photodétecteur envoie les informations de longueurs d'onde et de puissances transmises à un ordinateur qui enregistre les données. Grâce à un code MATLAB, la position des pics de résonance est extraite ce qui permet de calculer le changement d'indice de réfraction du milieu fluide homogène équivalent. Un schéma du montage est montré dans la figure R1.16.c.



## Couplage

Figure R1.16 a) Vue en coupe du guide de Nitrure de Silicium. b) Différence entre couplage par réseau de diffraction et couplage par la tranche c) Schéma du montage optique.

Avec le montage décrit ci-dessus, 2 types de mesures peuvent être réalisées : longueur d'onde fixe et variable. Pour le dispositif final, l'option de travailler à une longueur d'onde fixe est intéressante, car cela impliquerait une intégration moins coûteuse (un laser et un photodétecteur). Par contre, dans ce cas, la plage de travail est plus limitée à une demi-largeur de la résonance du dispositif.

L'autre option est d'exciter le dispositif avec plusieurs longueurs d'onde. Cela permet de détecter la forme du creux de transmission et d'avoir une plage de travail plus grande. L'inconvénient de cette méthode est la nécessité d'un système plus complexe et plus coûteux (utiliser plusieurs lasers ou un laser accordable et un spectromètre en sortie). Le choix dépendra du cahier des charges en sensibilité et de la plage dynamique du dispositif final, autrement dit de l'application visée.

Les mesures effectuées sur le banc de caractérisation sont de 2 types : mesure de changement d'indice de réfraction du volume fluide (mesures bulk) et de changement d'indice de la partie fonctionnalisée à la surface du dispositif. Les protocoles de mesure pour les 2 méthodes sont présentés ci-dessous.

Protocole pour les mesures bulk :

1. Mesure de la réponse du dispositif dans l'air
2. Injection dans la cellule micro fluide du liquide souhaité
3. Suivi en temps réel de la réponse avec le nouveau milieu



Pour l'instant le dispositif a été testé dans l'air, l'eau dé ionisée, de l'éthanol et avec une solution tampon saline (Phosphate Buffered Saline ou PBS) qui sera vraisemblablement le milieu d'analyse des molécules. Dans le futur, des liquides d'indice possédant des valeurs d'indice autour de celui du PBS pourront être achetés pour faire des mesures avec un pas constant. (voir producteur Cargille séries AAA entre 1,300 et 1,395, pas de 0,005, 0,01 ou sur mesure selon la disponibilité).

Protocole de mesure pour les mesures surfaciques (chimie non-différentielle) :

La réaction biotine-streptavidine a été choisie pour sa stabilité et facilité d'implémentation.

A) Absorption de l'albumine de sérum bovin (bovine serum albumin ou BSA)-biotine (1mg / 1mL):

1. Mesure de la réponse de l'anneau avec le buffer PBS
2. Injection de biotine attachée sur BSA (1mg / 1mL), mesure en temps réel pendant 30min jusqu'à atteinte d'un plateau du signal
3. Rinçage PBS de la surface, mesure en temps réel jusqu'à atteinte d'un plateau

B) Liaison de la biotine à la streptavidine ( $5\mu\text{g}/1\text{mL}$ )

1. Injection de streptavidine, mesure en temps réel jusqu'à atteinte d'un plateau<sup>13</sup>
2. Rinçage PBS de la surface, mesure en temps réel jusqu'à atteinte d'un plateau

La figure R1.17 montre le banc de caractérisation : les figures R1.17.a et R1.17.b montrent le synoptique du banc de caractérisation et du circuit complet, photonique et fluïdique. Les figures R1.17.c montre la photographie du banc de caractérisation et de l'échantillon avec le réservoir en PDMS.

---

<sup>13</sup> . Ce protocole a aussi été testé avec une méthode able (résonance des plasmons de surface ou Surface Plasmon Resonance ou SPR) pour confirmer que la chimie de surface fonctionne correctement.

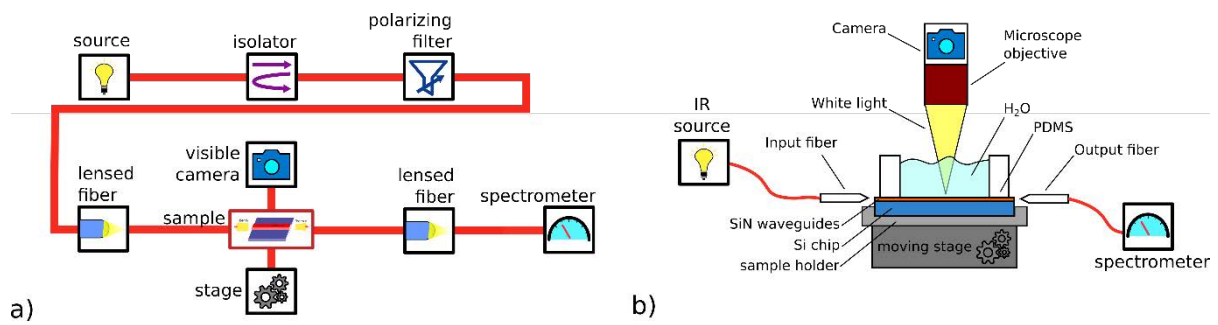


Figure R1.17 Banc de caractérisation a) Synoptique du banc de caractérisation b) Schéma du banc de caractérisation avec la partie microfluidique c) photographie du banc de caractérisation et du réservoir en PDMS

## Mesures bulk – mesures de sensibilité

Les résultats expérimentaux sont présentés et comparés aux simulations précédentes. Cette section est divisée en trois parties. La première détaille les premiers tests des dispositifs HPWG. La comparaison avec les simulations a conduit à de nouvelles investigations sur la géométrie des dispositifs et l'indice de réfraction des matériaux. Les caractérisations supplémentaires et le retour sur expérience finalisé par l'élaboration d'une deuxième série de dispositifs est exposé dans la deuxième partie. La troisième partie présente les résultats de la deuxième série de dispositifs et les conclusions sur les mesures bulk.

## Mesures bulk – premiers dispositifs

Avant les premières mesures, les écarts entre le SiN et l'au ont été mesurés au microscope électronique à balayage (ou MEB) pour avoir une mesure précise de l'espacement guide d'onde/métal (environ 10 nm d'incertitude). La figure R1.18 montre les schémas de la section transversale des trois résonateurs en anneau considérés dans cette étude. On peut remarquer que pour ces échantillons, l'alignement de l'au autour du SiN n'était pas encore entièrement optimisé (décalage de l'au 170 nm, 130 nm et 65 nm, comme le montre l'image R1.18). Les premiers résultats, calculés à la fois avec les méthodes de *peak-search* et de FFT (méthodes développées dans ce travail de thèse pour extraire la position du minimum de résonance avec la plus grande précision), sont présentés sur la figure R1.19 et comparés à la sensibilité simulée. Des simulations sont effectuées en prenant l'indice de réfraction de la littérature de l'au par Johnson et Christy (désormais Au JC)[17] et la géométrie du guide d'onde mesurée expérimentalement.

La première remarque concerne la sensibilité: la comparaison avec les résultats de simulation montre que la sensibilité est inférieure à celle attendue, à l'exception de la méthode de recherche de pic de l'échantillon PR22\_4G, qui a toutefois une grande incertitude.

La deuxième remarque est la comparaison entre les deux méthodes de calcul de décalage illustrées à la figure R1.19: la méthode de *peak-search* présente une incertitude similaire ou plus élevée que la méthode FFT comme indiqué dans la littérature. La comparaison a confirmé cette hypothèse, donc la méthode FFT est celle considérée dans ce travail. La

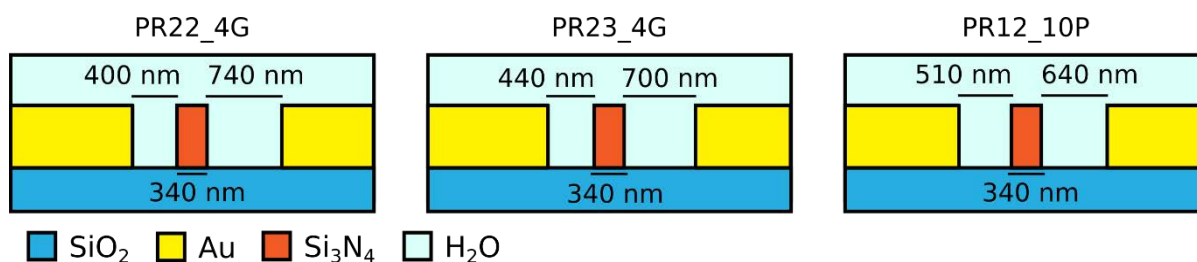


Figure R1.18 cross section of the three considered samples with the gap measured at the Electron Scanning Microscope.

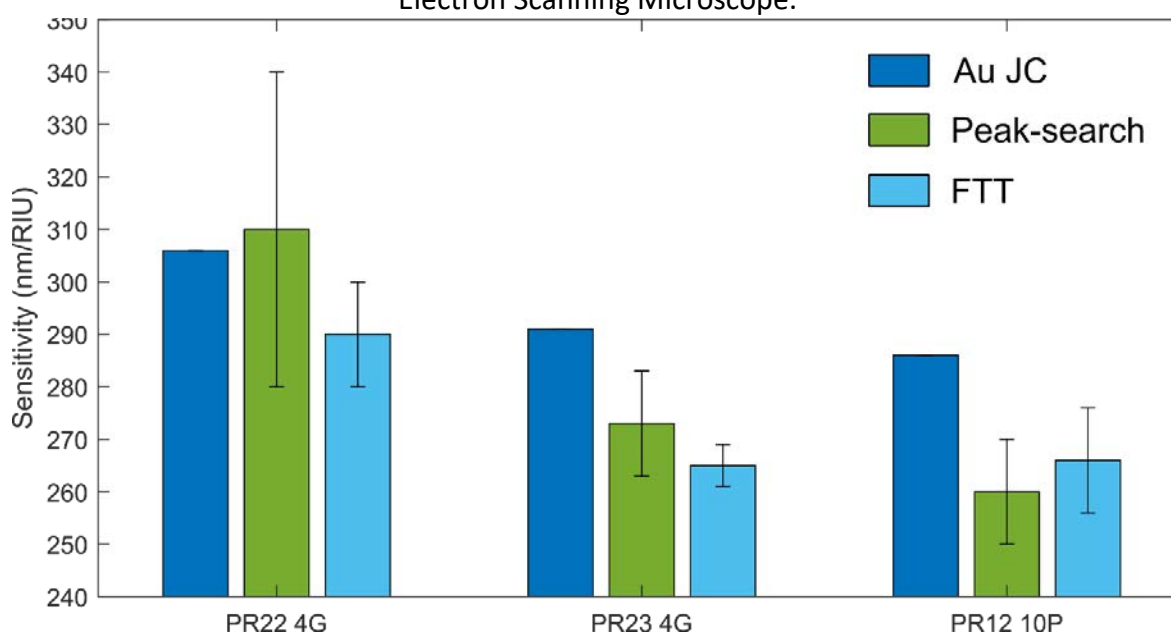


Figure R1.19 Etude comparative de la sensibilité du dispositif entre les simulations en considérant l'indice de réfraction de l'au Jonhson et Cristy (bleu foncé barres d'erreurs en noir) et les résultats expérimentaux obtenus avec les méthodes peak-search (vert) and FFT (bleu clair)

sensibilité plus faible des résultats expérimentaux par rapport aux simulations nécessite une analyse plus approfondie pour comprendre les raisons possibles de cet écart. Des mesures complémentaires ont été effectuées pour déterminer la géométrie réelle du dispositif et déterminer les indices de réfraction des matériaux. L'analyse de la géométrie a été déterminée avec un AFM et les indices de réfraction grâce à l'ellipsométrie. Les conclusions de cette étude montrent que l'au doit être déposé plus lentement (à 0.7 Å/min à la place de 8 Å/min) pour obtenir un indice de réfraction identique à la littérature et les guides d'onde sont plus larges et épais que prévu. Cela a permis de fabriquer une deuxième génération de dispositifs avec une partie métallique optimisée.

## Mesures bulk – comparaison entre la première et la deuxième série de dispositifs

Sur la base de la géométrie et des indices de réfraction mesurés grâce à l'analyse approfondie, les simulations sont ajustées afin d'étudier l'influence des paramètres de fabrication sur les performances.

Un histogramme similaire à celui de la figure R1.19 compare l'indice de réfraction de la littérature de Au JC, le Au INL déposé rapidement et l'influence de la couche d'adhésion de Cr. Les résultats de la simulation ont été comparés aux mesures des trois résonateurs en anneau HPWG précédemment analysés.

La figure R1.20 compare la littérature Au JC (jaune), l'INL Au rapide (bleu) et la couche d'adhésion Cr (bleu clair et bleu foncé) avec les résultats expérimentaux (gris de recherche de pic et rouge FFT). On peut remarquer que la sensibilité expérimentale est plus proche de celle des simulations avec INL Au et couche d'adhérence 5nm Cr, qui est le modèle le plus précis. La figure R1.20 compare les pertes des différentes configurations pour les trois échantillons.

La baisse de sensibilité et les pertes s'expliquent de la façon suivante:

1. La première considération est que le guide d'onde SiN n'est pas réellement en dessous du seuil de coupure sur la base des mesures AFM. Comme indiqué avant, la sensibilité du HPWG diminue lorsque le guide d'onde SiN est au-dessus de la coupure.
2. Le deuxième point concerne la constante diélectrique de l'Au: lorsque l'Au est déposé rapidement, le matériau est moins dense en raison de la distribution moins organisée des grains d'Au. Cela signifie que la valeur absolue de la partie réelle de la constante diélectrique diminue en raison de l'air à l'intérieur du matériau et, par conséquent, réduit les effets plasmoniques.
3. La troisième considération est que le Cr diminue la sensibilité et introduit des pertes de propagation supplémentaires. Cela est dû à sa constante diélectrique qui ne favorise pas l'effet plasmonique. Cependant, la présence de Cr est nécessaire car sans lui, Au n'adhérera pas au substrat.

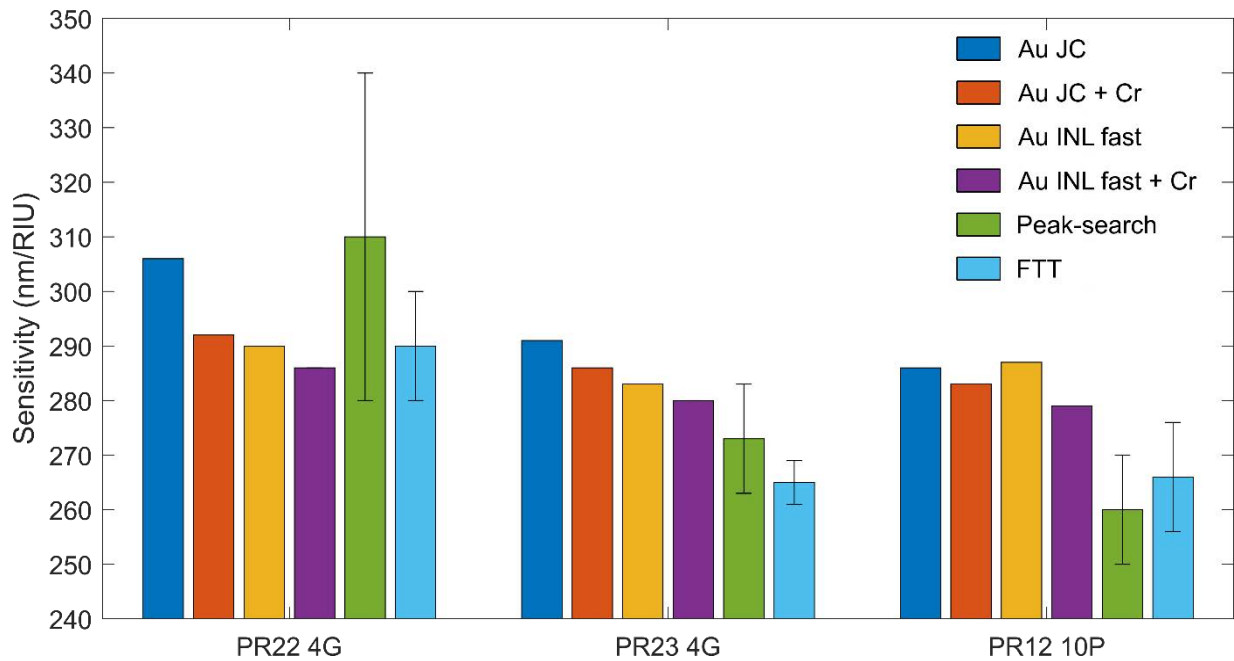


Figure R1.20 comparison of the sensitivity for simulated devices and the experimental results for three samples, PR22\_4G, PR23\_4G and PR12\_10P.

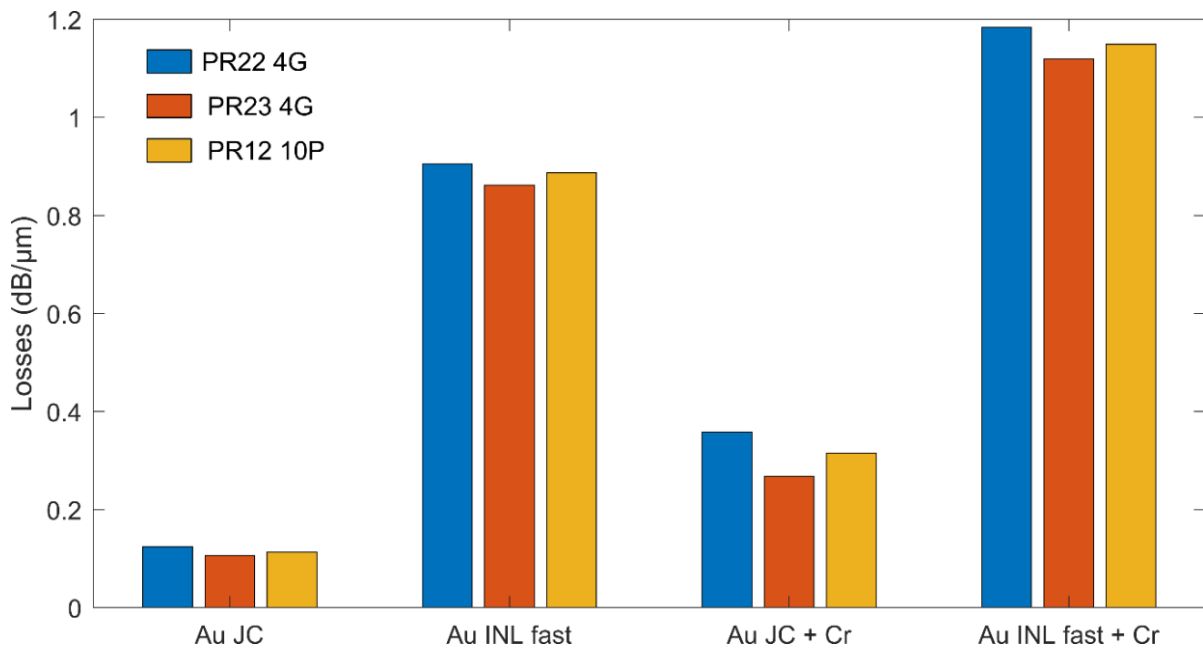


Figure R1.21 Simulation des pertes de propagation des 3 échantillons PR22\_4G, PR23\_4G et PR12\_10P, pour différentes configurations Au. Au INL dépôt rapide, Au+Cr et Au+Cr INL dépôt rapide. L'ajout de la couche d'accroche de Cr et la porosité induit par le dépôt rapide induisent un surcroît de pertes de propagation.

Le paragraphe suivant décrit les solutions pour optimiser la fabrication des patches plasmoniques en tenant compte de la considération susmentionnée.

Dans la deuxième série de dispositifs, les caractéristiques optimales ont été appliquées sur la base des considérations précédentes: l'Au a été déposé lentement pour améliorer ses effets

plasmoniques (Au INL slow). L'épaisseur de la couche d'adhérence Cr, fondamentale pour le dépôt d'Au, est réduite de 5 nm à 2 nm après avoir testé l'adhérence à travers un bain à ultrasons dans l'acétone. Concernant la largeur du SiN, des guides d'ondes de 340 nm de largeur nominale guident en fait. Il est intéressant de comparer la réponse à des guides d'ondes plus minces, de 300 nm de largeur. Les sections des nouveaux dispositifs sont représentées sur la figure R1.22. On peut remarquer que le processus d'alignement d'Au a été optimisé par le faible décalage latéral (environ 10 nm). Étant donné que ces effets ont été pris en compte au cours des derniers mois de ce projet de doctorat, seuls très peu de dispositifs ont les caractéristiques optimales et davantage d'analyses seront effectuées dans un futur proche.

La figure R1.22 compare les résultats expérimentaux entre les guides d'ondes SiN avec et sans Au à la fois 300 nm et 340 nm de largeur, lorsque seulement 10% de l'anneau est en HPWG. Il est important de rappeler le principe du «mode lift» que nous étudions: les simulations suggèrent que la sensibilité s'améliore lorsque les modes plasmoniques ont une forte interaction avec un guide d'onde sous la coupure (voir chapitre 4 pour plus de détails).

La première remarque concerne les résonateurs HPWG avec une largeur de SiN de 300 nm: l'amélioration de la sensibilité (de 210 à 320 nm / RIU) suggère que le mode du guide d'onde de SiN préalablement sous la coupure est correctement translaté au-dessus de la coupure grâce à l'interaction avec le mode plasmonique du métal, tout en confinant le flux d'énergie dans le liquide de détection. De plus, le résonateur est encore plus sensible par rapport aux résultats à 340 nm. La deuxième remarque concerne le guide d'onde à 340 nm: l'ajout de l'Au à 340 nm n'affecte pas beaucoup la sensibilité. Ce fait soutient l'hypothèse que les guides d'ondes à 340 nm sont en fait des guides d'ondes au-dessus de la coupure et qu'ils n'interagissent pas suffisamment avec les modes plasmoniques. Le facteur Q de ces résonateurs est dans la même gamme de valeurs, autour de  $1000 \pm 200$ . La variation est justifiée par les différentes sources de pertes (pertes plasmoniques ou radiations).

Nous sommes conscients que pour valider le concept, une analyse statistique doit être effectuée avec plusieurs dispositifs, afin de vérifier la répétabilité de ces résultats. Cela n'a pas été possible en raison d'un temps limité. Cependant, l'incertitude combinée (indiquée par les barres d'erreur de la figure R1.22) suggère que l'incertitude de fabrication, l'incertitude de température et l'incertitude des indices de réfraction ne devraient pas modifier de manière significative la tendance des résultats.

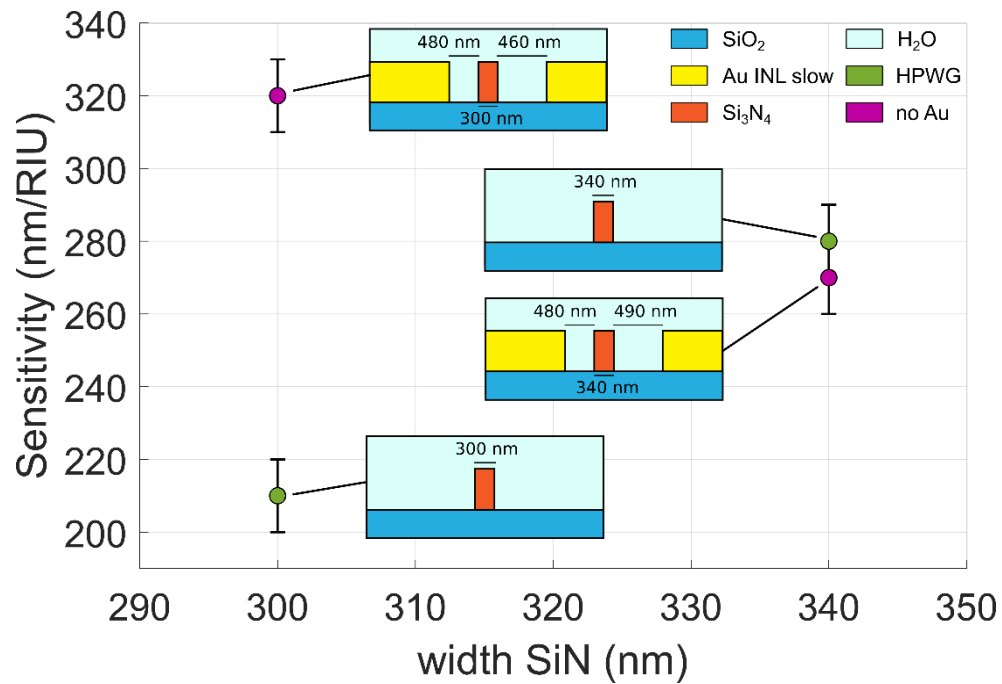


Figure R1.22 Sensibilité mesurée pour différents résonateurs avec 2 largeurs de guides d'onde SiN et avec ou sans Au.



## Mesures du adlayer

Des tests concernant les adlayer, fine couches biologiques, sont effectués avec la protéine de sérum albumine bovine (ou BSA). Comme expliqué au chapitre 3, le BSA est le meilleur candidat car il adhère à la plupart des surfaces et il a une épaisseur adaptée au HPWG (environ 4 nm). Étant une protéine, la solution tampon n'est pas H<sub>2</sub>O mais une solution saline tamponnée au phosphate (ou PBS). Le protocole de détection consiste à exposer l'échantillon à une concentration croissante de BSA, de 20 à 50 µmol/mL. Bien que le test préliminaire effectué sur des échantillons diélectriques ait montré une réponse au dépôt, nous ne pouvons pas encore tirer de conclusion sur la sensibilité en raison du manque de mesures de répétabilité sur les protéines. Les tests sont toujours en cours pour finaliser la répétabilité et l'étape suivante consistera à tester les échantillons HPWG.

## Fonctionnalisation différentielle

Une fois que les tests BSA ont fourni les résultats d'une fonctionnalisation homogène, l'étape suivante consiste à considérer l'avantage de la fonctionnalisation différentielle. La fonctionnalisation différentielle permet de localiser sélectivement les particules dans des parties bien définies du capteur. Lorsque ces parties sont les sites sensibles du capteur, la probabilité de détection de molécule augmente. Par conséquent, l'avantage de la fonctionnalisation différentielle est l'amélioration du signal pour les faibles concentrations d'analyte[18]. La fonctionnalisation différentielle est particulièrement stable entre les surfaces métalliques et diélectriques. En particulier, l'or est connu en biologie pour son affinité avec l'atome S dans des composés organiques appelés thiols. Cependant, l'affinité entre l'or et les thiols dépend fortement de la qualité de la surface de l'or, donc du dépôt et des étapes de fabrication précédentes. La première étape consiste alors à vérifier que la fonctionnalisation différentielle fonctionne sur l'or INL après toutes les étapes de fabrication. Cette étape a été faite avec des échantillons test où le lift-off n'avait pas marché complètement. Ils montrent que la fonctionnalisation marche avec le protocole de nettoyage. Afin de voir la position des thiols, des nanoparticules fluorescentes ont été attachées grâce à l'interaction biotine-streptavidine. Les images de fluorescence ont permis de vérifier que la fonctionnalisation était effectivement sélective entre l'or et le diélectrique. La prochaine étape sera de répéter le même protocole avec les échantillons de deuxième génération pour pouvoir mesurer le changement du pic de résonance pendant les différentes étapes.

# Conclusion

L'objectif de ce projet de thèse a été de concevoir, construire et tester un transducteur photonique compatible avec les systèmes Lab On Chip. Les principaux objectifs sur lesquels nous nous sommes concentrés sont: la transduction biologique sensible, compatible avec la fabrication industrielle en grands volumes et à faible coût, compacte et polyvalente pour différentes cibles biologiques. En d'autres termes, l'objectif de ce projet était de répondre à la question de recherche suivante:

"Comment concevoir et fabriquer un biocapteur compact basé sur un transducteur en photonique intégrée, simple à fonctionnaliser, compatible avec une plateforme industrielle et lab-on-chip, ayant une sensibilité égale ou supérieure à l'état de l'art?"

Pour répondre à cette question, l'état de l'art a été analysé et nous avons constaté que le guide d'onde hybride plasmonique (HPWG) était le plus compatible avec nos objectifs. Par ailleurs, sur la base d'un principe appelé *mode lift*, une nouvelle géométrie de HPWG a été brevetée. La simulation de la structure HPWG a permis de comprendre les mécanismes de couplage des modes à l'intérieur de la structure (plus précisément le guide d'onde plasmonique et le guide d'onde ruban).

La fabrication a été possible grâce à la collaboration de la salle blanche industrielle avec les deux salles blanches universitaires. L'un des avantages de la production industrielle est la grande reproductibilité des dispositifs: les mesures statistiques de la plate-forme DAPHNE donnent une idée de la variation de la géométrie fabriquée. Une fois que les wafers ont été structurés dans la salle blanche industrielle, le processus de fabrication en salle blanche de l'université était conçu pour ajouter les guides d'ondes métalliques. Parmi les nombreuses propositions, deux méthodes ont été explorées: la méthode du *lift-off* et la méthode CMP. Alors que la méthode CMP est compatible avec un procédé industriel, la méthode de *lift-off* est plus facile à mettre en œuvre et c'est celle qui a fourni les dispositifs caractérisés lors de ce projet.

Une fois les dispositifs fabriqués, la caractérisation était possible: les mesures préliminaires définissaient le liquide d'essai optimal (glucose monohydrate) et l'incertitude des mesures. Les échantillons de HPWG ont été caractérisés et on a découvert que la sensibilité expérimentale est inférieure aux simulations. Après avoir ajusté les paramètres de fabrication (principalement les taux et épaisseurs de dépôt d'Or et de Chrome), les dispositifs de deuxième génération indiquent que l'effet plasmonique du HPWG (appelé *mode lift*) améliore la sensibilité des guides d'ondes sous la coupure (de 210 nm/RIU à 320 nm/RIU lorsque seulement 10% de l'anneau a une section HPWG). Ce résultat est également comparé aux guides d'onde en ruban au-dessous de la coupure avec une augmentation de la sensibilité est de 40 nm / RIU pour 10% de l'anneau, ce qui démontre l'efficacité du concept de mode lift. Nous avons également montré la compatibilité des dispositifs fabriqués avec une fonctionnalisation différentielle, au moyen de nanoparticules fluorescentes. En raison de contraintes de temps, la présence des nanoparticules sera mesurée avec les dispositifs fabriqués lors de futures expériences.



## References

- [1] Alam, M. Z. (2013). Hybrid Plasmonic Waveguides theory and Applications. Library and Archives Canada = Bibliothèque et Archives Canada, Ottawa.
- [2] Alam, M. Z., Aitchison, J. S. et Mojahedi, M. (2013). Theoretical Analysis of Hybrid Plasmonic Waveguide. *IEEE Journal of Selected Topics in Quantum Electronics*, volume 19, numéro 3, p. 4602008 4602008.
- [3] Alam, M. Z., Aitchison, J. S. et Mojahedi, M. (2014). A marriage of convenience : Hybridization of surface plasmon and dielectric waveguide modes. *Laser & Photonics Reviews*, volume 8, numéro 3, p. 394 408.
- [4] Almeida, V. R., Xu, Q., Barrios, C. A. et Lipson, M. (2004). Guiding and con ning light in void nanostructure. *Optics Letters*, volume 29, numéro 11, p. 1209.
- [5] Barnes, W. L., Dereux, A. et Ebbesen, T. W. (2003). Surface plasmon subwavelength optics. *nature*, volume 424, numéro 6950, p. 824.
- [6] Berini, P. (2008). Bulk and surface sensitivities of surface plasmon waveguides. *New Journal of Physics*, volume 10, numéro 10, p. 105010.
- [7] Choo, S. J., Kim, J., Lee, K. W., Lee, D. H., Shin, H.-J. et Park, J. H. (2014). An integrated Mach Zehnder interferometric biosensor with a silicon oxynitride waveguide by plasma-enhanced chemical vapor deposition. *Current Applied Physics*, volume 14, numéro 7, p. 954 959.
- [8] Ciminelli, C., Dell’Olio, F., Conteduca, D., Campanella, C. M. et Armenise, M. N. (2014). High performance SOI microring resonator for biochemical sensing. *Optics & Laser Technology*, volume 59, numéro Supplement C, p. 60 67.
- [9] Ciminelli, C., Dell’Olio, F., Conteduca, D., Innone, F., Tatoli, T. et Armenise, M. N. (2016). New microphotonic resonant devices for label-free biosensing. Dans 2016 18th International Conference on Transparent Optical Networks (ICTON). p. 1 4.
- [10] Claes, T., Bogaerts, W. et Bienstman, P. (2010). Experimental characterization of a silicon photonic biosensor consisting of two cascaded ring resonators based on the Vernier-effect and introduction of a curve tting method for an improved detection limit. *Optics Express*, volume 18, numéro 22, p. 22747 22761.
- [11] Claes, T., Molera, J. G., Vos, K. D., Schacht, E., Baets, R. et Bienstman, P. (2009). Label-Free Biosensing With a Slot-Waveguide-Based Ring Resonator in Silicon on Insulator. *IEEE Photonics Journal*, volume 1, numéro 3, p. 197 204.
- [12] Dell’Olio, F. (2015). New ultrasensitive resonant photonic platform for label-free biosensing. *OSA*.
- [13] Guner, H., Ozgur, E., Kokturk, G., Celik, M., Esen, E., Topal, A. E., Ayas, S., Uludag, Y., Elbuken, C. et Dana, A. (2017). A smartphone based surface plasmon resonance imaging

---

(SPRi) platform for on-site biodetection. *Sensors and Actuators B : Chemical*, volume 239, p. 571 577.

- [14] HORIBA, L. (2018). Openplex - flexible surface plasmon resonance imaging system.
- [15] Iqbal, M., Gleeson, M. A., Spaugh, B., Tybor, F., Gunn, W. G., Hochberg, M., BaehrJones, T., Bailey, R. C. et Gunn, L. C. (2010). Label-Free Biosensor Arrays Based on Silicon Ring Resonators and High-Speed Optical Scanning Instrumentation. *IEEE Journal of Selected Topics in Quantum Electronics*, volume 16, numéro 3, p. 654 661.
- [16] Ma, T., Yuan, J., Sun, L., Li, F., Kang, Z., Yan, B., Sang, X., Wang, K., Wu, Q., Liu, H., Gao, J. et Yu, C. (2017). Highly Sensitive Biochemical Sensor Based on Two-Layer Dielectric Loaded Plasmonic Microring Resonator. *Plasmonics*, volume 12, numéro 5, p. 1417 1424.
- [17] Oulton, R. F., Sorger, V. J., Genov, D. A., Pile, D. F. P. et Zhang, X. (2008). A hybrid plasmonic waveguide for subwavelength confinement and long-range propagation. *Nature Photonics*, volume 2, numéro 8, p. 496.
- [18] Palazon, F., Léonard, D., Le Mogne, T., Zuttion, F., Chevalier, C., Phaner-Goutorbe, M., Souteyrand, I., Chevolot, Y. et Cloarec, J.-P. (2015). Orthogonal chemical functionalization of patterned gold on silica surfaces. *Beilstein Journal of Nanotechnology*, volume 6, p. 2272 2277.
- [19] Samusenko, A., Gandol, D., Pucker, G., Chalyan, T., Guider, R., Ghulinyan, M. et Pavesi, L. (2016). A SiON Microring Resonator-Based Platform for Biosensing at 850 nm. *Journal of Lightwave Technology*, volume 34, numéro 3, p. 969 977.
- [20] Spackova, B., Wrobel, P., Bockova, M. et Homola, J. (2016). Optical Biosensors Based on Plasmonic Nanostructures : A Review. *Proceedings of the IEEE*, volume 104, numéro 12, p. 2380 2408.
- [21] Steglich, P., Villringer, C., Pulwer, S., Heinrich, F., Bauer, J., Dietzel, B., Mai, C., Mai, A., Casalboni, M. et Schrader, S. (2017). Hybrid-Waveguide Ring Resonator for Biochemical Sensing. *IEEE Sensors Journal*, volume 17, numéro 15, p. 4781 4790.
- [22] Sun, X., Dai, D., Thylén, L. et Wosinski, L. (2015). Double-Slot Hybrid Plasmonic Ring Resonator Used for Optical Sensors and Modulators. *Photonics*, volume 2, numéro 4, p. 1116 1130.
- [23] Sun, X., Dai, D., Thylén, L. et Wosinski, L. (2015). High-sensitivity liquid refractiveindex sensor based on a Mach-Zehnder interferometer with a double-slot hybrid plasmonic waveguide. *Optics Express*, volume 23, numéro 20, p. 25688 25699.
- [24] Taniguchi, T., Hirowatari, A., Ikeda, T., Fukuyama, M., Amemiya, Y., Kuroda, A. et Yokoyama, S. (2016). Detection of antibody-antigen reaction by silicon nitride slot-ring biosensors using protein G. *Optics Communications*, volume 365, p. 16 23
- [25] Technologies, A. (2018). The digital olfaction company.



## FOLIO ADMINISTRATIF

### THESE DE L'UNIVERSITE DE LYON OPEREE AU SEIN DE L'INSA LYON

NOM : CALVO

DATE de SOUTENANCE : 21/07/2020

Prénoms : Michele

TITRE : Etude et réalisation de capteurs biologiques à base d'effets plasmoniques et fabriqués sur silicium

NATURE : Doctorat

Numéro d'ordre : 2020LYSEI055

Ecole doctorale : Electronique, l'Electrotechnique, l'Automatique

Spécialité : Nanophotonique

#### RESUME :

Ce projet de doctorat s'insère dans le domaine des biocapteurs et a pour objectif à long terme de développer un dispositif type Lab-On-Chip. Ce dernier doit être capable de détecter un analyte spécifique, tout en étant compact et bon marché, pour en permettre l'utilisation par des médecins, à l'hôpital ou chez les patients, sans avoir besoin d'un laboratoire entier. Cet objectif est possible avec un transducteur photonique qui converti efficacement la présence de l'analyte biologique en signal électrique. Pour cela, on combine deux types de guides d'onde, un de type ruban diélectrique et un autre de type plasmonique, pour en créer un guide hybride qu'associe les faibles pertes de l'un à la sensibilité de l'autre. L'élément innovant mis en évidence dans cette étude est la géométrie particulière de ce guide hybride (Hybrid Plasmonic WaveGuide), notamment la faible largeur du guide ruban diélectrique. Dans cette étude, le capteur est optimisé en partant de l'étude théorique, en passant par la simulation numérique, jusqu'à la fabrication et caractérisation du dispositif.

#### MOTS-CLÉS :

Lab-on-a-chip, photonique, plasmonique, photonique intégrée, résonateur en anneau, biocapteurs.

Laboratoire (s) de recherche : INL - Institut des Nanotechnologies de Lyon (INL) (UMR5270), Université de Sherbrooke, STMicroelectronics

Directeurs de thèse: Régis Orobtcouk, Paul G. Charrette

Président de jury : Christelle Monat

Composition du jury : Jean Claude Weeber, Gilles Lerondel, Andrea Melloni, Sylvie Menezo, Christelle Monat, Paul G. Charrette, Michael Canva, Régis Orobtcouk, Stephane Monfray